

An enhanced maximum-entropy based meshfree method: theory and applications

Thesis by
Siddhant Kumar

In Partial Fulfillment of the Requirements for the
Degree of
Doctor of Philosophy in Aeronautics

The logo for the California Institute of Technology (Caltech), featuring the word "Caltech" in a bold, orange, sans-serif font.

CALIFORNIA INSTITUTE OF TECHNOLOGY
Pasadena, California

2019
Defended March 18, 2019

© 2019

Siddhant Kumar

ORCID: 0000-0003-1602-8641

All rights reserved except where otherwise noted

To my parents

ACKNOWLEDGEMENTS

This thesis would not have been possible without the help and support of many people in my life. I would like to express them all my gratitude.

I would first like to thank my advisor, Professor Dennis Kochmann. You've taught me a great deal with your patience, intuition, and passion for research, and I mean it in the most sincere way that you are my academic role model. Between three universities in three different countries, it was amazing how well we worked with each other remotely until halfway into my PhD. You provided me with numerous inspirations in our early morning Skype calls, late-night email exchanges and spontaneous conversations when I just pop into your office. I'm excited to share the next stage of my research career with you by joining as a postdoc in your group. I look forward to many more fruitful discussions and collaborations.

I would also like to present my gratitude to Professor Kostas Danas. More than just my masters thesis at École Polytechnique, our work together laid the foundation of my PhD work and this thesis. I will always remember our discussions on how to bring context to numerical methods in applied mechanics, and learned that my research could also make concrete impact. It was my pleasure working with you and I hope we can collaborate again in the future.

I would like to thank Professor Michael Ortiz and Professor Kaushik Bhattacharya for generously taking out time to be part of the committee and providing feedback on the thesis. While we did not get a lot of opportunities to interact and exchange ideas, this thesis would not have been possible without the core concepts of solid mechanics that I learned in your Ae-102 classes, as well as your papers that provided a starting point for my research work.

I also want to thank all members of the Kochmann group at Caltech and ETH Zurich that I had the fortunate opportunity to work with: Vidyasagar, Abbas Tutcuoglu, Carlos Portela, Greg Philipot, Wei-Lin Tan, Ishan Tembhekar, Raphael Glaesener, Bastian Telgen, Vignesh Kannan, Claire Lestringant, Romik Khajehtourian, Manuel Weberndorfer, Roman Indergand, Yannick Hollenweger, among many others. I would like to extend my special thanks to Vidyasagar, Abbas, and Yannick, whom I've had close collaborations with. I would like to thank all the administrative staff at Caltech, and ETH Zurich. I would like to extend my special thanks to Maria and Denise for helping me navigate the administrative troubles. I would also like

to thank my office-mate, Manuel, for our nerdy conversation on C++, which has always motivated me to become better at programming.

I would like to thank Stephanie Tan for all the support and encouragement over the years. Thank you for sharing the moments of highs and lows and being a great friend.

Lastly, I would like to thank my parents. Your encouragements were never absent when I needed them most. Thank you for enduring hardships for over two decades to make sure that my academics were never compromised. Thank you for believing in me. I am extremely grateful.

ABSTRACT

This thesis develops an enhanced meshfree method based on the local maximum-entropy (max-ent) approximation and explores its applications. The proposed method offers an adaptive approximation that addresses the tensile instability which arises in updated-Lagrangian meshfree methods during severe, finite deformations. The proposed method achieves robust stability in the updated-Lagrangian setting and fully realizes the potential of meshfree methods in simulating large-deformation mechanics, as shown for benchmark problems of severe elastic and elastoplastic deformations. The improved local maximum-entropy approximation method is of a general construct and has a wide variety of applications. This thesis presents an extensive study of two applications – the modeling of equal-channel angular extrusion (ECAE) based on high-fidelity plasticity models, and the numerical relaxation of nonconvex energy potentials. In ECAE, the aforementioned enhanced maximum-entropy scheme allows the stable simulation of large deformations at the macroscale. This scheme is especially suitable for ECAE as the latter falls into the category of severe plastic deformation processes where simulations using mesh-based methods (e.g. the finite element method (FEM)) are limited due to severe mesh distortions. In the second application, the aforementioned max-ent meshfree method outperforms FEM and FFT-based schemes in numerical relaxation of nonconvex energy potentials, which is essential in discovering the effective response and associated energy-minimizing microstructures and patterns. The results from both of these applications show that the proposed method brings new possibilities to the subject of computational solid mechanics that are not within the reach of traditional mesh-based and meshfree methods.

PUBLISHED CONTENT AND CONTRIBUTIONS

- S. Kumar, K. Danas, and D. M. Kochmann. Enhanced local maximum-entropy approximation for stable meshfree simulations. *Computer Methods in Applied Mechanics and Engineering*, 344:858 - 886, 2019.
DOI: <https://doi.org/10.1016/j.cma.2018.10.030>
S.K. conceptualized the idea, implemented the numerical schemes, performed benchmark simulations, and wrote the manuscript under the guidance of K.D. and D.M.K.
- S. Kumar, A. Vidyasagar, and D. M. Kochmann. An assessment of numerical techniques to find energy-minimizing microstructures of nonconvex energy potentials. *Under review*, 2019.
S.K. developed and implemented the meshfree scheme. A.V. developed and implemented the FFT-scheme. S.K. performed all the simulations. S.K. and A.V. jointly wrote the manuscript under the guidance of D.M.K.
- S. Kumar[†], A. D. Tutcuoglu[†], Y. Hollenweger, and D. M. Kochmann. A multiscale meshfree approach to modeling ECAE. *In preparation*, 2019.
S.K. developed and implemented the macroscale model. A.T. developed and implemented the microscale and mesoscale models. S.K. and A.T. jointly wrote the manuscript under the guidance of D.M.K.

[†] Both authors contributed equally.

TABLE OF CONTENTS

Acknowledgements	iv
Abstract	vi
Published Content and Contributions	vii
Table of Contents	viii
List of Illustrations	x
List of Tables	xviii
Chapter I: Introduction	1
1.1 Motivation	1
1.2 Meshfree methods	3
1.2.1 Smoothed-particle hydrodynamics	4
1.2.2 Moving least squares	5
1.2.3 Reproducing kernel particle method	6
1.3 Limitations of meshfree methods	7
1.4 Maximum-entropy based meshfree methods	9
1.5 Outlook: Applications	12
1.5.1 Modeling of equal-channel angular extrusion based on high-fidelity plasticity models	12
1.5.2 Numerical energy relaxation in problems with nonconvex energetic potentials	13
1.6 Outline	14
Chapter II: Enhanced local maximum-entropy approximation for stable mesh-free simulations	16
2.1 Introduction	16
2.2 Enhanced local max-ent interpolation in updated-Lagrangian setting	18
2.2.1 Anisotropic local max-ent approximation	18
2.2.2 Quasi-static updated-Lagrangian formulation	25
2.2.3 Tensile instability	29
2.2.4 Anisotropic adaptivity and bounded shape function support	33
2.2.5 Treatment of essential boundary conditions and material interfaces	37
2.3 Benchmark tests	39
2.3.1 Benchmark I: extension of a hyperelastic block	41
2.3.2 Benchmark II: torsion of a hyperelastic cube	42
2.3.3 Benchmark III: hyperelastic laminate composite	45
2.3.4 Benchmark IV: high-volume-fraction composite with spherical inclusion	45
2.3.5 Benchmark V: Taylor anvil test	47
2.4 Conclusions	49
Appendices	52

2.A Derivation of solution (2.10)-(2.12) to constrained optimization problem in (2.9)	52
2.B Pseudo-code for hyperelastic boundary value problem	53
2.C Analytical solution of the finite-elasticity problem in Section 2.3.3	56
Chapter III: Modeling of equal-channel angular extrusion based on high-fidelity plasticity models	58
3.1 Introduction	58
3.2 Theory	61
3.2.1 Microscale: Copper material model	61
3.2.2 Mesoscale: Taylor model	63
3.2.3 Macroscale: Max-ent & updated-Lagrangian	64
3.3 Temporal evolution of internal variables	66
3.4 Results	69
3.4.1 Convergence with refinement in spatial and temporal discretization	70
3.4.2 Strain distribution and effect of channel geometry	70
3.4.3 Grain recrystallization and texture evolution	74
3.4.4 Mutli-pass ECAE	78
3.5 Conclusion	80
Appendices	83
3.A Simulation protocols	83
Chapter IV: Numerical energy relaxation in problems with nonconvex energetic potentials	85
4.1 Introduction: Energy relaxation and microstructural patterns	85
4.2 Numerical energy relaxation and pattern prediction	89
4.3 Numerical solution schemes	90
4.3.1 Finite element solution scheme	90
4.3.2 Spectral solution scheme	91
4.3.3 Max-ent solution scheme	93
4.3.4 Comparison of FEM, FFT and max-ent	95
4.4 Example 1: hyperelastic St. Venant-Kirchhoff solid	96
4.5 Example 2: phase transformations	98
4.5.1 A simple energetic model for phase transformations	98
4.5.2 Results for a double-well potential	103
4.5.3 Results for three-well potentials	103
4.6 Influence of spatial discretization and interfacial energy	108
4.6.1 Interfaces in the phase transformation model in 2D	110
4.6.2 Interfaces in the phase transformation model in 3D	116
4.6.3 Mesh-dependence of microstructures	119
4.6.4 Sharp vs. diffuse interfaces in the numerical schemes	120
4.7 Conclusions	122
Chapter V: Conclusion and future outlook	124
Bibliography	126

LIST OF ILLUSTRATIONS

<i>Number</i>	<i>Page</i>
1.1 Illustration of mesh distortion due to 90° rotation of a rigid circular inclusion (shaded blue) embedded in a soft matrix. (a,c) Initial spatial discretization in FEM and particle meshfree method, respectively. Dashed circle in (c) denotes the domain of influence of a node located inside the inclusion. (b,d) Post-deformation spatial discretization in FEM and particle meshfree method, respectively.	2
1.2 Illustration of (a) mesh-based and (b) meshfree shape function.	3
1.3 (a, b, c) Local max-ent shape functions $N^a(\mathbf{x})$ where a is the central node (located at $\mathbf{x}^a = (0.5, 0.5)^T$) of a 2D domain $\Omega = [0, 1]^2$ with equally spaced nodes (shown as black dots), evaluated for three different values of the locality parameter β . (d, e) Shape functions of nodes a lying on the corner and edge of the domain, respectively. (f) Shape function of an internal node a near the boundary $\partial\Omega$. Note that the shape function vanishes at the boundary, which demonstrates that the interpolation on the boundary is independent of the internal nodes.	11
1.4 Illustration of equal-channel angular extrusion (ECAE). A metal billet (shaded yellow) is extruded through a 90° angled channel (shaded blue) under the action of a plunger (denoted in red).	13
2.1 Local max-ent shape functions $N^a(\mathbf{x})$ evaluated at fixed interior point \mathbf{x} (viz., the central node) of a 2D node set with different choices of the locality parameter β . That is, the graphs show the value of each node's shape function N^a when evaluated at the central node, thus illustrating the contributions of nodal values to the interpolation at the central node. (We note that this visualization is different from that of Arroyo and Ortiz [7] and Figure 1.3 where $N^a(\mathbf{x})$ is plotted as a function of \mathbf{x} for fixed a). Cases (a,b,d) show the isotropic and (c,e) the anisotropic transition from global to local shape function support with increasing components of β	22

- 2.2 Local *max-ent* shape functions $N^a(\mathbf{x})$ evaluated at fixed point \mathbf{x} : (a) on an edge, (b) on a corner of a 2D node set. As in Figure 2.1, note that we do not plot a given shape function N^a as a function of position \mathbf{x} but we compute shape functions N^a at a given point \mathbf{x} 23
- 2.3 Illustration of the *total-Lagrangian* description (*dashed arrows*) where the current configuration is referenced to the initial configuration via the total deformation gradient \mathbf{F}_{n+1} , and of the *updated-Lagrangian* description (*solid arrows*) where the current configuration is referenced to the previous configuration via the incremental deformation gradient $\mathbf{F}_{n \rightarrow n+1}$. The red and black points denote material points and nodes, respectively. 30
- 2.4 For all shape functions evaluated at a material point initially at $x_0^p = 0.5$ on a 1D domain $\Omega_0 = [0, 1]$ with constant locality parameter $\beta_n^p = 1$, (a) values N^a of all $a = 1, \dots, n_n$ shape functions, plotted for different stretch ratios $\lambda = |\Omega_n|$; (b) associated internal nodal force kernels ($F_n^p \nabla_n N^a V_0^p$) of all shape functions evaluated for different stretches λ ; (c) internal nodal force kernels of selected nodes vs. strain $\varepsilon = \lambda - 1$; (d) internal nodal force on selected nodes vs. strain $\varepsilon = \lambda - 1$ 31
- 2.5 (a) Internal nodal force kernels and (b) internal nodal forces of selected nodes vs. strain $\varepsilon = \lambda - 1$, with an adaptively modified locality parameter $\beta_n^p \propto h_n^{-2}$ where h_n is the (uniform) nodal spacing and with an initial $\beta_0^p = 1$ 32
- 2.7 Evolution of the nodal connectivity surrounding a material point p (pink square) under significant affine shear deformation. Dashed lines denote the convex boundary of the cut-off region surrounding all nodes (blue solid circles) included in the material point's connectivity; nodal points missed by the isotropic update are shown as open (red) circles. Since, the simple shear deformation is isochoric, the isotropic update (2.46), shown as case (b), implies $R_1^p = R_0^p$ 36
- 2.8 Domains of nodal connectivity of four representative material points near an interface separating two different materials (indicated by the red and blue regions). Material points and nodes are denoted by open and filled dots, respectively. The hatched area around each material point indicates the cut-off region that encloses all nodes whose shape functions are contributing to the material point. 38

2.9	Shape function support for a material point (blue open dot) in the proximity of a non-convex material interface. The convex hull (indicated by black solid line) extends beyond the interface. However, only nodes in the blue region (indicated by blue filled dots) are considered during approximation construction. Nodes from the red region (indicated by red filled dots) that lie inside the convex hull are excluded from the approximation.	39
2.10	<i>Benchmark I</i> : extension of a hyperelastic block	43
2.11	<i>Benchmark II</i> : torsion of a hyperelastic cube	44
2.12	<i>Benchmark III</i> : hyperelastic laminate composite in a periodic RVE	46
2.13	<i>Benchmark IV</i> : hyperelastic high-volume-fraction composite with periodic spherical inclusions. (a) Initial state of the RVE with two hemispherical inclusions (both nodes and material points are shown in red and green) embedded in a matrix (both nodes and material points in blue). (b, c), (d,e), (f,g) show the deformed configuration and the stress distribution at 45%, 90%, and 135% extension, respectively. The stresses shown in (c, e, g) are the Cauchy stress component along the x -direction interpolated at the central plane of the RVE denoted by the red rectangles in (b, d, f). Due to the large deformations involved, the stress plots use different scales at each step for improved visibility.	48
2.14	<i>Benchmark V-(A)</i> : Taylor anvil test, showing (a) the initial specimen, (b) the time history of the mushroom radius, (c) the time history of the specimen height, and (d,e,f) cut-section views of the specimen near the wall with effective plastic strains evaluated at material points (nodes are shown as gray dots).	50
2.15	<i>Benchmark V-(B)</i> : Taylor anvil test, showing (a) the initial specimen, and (b,c,d) the effective plastic strains in the deformed sample, evaluated at the material points (nodes are shown as gray dots).	51
3.1	Illustration of the multiscale framework for simulating ECAE.	61
3.2	Illustration of the total- and updated-Lagrangian frameworks for simulating ECAE. The total deformation gradient F_{n+1} maps the initial configuration at time t_0 to the configuration at time t_{n+1} . The incremental deformation gradient $F_{n \rightarrow n+1}$ provides an incremental map between the configurations at t_n and t_{n+1}	65

3.3	Schematics of 3D ECAE model including initial configuration and boundary conditions on the specimen. All lengths are in non-dimensionalized units.	66
3.4	Illustration of the time integration scheme at the micro-, meso-, and macroscale with $n_m = 4$	68
3.5	Convergence of energy with respect to h -refinement. (a) Energy stored in the billet vs. time for four different nodal spacings. (b) Energy vs. nodal spacing evaluated at times $t \in \{t_{\max}/2, 3t_{\max}/4, t_{\max}\}$ as indicated in (a).	71
3.6	Convergence of energy with respect to temporal refinement. (a) Energy stored in the billet vs. time for four different time steps Δt . (b) Energy vs. time step Δt evaluated at times $t \in \{t_{\max}/2, 3t_{\max}/4, t_{\max}\}$ as indicated in (a).	72
3.7	Deformed spatial discretization at three different stages of the ECAE simulation. The yellow and red points denote material points and nodes, respectively.	73
3.8	Distribution of deformation gradient component F_{xy} for two different sets of chamfer dimensions. The black rectangles indicate regions of relatively homogeneous strain distribution compared to the billet ends. The red circles indicate regions of strong and localized strain inhomogeneity in the middle of the specimen. The plots are obtained by interpolating the deformation gradients onto the cross-sectional mid-plane via Gaussian interpolants of standard deviation equal to 0.3.	75
3.9	Temporal evolution of (a) number of active grains, and (b) average grain volume fraction, evaluated at three representative material points (indicated as A, B, and C).	77
3.10	Comparison of texture evolution when recrystallization is included vs. excluded. The pole figures are evaluated at four time steps for a representative material point indicated as red dot, along with position in the respective deformed configurations. The minimum and maximum values of each pole figure are denoted in blue and yellow boxes, respectively.	79
3.11	Evolution of (a) the total energy stored in the specimen, (b) the vertical force exerted by the plunger, when recrystallization is included/excluded.	80
3.12	Multi-pass ECAE	81

3.13	Texture evolution in multi-pass ECAE (described by the schematics in Figure 3.12a). The pole figures are evaluated at two time steps for a representative material point indicated as red dot, along with position in the respective deformed configurations. The minimum and maximum values of each pole figure are denoted in blue and yellow boxes, respectively.	82
4.1	Loss of convexity of the normalized energy $W(\gamma) = W(\mathbf{F}^0)/\lambda$ as the modulus ratio μ/λ decreases.	97
4.2	Relaxed energy densities computed by the FFT and max-ent schemes along with the analytical quasiconvex hull and the rank-one-convex hull (obtained from lamination) for case (i) : $\mu/\lambda = 10^{-5}$. The insets show energy-minimizing microstructural patterns predicted by the max-ent (top row) and FFT (bottom row) schemes at applied strain levels of $\gamma = 0.1, 0.2,$ and 0.3 (indicated as A, B, and C, respectively). Microstructural patterns are visualized by plotting the deformation gradient component F_{11}	99
4.3	(a) Relaxed energy densities computed by the FFT and max-ent schemes along with the analytical quasiconvex hull and the rank-one-convex hull (obtained from lamination) for case (ii) : $\mu/\lambda = 0.01$. (b) Convergence of the relaxed energy with h -refinement, computed by max-ent at different strain levels γ . Here, the error is defined as the difference between the numerically computed relaxed RVE energy density and the analytical quasiconvex energy at the three strain levels indicated by γ	99
4.4	Plot of $F^*(\mathbf{F})$ from (4.31) for the deformation gradient defined by (4.38) with $\mu = 1$ and $\kappa = 3$ for various values of k_T	102
4.5	Numerically computed relaxed energy density for the phase transformation model with a double-well energy. The dotted line denotes the nonconvex energy potential $W(\mathbf{F}^0)$ obtained from (4.24), while the solid line denotes the corresponding smoothed potential $F^*(\mathbf{F}^0)$ obtained from (4.31). Shown are the three curves obtained from the FFT, max-ent, and FEM schemes (the latter failing to converge early on).	104
4.6	Average RVE volume fraction of the second phase corresponding to the numerically computed relaxed energies shown in Fig. 4.5, using the phase transformation model with a double-well energy.	104

- 4.7 Microstructural patterns, color-coded by the dominant phase at each material point in the RVE, obtained numerically from energy relaxation using (a) the max-ent scheme, (b) the FFT scheme, and (c) the FEM scheme for case (i) with $\Psi_1 = 0$, $\Psi_2 = 0$. The two strain levels are indicated in Fig. 4.5, where the corresponding relaxed energy densities are shown. Here, the dominant phase is defined as the phase with higher volume fraction at a given material point. 105
- 4.8 (a) Numerically computed relaxed energy densities of the three-well phase transformation model for case (i): $\Psi_1 = 0$, $\Psi_2 = 4.5 \cdot 10^{-3}$, $\Psi_3 = 8 \cdot 10^{-3}$. The dotted line denotes the unrelaxed energy density (4.24), while the solid line denotes the corresponding smoothed energy density (4.31). (b) Average volume fractions of phases 2 and 3 corresponding to the relaxed energy curves, as obtained from the max-ent and FFT schemes (all three volume fractions sum up to 1). (c) and (d) Associated microstructural patterns, color-coded by the dominant phase at each point within the RVE, obtained from the max-ent and FFT schemes, respectively, at strain levels marked as A and B in (a) (the dominant phase is defined as the phase with highest volume fraction at a given point). 107
- 4.9 (a) Numerically computed relaxed energy densities of the three-well phase transformation model for case (ii): $\Psi_1 = 0$, $\Psi_2 = 4.5 \cdot 10^{-3}$, $\Psi_3 = 0$. The dotted line denotes the unrelaxed energy density (4.24), while the solid line denotes the corresponding smoothed energy density (4.31). (b) Average volume fractions of phases 2 and 3 corresponding to the relaxed energy curves, as obtained from the max-ent and FFT schemes (all three volume fractions sum up to 1). (c) and (d) Associated microstructural patterns, color-coded by the dominant phase at each point within the RVE, obtained from the max-ent and FFT schemes, respectively, at strain levels marked as A and B in (a) (the dominant phase is defined as the phase with highest volume fraction at a given point). 109
- 4.10 Microstructure patterns predicted by the FFT scheme at 256^3 spatial resolution for case (ii): $\Psi_1 = 0$, $\Psi_2 = 4.5 \cdot 10^{-3}$, $\Psi_3 = 0$. The microstructures are visualized by plotting the deformation gradient component F_{11} at strain levels marked as A and B in Figure 4.9a. . . . 110

4.11	Schematic of a laminate interface being unresolvable by the spatial discretization, leading to an approximate energy-minimizing laminate with either a <i>sharp-interface</i> or a <i>diffuse-interface</i> layer between laminate phases.	112
4.12	Schematics of shear cells in the diffuse interface layer model in 2D and 3D along with their nodal displacements. The interface width is exaggerated for illustration purposes; the real interface width of $2h$ is small relative to the RVE size.	113
4.13	Numerically relaxed energy density of a 2D RVE of side length 1, whose uniform spatial discretization with grid point spacing $h = 1/16$ limits the resolvability of the changing laminate volume fraction. Shown are the unrelaxed energy density as well as the approximate relaxed energies obtained from the <i>sharp-interface</i> scenario, (4.50), and from the <i>diffuse-interface</i> scenario, (4.52). Results are for $\xi_1 = 1.0$ and $\xi_2 = 1.2$, and the elastic moduli $\mu = 1$ and $\kappa = 3$	116
4.14	(a) Numerically relaxed energy density of a 3D RVE of side length 1, whose uniform spatial discretization with grid point spacing $h = 1/16$ limits the resolvability of the changing laminate volume fractions. Shown are the unrelaxed energy density as well as the approximate relaxed energies obtained from the <i>sharp-interface</i> scenario extended to 3D, (4.50), and from the <i>diffuse-interface</i> scenario, (4.55). Results are for $\xi_1 = 1.0$ and $\xi_2 = 1.2$, and the elastic moduli $\mu = 1$ and $\kappa = 3$. (b) Convergence of the relaxed energy to the quasiconvex hull (zero for $\hat{\lambda} \in [1, 1.2]$) at fixed $\hat{\lambda} = 1.075$ with h -refinement. (c) Convergence rate of the relaxed energy obtained from max-ent for different values of the locality parameter β	117
4.15	Numerically relaxed energy of a 3D RVE discretized by a $10 \times 10 \times 10$ mesh/point set modeled by the max-ent and FEM schemes, using the two-well phase-transformation model with the rotated transformation strains (4.56) and average deformation gradient (4.57). The inset shows an FEM mesh illustrating the laminate orientation with varying θ	120

4.16	Distribution of strain energy within a 3D RVE with $16 \times 16 \times 16$ spatial resolution, obtained by (a) the max-ent scheme (showing all material points) and (b) the FEM scheme (showing all quadrature points). The RVE is strained to $\hat{\lambda} = 1.075$, deliberately such that the optimal laminate interfaces yielding zero relaxed energy for a sharp-interface laminate do not coincide with any nodal planes of a discretized RVE.	121
------	--	-----

LIST OF TABLES

<i>Number</i>	<i>Page</i>
2.1 <i>Benchmark V-(A):</i> Comparison of results from Taylor anvil test . . .	47
3.1 Mean and standard deviation of deformation gradient over material points in the homogeneous section indicated by black rectangles in Figure 3.8. The deformation gradients are reported for $t = t_{\max}$	74
3.2 Microscale parameters of the copper material model.	83
3.3 Mesoscale parameters of the Taylor model.	84
3.4 Macroscale parameters defining the geometry, boundary conditions, and max-ent approximation scheme. Parameters marked with * are listed in non-dimensionalized units.	84

Chapter 1

INTRODUCTION

1.1 Motivation

The finite element method (FEM) has been widely successful in simulating the mechanics and physics of solids – from simple linear elasticity to complex multi-physics [218] and multiscale [73] problems, and is accepted as the standard numerical method across several industries. FEM traces its origins to the early works in variational calculus by Ritz [184], Rayleigh [183], and Galerkin [84]. The notion of a mesh or spatial discretization of a continuous domain into *finite elements* was introduced in the 1940s by Hrennikoff [101] and Courant [63], and later mathematically formalized into modern-day FEM in the 1970s [194]. Much of the success of FEM is attributed to the mathematically well-understood error bounds and convergence properties of the approximate solutions predicted by this method.

Unfortunately, FEM and other mesh-based methods have limited capabilities when solving complex problems. In order to achieve satisfactory accuracy and capture localized effects, complicated geometries often require high-resolution meshes and higher-order elements, which can be computationally expensive to simulate. Additionally, FEM approximates continuous fields with piece-wise polynomial functions, which is problematic when solving higher-order partial differential equations (PDEs). Furthermore, conventional FEM is significantly limited when solving problems involving large deformations that may lead to severe mesh distortions. In this latter context, problems associated with classical FEM are two-fold. First, formulating the governing equations in the initial or reference configuration (referred to as *total-Lagrangian* description) becomes inapplicable in case of large deformations, where the initial mesh loses relevance. Second, when formulated in the *updated-Lagrangian* or *Eulerian* settings, severe mesh distortion may lead to entangled or ill-shaped elements. As an instructive example, Figure 1.1 illustrates the mesh distortion due to rotation of a rigid inclusion embedded in a soft matrix.

Solutions to mesh-related problems in FEM include adaptive remeshing and mesh refinement. Such techniques are computationally expensive and heuristic in nature. Additionally, these methods require interpolation of fields when mapping stresses and strains from the old mesh to the new mesh, which can be complicated and prone

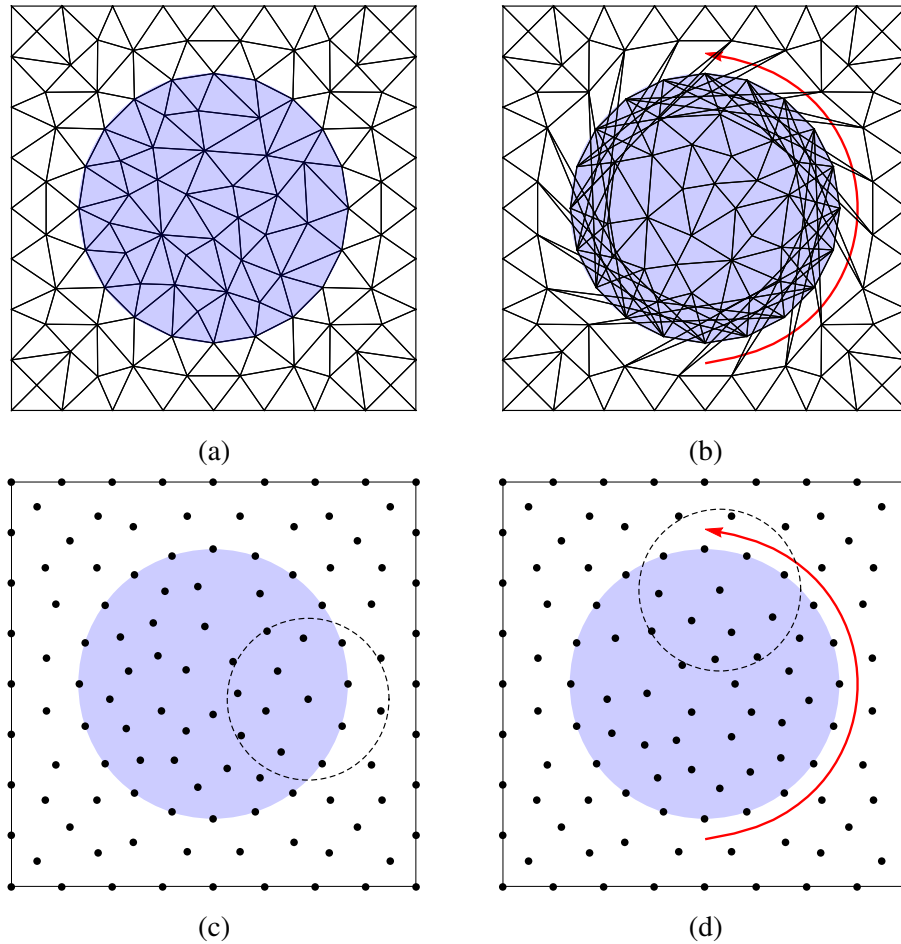


Figure 1.1: Illustration of mesh distortion due to 90° rotation of a rigid circular inclusion (shaded blue) embedded in a soft matrix. (a,c) Initial spatial discretization in FEM and particle meshfree method, respectively. Dashed circle in (c) denotes the domain of influence of a node located inside the inclusion. (b,d) Post-deformation spatial discretization in FEM and particle meshfree method, respectively.

to errors, particularly for complicated material models such as history-dependent constitutive laws (e.g. crystal plasticity) and multiscale models.

The *Arbitrary Lagrangian-Eulerian* (ALE) method [100] is a popular alternative to overcome mesh-based challenges by coupling Lagrangian and Eulerian descriptions, especially in the context of multiphase flows and fluid-structure interactions [69, 70, 187]. In ALE, the mesh is updated independent of the geometry in order to avoid ill-shaped or entangled elements that may result in a numerically unstable system. However, ALE methods face three limiting challenges [94] - (i) similar to adaptive remeshing, updating the mesh is computationally expensive, (ii) lacks robust algorithms to determine optimal mesh updates, and (iii) requires some prior

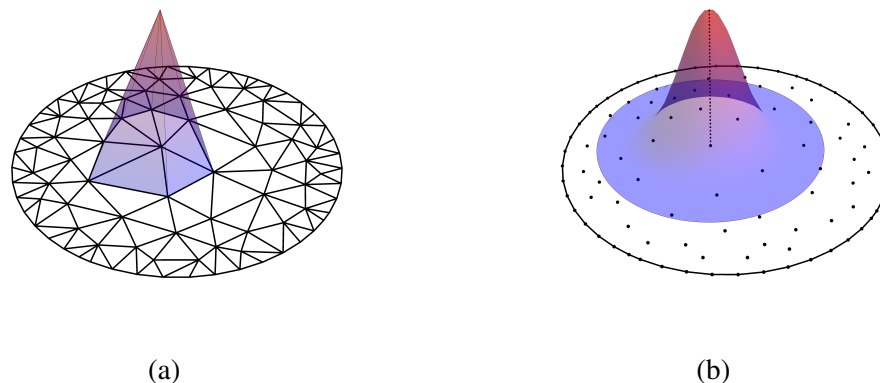


Figure 1.2: Illustration of (a) mesh-based and (b) meshfree shape function.

knowledge of the solution displacement field in order to advect the mesh.

1.2 Meshfree methods

In contrast to mesh-based methods, meshfree methods are more suited for simulations involving large deformations and distortions, and circumvent mesh-related problems by treating nodes as interacting particles. In mesh-based methods such as FEM, a global approximation of an arbitrary field is constructed by stitching together local approximations constructed within each element. On the other hand, meshfree methods create a global approximation directly using the known values at nodes and nodal positions, without using any mesh or stencil. Figure 1.2 illustrates a representative meshfree shape function, in contrast to a mesh-based shape function. Figure 1.1 illustrates by example how particle meshfree methods overcome problems like entangled elements encountered in conventional mesh-based methods such as FEM. Furthermore, meshfree approximants have compact support along with high order of continuity, sometimes even infinitely-differentiable [7], compared to FEM interpolation. Additionally, meshfree adaptive refinement is performed by directly inserting nodes, and is significantly easier compared to FEM where the mesh presents geometric and tessellation constraints. Meshfree methods have found several applications, especially in the context of large deformations, including rubber mechanics [44, 48], metal forming [45–47, 209, 212], geomechanics [5, 36, 54, 211], high-velocity impact simulations [17, 107, 109], bio-mechanics [52, 213], strain localization [136–139, 179], fracture mechanics [177, 178, 180, 181, 217], shape optimization [111–113], etc.

We now briefly review some of the popular meshfree methods and their limitations. For the purpose of subsequent discussions, consider a spatial discretization of domain $\Omega \subset \mathbb{R}^d$ into n nodes located at $\{\mathbf{x}^a \in \Omega, a = 1, \dots, n\}$. For an arbitrary field $f : \Omega \rightarrow \mathbb{R}$, we wish to construct an approximation of the form

$$f(\mathbf{x})^h = \sum_{a=1}^n N^a(\mathbf{x}) f^a, \quad \mathbf{x} \in \Omega, \quad (1.1)$$

where $N^a : \Omega \rightarrow \mathbb{R}$ denotes the shape function associated with node a , and $\{f^a = f(\mathbf{x}^a), a = 1, \dots, n\}$ is the set of known values of the field at nodal positions.

1.2.1 Smoothed-particle hydrodynamics

Meshfree methods trace their origin back to the 1970s and the introduction of smoothed-particle hydrodynamics (SPH) [146, 157] in astrophysics, followed by adoption in solid mechanics in the 1990s [25, 108, 142, 182]. In SPH, the approximation is constructed by convolution with a kernel $K(\mathbf{x}, h)$ as

$$f^h(\mathbf{x}) = \int_{\Omega} K(\mathbf{x} - \mathbf{y}, h) f(\mathbf{y}) d\mathbf{y}, \quad (1.2)$$

where h is a length scale parameter for the interpolation. If the kernel is a delta function, the convolution exactly reproduces the field. The kernel function is subject to certain constraints. The kernel must tend to the delta function in the limit $h \rightarrow 0$. Additionally, the kernel must be normalized, positive, symmetric, and have a compact support [156, 157]. The volume integral is further approximated as the volume-weighted sum over all the nodal values

$$f^h(\mathbf{x}) \approx \sum_{a=1}^n K(\mathbf{x} - \mathbf{x}^a, h) f^a V^a, \quad (1.3)$$

where $\{V^a, a = 1, \dots, n\}$ denotes the volume of the nodes. For computational efficiency, the compact support of kernels is exploited to only sum over the few nodes that lie in a neighborhood of the evaluation point. Comparing with the canonical form in (1.1), the SPH shape function associated with node a is given by

$$N^a(\mathbf{x}) = K(\mathbf{x} - \mathbf{x}^a, h) V^a. \quad (1.4)$$

The most commonly used kernels are the Gaussian kernels

$$K(\mathbf{x}, h) = c h^{-d} \exp\left(-\|\mathbf{x}\|^2 / h^2\right), \quad (1.5)$$

and the Schoenberg splines (M_α , $\alpha = 1, 2, 3, \dots$) [157, 191]

$$K(\mathbf{x}, h) = ch^{-d}M_\alpha(r, h) = \frac{ch^{-d}}{2\pi} \int_{-\infty}^{\infty} \left(\frac{\sin(kh/2)}{kh/2} \right)^\alpha \cos(kr) dk, \quad (1.6)$$

where $r = \|\mathbf{x}\|$ and c is a normalization constant whose value depends on the dimension d . The most commonly used spline kernel corresponds to $\alpha = 4$, and produces piece-wise cubic interpolation. The analytical expression of the cubic spline [157, 191] is given by,

$$M_4(r, h) = \begin{cases} \frac{1}{6} ((2 - r/h)^3 - 4(1 - r/h)^3), & \text{if } 0 \leq r/h \leq 1, \\ \frac{1}{6} ((2 - r/h)^3), & \text{if } 1 \leq r/h \leq 2, \\ 0, & \text{if } r/h > 2. \end{cases} \quad (1.7)$$

Unfortunately, the discrete form of SPH interpolation (1.3) is not zeroth-order consistent, i.e. it cannot exactly interpolate constant fields. This lack of consistency in the interpolation scheme results in poor convergence of the approximate solution. Several corrections [22, 30, 106, 156, 182] have been proposed to allow higher order consistency within SPH, albeit with limited robustness, particularly in non-uniform spatial discretizations in 2D and 3D.

1.2.2 Moving least squares

Moving least squares (MLS) was first introduced by Lancaster and Sakauskas [127] for interpolation of surfaces and later adopted by Nayroles et al. [162] and Belytschko et al. [21] into MLS-based meshfree methods, namely the *diffuse element method* (DEM) and the *element free Galerkin method* (EFG), respectively. MLS aims to create a polynomial interpolation computed via minimization of weighted least square error that is biased to nodes in the neighborhood of the evaluation point. An approximation of the form

$$f^h(\mathbf{x}) = \mathbf{P}(\mathbf{x})^T \mathbf{a} \quad (1.8)$$

is constructed, where \mathbf{P} is the monomial basis of degree p , and \mathbf{a} is a vector denoting coefficients of the polynomial interpolation. In one-dimensional setting, for example, $\mathbf{P}(x) = (1, x, x^2, \dots, x^p)^T$, and $\mathbf{a} = (a_0, a_1, a_2, \dots, a_p)^T$. The error in the approximation is defined as the sum of squared approximation error at each node weighted by a kernel/windowing function that is biased towards nodes

closer to the evaluation point,

$$\begin{aligned} J(\mathbf{x}, \mathbf{a}) &= \sum_{a=1}^n K(\mathbf{x} - \mathbf{x}^a, h) \left(f^h(\mathbf{x}^a) - f^a \right)^2 \\ &= \sum_{a=1}^n K(\mathbf{x} - \mathbf{x}^a, h) \left(\mathbf{P}(\mathbf{x}^a)^T \mathbf{a} - f^a \right)^2, \end{aligned} \quad (1.9)$$

where K is a kernel/window function as described in Section 1.2.1. The unknown coefficients, \mathbf{a} , are computed by minimizing the approximation error, i.e.

$$\mathbf{a}^*(\mathbf{x}) = \arg \min_{\mathbf{a}} J(\mathbf{x}, \mathbf{a}). \quad (1.10)$$

The optimization problem in 1.10 admits a unique minimizer computed as

$$\mathbf{a}^*(\mathbf{x}) = \mathbf{A}^{-1}(\mathbf{x})\mathbf{B}(\mathbf{x})\mathbf{f}, \quad (1.11)$$

where

$$\begin{aligned} \mathbf{A}(\mathbf{x}) &= \sum_{a=1}^n K(\mathbf{x} - \mathbf{x}^a, h) \mathbf{P}(\mathbf{x}^a) \mathbf{P}(\mathbf{x}^a)^T, \\ \mathbf{B}(\mathbf{x}) &= \left(K(\mathbf{x} - \mathbf{x}^1, h) \mathbf{P}(\mathbf{x}^1), K(\mathbf{x} - \mathbf{x}^2, h) \mathbf{P}(\mathbf{x}^2), \dots, K(\mathbf{x} - \mathbf{x}^n, h) \mathbf{P}(\mathbf{x}^n) \right), \\ \mathbf{f} &= \left(f^1, f^2, \dots, f^n \right)^T. \end{aligned}$$

Rewriting (1.8) in the form of (1.1), the MLS shape functions are given by

$$N^a(\mathbf{x}) = \mathbf{P}^T(\mathbf{x}) \mathbf{A}^{-1}(\mathbf{x}) \mathbf{B}_a(\mathbf{x}), \quad a = 1, \dots, n, \quad (1.12)$$

where \mathbf{B}_a denotes the a^{th} column of matrix \mathbf{B} .

1.2.3 Reproducing kernel particle method

Motivated by wavelet theory, Liu et al. [144] introduced the reproducing kernel particle method (RKPM) with the aim to improve the accuracy and consistency of SPH. RKPM introduces a correction function in the original formulation of SPH to ensure consistency in the approximation. The SPH approximation in (1.2) is modified as

$$f^h(\mathbf{x}) = \int_{\Omega} C(\mathbf{x}, \mathbf{y}) K(\mathbf{x} - \mathbf{y}, h) f(\mathbf{y}) d\mathbf{y}, \quad (1.13)$$

where $C(\mathbf{x}, \mathbf{x} - \mathbf{y})$ corresponds to the aforementioned correction.

Similar to MLS approximants, the approximation is also assumed to be of polynomial form of degree p (see (1.8)), i.e. $f^h(\mathbf{x}) = \mathbf{P}(\mathbf{x})^T \mathbf{a}$. Here, \mathbf{a} again denotes the

unknown polynomial coefficients. Analogous to discrete least square error in MLS (see (1.8) and (1.10)), a continuous form of least square error is defined as

$$J(\mathbf{x}) = \int_{\Omega} K(\mathbf{x} - \mathbf{y}, h) \left(f^h(\mathbf{y}) - f(\mathbf{y}) \right) d\mathbf{y}; \quad (1.14)$$

followed by minimization with respect to \mathbf{a} in the continuous setting. The said minimization further yields the following optimal approximation (for derivations, see [144])

$$f^h(\mathbf{x}) = \mathbf{P}^T(\mathbf{x})\mathbf{M}(\mathbf{x})^{-1} \left[\int_{\Omega} \mathbf{P}(\mathbf{y})K(\mathbf{x} - \mathbf{y}, h)f(\mathbf{y}) d\mathbf{y} \right], \quad (1.15)$$

where $\mathbf{M}(\mathbf{x}) = \int_{\Omega} \mathbf{P}(\mathbf{y})\mathbf{P}(\mathbf{y})^T K(\mathbf{x} - \mathbf{y}, h)f(\mathbf{y}) d\mathbf{y}$.

Comparing (1.13) and (1.15), the correction function is given by

$$C(\mathbf{x}, \mathbf{y}) = \mathbf{P}^T(\mathbf{x})\mathbf{M}(\mathbf{x})^{-1}\mathbf{P}(\mathbf{y}). \quad (1.16)$$

Analogous to nodal integration in SPH, discretization of approximation in (1.13) yields the RKPM shape functions computed as

$$N^a(\mathbf{x}) = C(\mathbf{x}, \mathbf{x}^a)K(\mathbf{x} - \mathbf{x}^a, h)V^a, \quad a = 1, \dots, n. \quad (1.17)$$

1.3 Limitations of meshfree methods

Meshfree methods have problems that are different from those of mesh-based methods such as FEM. Most meshfree approximations, including SPH, RKPM, and MLS-based schemes, do not possess the Kronecker delta property, i.e. $N^a(\mathbf{x}^b) \neq \delta^{ab}$ for $a, b = 1, \dots, n$. As a result, interpolation at the boundary is not independent of the internal nodes, and special treatments are needed for application of boundary conditions, e.g., Lagrange multipliers, penalty methods, Nitsche's method, ghost particles, transition to FEM near the boundary, etc. [8, 19, 30, 31, 38, 43, 58, 78, 92, 144, 149, 150, 164, 215]. However, these techniques further aggravate consistency issues in meshfree methods (and particularly in SPH).

In addition, meshfree methods suffer from accuracy, convergence, and stability related issues in domain integration (in a Galerkin setting). The early works [19, 21, 143] on meshfree methods approximated domain integrals by Gauss quadrature over a background mesh. However, the non-local nature of meshfree approximants results in a mismatch between quadrature cells and nodal shape function supports, particularly in non-uniform discretizations. Dolbow and Belytschko [68] showed that this mismatch introduces significant quadrature errors and causes poor

convergence rates. While high-order quadrature can restore acceptable accuracy and convergence rates [10, 51, 68], the added computational cost becomes a limiting factor. Griebel and Schweitzer [91] and Liu and Belytschko [145] have proposed algorithms for constructing integration cells in consideration with meshfree supports that minimize quadrature errors. However, such techniques can be computationally expensive and even inapplicable for complex geometries.

On the other hand, direct nodal integration (DNI) schemes have gained popularity because they do not require the use of a background mesh and hence are truly mesh-free. Such schemes approximate a domain integral by volume-weighted sums over nodes (see e.g. (1.3)). However, naive DNI also suffers from poor accuracy and convergence rates [18, 49, 51]. Several modifications and corrections have been introduced in the past two decades that significantly and robustly improve the accuracy and convergence properties, such as stabilized conforming nodal integration (SCNI) [49], stabilized non-conforming nodal integration (SNNI) [53], and variationally consistent integration (VCI) [51].

Compared to accuracy and convergence, achieving stability in nodal integration has been more challenging [18, 24, 49] and is an active topic of research in the meshfree community. Belytschko et al. [24] identified two kinds of instabilities - (i) a rank-deficiency instability, and (ii) a tensile instability. The rank deficiency instability arises from presence of zero energy modes. Several improvements have been proposed to stabilize these modes in nodal integration schemes [49, 50, 176]. Alternatively, the rank-deficiency can be eliminated by sampling (for the purpose of quadrature) at points away from the nodes, called stress-points [71, 72] or material points [132]. Unlike the rank-deficiency instability, the tensile instability [24, 71, 72, 197] arises only in the updated-Lagrangian setting. While using (total)-Lagrangian kernels circumvents this instability, it limits the potential of meshfree methods in simulating large-deformation mechanics. Tensile instability is a purely numerical instability in meshfree methods that arises from interaction of the stress tensor and the evolution of the updated-Lagrangian/Eulerian kernels, even if the material model and the approximations schemes are stable individually. In a rigorous stability analysis, Belytschko et al. [24] showed that increasing nodal spacing and separation of adjacent shape function supports during a tensile deformation lead to a spurious loss in (post-discretization or effective) stiffness. Swegle et al. [197] provided an intuitive explanation of this instability, including an example of SPH applied to linear elasticity in a one-dimensional setting.

1.4 Maximum-entropy based meshfree methods

More recently, the class of maximum-entropy (*max-ent*) approximation schemes has attracted interest among meshfree particle methods, as it addresses the majority of the aforementioned limitations highlighted in Section 1.3. Sukumar [195] employed the maximization of information entropy [105] encoded in the approximation to formulate meshfree interpolants on polygonal elements, while Arroyo and Ortiz [7] used a Pareto compromise between locality of approximation and maximization of information entropy to create the *local max-ent* shape functions. Li et al. [132] utilized the local max-ent scheme to develop the optimal transport method (OTM) for dynamic simulations of fluid and plastic flows involving severe distortion. Further advances in the area of max-ent approximations include the convergence analysis of Bompadre et al. [29], the variational formulation of the optimal support size of max-ent shape functions [186], max-ent schemes with arbitrary order of consistency [88], as well as tools to evaluate derivatives of max-ent shape functions near the boundary [90]. Some of the recent and interesting applications of max-ent based approximation schemes include phase-field modeling of bio-membranes [172, 185], high-velocity impact [133], metal processing [80], fluid-structure interaction [77], fracture modeling [4, 134, 171], coarse-graining in molecular simulations [118], etc.

We now briefly review the local max-ent approximation introduced by Arroyo and Ortiz [7]. Based on a probabilistic interpretation of shape functions, the total information entropy \mathcal{H} encoded in the set of shape functions $\mathcal{N} = \{N^1, \dots, N^n\}$, following Jaynes [105], as well as the locality U of the set of shape functions are defined as, respectively,

$$H[\mathcal{N}] = - \sum_{a=1}^n \int_{\Omega} N^a(\mathbf{x}) \ln N^a(\mathbf{x}) dV, \quad (1.18)$$

$$U[\mathcal{N}] = \sum_{a=1}^n \int_{\Omega} N^a(\mathbf{x}) \|\mathbf{x} - \mathbf{x}^a\|^2 dV. \quad (1.19)$$

A Pareto optimality between maximum entropy and minimum locality of the approximation is found by introducing the functional $F[\mathcal{N}] = \beta U[\mathcal{N}] - H[\mathcal{N}]$ with β being a scalar parameter controlling the locality of the approximation scheme. The local max-ent shape functions are computed as solution to the optimization problem $\mathcal{N} = \arg \min F[\mathcal{N}]$ subject to the constraints of positivity of all shape functions as well as zeroth- and first-order consistency of the shape functions. The minimization

can be carried out pointwise, leading to the max-ent shape functions [7]

$$N^a(\mathbf{x}) = \frac{1}{Z(\mathbf{x}, \boldsymbol{\lambda}^*(\mathbf{x}))} \exp \left[-\beta \|\mathbf{x} - \mathbf{x}^a\|^2 + \boldsymbol{\lambda}^*(\mathbf{x}) \cdot (\mathbf{x} - \mathbf{x}^a) \right], \quad a = 1, \dots, n, \quad (1.20)$$

where the partition function Z and vector $\boldsymbol{\lambda}^*$ are defined as, respectively

$$Z(\mathbf{x}, \boldsymbol{\lambda}) = \sum_{a=1}^n \exp \left[-\beta \|\mathbf{x} - \mathbf{x}^a\|^2 + \boldsymbol{\lambda} \cdot (\mathbf{x} - \mathbf{x}^a) \right], \quad (1.21)$$

and

$$\boldsymbol{\lambda}^*(\mathbf{x}) = \arg \min_{\boldsymbol{\lambda} \in \mathbb{R}^d} \ln Z(\mathbf{x}, \boldsymbol{\lambda}). \quad (1.22)$$

The minimization problem in (1.22) can be solved numerically with a nonlinear iterative solver such as the Newton-Raphson method. The spatial derivatives of the local max-ent shape functions follow as

$$\nabla N^a(\mathbf{x}) = -N^a(\mathbf{x}) \mathbf{J}(\mathbf{x})^{-1} (\mathbf{x} - \mathbf{x}^a), \quad (1.23)$$

with

$$\mathbf{J}(\mathbf{x}) = \sum_{a=1}^n N^a(\mathbf{x}) (\mathbf{x} - \mathbf{x}^a) \otimes (\mathbf{x} - \mathbf{x}^a). \quad (1.24)$$

The local max-ent approximation offers the following advantages over other mesh-free approximations.

- By varying the locality parameter β , the local max-ent shape functions provide a seamless transition from a nonlocal meshless approximation with global shape functions ($\beta \rightarrow 0^+$) to a simplicial FE interpolation with local shape function support ($\beta \rightarrow +\infty$) [7, 126], as illustrated in Figure 1.3.
- The zeroth- and first-order consistency are built into the underlying optimization problem and ensure that affine functions are exactly interpolated.
- The max-ent shape functions possess the weak Kronecker property, i.e. shape function associated with an internal node vanishes at the boundary. This is illustrated in Figure 1.3f by the shape function of a node located close to the boundary. As a consequence, interpolation at the boundary is independent of information at the interior nodes. Therefore, essential boundary conditions can be directly imposed, unlike when using other meshless approximants [78] such as SPH, RKPM, and MLS-based schemes.

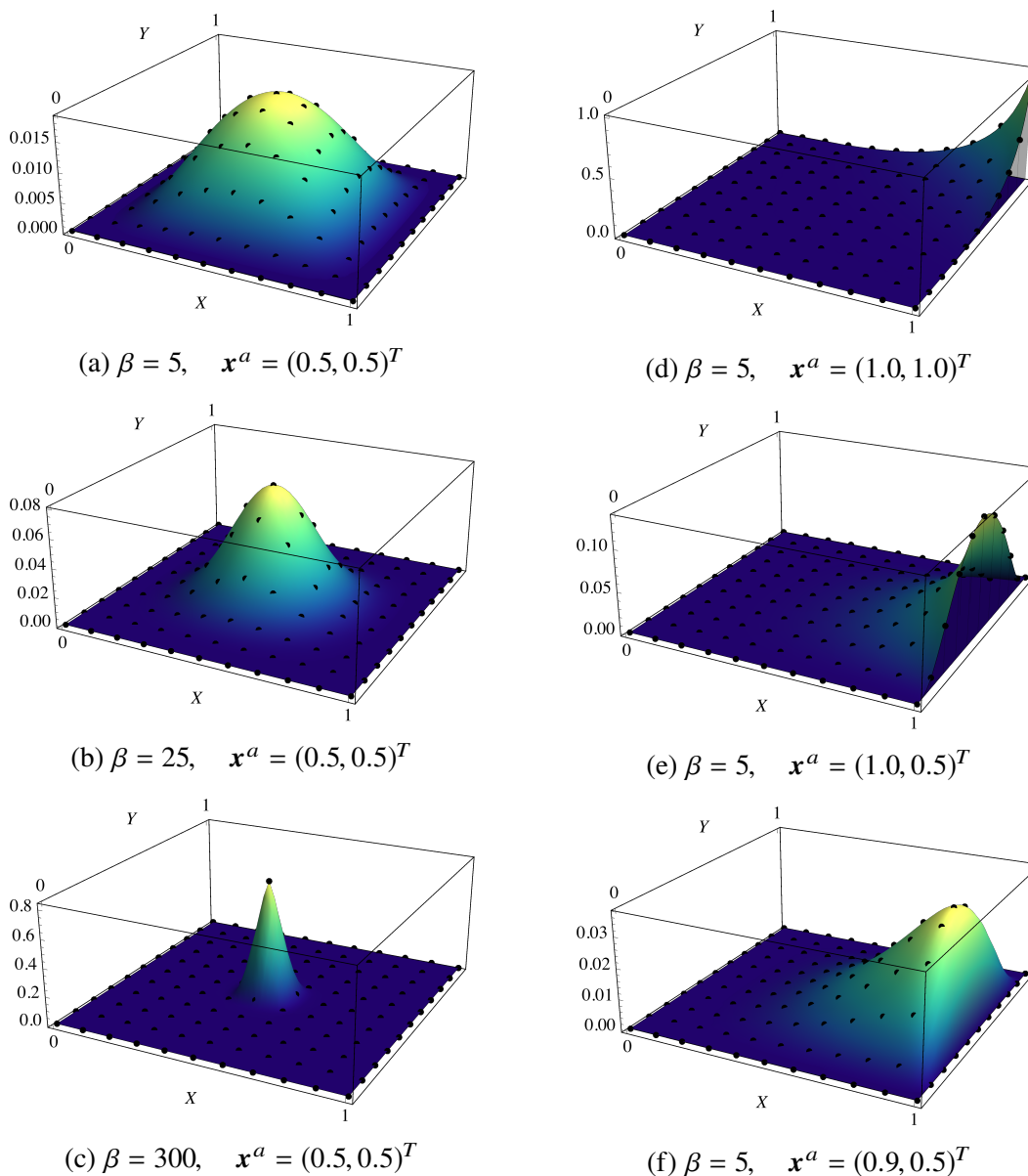


Figure 1.3: (a, b, c) Local max-ent shape functions $N^a(\mathbf{x})$ where a is the central node (located at $\mathbf{x}^a = (0.5, 0.5)^T$) of a 2D domain $\Omega = [0, 1]^2$ with equally spaced nodes (shown as black dots), evaluated for three different values of the locality parameter β . (d, e) Shape functions of nodes a lying on the corner and edge of the domain, respectively. (f) Shape function of an internal node a near the boundary $\partial\Omega$. Note that the shape function vanishes at the boundary, which demonstrates that the interpolation on the boundary is independent of the internal nodes.

However, tensile instability also arises in meshfree kernels/methods based on the local max-ent approximations, when applied to finite deformations in the context of updated-Lagrangian simulations. Note that the local max-ent scheme is a stable approximation scheme by itself, as shown by the convergence analysis of Bompadre et al. [29]. The tensile instability arises in the *implementation* of the local max-ent scheme as an updated-Lagrangian meshfree method. Motivated to eliminate tensile instability, we propose an enhanced max-ent based approximation that leverages a novel adaptivity scheme to allow for stable meshfree simulations. This is one of the major contributions of this thesis, and is explained in detail in Chapter 2. To the best of author's knowledge, the proposed adaptive scheme together with the enhanced max-ent approximation is the first to achieve robust stability in the updated-Lagrangian setting, and fully realizes the potential of meshfree methods in simulating large-deformation mechanics within both (quasi-)static and dynamic problems.

1.5 Outlook: Applications

This thesis further explores two different applications of the aforementioned maximum-entropy based meshfree method.

1.5.1 Modeling of equal-channel angular extrusion based on high-fidelity plasticity models

Equal-channel angular extrusion (ECAE) is a metal forming technique where a metal or alloy specimen is extruded through a channel with a 90° bend without significant change in cross-sectional area of the specimen. Figure 1.4 illustrates the schematics of the extrusion process. ECAE falls into the general class of *severe plastic deformation* (SPD) processes that significantly improve bulk properties (e.g., strength, ductility, fatigue resistance, etc.) of metal and alloys. This is achieved by inducing ultra-fine grain refinement in metals via application of large plastic strains. Simulating these large strains in SPD processes, and in particular ECAE, by mesh-based methods such as FEM is severely limited, and require the use of a meshfree method for better accuracy and convergence.

Furthermore, SPD processes, including ECAE, are essentially multiscale in nature. At the microscale, grain refinement is governed by recrystallization (nucleation and migration) of grains, while the macroscale response is modeled as a mechanical boundary value problem involving severe plastic strains. There have been multiple studies for modeling recrystallization [67, 98, 102, 190, 193, 202, 203]; however,

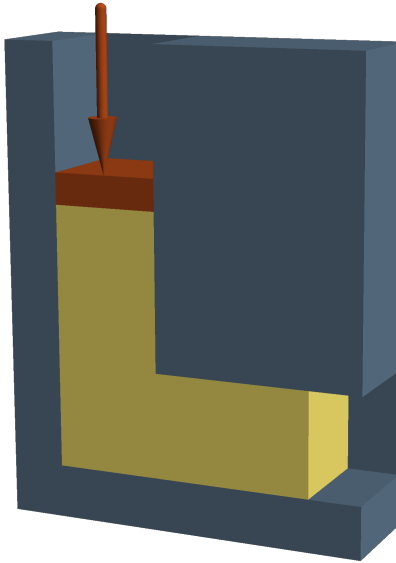


Figure 1.4: Illustration of equal-channel angular extrusion (ECAE). A metal billet (shaded yellow) is extruded through a 90° angled channel (shaded blue) under the action of a plunger (denoted in red).

they have been limited to a material point setting. On the other hand, modeling of ECAE [2, 65, 76, 83, 104, 147, 148, 189] at the macroscale has been limited to FEM and SPH based simulations with simple elasto-plastic constitutive laws that lack high-fidelity description of grain refinement at the microscale. Additionally, the well-known problems in SPH (treatment of boundary conditions, poor accuracy, lack of consistency, and instabilities; see Sections 1.2.1 and 1.3) motivate the use of a modern-day meshfree method. In this thesis, we develop a multiscale model of the ECAE process, in which we use the stabilized max-ent scheme introduced in Chapter 2 at the macroscale, coupled with a microstructural evolutionary model (including grain refinement and texture evolution) introduced by Tutcuoglu et al. [202] at the micro- and mesoscale.

1.5.2 Numerical energy relaxation in problems with nonconvex energetic potentials

Energy-minimizing microstructures and patterns naturally emerge in problems with non-quasiconvex potential energy landscapes such as those related to, e.g., phase transformations [57], deformation twinning [56], hyperelasticity [128], and finite-strain crystal plasticity [66, 119, 168]. The challenges associated with nonconvex energy potentials are (i) the prediction of such emergent microstructural patterns, and (ii) the resulting effective, macroscale mechanical behavior of the material.

Mathematically speaking, the experimentally observed microstructural patterns are infimizing sequences associated with the quasiconvex hull of the underlying non-(quasi)convex energy potential [11, 27, 55, 74, 89]. Therefore, identifying both the effective response and the microstructural features is intimately tied to finding the quasiconvex hull.

Due to the nonlocal nature of the notion of quasiconvexity, quasiconvexification of the energy density in such problems has traditionally been limited to (semi-) analytical techniques [60, 117, 154] such as finding matching upper and lower bounds (and using, e.g., recursive lamination and polyconvexification for the upper and lower bounds, respectively [9, 13, 95, 168]). Numerical techniques such as FEM simulations of representative volume elements (RVE) [16, 41] are severely limited by the ill-conditioning resulting from the loss of convexity; they have been restricted to geometrically simple problems, oftentimes assuming two-dimensional (2D) situations. In the context of numerically quasiconvexifying complex material models in 2D and 3D, we present a new numerical avenue based on meshfree max-ent approximation, and compare its performance with two numerical techniques – classical FEM, and a FFT-based [205] methods. We show that max-ent approximation leverages its non-local and infinitely-differentiable property of the shape functions to produce superior numerical approximation of the quasiconvex hull compared to the FEM and FFT schemes.

1.6 Outline

In Chapter 2, we explicate the enhanced local max-ent approximation scheme. We then formulate and discretize an updated-Lagrangian formulation of a quasistatic boundary value problem. Finally, we examine the source of tensile instability and derive an adaptivity scheme to incrementally update shape function in order to achieve stability. The chapter concludes with a suite of benchmarks demonstrating the benefits and capabilities of the proposed scheme.

As a demonstration of an application extending from Chapter 2, we introduce a multiscale framework of copper under ECAE in Chapter 3. This framework ranges from microscale, to mesoscale, then to macroscale. The application of the proposed max-ent method pertains to simulation on the macroscale. We present a Taylor model at the mesoscale that captures grain recrystallization, coupled with a crystal plasticity model representative of the material response of copper at the microscale. We discuss the computational challenges in simulating such processes, particularly

related to distortion in the spatial discretization, boundary conditions, and numerical time-integration of internal variables. The rest of this chapter discusses the strain distribution and grain refinement in a specimen undergoing ECAE.

In Chapter 4, we showcase the application of the max-ent method in numerical energy relaxation of nonconvex energy potentials at the representative volume element (RVE) level. We perform a detailed comparison of results achieved by the max-ent, FEM and FFT methods by investigating the following benchmarks (introduced by Vidyasagar [205]) – (i) the hyperelastic Saint Venant-Kirchhoff model, and (ii) a finite-strain double- and multi-phase solid-solid transformation model. We conclude this chapter by analyzing the numerical limitations of the aforementioned methods arising from the inability of the spatial discretization to resolve general energy-minimizing microstructural patterns.

Chapter 5 finally summarizes the contributions of this thesis and provides an outlook for future applications of max-ent based meshfree methods.

ENHANCED LOCAL MAXIMUM-ENTROPY APPROXIMATION FOR STABLE MESHFREE SIMULATIONS

Research presented in this chapter has been adapted from the following publication:

S. Kumar, K. Danas, and D. M. Kochmann. Enhanced local maximum-entropy approximation for stable meshfree simulations. *Computer Methods in Applied Mechanics and Engineering*, 344:858 - 886, 2019.

DOI: <https://doi.org/10.1016/j.cma.2018.10.030>

2.1 Introduction

So far we have introduced the premise of this research and its potential applications. In this chapter, we detail the technical core of the proposed maximum-entropy approximation method for stable meshfree simulations. Addressing tensile instability is a long standing open problem in the area of meshfree methods. While there have been some efforts to improve stability by introducing stress point integration [71, 72, 197], these techniques do not suppress tensile instability. For example, Belytschko et al. [24] showed that stress point integration only delays the onset of tensile instability with increasing deformation. The authors concluded that, if stress point integration and “a reasonable constitutive law is used, the tensile instability can be avoided” because the material necessarily undergoes yielding, failure, damage, fracture, etc. before the tensile instability appears. Clearly, this solution places a major constraint on range of materials and physics that can be simulated with meshfree methods. For example, hyperelasticity avoids material instability and localization and therefore necessarily runs into the regime where the tensile instability classically occurs (physically, it is highly relevant for, e.g., rubber elasticity). Belytschko et al. [24] also hinted at adaptively correcting the shape function supports as nodal spacing increases in order to alleviate tensile instability. In the context of max-ent approximations, Li [135] proposed the use of an isotropic adaptive evolution of shape functions to overcome the problems associated with tensile instability. Despite this adaptive evolution of shape functions, that scheme is still prone to tensile instability in case of anisotropic deformations (as will be demonstrated in Section 2.2.4).

In this chapter, we present an improved meshfree approximation scheme which is based on the local max-ent strategy. The improved version is specifically designed for severe, finite deformation and offers significantly enhanced stability as opposed to the original formulation. This is achieved by (i) formulating the quasistatic mechanical boundary value problem in a suitable updated-Lagrangian setting, (ii) introducing anisotropy in the shape function support to accommodate directional variations in nodal spacing with increasing deformation and eliminate tensile instability, (iii) spatially bounding and evolving shape function support to restrict the domain of influence and increase efficiency, (iv) truncating shape functions at interfaces in order to stably represent multi-component systems like composites or polycrystals. The new scheme is applied to benchmark problems of severe elastic and elastoplastic deformation that demonstrate its performance both in terms of accuracy (as compared to exact solutions and, where applicable, finite element simulations) and efficiency. More importantly, the presented formulation overcomes the classical tensile instability found in most meshfree methods, as shown for stable simulations of, e.g., the inhomogeneous extension of a hyperelastic block up to 100% or the torsion of a hyperelastic cube by 200° – both in an updated Lagrangian setting and without the need for remeshing.

The chapter is organized as follows. In Section 2.2.1, we present modified local max-ent shape functions that are based on an anisotropic Pareto optimality between maximizing information entropy and minimizing shape function width, which will play a crucial role in eliminating the tensile instability under large deformations. In Section 2.2.2, we begin with a quasistatic total-Lagrangian formulation of the mechanical boundary value problem and transform it into a spatially discretized, quasistatic updated-Lagrangian formulation. In Section 2.2.3, we examine the tensile instability through an instructive one-dimensional toy problem and, motivated by the same, in Section 2.2.4 we present a new, anisotropic adaption scheme for the evolution of the shape function support that is able to cope with tensile instability. Next, in Section 2.2.5, we discuss the application of essential boundary conditions and propose a simple, computationally inexpensive scheme that leverages the weak Kronecker delta property of local max-ent shape functions to accurately capture discontinuous derivatives across material interfaces. Section 2.3 summarizes a suite of numerical benchmark simulations of representative boundary value problems. We demonstrate that the enhanced local max-ent scheme introduced here provides better convergence and better handling of severe distortions than FEM. It accurately captures discontinuous derivatives across material interfaces and, most remarkably,

avoids the common tensile instability associated with anisotropically increasing nodal spacings (for better understanding of the numerical implementation, a pseudo-code for solving simple hyperelasticity problems is included in Appendix 2.B). Finally, Section 2.4 concludes our investigation.

2.2 Enhanced local max-ent interpolation in updated-Lagrangian setting

The local max-ent scheme (see Section 2.2.1 for brief review) belongs to the class of convex approximation schemes and provides a seamless transition between finite elements (FE) and meshfree interpolations. The approximation scheme is based on a compromise between minimizing the width of the shape function support and maximizing the information entropy of the approximation. Building upon the idea of anisotropic shape functions [7], we here introduce an enhanced version of the original local max-ent scheme, which uses an anisotropic support to deal with tensile instability in an updated Lagrangian formulation.

2.2.1 Anisotropic local max-ent approximation

Consider a finite set of n_n distinct nodes in d dimensions, $\mathcal{X} = \{\mathbf{x}^a, a = 1, \dots, n_n\}$ with nodal positions $\mathbf{x}^a \in \mathbb{R}^d$. The domain bounded by convex hull of the node set is denoted by $\Omega \subset \mathbb{R}^d$. Let $u : \Omega \rightarrow \mathbb{R}$ be a function that we aim to approximate based on the known values of the function at nodes, $\{u^a = u(\mathbf{x}^a), a = 1, \dots, n_n\}$. We wish to construct an approximation of the type

$$u^h(\mathbf{x}) = \sum_{a=1}^{n_n} u^a N^a(\mathbf{x}), \quad \mathbf{x} \in \Omega, \quad (2.1)$$

where $N^a : \Omega \rightarrow \mathbb{R}$ denotes the shape function corresponding to node a . Shape functions are subject to the constraints

$$N^a(\mathbf{x}) \geq 0 \quad \forall \mathbf{x} \in \Omega, \quad (2.2a)$$

$$\sum_{a=1}^{n_n} N^a(\mathbf{x}) = 1 \quad \forall \mathbf{x} \in \Omega, \quad (2.2b)$$

$$\sum_{a=1}^{n_n} \mathbf{x}^a N^a(\mathbf{x}) = \mathbf{x} \quad \forall \mathbf{x} \in \Omega. \quad (2.2c)$$

The first constraint (2.2a) ensures the non-negativity of shape functions¹. The second constraint (2.2b) enforces zeroth-order consistency (i.e., constant functions are

¹One may also relax the first constraint and admit negative values of shape functions, see e.g. [29], which however is not the focus here.

exactly approximated), and whereas third constraint (2.2c) enforces first-order consistency and guarantees the exact interpolation of affine functions. These together ensure that the scheme is consistent under h -refinement. Local max-ent schemes that satisfy higher-order consistency are also possible [88] but the formulation becomes increasingly complex. Hence, we limit ourselves to first-order consistency for the scope of this contribution.

We define the *width* of a shape function N^a as²

$$U^a[N^a, \boldsymbol{\beta}] = \int_{\Omega} N^a(\mathbf{x}) \|\mathbf{x} - \mathbf{x}^a\|_{\boldsymbol{\beta}}^2 dV = \int_{\Omega} N^a(\mathbf{x}) (\mathbf{x} - \mathbf{x}^a) \cdot \boldsymbol{\beta} (\mathbf{x} - \mathbf{x}^a) dV, \quad (2.3)$$

where $\boldsymbol{\beta} \in \mathbb{R}^{d \times d}$ is a constant, positive-definite metric tensor defining the Euclidean distance in Ω . Further, $\boldsymbol{\beta}$ is a tensorial analogue of the scalar locality parameter in the original formulation of Arroyo and Ortiz [7]. A measure of the total width for the set of shape functions $\mathcal{N} = \{N^a, a = 1, \dots, n_n\}$ follows as the sum of individual shape function widths, viz.,

$$U[\mathcal{N}, \boldsymbol{\beta}] = \sum_{a=1}^{n_n} U^a[N^a, \boldsymbol{\beta}] = \int_{\Omega} \sum_{a=1}^{n_n} N^a(\mathbf{x}) \|\mathbf{x} - \mathbf{x}^a\|_{\boldsymbol{\beta}}^2 dV. \quad (2.4)$$

Minimum shape function support or maximum locality requires minimizing the functional $U[\mathcal{N}]$ with respect to all shape functions subject to constraints (2.2). The resulting scheme is equivalent to using linear interpolants on a Delaunay triangulation of the node set \mathcal{X} [7].

By interpreting the shape functions as probability distributions, the information entropy encoded in the shape functions evaluated at a point $\mathbf{x} \in \Omega$ is defined as [7]

$$H[\mathcal{N}](\mathbf{x}) = - \sum_{a=1}^{n_n} N^a(\mathbf{x}) \ln N^a(\mathbf{x}). \quad (2.5)$$

The total information entropy is obtained by integration over the entire domain Ω , i.e.,

$$H[\mathcal{N}] = - \int_{\Omega} \sum_{a=1}^{n_n} N^a(\mathbf{x}) \ln N^a(\mathbf{x}) dV. \quad (2.6)$$

Intuitively, the approximation scheme should be based on a minimum inference bias by the nodal positions, which is equivalent to the maximum information entropy

²Here and in the following, we use classical tensor and index notation common to continuum mechanics. Specifically, dots denote inner products of tensors of equal order, so $\mathbf{v} \cdot \mathbf{u} = v_i u_i$ and $\mathbf{T} \cdot \mathbf{S} = T_{ij} S_{ij}$ for vectors $\mathbf{v}, \mathbf{u} \in \mathbb{R}^d$ and second-order tensors $\mathbf{T}, \mathbf{S} \in \text{GL}(d)$. For tensors as linear mappings of vectors we write $[\mathbf{T}\mathbf{v}]_j = T_{ij} v_j$ and analogously $[\mathbf{S}\mathbf{T}]_{ij} = S_{ik} T_{kj}$. Outer products are represented by $[\mathbf{v} \otimes \mathbf{u}]_{ij} = v_i u_j$.

[105]. This requires maximizing the information entropy functional $H[\mathcal{N}]$ with respect to all shape functions subject to constraints (2.2). Consequently, the resulting shape functions have a global support that is too large for a reasonable approximation. Arroyo and Ortiz [7] proposed a Pareto optimality between the competing optimizations (minimum locality vs. maximum entropy) to find the shape functions. In adopting their approach, we define the functional

$$\begin{aligned} F[\mathcal{N}, \boldsymbol{\beta}] &= U[\mathcal{N}, \boldsymbol{\beta}] - H[\mathcal{N}] \\ &= \int_{\Omega} \sum_{a=1}^{n_n} \left(N^a(\mathbf{x}) \|\mathbf{x} - \mathbf{x}^a\|_{\boldsymbol{\beta}}^2 + N^a(\mathbf{x}) \ln N^a(\mathbf{x}) \right) dV, \end{aligned} \quad (2.7)$$

where the metric tensor $\boldsymbol{\beta}$ acts as a parameter controlling the Pareto optimality and is referred to the *locality parameter* in subsequent discussions. For given $\boldsymbol{\beta}$, the local max-ent shape functions are thus computed as

$$\mathcal{N}_{\boldsymbol{\beta}} = \arg \min \{ F[\mathcal{N}, \boldsymbol{\beta}] \text{ s.t. (2.2)} \}. \quad (2.8)$$

For example, consider the simple isotropic case of $\boldsymbol{\beta} = \beta \mathbf{I}$, where β is a scalar parameter [7]. In the limiting case of $\beta \rightarrow \infty$, the problem reduces to minimizing locality, which results in affine interpolation on a Delaunay triangulation. In contrast, when $\beta \rightarrow 0$, the problem reduces to maximizing information entropy with no regard to locality of the approximation. A detailed discussion for general anisotropic locality parameter is presented later in this section.

The structure of the minimization problem in (2.8) admits a pointwise optimization, so the shape functions at a point $\mathbf{x} \in \Omega$ are given by

$$\begin{aligned} \{N^1(\mathbf{x}), \dots, N^{n_n}(\mathbf{x})\}_{\boldsymbol{\beta}} &= \arg \min \left[\sum_{a=1}^{n_n} \left(N^a(\mathbf{x}) \|\mathbf{x} - \mathbf{x}^a\|_{\boldsymbol{\beta}}^2 + N^a(\mathbf{x}) \ln N^a(\mathbf{x}) \right) \right] \\ \text{subject to } &\begin{cases} N^a(\mathbf{x}) \geq 0, & a = 1, \dots, n_n \\ \sum_{a=1}^{n_n} N^a(\mathbf{x}) = 1 \\ \sum_{a=1}^{n_n} N^a(\mathbf{x}) \mathbf{x}^a = \mathbf{x}. \end{cases} \end{aligned} \quad (2.9)$$

Analogous to the isotropic formulation of Arroyo and Ortiz [7], there exists a unique set of minimizers given by

$$N^a(\mathbf{x}) = \frac{1}{Z(\mathbf{x}, \boldsymbol{\lambda}^*(\mathbf{x}))} \exp \left[-\|\mathbf{x} - \mathbf{x}^a\|_{\boldsymbol{\beta}}^2 + \boldsymbol{\lambda}^*(\mathbf{x}) \cdot (\mathbf{x} - \mathbf{x}^a) \right], \quad a = 1, \dots, n_n, \quad (2.10)$$

where we define the partition function $Z : \mathbb{R}^d \times \mathbb{R}^d \rightarrow \mathbb{R}$ as

$$Z(\mathbf{x}, \boldsymbol{\lambda}) = \sum_{a=1}^{n_n} \exp \left[-\|\mathbf{x} - \mathbf{x}^a\|_{\boldsymbol{\beta}}^2 + \boldsymbol{\lambda} \cdot (\mathbf{x} - \mathbf{x}^a) \right], \quad (2.11)$$

and a unique minimizer $\boldsymbol{\lambda}^*$ as

$$\boldsymbol{\lambda}^*(\mathbf{x}) = \arg \min_{\boldsymbol{\lambda} \in \mathbb{R}^d} \ln Z(\mathbf{x}, \boldsymbol{\lambda}). \quad (2.12)$$

The derivation of (2.10)-(2.12) with the newly introduced tensorial locality parameter $\boldsymbol{\beta}$ is summarized in Appendix 2.A.

Again following Arroyo and Ortiz [7], the spatial derivatives of the shape functions are given by

$$\nabla N^a(\mathbf{x}) = -N^a(\mathbf{x}) \mathbf{J}(\mathbf{x}, \boldsymbol{\lambda}^*(\mathbf{x}))^{-1} (\mathbf{x} - \mathbf{x}^a) \quad (2.13)$$

where

$$\mathbf{J}(\mathbf{x}, \boldsymbol{\lambda}) = \frac{\partial^2 \ln Z(\mathbf{x}, \boldsymbol{\lambda})}{\partial \boldsymbol{\lambda} \partial \boldsymbol{\lambda}} = \sum_{a=1}^{n_n} N^a(\mathbf{x}, \boldsymbol{\lambda}) (\mathbf{x} - \mathbf{x}^a) \otimes (\mathbf{x} - \mathbf{x}^a) - \mathbf{r}(\mathbf{x}, \boldsymbol{\lambda}) \otimes \mathbf{r}(\mathbf{x}, \boldsymbol{\lambda}) \quad (2.14)$$

and

$$\mathbf{r}(\mathbf{x}, \boldsymbol{\lambda}) = \frac{\partial \ln Z(\mathbf{x}, \boldsymbol{\lambda})}{\partial \boldsymbol{\lambda}} = \sum_{a=1}^{n_n} N^a(\mathbf{x}, \boldsymbol{\lambda}) (\mathbf{x} - \mathbf{x}^a). \quad (2.15)$$

For a detailed derivation, the reader is referred to the analogous isotropic case presented by Arroyo and Ortiz [7]. Note that $\boldsymbol{\beta}$ is assumed to be constant when constructing the approximation and when computing the above gradients of the shape functions. The justification of this assumption will be discussed in Section 2.2.3, where the spatial discretization scheme is presented.

The transition from a scalar to a tensorial locality parameter is essential and allows for anisotropic adaptivity of the shape functions, which forms the basis for our approach to dealing with tensile instability, as will be demonstrated in Section 2.2.4. Note that, for variational problems, the locality parameter $\boldsymbol{\beta}$ can be included in the global functional to yield shape function supports that are optimal with respect to the total potential energy [186]. However, this introduces additional complexity, both theoretical and computational, and will not be pursued here. Instead, the locality parameter $\boldsymbol{\beta}$ is defined by the user and chosen based on the initial nodal spacing and the physics of the problem.

Figure 2.1 illustrates the transition of the shape function support from global to local and from isotropic to anisotropic, as the locality parameter $\boldsymbol{\beta}$ changes. We

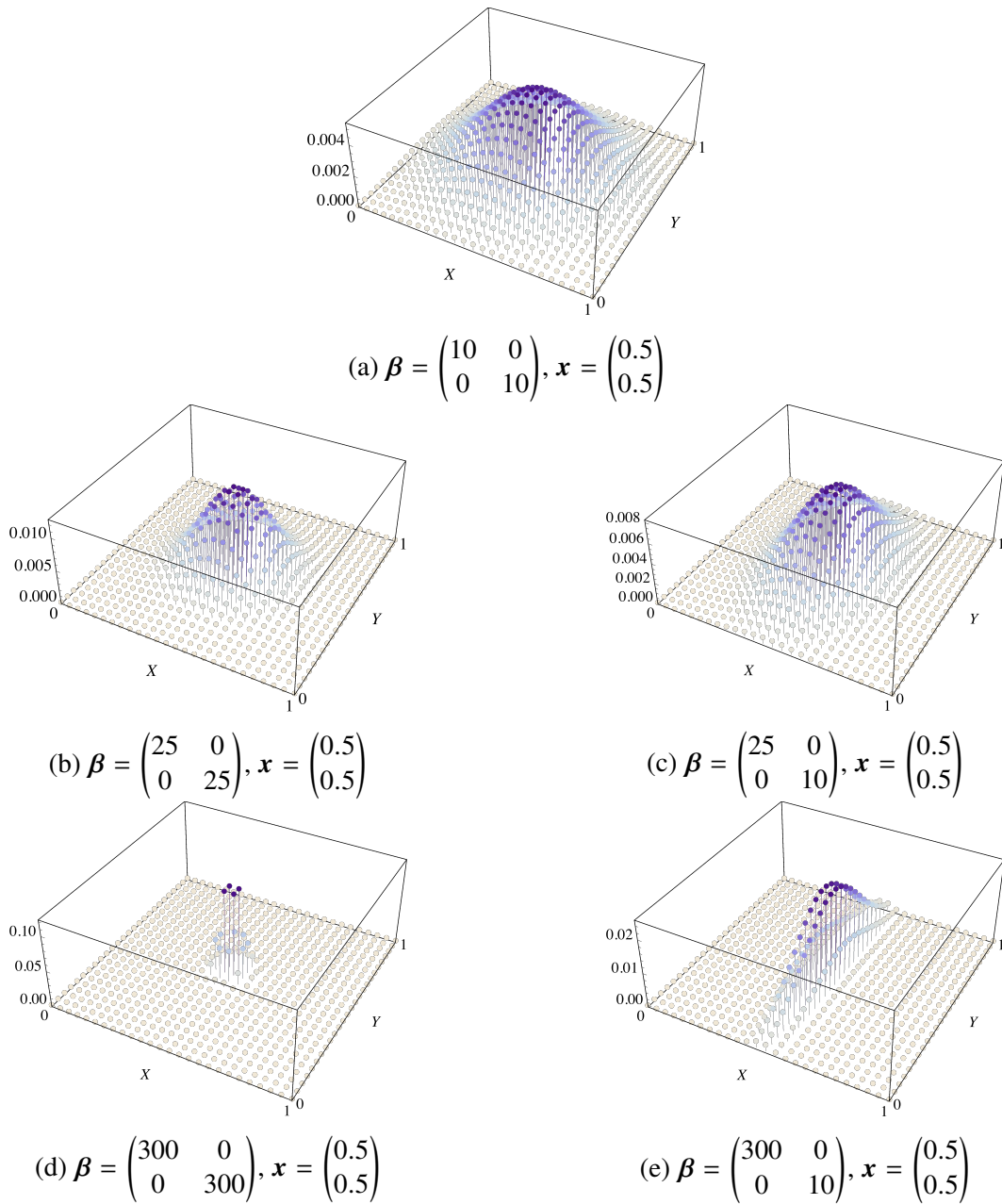


Figure 2.1: Local max-ent shape functions $N^a(\mathbf{x})$ evaluated at fixed interior point \mathbf{x} (viz., the central node) of a 2D node set with different choices of the locality parameter β . That is, the graphs show the value of each node's shape function N^a when evaluated at the central node, thus illustrating the contributions of nodal values to the interpolation at the central node. (We note that this visualization is different from that of Arroyo and Ortiz [7] and Figure 1.3 where $N^a(\mathbf{x})$ is plotted as a function of \mathbf{x} for fixed a). Cases (a,b,d) show the isotropic and (c,e) the anisotropic transition from global to local shape function support with increasing components of β .

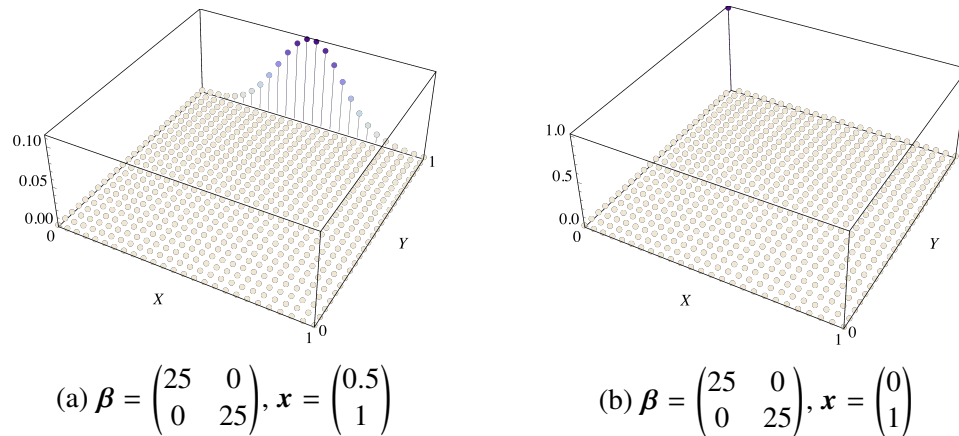


Figure 2.2: Local *max-ent* shape functions $N^a(\mathbf{x})$ evaluated at fixed point \mathbf{x} : (a) on an edge, (b) on a corner of a 2D node set. As in Figure 2.1, note that we do not plot a given shape function N^a as a function of position \mathbf{x} but we compute shape functions N^a at a given point \mathbf{x} .

emphasize that, instead of plotting a particular shape function evaluated at different points in space as commonly shown in the literature, Figure 2.1 illustrates the shape function values of each node evaluated at a fixed point (thus demonstrating the influence of each nodal contribution at that location in space). This is required since shape functions are no longer associated with nodes only – viewed from different material points with different β -tensors, a shape function evaluated at a node may have distinct values for each material point under consideration. In addition, shape functions are only evaluated at material points and there is no unique definition of those at nodes. In the limit of any eigenvalue of β tending to $+\infty$, the functional F in (2.7) is dominated by the shape function width. As a result, the shape functions reduce to simplicial interpolation on a Delaunay triangulation of the node set in the corresponding eigen-direction (see Figures 2.1d and 2.1e). In particular, Figure 2.1e illustrates global support in one direction and convergent linear interpolation in the perpendicular direction. Unlike the FE method, the local max-ent scheme does not satisfy the strong Kronecker property at the nodes, i.e., it is an approximation and not an interpolation. However, it does satisfy the weak Kronecker property at the boundary nodes [7]. Figure 2.2 shows the shape function support when evaluated at points on the convex hull of the node set. When the evaluation point lies on an edge (see Figure 2.2a), shape functions of interior nodes vanish at the point and the approximation only depends on boundary nodes. Further, if the evaluation point coincides with a corner node, shape functions evaluate to zero for all nodes but the corner node itself. More generally for convex schemes

like local max-ent, the shape function support of interior nodes terminates at the convex hull and, consequently, the approximation on the boundary is independent of interior nodes. This fact is advantageous for straightforward application of essential boundary conditions. In contrast, non-convex approximation schemes such as smoothed particle hydrodynamics (SPH), element-free Galerkin method (EFG), reproducing kernel particle method (RKPM), etc. do not satisfy this property and require additional methods for imposing essential boundary conditions [19, 30, 78, 144].

The minimization problem in (2.12) can be solved in a few Newton-Raphson iterations. The derivative and Hessian matrix of the objective function are given by (2.15) and (2.14) respectively, and the Newton step

$$\boldsymbol{\lambda} \leftarrow \boldsymbol{\lambda} - \mathbf{J}(\mathbf{x}, \boldsymbol{\lambda})^{-1} \mathbf{r}(\mathbf{x}, \boldsymbol{\lambda}) \quad (2.16)$$

is iterated until convergence. In the limit of the approximation converging to linear interpolation along any direction (some eigenvalue of $\boldsymbol{\beta} \rightarrow +\infty$), the Hessian matrix becomes singular when the guess for $\boldsymbol{\lambda}$ is far away from the unique minimizer $\boldsymbol{\lambda}^*$. Li [135] suggested the use of a steepest descent technique in this case. Alternatively, we found that the regularized Newton method proposed by Polyak [174] and applied to local max-ent by Foca [80] gives a faster convergence in the aforementioned limit of large eigenvalues of $\boldsymbol{\beta}$. We consider the modified objective function

$$F(\mathbf{x}, \boldsymbol{\lambda}, \boldsymbol{\zeta}) = \ln Z(\mathbf{x}, \boldsymbol{\zeta}) + \frac{1}{2} \left\| \frac{\partial \ln Z(\mathbf{x}, \boldsymbol{\lambda})}{\partial \boldsymbol{\lambda}} \right\| \|\boldsymbol{\zeta} - \boldsymbol{\lambda}\|^2. \quad (2.17)$$

Since $\ln Z(\mathbf{x}, \boldsymbol{\zeta})$ is a convex function and $\left\| \frac{\partial \ln Z(\mathbf{x}, \boldsymbol{\lambda})}{\partial \boldsymbol{\lambda}} \right\| \|\boldsymbol{\zeta} - \boldsymbol{\lambda}\|^2 \geq 0$, the regularized function $F(\mathbf{x}, \boldsymbol{\lambda}, \boldsymbol{\zeta})$ is strongly convex in $\boldsymbol{\zeta}$. The minimizer of (2.12) is given by

$$\boldsymbol{\lambda}^*(\mathbf{x}) = \arg \min_{\boldsymbol{\zeta} \in \mathbb{R}^d} F(\mathbf{x}, \boldsymbol{\lambda}, \boldsymbol{\zeta})|_{\boldsymbol{\zeta}=\boldsymbol{\lambda}}. \quad (2.18)$$

The derivative and Hessian matrix of the objective function in (2.18) are obtained as

$$\left. \frac{\partial F(\mathbf{x}, \boldsymbol{\lambda}, \boldsymbol{\zeta})}{\partial \boldsymbol{\zeta}} \right|_{\boldsymbol{\zeta}=\boldsymbol{\lambda}} = \mathbf{r}(\mathbf{x}, \boldsymbol{\lambda}), \quad \left. \frac{\partial F(\mathbf{x}, \boldsymbol{\lambda}, \boldsymbol{\zeta})}{\partial \boldsymbol{\zeta} \partial \boldsymbol{\zeta}} \right|_{\boldsymbol{\zeta}=\boldsymbol{\lambda}} = \mathbf{J}(\mathbf{x}, \boldsymbol{\lambda}) + \|\mathbf{r}(\mathbf{x}, \boldsymbol{\lambda})\| \mathbf{I}. \quad (2.19)$$

Clearly, the regularized Hessian is non-singular even when $\mathbf{J}(\mathbf{x}, \boldsymbol{\lambda})$ is singular. Therefore, the regularized Newton step for any $\boldsymbol{\lambda} \neq \boldsymbol{\lambda}^*$, viz.

$$\boldsymbol{\lambda} \leftarrow \boldsymbol{\lambda} - (\mathbf{J}(\mathbf{x}, \boldsymbol{\lambda}) + \|\mathbf{r}(\mathbf{x}, \boldsymbol{\lambda})\| \mathbf{I})^{-1} \mathbf{r}(\mathbf{x}, \boldsymbol{\lambda}), \quad (2.20)$$

is expected to provide more robust convergence for the aforementioned limiting case.

2.2.2 Quasi-static updated-Lagrangian formulation

In a classical total-Lagrangian description, the initial configuration is always the reference at any time or load steps. However, in simulations involving large deformations and distortions, the initial reference configuration often loses its meaning. An updated-Lagrangian formulation overcomes this limitation by using the deformed configuration of the previous step as the reference in an incremental fashion. For instructive purposes, we first describe a quasi-static variational problem in the *total-Lagrangian setting* and then reformulate it in an updated-Lagrangian framework. The proposed scheme is general to all approximation schemes and is not limited to local max-ent shape functions. Also, even though we limit our derivation to finite elasticity, the method can easily be extended to a more general class of variational material models (e.g., by using variational constitutive updates for inelasticity [169]).

We assume an incremental setting in which Ω_n refers to the n^{th} configuration of a body Ω (likewise, all fields are denoted by subscripts $(\cdot)_n$), and in particular $n = 0$ corresponds to the initial configuration with domain Ω_0 . Consider the total potential energy at step n with respect to the initial domain Ω_0 :

$$I[\varphi_n] = \int_{\Omega_0} W(\mathbf{F}_n) dV - \int_{\Omega_0} \rho_0 \mathbf{B}_n \cdot \varphi_n dV - \int_{\partial\Omega_0^N} \hat{\mathbf{T}}_n \cdot \varphi_n dS, \quad (2.21)$$

where $W : GL_+(d) \rightarrow \mathbb{R}$ denotes the strain energy density, $\mathbf{F} = \text{Grad } \varphi$ is the deformation gradient, $\varphi : \Omega \rightarrow \mathbb{R}^d$ is the deformation mapping, \mathbf{B} represents body forces and $\hat{\mathbf{T}}$ constant surface tractions applied over the Neumann boundary $\partial\Omega_0^N \subset \partial\Omega_0$. All quantities are defined at a step $n \geq 0$. We seek solutions as infimizers of the total potential energy³, specifically,

$$\varphi_n = \arg \inf \{ I[\varphi] : \varphi \in \mathcal{U}_n \}, \quad (2.22)$$

where

$$\mathcal{U}_n = \{ \varphi \in H^1(\Omega_0) : \varphi = \hat{\varphi}_n \text{ on } \partial\Omega_0^D \} \quad (2.23)$$

defines the set of admissible solutions with $\hat{\varphi}_n$ denoting essential boundary conditions at step n defined on the Dirichlet boundary $\partial\Omega_0^D \subset \Omega_0$. Without loss of generality, we make two assumptions: the initial configuration is undeformed (i.e., $\mathbf{F}_0 = \mathbf{I}$), and the initial and deformed coordinate systems coincide. The latter allows

³Note that in subsequent benchmark examples the energy density is chosen to be quasiconvex, so that unique solutions may be found. However, the same numerical procedure can, in principle, be extended to non-convex potentials, in which the formation of microstructure is implied.

us to define the total displacement field at step n as $\mathbf{u}_n(\mathbf{x}) = \boldsymbol{\varphi}_n(\mathbf{x}_0) - \mathbf{x}_0$, and we seek solutions in terms of the displacement field. We thus write the deformation gradient as

$$\mathbf{F}_n = \frac{\partial \boldsymbol{\varphi}_n}{\partial \mathbf{x}_0} = \mathbf{I} + \nabla_0 \mathbf{u}_n, \quad (2.24)$$

where $\nabla_m = \frac{\partial}{\partial \mathbf{x}_m}$ is the spatial derivative with respect to the m^{th} configuration.

Let us introduce a discretized approximation based on the above modified local max-ent scheme, which gives

$$\mathbf{u}_n(\mathbf{x}_0) \approx \mathbf{u}_n^h(\mathbf{x}_0) = \sum_{a=1}^{n_n} \mathbf{u}_n^a N^a(\mathbf{x}_0) \quad \Rightarrow \quad \mathbf{F}_n \approx \mathbf{F}_n^h = \mathbf{I} + \sum_{a=1}^{n_n} \mathbf{u}_n^a \otimes \nabla_0 N^a(\mathbf{x}_0), \quad (2.25)$$

where the shape functions $N^a(\mathbf{x}_0)$ are computed in the initial configuration Ω_0 . The set of all nodal displacements are denoted by $\mathbf{U}_n = \{\mathbf{u}_n^1, \dots, \mathbf{u}_n^{n_n}\}$. Computing the first variation of (2.21) and inserting the approximate fields at step n yields the discretized stationary condition in terms of nodal force balance:

$$\mathbf{f}_n^a(\mathbf{U}_n) = \mathbf{f}_{\text{int},n}^a(\mathbf{U}_n) - \mathbf{f}_{\text{ext},n}^a = \mathbf{0}, \quad a = 1, \dots, n_n. \quad (2.26)$$

The internal force vector acting on node a is given by

$$\mathbf{f}_{\text{int},n}^a(\mathbf{U}_n) = \int_{\Omega_0} \mathbf{P}(\mathbf{F}_n) \cdot \nabla_0 N^a(\mathbf{x}_0) dV \quad (2.27)$$

with the first Piola-Kirchhoff stress tensor $\mathbf{P} = \partial W / \partial \mathbf{F}$. Analogously, the external force on node a is

$$\mathbf{f}_{\text{ext},n}^a = \int_{\Omega_0} \rho_0 \mathbf{B}_n N^a(\mathbf{x}_0) dV + \int_{\partial \Omega_0^N} \hat{\mathbf{T}}_n N^a(\mathbf{x}_0) dS. \quad (2.28)$$

Solving the quasi-static system of equations in (2.26) calls for a robust and efficient iterative solver, which for optimal convergence rates uses the consistent tangent such as the family of Newton-Raphson methods.

To this end, the submatrices of the tangent matrix \mathbf{T}_n and its components are computed as

$$\mathbf{T}_n^{ab} = \frac{\partial \mathbf{f}_n^a}{\partial \mathbf{u}_n^b}(\mathbf{U}_n), \quad \left(\mathbf{T}_n^{ab} \right)_{ik} = \int_{\Omega_0} \mathbb{C}_{ijkl}(\mathbf{F}_n) \nabla_0 N_j^a(\mathbf{x}_0) \nabla_0 N_l^b(\mathbf{x}_0) dV - \frac{\partial \left(\mathbf{f}_{\text{ext},n}^a \right)_i}{\partial \left(\mathbf{u}_n^b \right)_k}, \quad (2.29)$$

where we used indicial notation with the classical summation convention and the incremental stiffness tensor $\mathbb{C}_{ijkl} = \partial P_{ij} / \partial F_{kl}$. Once the nodal displacements are

found, the total strain energy of the domain at step n is given by the first term in (2.21), i.e., $E_n(\mathbf{U}_n) = \int_{\Omega_0} W(\mathbf{F}_n) dV$. This completes the total-Lagrangian description at the n^{th} step with respect to the initial configuration as reference.

To transform the formulation into an *updated-Lagrangian* framework, we introduce an incremental deformation gradient $\mathbf{F}_{n \rightarrow n+1}$ which maps the configuration from step n to $n + 1$ as

$$\mathbf{F}_{n \rightarrow n+1} = \frac{\partial \boldsymbol{\varphi}_{n+1}}{\partial \mathbf{x}_n} = \mathbf{I} + \boldsymbol{\nabla}_n(\mathbf{u}_{n+1} - \mathbf{u}_n). \quad (2.30)$$

Under the assumption that the step size is sufficiently small, the incremental deformation gradient can be related to total deformation gradient by the composition

$$\mathbf{F}_{n+1} \approx \mathbf{F}_{n \rightarrow n+1} \mathbf{F}_n. \quad (2.31)$$

Note that the mapping of gradients between the reference and current configurations is

$$\boldsymbol{\nabla}_0(\cdot) = \frac{\partial(\cdot)}{\partial \mathbf{x}_0} = \frac{\partial \mathbf{x}_n}{\partial \mathbf{x}_0} \frac{\partial(\cdot)}{\partial \mathbf{x}_n} = \mathbf{F}_n \boldsymbol{\nabla}_n(\cdot), \quad (2.32)$$

while the density and volume integral are transformed, respectively, according to

$$\rho_0 = J_n \rho_n, \quad \int_{\Omega_0} (\cdot) dV = \int_{\Omega_n} \frac{1}{J_n} (\cdot) dV \quad \text{with} \quad J_n = \det \mathbf{F}_n. \quad (2.33)$$

To arrive at a consistent updated-Lagrangian description, we start with the total-Lagrangian description at step $n+1$, analogous to (2.27), but now computing all shape functions with respect to the Ω_n instead of Ω_0 . By exploiting the transformations (2.32) and (2.33), the internal nodal forces at step $n + 1$ are thus given by

$$\begin{aligned} \mathbf{f}_{\text{int},n+1}^a(\mathbf{U}_{n+1}) &= \int_{\Omega_0} \mathbf{P}(\mathbf{F}_{n+1}) \cdot \boldsymbol{\nabla}_0 N^a(\mathbf{x}_n) dV \\ &= \int_{\Omega_n} \frac{1}{J_n} \mathbf{P}(\mathbf{F}_{n \rightarrow n+1} \mathbf{F}_n) \mathbf{F}_n^T \boldsymbol{\nabla}_n N^a(\mathbf{x}_n) dV = \mathbf{f}_{\text{int},n+1}^a(\Delta \mathbf{U}_n) \end{aligned} \quad (2.34)$$

where $\Delta \mathbf{U}_n = \mathbf{U}_{n+1} - \mathbf{U}_n$ is the vector of nodal displacement increments from Ω_n to Ω_{n+1} . Note that the term $J_n^{-1} \mathbf{P}(\mathbf{F}_{n \rightarrow n+1} \mathbf{F}_n) \mathbf{F}_n^T$ in (2.34) can be interpreted as the pull-back of the Cauchy stress tensor from Ω_{n+1} to Ω_n or, alternatively, as the push-forward of the first Piola-Kirchhoff stress tensor from Ω_0 to Ω_n . This formulation is a compromise between classical incremental/rate formulations and variational modeling which typically uses a total-Lagrangian setting.

The transformation of the external nodal forces (2.28) occurs in a similar fashion (using (2.32), (2.33)), leading to

$$\mathbf{f}_{ext,n+1}^a = \int_{\Omega_n} \rho_n \mathbf{B}_{n+1} N^a(\mathbf{x}_n) dV + \int_{\partial\Omega_n^N} \hat{\mathbf{T}}_{n+1} N^a(\mathbf{x}_n) dS, \quad (2.35)$$

where \mathbf{B}_{n+1} and $\hat{\mathbf{T}}_{n+1}$ are now defined in the n^{th} configuration. Further, the tangent matrix components of (2.29) and the total strain energy transform into, respectively,

$$\left(\mathbf{T}_{n+1}^{ab} \right)_{ik} = \int_{\Omega_n} \mathbb{C}_{ijkl}(\mathbf{F}_{n \rightarrow n+1} \mathbf{F}_n) F_{qj} \nabla_n N_q^a(\mathbf{x}_n) F_{rl} \nabla_n N_r^b(\mathbf{x}_n) J_n^{-1} dV - \frac{\partial \left(f_{ext,n+1}^a \right)_i}{\partial \left(\Delta u_{n+1}^b \right)_k} \quad (2.36)$$

and

$$E_{n+1}(\Delta U_n) = \int_{\Omega_n} \frac{1}{J_n} W(\mathbf{F}_{n \rightarrow n+1} \mathbf{F}_n) dV. \quad (2.37)$$

To construct a numerical approximation of the spatial integrals in the above expressions for energy, forces and tangent matrix, we introduce a second set of n_p so-called *material points* which discretize the mass distribution in the domain according to [132]

$$\rho_n(\mathbf{x}_n) = \sum_{p=1}^{n_p} \rho_n^p V_n^p \delta(\mathbf{x}_n - \mathbf{x}_n^p) = \sum_{p=1}^{n_p} m^p \delta(\mathbf{x}_n - \mathbf{x}_n^p), \quad (2.38)$$

where ρ_n^p , V_n^p , and m^p are, respectively, the mass density, volume, and mass associated with the p^{th} material point located at $\mathbf{x}_n^p \in \Omega_n$. In order to distinguish nodes from material points, in the following superscripts $\{a, b\}$ and p are reserved for nodes and material points, respectively.

Material points are meshfree analogues of quadrature points in conventional FEM, where sampling is performed for the purpose of numerical integration. At the initial step, the p^{th} material point is assigned a density $\rho_0^p = \rho(\mathbf{x}_0)$ based on the mass density field ρ in the initial configuration. The initial material point volume V_0^p is computed from an ad-hoc triangulation of the initial configuration (which is discarded afterwards, as discussed below), akin to the volume of an element in the FEM context. Here, we enforce the local conservation of mass [132], so that each material point carries a constant mass ($m^p = \rho_n^p V_n^p = \text{const. } \forall n \geq 0$), while the density and volume are updated accordingly at every step, resulting in

$$\rho_{n+1}^p = \frac{\rho_n^p}{\det \mathbf{F}_{n \rightarrow n+1}^p} = \frac{\rho_0^p}{J_{n+1}^p}, \quad V_{n+1}^p = V_n^p \det \mathbf{F}_{n \rightarrow n+1}^p = V_0^p J_{n+1}^p, \quad (2.39)$$

where $\mathbf{F}_{n \rightarrow n+1}^p = \mathbf{F}_{n \rightarrow n+1}(\mathbf{x}^p)$ is the incremental deformation gradient at the material point p . Nodes do not carry mass nor volume and solely provide the kinematic interpolation required at the material points, while the constitutive laws are evaluated at the material points only. Figure 2.3 illustrates the evolution of material points and nodes in the total- and updated-Lagrangian settings.

Integration over the domain Ω_n is now approximated by a sum over the material points weighted by their respective volumes:

$$\int_{\Omega_n} \phi(\mathbf{x}_n) dV \approx \sum_{p=1}^{n_p} \phi(\mathbf{x}_n^p) V_n^p, \quad (2.40)$$

where $\phi : \Omega_n \rightarrow \mathbb{R}$ is an arbitrary function. When applied to the meshfree governing equations, the update-Lagrangian description with material point sampling leads to the following set of equations:

$$\mathbf{F}_{n \rightarrow n+1}^p(\Delta U_n) = \mathbf{I} + \sum_{a=1}^{n_n} \Delta \mathbf{u}_n^a \otimes \nabla_n N^a(\mathbf{x}_n^p) \quad \text{and} \quad \mathbf{F}_{n+1}^p = \mathbf{F}_{n \rightarrow n+1}^p \mathbf{F}_n^p, \quad (2.41a)$$

$$\mathbf{f}_{\text{int},n+1}^a(\Delta U_n) = \sum_{p=1}^{n_p} \frac{V_n^p}{J_n^p} \mathbf{P}(\mathbf{F}_{n \rightarrow n+1}^p \mathbf{F}_n^p) \mathbf{F}_n^{pT} \nabla_n N^a(\mathbf{x}_n^p), \quad (2.41b)$$

$$\mathbf{f}_{\text{ext},n+1}^a = \sum_{p=1}^{n_p} \rho_n^p V_n^p \mathbf{B}_{n+1}(\mathbf{x}_n^p) N^a(\mathbf{x}_n^p) + \int_{\partial \Omega_n^N} \hat{\mathbf{T}}_{n+1} N^a(\mathbf{x}_n) dS, \quad (2.41c)$$

$$\left(T_{n+1} \right)_{ik}^{ab}(\Delta U_n) = \sum_{p=1}^{n_p} \mathbb{C}_{ijkl}(\mathbf{F}_{n \rightarrow n+1}^p \mathbf{F}_n^p) (F_n^p)_{qj} \nabla_n N_q^a(\mathbf{x}_n^p) (F_n^p)_{rl} \nabla_n N_r^b(\mathbf{x}_n^p) \frac{V_n^p}{J_n^p} - \frac{\partial \left(f_{\text{ext},n+1}^a \right)_i}{\partial \left(\Delta u_n^b \right)_k}, \quad (2.41d)$$

$$E_{n+1}(\Delta U_n) = \sum_{p=1}^{n_p} \frac{V_n^p}{J_n^p} W(\mathbf{F}_{n \rightarrow n+1}^p \mathbf{F}_n^p). \quad (2.41e)$$

2.2.3 Tensile instability

Belytschko et al. [24] provided a unified analysis of stability for meshfree particle methods. In particular, they identified two distinct instabilities – (i) an instability due to presence of spurious modes introduced by the rank-deficiency of the discretization operator, and (ii) tensile instability. The first instability is particular

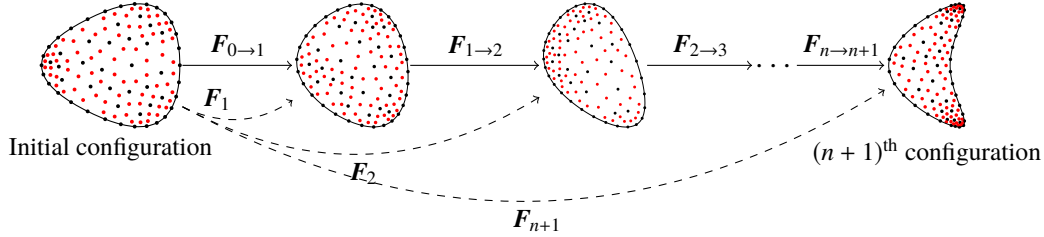


Figure 2.3: Illustration of the *total-Lagrangian* description (*dashed arrows*) where the current configuration is referenced to the initial configuration via the total deformation gradient \mathbf{F}_{n+1} , and of the *updated-Lagrangian* description (*solid arrows*) where the current configuration is referenced to the previous configuration via the incremental deformation gradient $\mathbf{F}_{n \rightarrow n+1}$. The red and black points denote material points and nodes, respectively.

to nodal integration, and stress-point integration has been shown to eliminate this type of instability; see, e.g., [24, 71, 72, 182]. Similar to stress-points, material point integration also alleviates the instability due to rank-deficiency by performing quadrature away from the nodes. By contrast, tensile instability is more nefarious and appears when updated-Lagrangian/Eulerian discretization kernels are used. Tensile instability can be eliminated by using (total) Lagrangian kernels [24], but this defeats the purpose of using particle-based meshfree methods. Here, we study the tensile instability with local max-ent shape functions in a simplified 1D setting, which will later motivate our solution for dealing with this type of instability in general 3D problems.

As an instructive example, consider a 1D chain of $n_n = 50$ equally-spaced nodes whose positions in the initial configuration $\Omega_0 = [0, 1]$ are $x_0^a = \frac{a-1}{n_n-1}$, $a = 1, \dots, n_n$. Assume there is initially only a single material point ($n_p = 1$), located at $x_0^p = 0.5$ and carrying an initial volume $V_0^1 = 1$ equal to the unit length of the chain, and a constant unit stiffness (linear elastic constitutive law). The chain is now stretched by a ratio $\lambda > 1$, while keeping the locality parameter β^1 constant. Because the shape functions are dependent on the nodal positions, increasing the nodal spacings under extension results in a localization of the shape function support at the material point, see Figure 2.4a; i.e., fewer and fewer nodes contribute to the approximation of the fields of interest at the material point.

Recall that the internal nodal forces (2.41b) are given by the product of the first Piola-Kirchoff stress tensor with a discretization kernel $\mathbf{F}_n^{pT} \nabla_n N^a(\mathbf{x}_n^p) V_n^p / J_n^p = \mathbf{F}_n^{pT} \nabla_n N^a(\mathbf{x}_n^p) V_0^p$. Figure 2.4b shows the changing nodal kernel values with increasing nodal spacing (i.e., increasing applied stretch λ). From the point of view

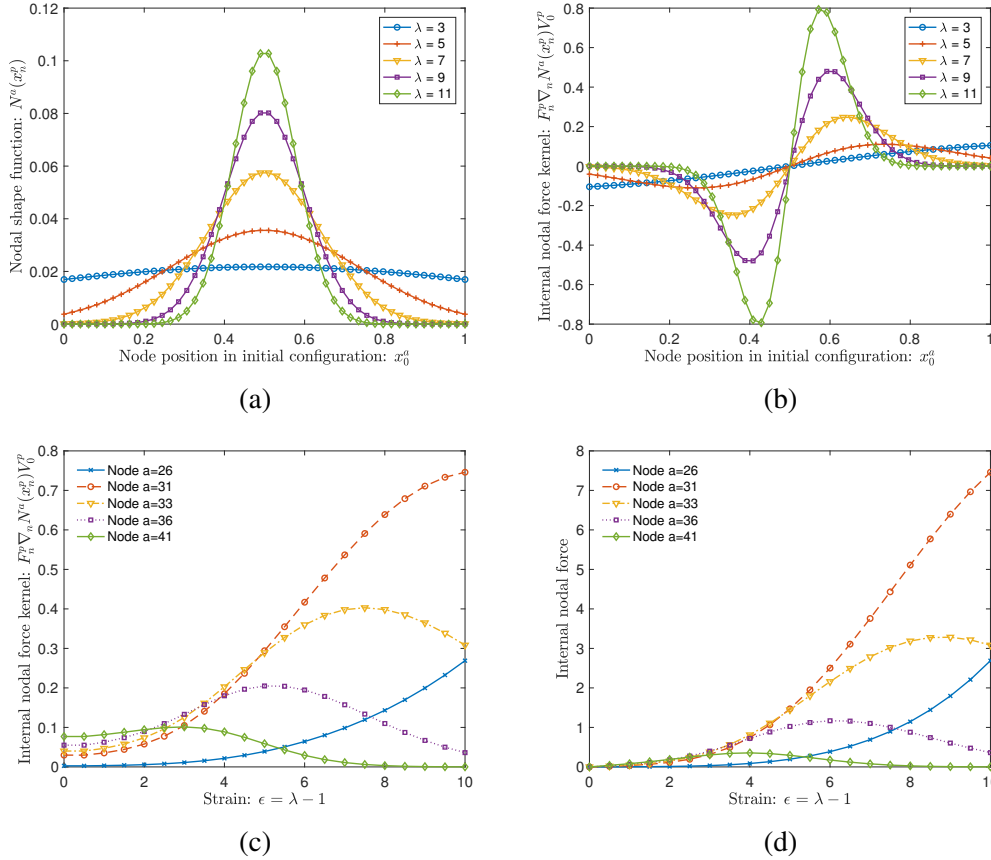


Figure 2.4: For all shape functions evaluated at a material point initially at $x_0^p = 0.5$ on a 1D domain $\Omega_0 = [0, 1]$ with constant locality parameter $\beta_n^p = 1$, (a) values N^a of all $a = 1, \dots, n_n$ shape functions, plotted for different stretch ratios $\lambda = |\Omega_n|$; (b) associated internal nodal force kernels ($F_n^p \nabla_n N^a V_0^p$) of all shape functions evaluated for different stretches λ ; (c) internal nodal force kernels of selected nodes vs. strain $\varepsilon = \lambda - 1$; (d) internal nodal force on selected nodes vs. strain $\varepsilon = \lambda - 1$.

of any particular node, increasing the stretch λ leads to changes in its kernel value (evaluated at the material point p), which first increases strongly and then decays to zero as the shape function support increasingly localizes, as illustrated in Figure 2.4c. Internal nodal forces can be computed using the kernel values and the stress (from linear elastic constitute law). The non-monotonic behavior of the kernel (with respect to stretch ratio λ) results in a non-monotonic nodal force that starts to decrease after a certain strain, as shown in Figure 2.4d. This phenomenon of non-physical stiffness is called tensile instability, and is a purely numerical artifact arising due to the changing nature of the discretization kernel; see Swegle et al. [197] for a related discussion in the context of SPH. In summary, increasing nodal spacings causes a localization of the shape function support, which in turn leads to

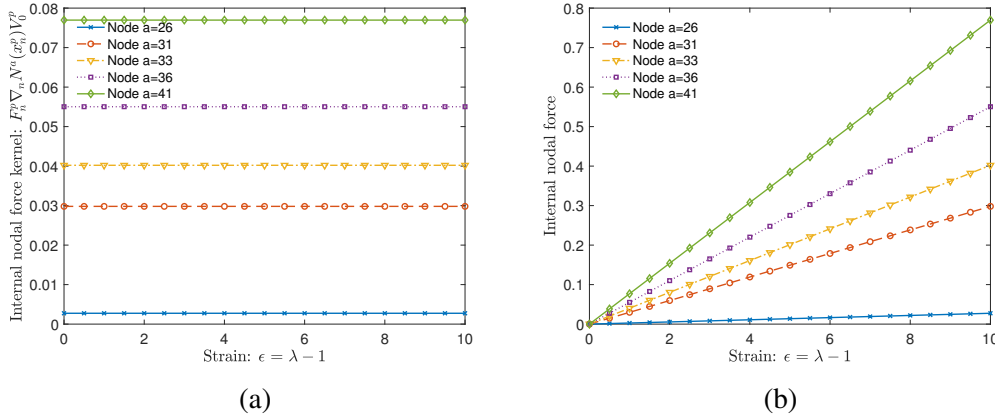


Figure 2.5: (a) Internal nodal force kernels and (b) internal nodal forces of selected nodes vs. strain $\epsilon = \lambda - 1$, with an adaptively modified locality parameter $\beta_n^p \propto h_n^{-2}$ where h_n is the (uniform) nodal spacing and with an initial $\beta_0^p = 1$.

tensile instability.

As suggested by Arroyo and Ortiz [7] and Li et al. [132], the tensile instability can be overcome by evolving the locality parameter of the local max-ent shape functions at every step. In their isotropic max-ent framework, those authors introduced a non-dimensional constant γ such that $\beta = \gamma/h^2$, where h is some appropriate measure of average nodal spacing at a given time or load step⁴. In the simple problem of a 1D node set as in Figure 2.4, evolving β as per the aforementioned scheme, i.e.,

$$\beta_{n+1}^p = \frac{\gamma}{(h_{n+1}^p)^2} = \beta_n^p \left(\frac{h_n^p}{h_{n+1}^p} \right)^2, \quad (2.42)$$

produces exactly coincident shape function support at every step and hence correctly reproduces constant nodal force kernels and linear nodal force responses as shown in Figure 2.5. This adaptivity scheme can then be extended to higher dimensions as

$$\beta_{n+1}^p = \frac{1}{(J_{n \rightarrow n+1}^p)^{2/3}} \beta_n^p \quad (2.43)$$

where β_n^p is the locality parameter at n^{th} step, and where it is assumed that $(J_{n \rightarrow n+1}^p)^{1/3}$ is a reasonable estimate of the relative average nodal spacing around material point p . Although well suited for 1D, the isotropic nature of this scheme does not properly

⁴Note that Li et al. [132] focused on dynamic problems solved by explicit updates, whereas we are concerned with a quasistatic formulation. Therefore, the terminology of time vs. load steps is, in principle, interchangeable.

account for direction-dependent changes in nodal spacing and hence is severely limited in the amount of anisotropic deformation that can be simulated before the onset of tensile instability. As a simple example, consider a uniaxial extension test in 2D, which leads to strongly increasing nodal spacings in the extension direction, whereas the Poisson effect results in nodal spacings shrinking in the transverse directions at the same time.

Local updates of the locality parameter of type (2.43) have an essential consequence, which is key to the proposed methodology and a departure from classical discretization schemes including the original maximum-entropy approximants of Arroyo and Ortiz [7]. Here, β^p is defined and updated only at each material point p , where it is needed to evaluate shape functions $N^a(\mathbf{x}_n^p)$ and their gradients $\nabla N^a(\mathbf{x}_n^p)$ for the numerical integration of energy, forces and stiffness tensors according to (2.40). Therefore, neither a shape function N^a nor a node a is associated with a specific β but, depending on the material point p at \mathbf{x}^p where shape functions are to be evaluated, all shape functions N^a ($a = 1, \dots, n$) are computed using the very same β^p of that material point. As a practical consequence, shape functions cannot be evaluated at nodes, only at material points. It also means that there is no such thing as unique shape functions $N^a(\mathbf{x})$, rather we have $N^a = N^a(\mathbf{x}, \beta)$ and β varies based on where the shape function is being evaluated – here, $N^a(\mathbf{x}^p) = N^a(\mathbf{x}^p, \beta^p)$. Hence we also cannot plot *the* shape function N^a for any node a (this is why we chose the discrete visualization in Fig. 2.1). This choice is necessitated by the specific adaptivity scheme used here (see (2.43) and its anisotropic generalization in Section 2.2.4 below).

While a node might inherit different β when computing shape functions at different material points, it will be equal for all nodes in the context of the local approximation at a given material point. We also note that shape functions and shape function derivatives at step $(n + 1)$ are calculated based on the previous values β_n^p . Therefore, we may drop the spatial dependence on the shape functions through β when calculating their gradients in (2.13), as is also done for the nodal locations in the updated-Lagrangian setting.

2.2.4 Anisotropic adaptivity and bounded shape function support

To eliminate tensile instability in higher dimensions, we need to anisotropically update the support of the max-ent shape functions; i.e., the Pareto optimality between shape function width and information entropy should be updated differently for each

dimension based on the local deformation, which is exactly why a tensor-valued locality parameter $\boldsymbol{\beta}$ was introduced in (2.3). Assuming the step size between configurations n and $n + 1$ is sufficiently small, the invariance of the shape function support in (2.10) implies

$$\begin{aligned} N_n^a(\mathbf{x}_n^p) &= N_{n+1}^a(\mathbf{x}_{n+1}^p) \\ \implies (\mathbf{x}_n^p - \mathbf{x}_n^a) \cdot \boldsymbol{\beta}_n^p(\mathbf{x}_n^p - \mathbf{x}_n^a) &= (\mathbf{x}_{n+1}^p - \mathbf{x}_{n+1}^a) \cdot \boldsymbol{\beta}_{n+1}^p(\mathbf{x}_{n+1}^p - \mathbf{x}_{n+1}^a). \end{aligned} \quad (2.44)$$

If the effective support size of N^a is reasonably small to approximate the local deformation with an affine map, we may exploit the incremental deformation gradient to obtain the approximation

$$\boldsymbol{\beta}_{n+1}^p = (\mathbf{F}_{n \rightarrow n+1}^p)^{-\text{T}} \boldsymbol{\beta}_n^p (\mathbf{F}_{n \rightarrow n+1}^p)^{-1}. \quad (2.45)$$

Hence, even if we start with an isotropic shape function support, anisotropy is introduced incrementally through the deformation gradient at a given material point p . We will refer to this scheme as *anisotropic adaptivity* of the shape function support. Figure 2.6 compares the evolution of a representative shape function support based on a 2D node set that is stretched uniaxially. It is evident from Figure 2.6d that the effective support size along the direction of stretch is maintained for anisotropic adaptivity of the locality parameter, whereas it becomes localized for constant and isotropic adaptive locality parameters in Figure 2.6b and Figure 2.6c, respectively.

When local max-ent shape functions span over all nodes in the domain, their global support makes the implementation computationally impractical. However, shape functions decay exponentially with distance from their respective node according to (2.10), implying that only a few nodes relatively close to a material point are significant to the approximation accuracy at that material point. Hence, it is practical to construct the approximation based only on nodes that lie inside a cut-off region centered around each material point. An analogous remapping of nodes to material points was discussed for the OTM method [132]. Since the shape functions decay as $\exp(-\beta \|\mathbf{x} - \mathbf{x}_a\|^2)$, the original formulation by [7] suggests the use of a cut-off sphere whose radius is given by $R_{cut} = \sqrt{(-\log \epsilon)/\beta}$, where $0 < \epsilon \leq 1$ is a small tolerance, so the shape function support is truncated beyond the cut-off sphere.

In an updated-Lagrangian setting, the cut-off limits must evolve according to the local deformation; otherwise, a loss in connectivity will effectively result in the localization of shape functions. For example, analogous to the isotropic adaptivity

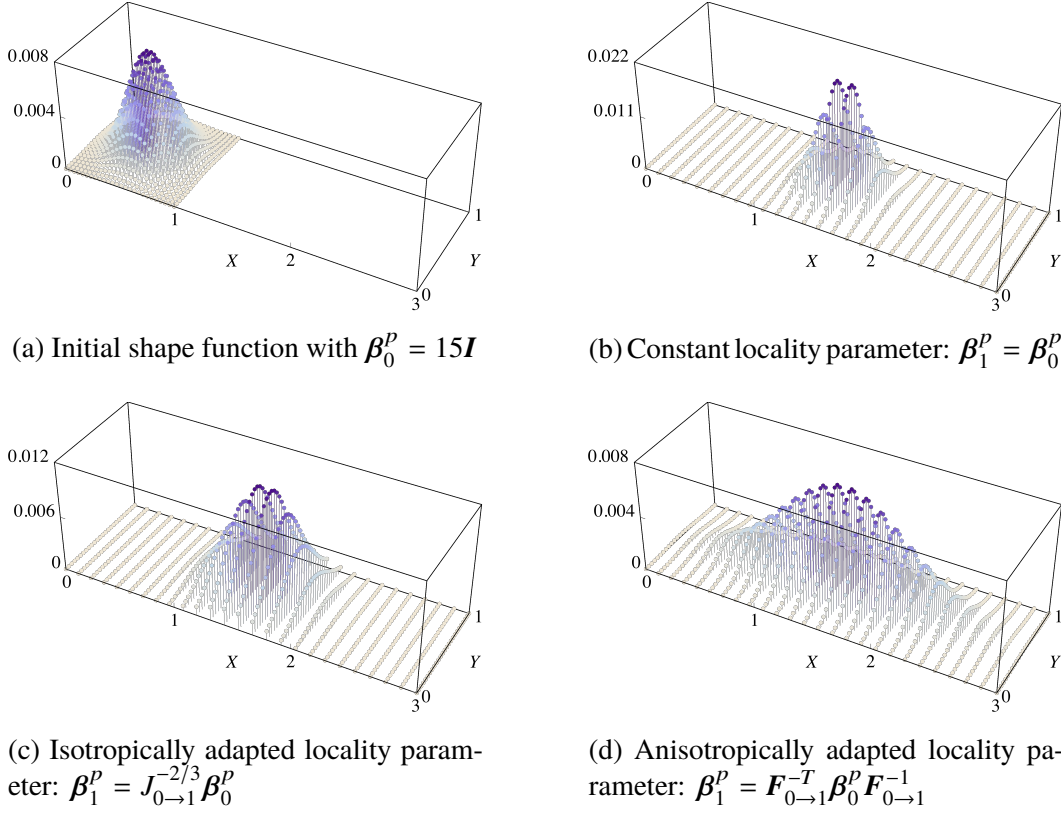


Figure 2.6: Shape function support of a material point initially located at $\mathbf{x}_0^p = (0.5, 0.5)^T$ under homogeneous anisotropic deformation described by the total deformation gradient $\mathbf{F}_{0 \rightarrow 1} = \begin{pmatrix} 3 & 0 \\ 0 & 1 \end{pmatrix}$.

scheme (2.43), the radius of a cut-off sphere centered at a material point p can be updated by

$$R_{cut,n+1}^p = (J_{n \rightarrow n+1}^p)^{1/3} R_{cut,n}^p. \quad (2.46)$$

However, it is not surprising that updating the cut-off radius isotropically as in (2.46) will result in a severe loss of connectivity during anisotropic deformation and ultimately give rise to tensile instability. Instead, we propose the use of cut-off ellipsoids to improve the connectivity updates. Using ellipsoidal cut-off regions also provides a better approximation when the spatial distribution of nodes is highly anisotropic.

We define that, at the n^{th} step, the connectivity of each material point \mathbf{x}_n^p includes all nodes \mathbf{x}_n^a which lie inside the ellipsoid described by

$$(\mathbf{x}_n^a - \mathbf{x}_n^p) \cdot \mathbf{M}_n^p (\mathbf{x}_n^a - \mathbf{x}_n^p) \leq 1, \quad (2.47)$$

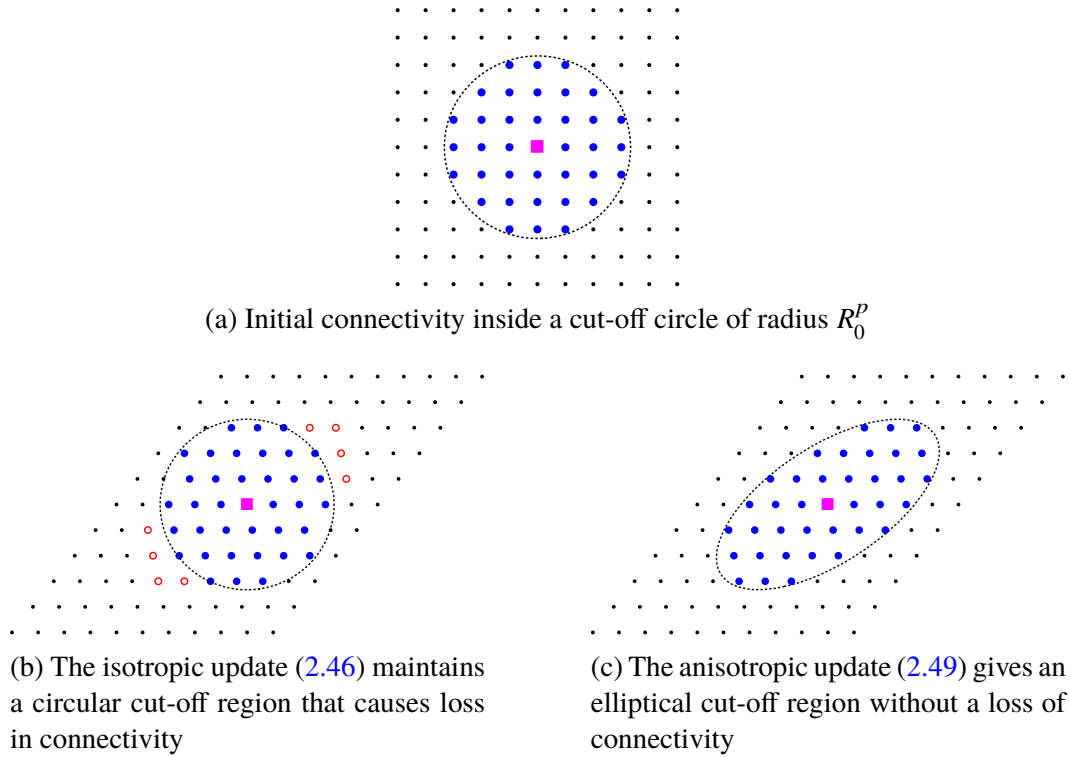


Figure 2.7: Evolution of the nodal connectivity surrounding a material point p (pink square) under significant affine shear deformation. Dashed lines denote the convex boundary of the cut-off region surrounding all nodes (blue solid circles) included in the material point's connectivity; nodal points missed by the isotropic update are shown as open (red) circles. Since, the simple shear deformation is isochoric, the isotropic update (2.46), shown as case (b), implies $R_1^p = R_0^p$.

where \mathbf{M}_n^p is a $d \times d$ matrix with d positive eigenvalues. At the initial configuration, the cut-off ellipsoid can be chosen appropriately based on the tolerance ϵ and the average nodal spacing in each direction around the material point. To avoid any significant loss in connectivity, the ellipsoid is updated based on the deformation map at every material point p according to

$$(\mathbf{x}_n^a - \mathbf{x}_n^p) \cdot \mathbf{M}_n^p (\mathbf{x}_n^a - \mathbf{x}_n^p) = (\mathbf{x}_{n+1}^a - \mathbf{x}_{n+1}^p) \cdot \mathbf{M}_{n+1}^p (\mathbf{x}_{n+1}^a - \mathbf{x}_{n+1}^p), \quad (2.48)$$

which, under the assumption that the step size and changes in ellipsoid size are sufficiently small, gives the scheme for updating the anisotropic connectivity:

$$\mathbf{M}_{n+1}^p = (\mathbf{F}_{n \rightarrow n+1}^p)^{-T} \mathbf{M}_n^p (\mathbf{F}_{n \rightarrow n+1}^p)^{-1}. \quad (2.49)$$

This is analogous to the update of the locality parameter β , see (2.45). Figure 2.7 illustrates how an anisotropic ellipsoidal cut-off region better maintains connectivity compared to the isotropic scheme for the case of significant shear deformation.

2.2.5 Treatment of essential boundary conditions and material interfaces

Local max-ent is not interpolatory, i.e., it does not satisfy the strong Kronecker property. However, it does satisfy the weak Kronecker property on the boundary. Precisely, if \mathbf{x} lies on the convex hull Ω of the domain, then $N^a(\mathbf{x})$ is zero if the node located at \mathbf{x}^a lies in the interior of the Ω . This implies that interpolation on the boundary depends only on boundary nodes and is independent of the interior nodes. Therefore, essential boundary conditions can be applied without modifications of the shape function support. Note that the max-ent shape functions only satisfy consistency up to first-order and hence can only impose at most affine boundary conditions exactly; however, this error vanishes with h -refinement as the essential boundary conditions are recovered as a converging sequence of piecewise-linear functions. Also, for problems involving non-convex domains, the weak Kronecker property is not satisfied on the non-convex part of the boundary. Several techniques like the visibility criterion [19, 125], diffraction method [23, 165] and the transparency method [165] have been proposed to deal with non-convex domains in element-free Galerkin methods and can be extended to max-ent approximants. However, all of those have limitations for interpolation on non-convex boundaries; see, e.g., Belytschko et al. [21] for a review. Alternatively, the max-ent shape function support can be seamlessly made highly local (by increasing the eigenvalues of the locality parameter β) in the proximity of a non-convex boundary and hence minimizing the extraneous non-convex region included in the convex hull of shape function support [88]; but requires manual control for problems involving complicated geometries.

Discontinuous derivatives like material discontinuities also pose a challenge in meshfree methods. In conventional FE methods, nodes can conveniently be chosen such that a discontinuity like a material interface does not pass through any element. As a result, capturing solutions with discontinuous derivatives while ensuring displacement continuity across the material interface is straightforward. In contrast, without proper treatment, the support of non-local meshfree shape functions like max-ent spreads across any discontinuity, which leads to incorrectly smearing out of the interface. The problem is fundamentally the same as the inability to apply essential boundary conditions. Several complicated techniques have been introduced such as additional special shape functions with discontinuous derivatives [124], including Lagrange multipliers [62], and the transition to finite elements near interfaces [20, 103, 123].

The local max-ent scheme allows for a straightforward solution for capturing dis-

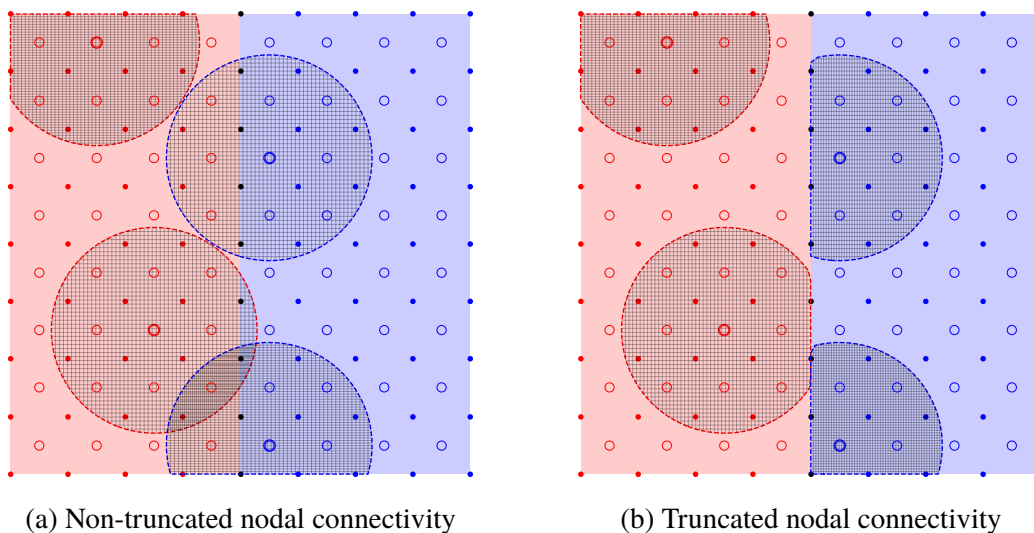


Figure 2.8: Domains of nodal connectivity of four representative material points near an interface separating two different materials (indicated by the red and blue regions). Material points and nodes are denoted by open and filled dots, respectively. The hatched area around each material point indicates the cut-off region that encloses all nodes whose shape functions are contributing to the material point.

continuous derivatives. Our approach is inspired by the technique developed by Cordes and Moran [62] for material interfaces in the element-free Galerkin method. Consider the example problem of a 2D domain containing two materials separated by an interface, as illustrated in Figure 2.8. The spatial discretization is chosen such that the interface contains only nodes and no material points. Each material point and node is assigned uniquely to one material, while the interface nodes belong to both and are shared by both regions⁵.

As a crucial step, the shape function support and the resulting connectivity of each material point is truncated to include only those nodes that belong to the same material as the material point itself (see Figure 2.8b). This ensures that the kinematic interpolation at any material point does not explicitly depend on nodes from the other side of the interface. Since the interfacial nodes are shared by both regions and because of the weak Kronecker property, displacement continuity at the interface is automatically ensured. As a result, there is no smoothing nor spurious oscillations across the discontinuity, and discontinuous derivatives are captured accurately (Section 2.3.3 presents a numerical validation example). The

⁵Note that the assignment of nodes to the different materials occurs only for purpose of shape function definitions, whereas the materials' constitutive models are evaluated only at the material points. This justifies the unique assignment of material points and the non-unique assignment of nodes to the materials

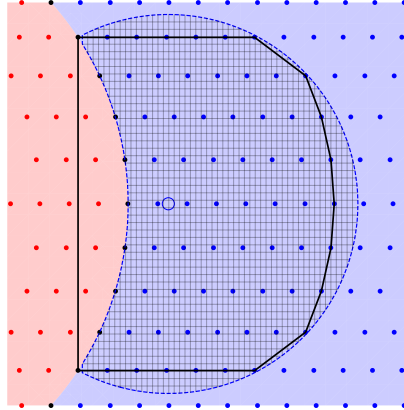


Figure 2.9: Shape function support for a material point (blue open dot) in the proximity of a non-convex material interface. The convex hull (indicated by black solid line) extends beyond the interface. However, only nodes in the blue region (indicated by blue filled dots) are considered during approximation construction. Nodes from the red region (indicated by red filled dots) that lie inside the convex hull are excluded from the approximation.

simplicity and the fact that no additional computational costs are associated with this scheme is particularly advantageous for higher-dimensional problems involving multiple material interfaces such as polycrystals, high-volume-fraction composites (e.g., cermets or magneto-rheological elastomers), and fluid-structure interactions.

Note that in problems with complex geometry or large deformations, there may be curved material interfaces that give rise to non-convex sub-regions (see e.g. Figure 2.9). As a result, the convex hull of the nodal connectivity extends beyond the interface. However, as per the proposed scheme, nodes from the other side of the material interface are still excluded and the approximation at the material point remains unaffected by the kinematics of nodes across the interface. Analogous to the case of non-convex boundaries, the extraneous region of the convex hull will diminish with h -refinement or, alternatively, can be minimized by seamlessly increasing the locality of the shape functions near the interfaces.

2.3 Benchmark tests

We present a selection of benchmark simulations in three dimensions to study the performance of the proposed enhanced local max-ent scheme in problems involving large deformation. The first benchmark test simulates the inhomogeneous extension of a hyperelastic block to demonstrate the convergence rate and accuracy of the proposed scheme. The second benchmark simulates the torsion of a hyperelastic

cube to illustrate its ability to simulate severe deformation and distortion. The third benchmark showcases the stretching of a periodic representative volume element (RVE) of a two-phase laminate composite to demonstrate the capability to accurately capture discontinuous derivatives using truncated shape function supports. The fourth benchmark simulates two spherical inclusions in a high-volume-fraction composite RVE undergoing such severe deformation that the initially distant inclusions get almost into Hertzian contact. The fifth and final benchmark simulates the elastoplastic response of a cylindrical specimen impacting a wall at high speed, classically known as the Taylor anvil test. Importantly, all five benchmarks demonstrate that the proposed adaptive use of anisotropic shape function supports successfully eliminates tensile instability in the updated-Lagrangian framework up to very large deformations. In fact, without the framework introduced here, all benchmark simulations become unstable even for small deformations. Even with the best chosen parameters, the non-adaptive updated-Lagrangian framework could only simulate no more than 10% of the deformations (in all benchmarks shown here) that our new framework can handle.

All simulations follow the same protocol to set up the initial configuration. Once the initial set of nodes is defined, an ad-hoc mesh is created by applying Delaunay triangulation to the initial node set. Next, a material point is inserted at the barycenter of each simplicial element with an initial volume V_0^p equal to the product of simplicial quadrature weight and volume of the containing simplex. The initial value of the locality parameter associated with each material point is set to $\beta_0^p = \gamma h_p^{-2} \mathbf{I}$, where h_p is the average distance between the associated material point and nodes of the surrounding element in the initial mesh⁶, and γ is a user input, as discussed in Section 2.2.3. The mesh creation is a one-time process and the ad-hoc mesh is discarded after the initial material point setup. The initial connectivity of each material point is given by the cutoff ellipsoid associated with $\mathbf{M}_n^p = R_{cut,p}^{-2} \mathbf{I}$, where $R_{cut,p} = \sqrt{(-\log \epsilon) h_p^2 / \gamma}$, and $\epsilon = 10^{-6}$. Only one material point is used per tetrahedron in the initial auxiliary mesh. The proposed scheme to overcome tensile instability is, in principle, independent of the number of material points and certainly extensible to higher-order integration (i.e., to larger numbers of integration points per tetrahedron in the auxiliary mesh). We have experimented with using a higher number of material points per tetrahedron and, while minor improvements are seen,

⁶We note that all (structured and unstructured) node sets used in the following benchmark simulations have sufficient regularity for an isotropic initial β . In case of strongly anisotropic initial configurations, it is straightforward to adapt the definition of β_0^p accordingly.

we could not draw any general conclusions. Our focus here is on overcoming the tensile instability (which is achieved with only a single integration point per initial tetrahedron in all examples shown). The effects of numerical quadrature were studied by Arroyo and Ortiz [7] in the context of (isotropic) local maximum-entropy approximants, which also extend to our method.

As a representative example, all hyperelastic benchmark simulations (wherever applicable) use a compressible Neo-Hookean constitutive model to incorporate material non-linearity. The specific strain energy density is given by

$$W(\mathbf{F}) = \frac{\mu}{2} \left[\text{tr} \left(\mathbf{F}^T \mathbf{F} \right) J^{-2/3} - 3 \right] + \frac{\kappa}{2} (J - 1)^2, \quad (2.50)$$

where μ and κ are the shear and bulk moduli, respectively, and $J = \det \mathbf{F}$. For simplicity, all subsequent simulation results are based on non-dimensional material and geometry parameters. We note that the presented max-ent and updated-Lagrangian schemes are sufficiently general to apply to, in principle, arbitrary material constitutive laws including elastoplasticity (see benchmark V in Section 2.3.5); and may make use of the extension in Li et al. [132] for general inelastic solids via variational constitutive updates [169].

Newton-Raphson iteration is used to solve for the nodal displacements at each load step (or time step in case of the fifth, dynamic benchmark in Section 2.3.5 where explicit time integration is used). After every load/time step, the reference configuration is updated according to the updated-Lagrangian framework. Where applicable, obtained simulation results are compared to those of (total-Lagrangian) FEM overkill simulations (using 10-node tetrahedral elements). Since comparing quantities such as the strain energy entails ambiguity due to the different reference configurations in the total- vs. updated-Lagrangian settings, we use force-displacement curves as a comparison metric, because they are independent of the choice of reference configuration.

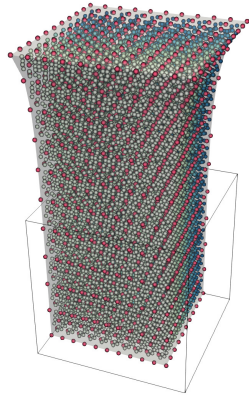
2.3.1 Benchmark I: extension of a hyperelastic block

The first benchmark test aims to reproduce the numerical experiment in the original formulation by Arroyo and Ortiz [7] as a baseline. We simulate a hyperelastic Neo-Hookean cube that is stretched vertically with the top and bottom faces being fixed in all directions – due to symmetry it is sufficient to model one eighth of the block with the top face fixed, two adjacent side faces traction-free and symmetry boundary conditions applied on the rest of the faces, while the bottom face is vertically fixed and free to deform in-plane. The shear and bulk moduli are set to $\mu = 5$ and

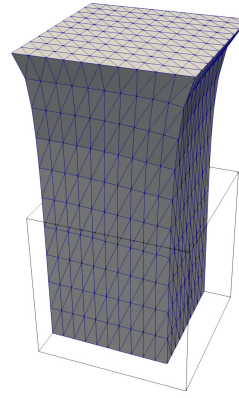
$\kappa = 10$, respectively. The cube is deformed up to 100% extension in 50 load steps (see Video 1) and the total vertical reaction force on the top face is recorded. Figure 2.10a and 2.10b show the final deformed state obtained using local max-ent and FEM. For the purpose of a convergence study, the initial spatial discretization is a uniform grid of nodes with varying degrees of nodal spacing (see Figure 2.10c), and different values of γ to initialize the locality parameter β . Due to highly nonlinear deformations, an overkill FEM simulation with $20 \times 20 \times 20$ elements is used as a proxy for the exact solution. Figure 2.10d illustrates the convergence in the reaction force with refinement of the spatial discretization. Three important observations are made: (i) The error produced by the local max-ent simulations is always smaller than that of FEM, implying improved accuracy, as similarly observed by Arroyo and Ortiz [7] for the same benchmark. (ii) The shown errors corresponding to larger values of γ approach the FEM errors, which is corroborated by the fact that larger γ implies higher locality in interpolation, thus tending towards the affine interpolation of FEM. (iii) More importantly, the error produced by the updated-Lagrangian formulation is lower than that obtained from total-Lagrangian calculations with the same γ , which is expected due to the large deformations involved.

2.3.2 Benchmark II: torsion of a hyperelastic cube

We simulate the torsion response of a hyperelastic Neo-Hookean cube with fixed top and bottom faces (this time the entire cube is modeled, see Figure 2.11a-2.11d). The cube is deformed in incremental torsion steps of $0.05 \text{ rad} \approx 2.86^\circ$ twist angle per step (see Video 2). For added complication, the shear and bulk moduli are set to $\mu = 5$ and $\kappa = 100$, respectively. We note that Ortiz et al. [166, 167] have developed maximum-entropy meshfree methods suited to near-incompressible and incompressible materials. However, to avoid issues related to volumetric locking, we do not consider truly incompressible materials within the scope of this work. The initial spatial discretization is a uniform grid of nodes with varying degrees of nodal spacing. The initial locality parameter for each material point is set isotropically using $\gamma = 6.0$. Figure 2.11e shows the total vertical reaction force on the top face in response to the applied torsion. Remarkably, the enhanced local max-ent scheme is able to simulate up to 200° degrees of torsion, which is significantly higher than the maximum torsion of 144° degrees achievable by our comparison FEM simulation. Moreover, local max-ent achieves a similar level of accuracy with the number of material points being only one-sixth the number of elements in FEM. These observations demonstrate the superior capability of the enhanced local



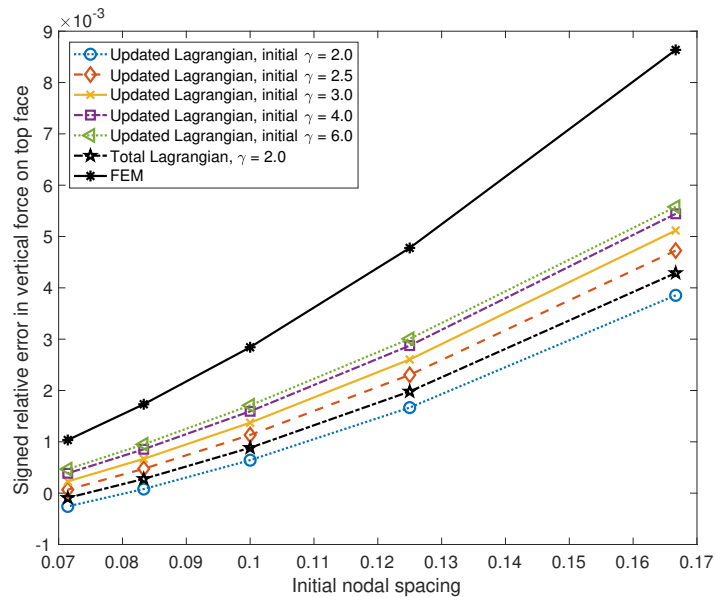
(a) Deformation at 100% extension using local max-ent



(b) Deformation at 100% extension using FEM

Initial discretization	Nodal spacing per side length	No. of nodes	No. of material points
6×6×6	0.1667	559	2592
8×8×8	0.1250	1241	6144
10×10×10	0.1	2331	12000
12×12×12	0.0833	3925	20736
14×14×14	0.0714	6119	32928

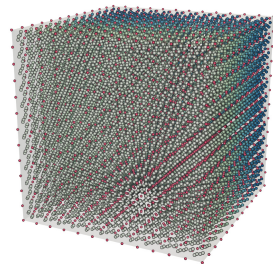
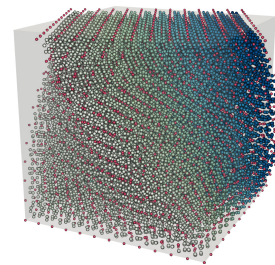
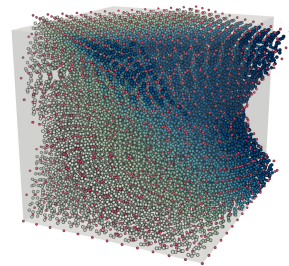
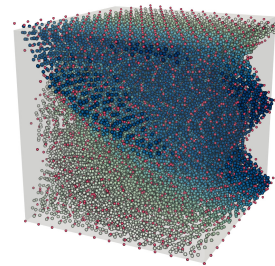
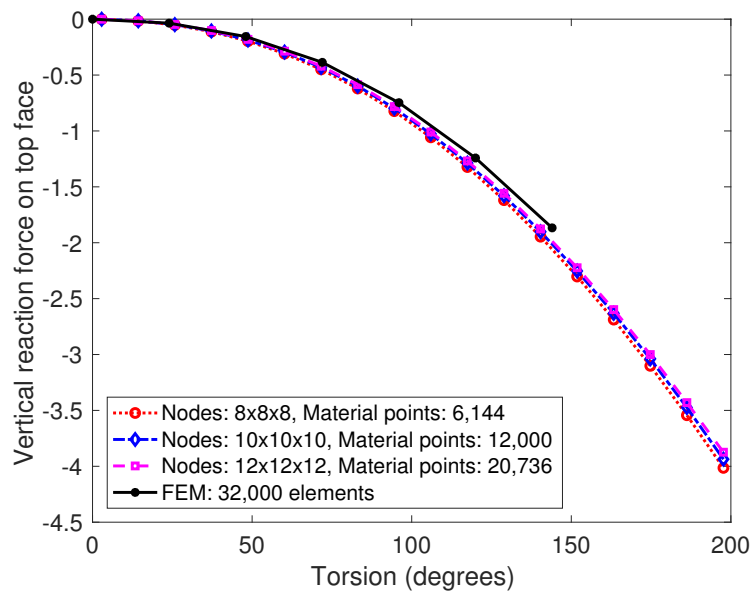
(c) Spatial discretization schemes for varying nodal spacing



(d) Signed relative error in the vertical reaction force on the top face

Figure 2.10: *Benchmark I*: extension of a hyperelastic block

max-ent scheme to simulate problems that are highly prone to mesh distortion and tensile instability.

(a) Initial state at 0° applied torsion(b) Deformation at 65.9° applied torsion(c) Deformation at 131.8° applied torsion(d) Deformation at 200.5° applied torsion

(e) Vertical reaction force vs. torsional angle (in degrees)

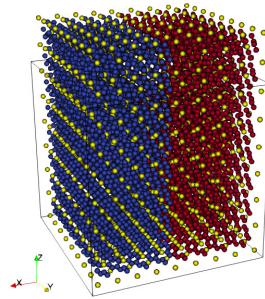
Figure 2.11: *Benchmark II*: torsion of a hyperelastic cube

2.3.3 Benchmark III: hyperelastic laminate composite

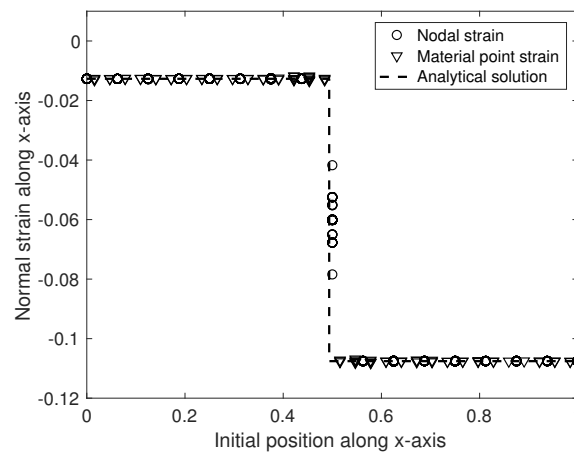
We simulate the response of an RVE made of a hyperelastic two-phase laminate composite subjected to uniaxial extension with traction-free lateral faces. As illustrated in Figure 2.12a, the RVE consists of a material interface normal to the x -axis separating the two Neo-Hookean materials. To pronounce the discontinuity in derivatives across the interface, the elastic moduli are chosen such that one phase is highly compressible ($\mu = 1, \kappa = 1$), whereas the other phase is relatively less compressible ($\mu = 5, \kappa = 100$). Periodic boundary conditions are imposed on the RVE. The initial spatial discretization is a uniform grid of $9 \times 9 \times 9$ nodes. The locality parameter for each material point is initialized using $\gamma = 2.0$. The normal strain along the x -axis is computed at each material point and node up to 25% extension. The specific geometry admits an analytical solution within finite elasticity, which predicts homogeneous deformation in each phase with a discontinuity in the deformation gradient at the material interface. A derivation of the (semi-)analytical solution is presented in Appendix 2.C. Figure 2.12 shows the strain distribution when computed with and without shape function support truncation at the interface, respectively. With truncated support as discussed in Section 2.2.5, the discontinuity is accurately captured by the numerical solution (Figure 2.12b), whereas spurious oscillations are observed when the support truncation is deactivated (Figure 2.12c).

2.3.4 Benchmark IV: high-volume-fraction composite with spherical inclusion

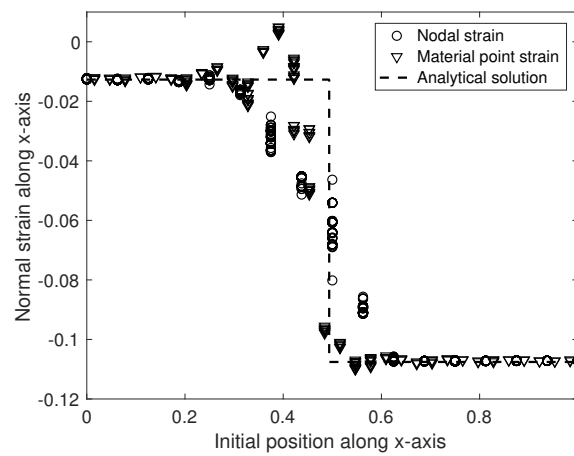
We consider a hyperelastic composite consisting of a periodic array of spherical inclusions embedded in a matrix. In order to accurately model the inclusions while approaching contact under straining, we simulate a cubic RVE containing two hemispheres of the inclusion phase, each of radius 0.45 with a spacing of 0.1 in between (see Figure 2.13a). We are interested in the stress distribution inside the RVE under uniaxial extension with traction-free lateral faces. Each inclusion (shown in red and green) is modeled by a stiff material ($\mu = 500, \kappa = 500$) relative to a soft matrix ($\mu = 1, \kappa = 1$). Periodic boundary conditions are imposed on the RVE. The locality parameter for each material point is initialized using $\gamma = 6.0$. The RVE is incrementally stretched as much as possible until the poles of the hemispheres almost come into contact. Figure 2.13 shows the deformation and reports the normal Cauchy stress distribution at different levels of extension. Remarkably, at 135% extension the inclusions almost come into contact, which is accompanied by a significant and localized increase in the compressive stress near the apparent point of contact (Figure 2.13g). Due to the relatively soft matrix, the stress distribution



(a) Deformation at 25% extension. The nodes are represented by yellow dots, and the material points for the two laminates are shown as red and blue dots.



(b) With shape function support truncation at the interface



(c) Without shape function support truncation at the interface

Figure 2.12: *Benchmark III*: hyperelastic laminate composite in a periodic RVE

	Final height (mm)	Final mushroom radius (mm)	Max. effective plastic strain
Kamoulakis [110]: FEM	21.47-21.66	7.02-7.12	2.47-3.24
Zhu and Cescotto [216]: FEM	21.26-21.49	6.89-7.18	2.75-3.03
Camacho and Ortiz [37]: FEM	21.42-21.44	7.21-7.24	2.97-3.25
Li et al. [132]: OTM	21.43	6.8	3.0
Belytschko et al. [24]: EFG (using cell structures)	21.46	7.13	3.33
Belytschko et al. [24]: EFG (using stress points)	21.46	6.98	3.18
This method	21.45	6.84	2.69

Table 2.1: *Benchmark V-(A)*: Comparison of results from Taylor anvil test

is akin to the Hertzian solution for elastic bodies in contact. Note that the chosen material models do not capture phenomena like inelasticity or damage near the point of contact; the purpose of this particular benchmark is to demonstrate the numerical capabilities of the method. It becomes apparent that the proposed framework is capable of simulating matrix material being squeezed out quasistatically between the inclusions to allow for contact to happen. By contrast, such simulation are not easily feasible with FEM due to the large mesh distortion and entanglement in the narrow region between the two inclusions.

2.3.5 Benchmark V: Taylor anvil test

As our final example, we depart from hyperelastic constitutive laws and quasistatic simulations. We simulate the elastoplastic dynamic response of a copper specimen impacting a wall at high speed (see Figure 2.14a), classically known as [Taylor's](#) anvil test (1948). The specimen is a homogeneous cylinder whose material response is described by von Mises (J_2) plasticity with linear isotropic hardening (the mass density is 8930 kg/m³, Young's modulus 117 GPa, Poisson's ratio 0.35, yield stress 400 MPa, and plastic modulus 100 MPa). The wall is assumed to be frictionless and oriented normal to the initial velocity of the specimen. A 3D simulation using explicit dynamics is performed. We note that, when using explicit time integration, the proposed method is similar to the Optimal Transportation Meshfree method of Li et al. [132] with the exception of the anisotropic shape functions and adaptivity schemes proposed here. The following two scenarios are simulated.

Case (A): a specimen of radius 3.2 mm and length 32.4 mm impacts the wall at a speed of 227 m/s (see Figure 2.14a). The cylinder is discretized into 11,313

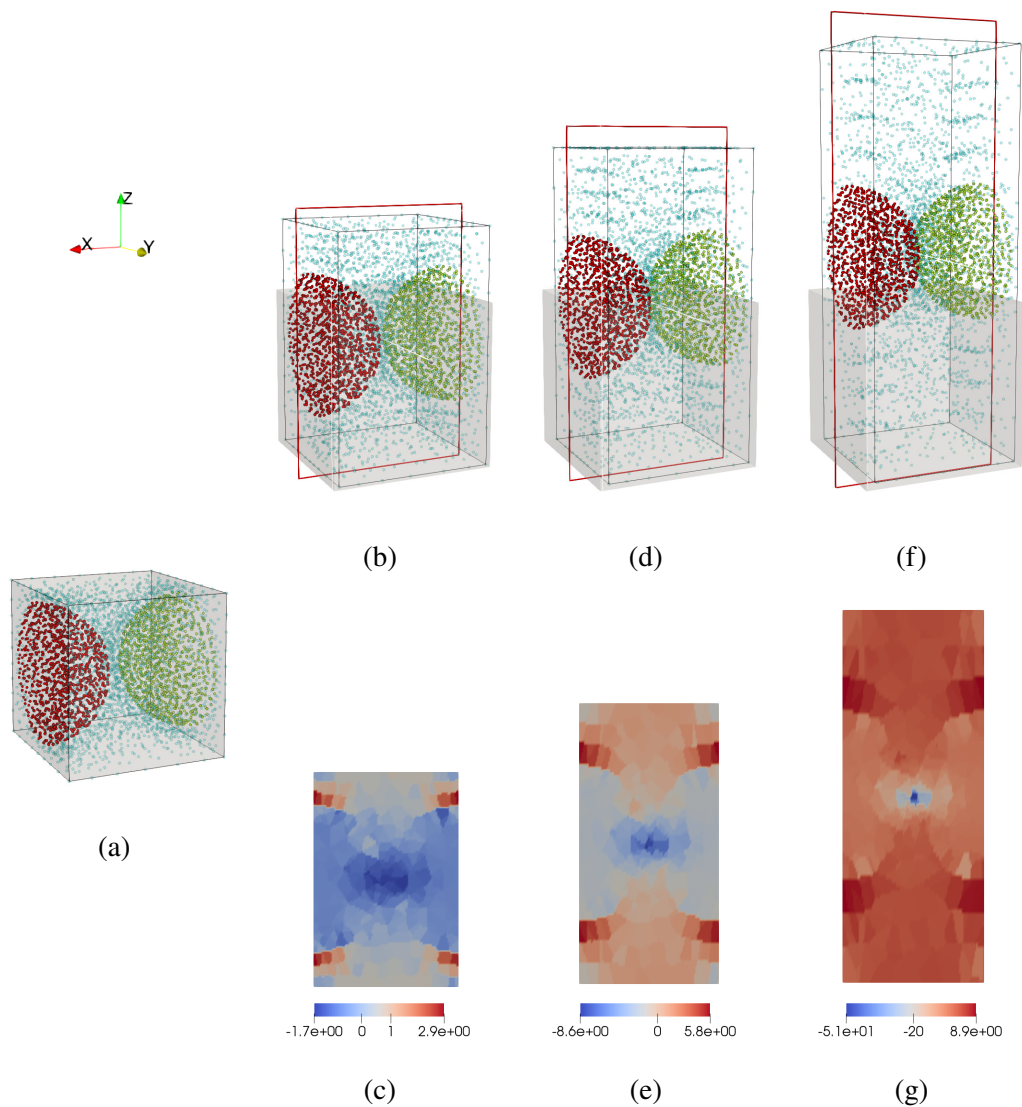


Figure 2.13: *Benchmark IV*: hyperelastic high-volume-fraction composite with periodic spherical inclusions. (a) Initial state of the RVE with two hemispherical inclusions (both nodes and material points are shown in red and green) embedded in a matrix (both nodes and material points in blue). (b, c), (d,e), (f,g) show the deformed configuration and the stress distribution at 45%, 90%, and 135% extension, respectively. The stresses shown in (c, e, g) are the Cauchy stress component along the x -direction interpolated at the central plane of the RVE denoted by the red rectangles in (b, d, f). Due to the large deformations involved, the stress plots use different scales at each step for improved visibility.

nodes and 52,608 material points with the help of an initial tetrahedral mesh. A stable time step of $0.01 \mu\text{s}$ is chosen and the results at time $80 \mu\text{s}$ are compared to those obtained by FEM [37, 110, 216], EFG [24], and OTM [132] in Table 2.1. Figures 2.14b and 2.14c show the time history of the mushroom radius and height of the specimen, respectively (see Belytschko et al. [24] for comparison). Figures 2.14d-2.14f show the evolution of effective plastic strain at different times during the impact. The results closely match those reported in the literature and obtained using the aforementioned methods.

Case (B): a specimen of radius 3.2 mm and length 12.8 mm impacts the wall at a speed of 750 m/s (see Figure 2.15a). The cylinder is discretized into 5,483 nodes and 26,176 material points with the help of an initial tetrahedral mesh. A stable time step of $0.0025 \mu\text{s}$ is chosen, and the evolution of the effective plastic strain at different times during the impact is shown in Figure 2.15. While case (A) is a well-known benchmark with experimental validation, (B) serves as a numerical experiment without validation, proposed by Li et al. [132], to push the robustness of the numerical scheme to extremes. In the latter case, due to considerably higher speed at impact, the specimen undergoes severe plastic flow and flattens out. Particularly in the mushroom region, the nodal spacing increases rapidly, which may cause tensile instability. In fact, without the anisotropic adaptive scheme outlined here, tensile instability emerges early on during the simulation at around $2.75 \mu\text{s}$.

This last benchmark shows that the proposed method equally applies to inelastic constitutive laws and that the adaptivity scheme ensures the stability of the updated-Lagrangian kernel in scenarios exhibiting severe deformation such as during plastic flow. The benchmark further demonstrates that the adaptivity scheme is not limited to quasistatic settings but can be extended without significant modifications to dynamics.

2.4 Conclusions

We have presented a meshfree simulation framework with significantly enhanced stability, particularly for boundary value problems involving severe, finite deformations. We have formulated an updated-Lagrangian scheme based on an incremental deformation map and material point sampling. The scheme utilizes an improved local maximum-entropy approximation that is extended to admit anisotropic shape function support. This is achieved by establishing an anisotropic compromise between minimal shape function widths and maximal information entropy via a ten-

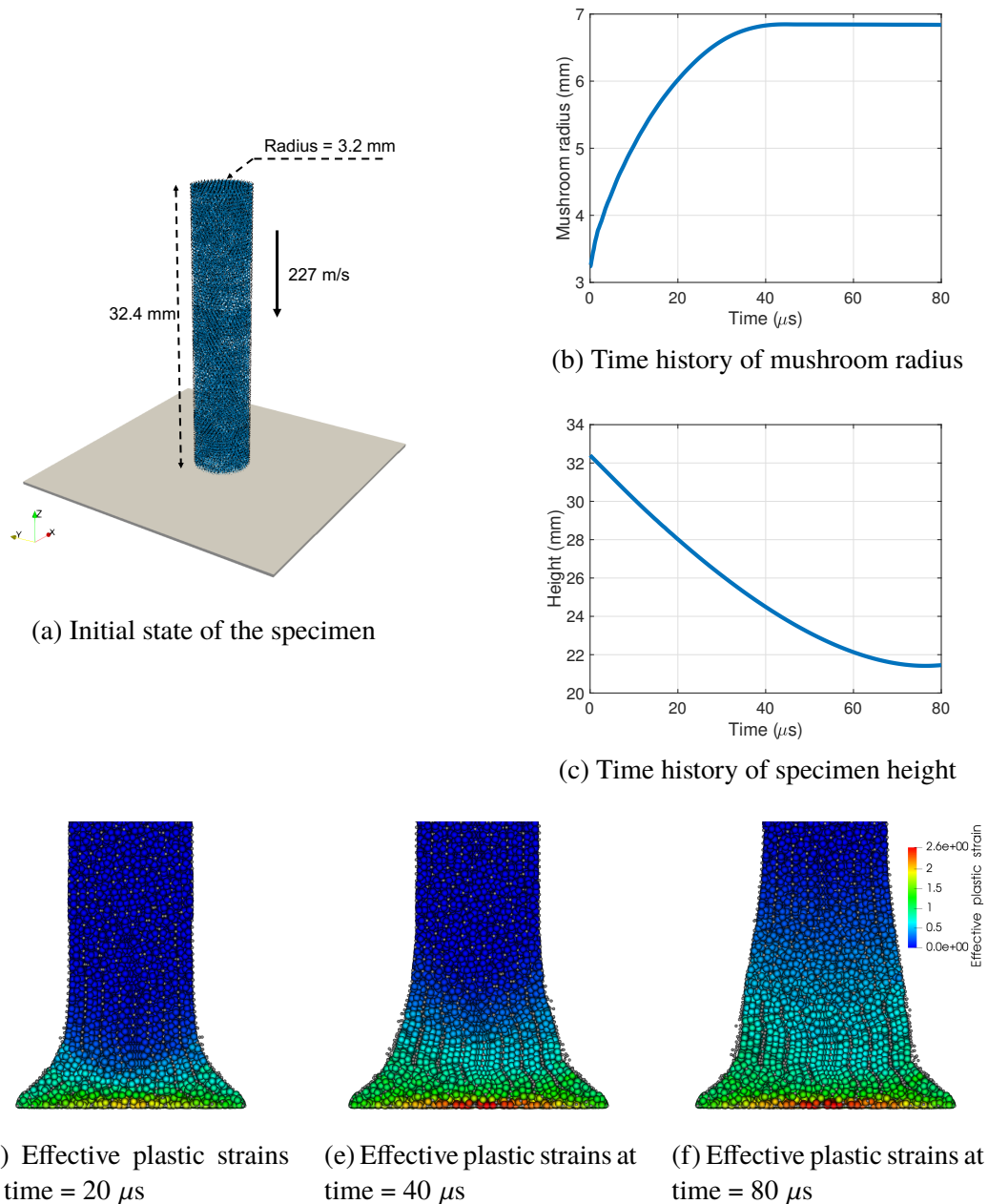


Figure 2.14: *Benchmark V-(A)*: Taylor anvil test, showing (a) the initial specimen, (b) the time history of the mushroom radius, (c) the time history of the specimen height, and (d,e,f) cut-section views of the specimen near the wall with effective plastic strains evaluated at material points (nodes are shown as gray dots).

serial locality parameter, in an extension of the original max-ent scheme of Arroyo and Ortiz [7]. We have introduced an adaptive scheme for the anisotropic evolution of shape function support and nodal connectivity, which jointly suppress tensile instability up to large deformations, as demonstrated by several benchmark tests. The

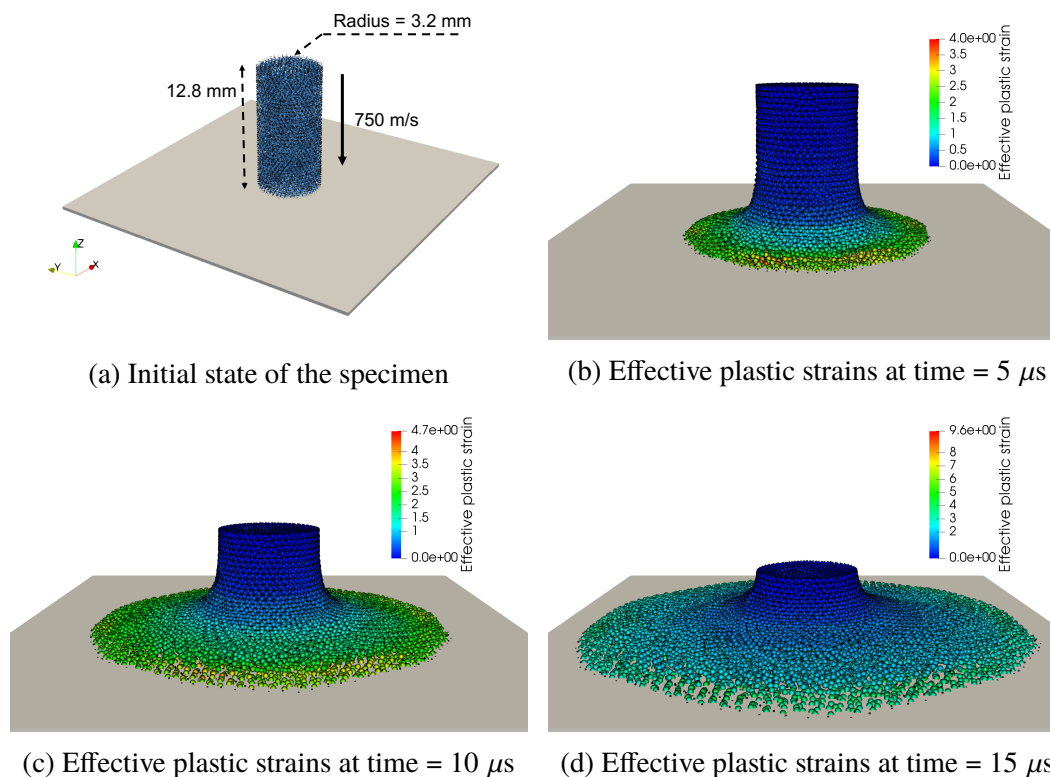


Figure 2.15: *Benchmark V-(B)*: Taylor anvil test, showing (a) the initial specimen, and (b,c,d) the effective plastic strains in the deformed sample, evaluated at the material points (nodes are shown as gray dots).

weak Kronecker property of the original max-ent formulation is retained, which allows for the direct application of essential boundary conditions. We have also presented a scheme that utilizes truncated shape function connectivity to accurately capture discontinuous derivatives across material interfaces as found, e.g., in composite materials. The entire simulation framework has been tested through several hyperelastic and elastoplastic benchmark problems involving severe deformations, and we observed faster convergence and the ability to simulate significantly larger distortions as compared to classical FEM and total-Lagrangian meshfree formulations. We also demonstrated the performance of the methodology in dynamic problems and reported excellent agreement of simulated Taylor impact results with those reported in the literature. The presented approximation scheme as well as the updated-Lagrangian setting are sufficiently general to apply to other problems beyond the scope of the present investigation, including multi-physics problems and incompressible materials, which will be presented in a subsequent study.

APPENDIX

2.A Derivation of solution (2.10)-(2.12) to constrained optimization problem in (2.9)

The following derivation follows closely that presented by Arroyo and Ortiz [7], here modified for the proposed scheme and filling in details. The first-order consistency condition in (2.2) can be reformulated by substituting the zeroth-order consistency condition as

$$\sum_{a=1}^{n_n} N^a(\mathbf{x}) \mathbf{x}^a - \left(\sum_{a=1}^{n_n} N^a \right) \mathbf{x} = \sum_{a=1}^{n_n} N^a(\mathbf{x}) (\mathbf{x}^a - \mathbf{x}) = \mathbf{0}. \quad (2.51)$$

The Lagrangian associated with the constrained optimization in (2.9) is therefore given by

$$L(\mathcal{N}_\beta, \lambda_0, \boldsymbol{\lambda}) = \sum_{a=1}^{n_n} f(N^a, \boldsymbol{\beta}) + \lambda_0 \left(\sum_{a=1}^{n_n} N^a - 1 \right) + \boldsymbol{\lambda} \cdot \left(\sum_{a=1}^{n_n} N^a (\mathbf{x}^a - \mathbf{x}) \right), \quad (2.52)$$

where $\lambda_0 \in \mathbb{R}$ and $\boldsymbol{\lambda} \in \mathbb{R}^d$ are Lagrange multipliers, and

$$f(N^a, \boldsymbol{\beta}) = N^a \|\mathbf{x} - \mathbf{x}^a\|_\beta^2 + N^a \ln N^a(\mathbf{x}). \quad (2.53)$$

Stationarity of (2.52) with respect to $N^a(\mathbf{x})$ for $a = 1, \dots, n_n$ yields

$$\frac{\partial L}{\partial N^a(\mathbf{x})} = \|\mathbf{x} - \mathbf{x}^a\|_\beta^2 + 1 + \ln N^a + \lambda_0 + \boldsymbol{\lambda} \cdot (\mathbf{x}^a - \mathbf{x}) = 0 \quad \forall a = 1, \dots, n_n \quad (2.54)$$

whose solution reads

$$N^a(\mathbf{x}) = \frac{\exp\left(-\|\mathbf{x} - \mathbf{x}^a\|_\beta^2 + \boldsymbol{\lambda} \cdot (\mathbf{x} - \mathbf{x}^a)\right)}{\exp(1 + \lambda_0)}. \quad (2.55)$$

Note that the exponential form ensures the positivity constraint on the shape functions. The Lagrange dual function is given by

$$g(\lambda_0, \boldsymbol{\lambda}) = \inf_{N^a(\mathbf{x}) \geq 0, a=1, \dots, n_n} L(\mathcal{N}_\beta). \quad (2.56)$$

The function conjugate of $f(N^a, \boldsymbol{\beta})$ is obtained as

$$f^*(Q^a, \boldsymbol{\beta}) = \sup_{N^a} (Q^a N^a - f(N^a, \boldsymbol{\beta})). \quad (2.57)$$

Stationarity with respect to N^a requires

$$Q^a - \|\mathbf{x} - \mathbf{x}^a\|_\beta^2 - 1 - \ln N^a = 0 \quad \Rightarrow \quad N^a = \exp\left(Q^a - \|\mathbf{x} - \mathbf{x}^a\|_\beta^2 - 1\right). \quad (2.58)$$

Therefore, the conjugate function $f^*(Q^a, \boldsymbol{\beta})$ is given by

$$f^*(Q^a, \boldsymbol{\beta}) = \exp\left(Q^a - \|\mathbf{x} - \mathbf{x}^a\|_{\boldsymbol{\beta}}^2 - 1\right). \quad (2.59)$$

Rewriting the Lagrange dual function (2.56) in terms of the function conjugate [32] gives

$$g(\lambda_0, \boldsymbol{\lambda}) = -\lambda_0 - \sum_{a=1}^{n_n} f^*(-\lambda_0 - \boldsymbol{\lambda} \cdot (\mathbf{x}^a - \mathbf{x}), \boldsymbol{\beta}). \quad (2.60)$$

Substituting (2.59) gives

$$g(\lambda_0, \boldsymbol{\lambda}) = -\lambda_0 - \sum_{a=1}^{n_n} \exp\left(-\lambda_0 - \boldsymbol{\lambda} \cdot (\mathbf{x}^a - \mathbf{x}) - \|\mathbf{x} - \mathbf{x}^a\|_{\boldsymbol{\beta}}^2 - 1\right). \quad (2.61)$$

Maximizing the Lagrange dual function with respect to λ_0 results in

$$\exp(1 + \lambda_0^*) = \sum_{a=1}^{n_n} \exp\left(-\|\mathbf{x} - \mathbf{x}^a\|_{\boldsymbol{\beta}}^2 + \boldsymbol{\lambda} \cdot (\mathbf{x} - \mathbf{x}^a)\right) = Z(\mathbf{x}, \boldsymbol{\lambda}), \quad (2.62)$$

so that the Lagrange dual function reduces to

$$g(\lambda_0^*, \boldsymbol{\lambda}) = -\lambda_0^* - 1 = -\ln Z(\mathbf{x}, \boldsymbol{\lambda}). \quad (2.63)$$

Finally, maximizing the reduced Lagrange dual function with respect to $\boldsymbol{\lambda}$ gives

$$\boldsymbol{\lambda}^* = \arg \min_{\boldsymbol{\lambda} \in \mathbb{R}^d} \ln Z(\mathbf{x}, \boldsymbol{\lambda}). \quad (2.64)$$

2.B Pseudo-code for hyperelastic boundary value problem

The following algorithms summarize the numerical realization of the presented updated-Lagrangian meshfree framework for the example of a hyperelastic boundary value problem at finite strains.

Algorithm 1 Example algorithm for a hyperelasticity simulation using anisotropic local max-ent

- 1: Initialize the spatial discretization (Algorithm 2)
 - 2: **for** each material point $p = 1, \dots, n_p$ **do**
 - 3: Set initial configuration as undeformed: $\mathbf{F}_0^p = \mathbf{I}$
 - 4: **end for**
 - 5: **for** $n = 0, \dots, \#$ of quasistatic load or time steps **do**
 - 6: Compute/update shape functions (Algorithm 3)
 - 7: Compute nodal displacement increments $\Delta \mathbf{U}_n$ by assembly and iterative solution (Algorithm 4)
 - 8: Update Lagrangian (Algorithm 5)
 - 9: **end for**
-

Algorithm 2 : Initialize the spatial discretization

Input: γ, c

- 1: Create a simplicial mesh based on a given geometry
 - 2: Initialize n_n nodes at mesh vertices \mathbf{x}_0^a ($a = 1, \dots, n_n$)
 - 3: Initialize n_p material points at the simplex quadrature points \mathbf{x}_0^p ($p = 1, \dots, n_p$)
 - 4: Initialize all material point densities: $\rho_0^p = \rho_0(\mathbf{x}_0^p)$
 - 5: Initialize all material point volumes: $V_0^p = \text{quadrature weight} \times \text{simplex volume}$
 - 6: Initialize the locality parameter for each material point: $\beta_0^p = \gamma \left(h_0^p\right)^{-2} \mathbf{I}$, where h_0^p is the mean distance from \mathbf{x}_0^p to nodes of the surrounding elements in the mesh
 - 7: Initialize cut-off region (ellipsoid) for each material point: $\mathbf{M}_0^p = \left(c h_0^p\right)^{-2} \mathbf{I}$
 - 8: Discard the mesh
-

Algorithm 3 : Compute/update shape functions

- 1: **for** each material point $p = 1, \dots, n_p$ **do**
 - 2: Find nodal connectivity based on cut-off region $S_n^p = \{\mathbf{x}_n^a : (\mathbf{x}_n^a - \mathbf{x}_n^p) \cdot \mathbf{M}_n^p(\mathbf{x}_n^a - \mathbf{x}_n^p) \leq 1\}$
 - 3: **if** $\text{size}(S_n^p) \geq (d + 1)$ **and** $\mathbf{x}_n^p \in \text{conv}(S_n^p)$ **then**
 - 4: // Compute shape functions:
 - 5: Guess $\lambda \leftarrow (0, \dots, 0)^T$
 - 6: **while** $\ln(Z(\mathbf{x}_n^p, \lambda)) > \text{Tolerance}$ **do**
 - 7: $\lambda \leftarrow \lambda - (J(\mathbf{x}_n^p, \lambda) + \|\mathbf{r}(\mathbf{x}_n^p, \lambda)\| \mathbf{I})^{-1} \mathbf{r}(\mathbf{x}_n^p, \lambda)$
 - 8: **end while**
 - 9: $\lambda^* = \lambda$
 - 10: Evaluate shape functions at \mathbf{x}_n^p : $\mathcal{N}_{\beta_n^p}^p = \{N^a(\mathbf{x}_n^p) : \mathbf{x}_n^a \in S_n^p\}$
 - 11: **else**
 - 12: **Error:** Insufficient nodal connectivity
 - 13: **end if**
 - 14: **end for**
-

Algorithm 4 : Assembly and solver

Input: ΔU_n (initial guess = solution of previous step)

- 1: **do**
- 2: Initialize global force vector and tangent matrix: $\mathbf{f}_{n+1} \leftarrow \mathbf{0}$, $\mathbf{T}_{n+1} \leftarrow \mathbf{0}$
- 3: **for** each material point $p = 1, \dots, n_p$ **do**
- 4: Compute incremental deformation gradient: $\mathbf{F}_{n \rightarrow n+1}^p \leftarrow \mathbf{I} + \sum_{a \in S_n^p} \Delta \mathbf{u}_n^a \otimes \nabla_n N^a(\mathbf{x}_n^p)$
- 5: Compute total deformation gradient: $\mathbf{F}_{n+1}^p \leftarrow \mathbf{F}_{n \rightarrow n+1}^p \mathbf{F}_n^p$
- 6: **for** all nodes a in S_n^p **do**
- 7: Compute and assemble internal nodal forces:

$$\mathbf{f}_{n+1}^a \leftarrow \mathbf{f}_{n+1}^a + \frac{V_n^p}{J_n^p} \mathbf{P}(\mathbf{F}_{n \rightarrow n+1}^p \mathbf{F}_n^p) \mathbf{F}_n^{pT} \nabla_n N^a(\mathbf{x}_n^p)$$

- 8: **for** all nodes b in S_n^p **do**
- 9: Compute and assemble tangent matrix:

$$\left(\mathbf{T}_{n+1} \right)_{ik}^{ab} \leftarrow \left(\mathbf{T}_{n+1} \right)_{ik}^{ab} + \mathbb{C}_{ijkl}(\mathbf{F}_{n \rightarrow n+1}^p \mathbf{F}_n^p) (F_n^p)_{qj} \nabla_n N_q^a(\mathbf{x}_n^p) (F_n^p)_{rl} \nabla_n N_r^b(\mathbf{x}_n^p) \frac{V_n^p}{J_n^p}$$

- 10: **end for**
- 11: **end for**
- 12: **end for**
- 13: **for** each node $a = 1, \dots, n_n$ **do**
- 14: Assemble external forces: $\mathbf{f}_{n+1}^a \leftarrow \mathbf{f}_{n+1}^a - \mathbf{f}_{\text{ext},n+1}^a$
- 15: **for** each node $b = 1, \dots, n_n$ **do**
- 16: Assemble external tangent matrix: $\left(\mathbf{T}_{n+1} \right)_{ik}^{ab} \leftarrow \left(\mathbf{T}_{n+1} \right)_{ik}^{ab} - \frac{\partial (f_{\text{ext},n+1}^a)_i}{\partial (\Delta u_n^b)_k}$,
- 17: **end for**
- 18: **end for**
- 19: Apply essential boundary conditions to force vector and tangent matrix
- 20: Newton-Raphson step: $\Delta U_n \leftarrow \Delta U_n - \mathbf{T}_{n+1}^{-1} \mathbf{f}_{n+1}$
- 21: **while** ($\|\mathbf{f}_{n+1}\| > \text{Tolerance}$)

Return: ΔU_n

Algorithm 5 : Update Lagrangian

Input: ΔU_n (solution)

- 1: **for** each material point $p = 1, \dots, n_p$ **do**
- 2: Compute incremental deformation gradient:

$$\mathbf{F}_{n \rightarrow n+1}^p = \mathbf{I} + \sum_{a \in S_n^p} \Delta \mathbf{u}_n^a \otimes \nabla_n N^a(\mathbf{x}_n^p)$$

- 3: Compute total deformation gradient: $\mathbf{F}_{n+1}^p = \mathbf{F}_{n \rightarrow n+1}^p \mathbf{F}_n^p$
 - 4: Update material point density: $\rho_{n+1}^p = \rho_n^p (\det \mathbf{F}_{n \rightarrow n+1}^p)^{-1}$
 - 5: Update material point volume: $V_{n+1}^p = V_n^p \det \mathbf{F}_{n \rightarrow n+1}^p$
 - 6: Update locality parameter: $\boldsymbol{\beta}_{n+1}^p = (\mathbf{F}_{n \rightarrow n+1}^p)^{-T} \boldsymbol{\beta}_n^p (\mathbf{F}_{n \rightarrow n+1}^p)^{-1}$
 - 7: Update cut-off region: $\mathbf{M}_{n+1}^p = (\mathbf{F}_{n \rightarrow n+1}^p)^{-T} \mathbf{M}_n^p (\mathbf{F}_{n \rightarrow n+1}^p)^{-1}$
 - 8: **end for**
-

2.C Analytical solution of the finite-elasticity problem in Section 2.3.3

Consider a hyperelastic cube of unit length composed of two perfectly bonded Neo-Hookean materials denoted by symbols A and B , which are arranged into a laminate whose material interface is given by the plane $x = 0.5$ in the initial configuration (see Figure 2.12). μ_i and κ_i denote the shear and bulk moduli, respectively, of material i . For the prescribed boundary conditions, the overall deformation gradient of the laminate is given by

$$\mathbf{F} = \begin{pmatrix} \lambda_1 & 0 & 0 \\ 0 & \lambda_2 & 0 \\ 0 & 0 & \lambda_3 \end{pmatrix}, \quad (2.65)$$

where λ_1 , λ_2 , and λ_3 are the stretch ratios along the x -, y -, and z -axes, respectively. Note that λ_3 is a known value and is equal to the stretch applied by the boundary conditions. Assuming that no instability occurs, the deformation is homogeneous within each material and the deformation gradient for each material region is given by

$$\mathbf{F}^A = \begin{pmatrix} \lambda_1^A & 0 & 0 \\ 0 & \lambda_2 & 0 \\ 0 & 0 & \lambda_3 \end{pmatrix} \quad \text{and} \quad \mathbf{F}^B = \begin{pmatrix} \lambda_1^B & 0 & 0 \\ 0 & \lambda_2 & 0 \\ 0 & 0 & \lambda_3 \end{pmatrix}, \quad (2.66)$$

where λ_1^A and λ_1^B are the stretch ratios for each material along the x -axis. Since the initial thickness of each laminate phase is the same, the overall stretch ratio λ_1 is related to λ_1^A and λ_1^B via

$$\lambda_1 = \frac{1}{2} \lambda_1^A + \frac{1}{2} \lambda_1^B. \quad (2.67)$$

The overall strain energy density $\Pi = \langle W \rangle$ of the laminate block, using (2.50), is thus given by

$$\begin{aligned} \Pi(\lambda_1^A, \lambda_1^B, \lambda_2, \lambda_3) = & \frac{1}{2} \left(\frac{\mu_A}{2} \left[\text{tr} \left(\mathbf{F}^{A\text{T}} \mathbf{F}^A \right) (J^A)^{-2/3} - 3 \right] + \frac{\kappa_A}{2} (J^A - 1)^2 \right) \\ & + \frac{1}{2} \left(\frac{\mu_B}{2} \left[\text{tr} \left(\mathbf{F}^{B\text{T}} \mathbf{F}^B \right) (J^B)^{-2/3} - 3 \right] + \frac{\kappa_B}{2} (J^B - 1)^2 \right). \end{aligned} \quad (2.68)$$

The principle of minimum potential energy requires that for a given applied λ_3

$$(\lambda_1^A, \lambda_1^B, \lambda_2) = \arg \min \Pi(\lambda_1^A, \lambda_1^B, \lambda_2, \lambda_3), \quad (2.69)$$

where the objective function being minimized is convex and admits a unique solution. Hence, the optimization problem in (2.69) can be easily solved numerically to yield the required stretch ratios.

MODELING OF EQUAL-CHANNEL ANGULAR EXTRUSION BASED ON HIGH-FIDELITY PLASTICITY MODELS

Research presented in this chapter has been adapted from the following publication:

S. Kumar[†], A. D. Tutcuoglu[†], Y. Hollenweger, and D. M. Kochmann. A multiscale meshfree approach to modeling ECAE. *In preparation*, 2019.

[†] Both authors contributed equally to this work.

3.1 Introduction

Macroscale mechanical properties of metals and alloys are directly linked to grain sizes and orientations at the microscale. For example, inducing ultrafine grain (UFG) refinement in a metal specimen by applying severe plastic deformation (SPD) [39, 75, 204] is known to significantly improve its strength according to the Hall-Petch relation [97, 173]. Valiev et al. [204] define UFG materials as bulk solids with microstructure containing dominantly equiaxed grains on the sub-micrometer scale with high-angle grain boundaries. Therefore, by applying severe plastic strains to create a high density of crystalline defects that further induce UFG refinements, SPD processes significantly improve the bulk properties of metals at the macroscale. The history of SPD goes back to Nobel Prize winning work by Bridgman [33, 34, 35]. Modern-day SPD processes for UFG refinement include equal-channel angular extrusion (ECAE) [192], high pressure torsion (HPT) [33], accumulative roll bonding (ARB) [188], repetitive corrugation and straightening (RCS) [196], etc. Detailed reviews of SPD processes can be found in [75]. Among the class of SPD processes, ECAE has particularly attracted interest for achieving UFG refinement [104, 192] because it conserves the cross-sectional area of the specimen. This is achieved by extruding a specimen around a 90° corner that produces severe shear strains. Furthermore, the specimen can be subjected to multiple extrusions, by rotating and shearing in different planes. This allows activation of multiple slip systems and produces round equiaxed grains.

Optimization of ECAE parameters to achieve desirable bulk properties in a wide range of metals and alloys motivates a numerical simulation framework to complement expensive experimentation. Initial attempts at modeling ECAE were based

on finite element method (FEM). Some of the notable works include the analysis of friction and effects of channel geometry in ECAE by Luis et al. [147] and Fu et al. [83], and the optimal design of ECAE parameters based on homogeneity of strain distribution in the specimen by Djavanroodi et al. [65]. However, FEM based models have been limited to simulations with simple elasto-plastic constitutive laws with linear or power law hardening. This limitation is partly attributed to remeshing in mesh-based modeling such as FEM. Remeshing is necessary to avoid numerical artifacts and instabilities due to the distortion and entanglement of elements as the mesh deforms around the corner. The application of remeshing, however, requires interpolation of the data at the quadrature points to map material point descriptions, including information of the several grains at each point, from the old to the new mesh. While simple plasticity laws based on the additive decomposition of elastic and inelastic strains in a small strain framework may provide acceptable conditions for this, crystal plasticity frameworks in finite deformations endowed with a multiplicative decomposition represent a more challenging environment.

In contrast, meshfree methods do not experience mesh-related issues arising from the severe distortions in ECAE. Therefore, these methods do not require remeshing and hence allow for more complex plasticity models. Smoothed-particle hydrodynamics (SPH) (see Section 1.2.1 for brief review) has recently attracted interest for modeling ECAE, and in general SPD processes. Fagan et al. [76] showed that SPH provided better accuracy and robustness than FEM, albeit their simulations were based on elasto-plastic constitutive law with linear isotropic hardening. Ma and Hartmaier [148] were the first to develop an SPH formulation with crystal plasticity model, and study face center cubic (FCC) polycrystals under ECAE. However, to address the issue of lack of treatment for boundary conditions in SPH, they assumed linear elasticity at the boundary nodes and constrained the motion along the channel walls accordingly. Additional well-known problems in SPH methods, including poor accuracy, lack of consistency, and instabilities (see Sections 1.2.1 and 1.3), motivate the use of a modern-day meshfree method. Furthermore, all previous attempts, both mesh-based and meshfree, simulate the process in a dynamics framework, which does not strongly replicate the quasi-static processing conditions of ECAE.

While the aforementioned works concern the macroscale modeling only, a high fidelity description of ECAE also requires integration of the complex recrystallization mechanisms at the mesoscale to understand the effects of grain refinement on bulk properties. Previous attempts have been limited in capturing this multi-scale nature

of ECAE. Saitoh and Ohnishi [189] included a phenomenological grain refinement model in their SPH framework, although their simplified model does not have any notion of physical grains (with individual inelastic deformation states) or texture evolution. Sivakumar and Ortiz [193] used sequential lamination to model microstructures and predict texture evolution in Al-Cu alloy under ECAE. The study, however, was limited to shearing of a single material point as an idealization of the complex deformations in ECAE. Additionally, it did not account for multiple slip planes as well as nucleation of grains [175, 190].

On the other hand, there has been extensive research on physically representative models for grain recrystallization, in particular dynamic recrystallization such as cellular automata, Monte-Carlo Potts, and vertex methods [67, 98, 102, 190]. Although these models provide accurate descriptions of nucleation and migration of grains at the mesoscale, their integration into multiscale frameworks has largely been infeasible due to their high computational costs. Recently, Tutcuoglu et al. [202] introduced a Taylor model for capturing discontinuous dynamic recrystallization and showed good agreement in terms of microstructural evolution, texture evolution as well as the homogenized stress response compared to a fully-resolved Monte-Carlo Potts model [203], in spite of significantly reduced computational costs.

In this contribution, we develop a multiscale meshfree framework to simulate copper undergoing ECAE (see Figure 3.1 for illustration), which to the best of our knowledge is the first such attempt. We employ the following strategies to bridge the multiple scales in ECAE – from micro- to macroscale.

- *Macroscale*: Quasi-static mechanical boundary value problem is simulated using the enhanced max-ent approximation and the updated-Lagrangian formulation introduced in Chapter 2.
- *Mesoscale*: Dynamic recrystallization at the polycrystal level is captured by the Taylor model of Tutcuoglu et al. [202] to track grain refinement and texture evolution.
- *Microscale*: A finite-deformation crystal plasticity model with multiple slip systems is used to model the response of individual grains of copper.

The remainder of this contribution is organized as follows. Section 3.2 introduces the theory of the multiscale framework. Section 3.3 discusses the numerical scheme for time evolution of internal variables in the aforementioned framework.

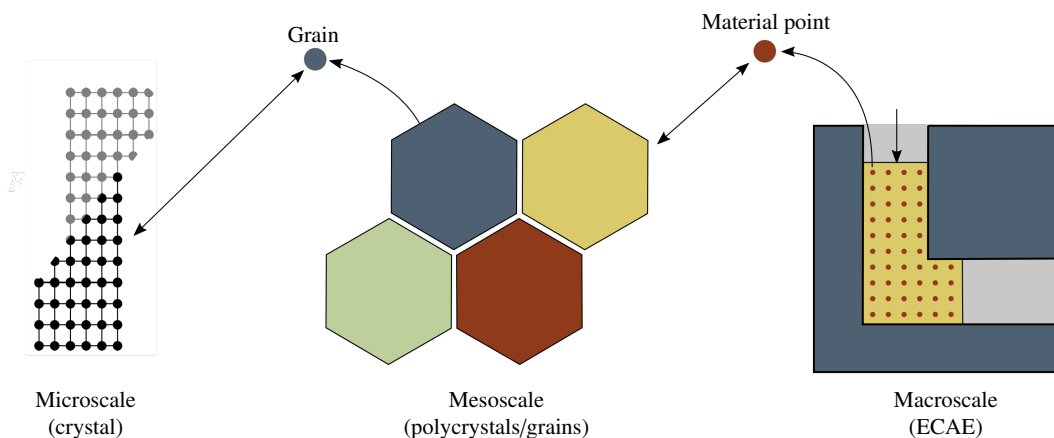


Figure 3.1: Illustration of the multiscale framework for simulating ECAE.

In Section 3.4, we present the results of simulating ECAE using this approach. Section 3.4.1 reports a convergence study with respect to spatial and temporal discretization. Section 3.4.2 studies the strain distribution in a specimen as it undergoes ECAE, as well as the effects of channel geometry. Section 3.4.3 explains the effects of recrystallization (migration and nucleation) on grain refinement and texture evolution. In Section 3.4.4, we briefly explore the possibility of simulating multiple passes of ECAE. Finally, Section 3.5 concludes our investigation and lists some future outlooks of this approach.

3.2 Theory

3.2.1 Microscale: Copper material model

Following the work of Tutcuoglu et al. [203], we introduce a material model for fcc copper endowed with $n_S = 12$ slip systems. Slip directions and normals in the reference configuration are denoted by \tilde{s}^α and \tilde{m}^α , $\alpha \in \{1, \dots, n_S\}$. Based on a grain's crystallographic orientation, we introduce a rotation tensor $\mathbf{R} \in \text{SO}(3)$ by which the slip directions and normals in the global coordinate system can be expressed as $s^\alpha = \mathbf{R}\tilde{s}^\alpha$ and $m^\alpha = \mathbf{R}\tilde{m}^\alpha$, respectively. The inelastic deformation state is captured by a set of internal variables $\mathbf{Q} = \{\mathbf{g}, \mathbf{F}^{\text{in}}\}$, where $\mathbf{g} \in \mathbb{R}^{n_S}$ denotes a measure of the accumulated slip and $\mathbf{F}^{\text{in}} \in \text{GL}(3)$ represents the isochoric inelastic deformation gradient. The total deformation gradient is related to the inelastic deformation gradient by the multiplicative composition

$$\mathbf{F} = \mathbf{F}^e \mathbf{F}^{\text{in}}, \quad (3.1)$$

where $\mathbf{F}^e \in \text{GL}(3)$ denotes the elastic deformation gradient. The volume-preserving time-evolution of the inelastic deformation gradient depends on the inelastic velocity gradient \mathbf{l}^{in} and slip rates $\dot{\boldsymbol{\gamma}} \in \mathbb{R}^{n_S}$ as

$$\dot{\mathbf{F}}^{\text{in}} = \mathbf{l}^{\text{in}} \mathbf{F}^{\text{in}}, \quad \text{where} \quad \mathbf{l}^{\text{in}} = \sum_{\alpha=1}^{n_S} \dot{\gamma}^\alpha \mathbf{s}^\alpha \otimes \mathbf{m}^\alpha. \quad (3.2)$$

Since Tutcuoglu et al. [202] provide an in-depth analysis of the energetics that govern this material model, we only provide a brief summary here. The effective total energy at time t , excluding losses due to dissipation, is given by

$$W(\mathbf{F}, \mathbf{Q}, t) = W^e(\mathbf{F}^e) + \int_{t_0}^t \dot{W}^{\text{in}}(\mathbf{g}(\tau)) d\tau. \quad (3.3)$$

$W^e(\mathbf{F}^e)$ represents a compressible Neo-Hookean strain energy density given by

$$W^e(\mathbf{F}^e) = \frac{\mu}{2} \left((J^e)^{-2/3} \text{tr}(\mathbf{F}^{eT} \mathbf{F}^e) - 3 \right) + \frac{\kappa}{2} \left((J^e)^2 - 1 \right), \quad (3.4)$$

where μ and κ are the shear and bulk moduli, respectively, and $J^e = \det \mathbf{F}^e$. The time evolution for slip $\boldsymbol{\gamma}$ follows a power-law

$$\dot{\gamma}^\alpha = \dot{\gamma}_0 \left(\frac{|\tau^\alpha|}{G_r^\alpha} \right)^m \text{sign}(\tau^\alpha), \quad \alpha \in \{1, \dots, n_S\}, \quad (3.5)$$

where $\tau^\alpha = \mathbf{m}^\alpha \cdot \boldsymbol{\Sigma}^e \mathbf{s}^\alpha$ represents the resolved shear stress on the slip system α , with Mandel stress tensor $\boldsymbol{\Sigma}^e = (\mathbf{F}^e)^T \mathbf{P} (\mathbf{F}^{\text{in}})^T$ and first Piola-Kirchhoff stress tensor \mathbf{P} . G_r^α denotes the respective total shear resistance, which decomposes as $G_r^\alpha = G_0 + G^\alpha$ into a constant slip resistance contribution G_0 and a variable contribution $G^\alpha = \sum_{\beta=1}^{n_S} Q(\delta_{\alpha\beta} + q(1 - \delta_{\alpha\beta}))g^\beta$, with plastic modulus Q , latent hardening multiplier q and Kronecker delta δ . The time evolution for \mathbf{g} is derived from energetics (see e.g. [151, 202]) and given as

$$\dot{g}^\alpha = (1 - Bg^\alpha) \frac{\tau^\alpha}{G_r^\alpha} \dot{\gamma}^\alpha, \quad (3.6)$$

where B denotes a saturation factor. Mellbin et al. [151] showed that the time evolution laws in (3.5) and (3.6) satisfy the dissipation inequality. Finally, the inelastic energy density excluding losses due to dissipation is obtained as

$$W^{\text{in}} = \int_{t_0}^t \dot{W}^{\text{in}}(\mathbf{g}(\tau)) d\tau = \int_{t_0}^t \sum_{\alpha=1}^{n_S} \tau^\alpha (1 - Bg^\alpha) \frac{G^\alpha}{G_r^\alpha} \dot{\gamma}^\alpha d\tau, \quad (3.7)$$

where t_0 denotes the time at which a grain is initiated, e.g. through nucleation.

3.2.2 Mesoscale: Taylor model

The Taylor model idealizes the notion of a material point containing N_g number of grains by endowing each grain with a volume fraction $\eta_{i \in \{1, \dots, N_g\}} \equiv V_{i \in \{1, \dots, N_g\}}/V$, where V_i denotes the volume of the i^{th} grain and V denotes the material point volume. It assumes that all grains interact with each other, and ignores any notion of selected interaction between grains based on proximity. The model further assumes that each grain experiences the same total deformation gradient \mathbf{F} . This evidently satisfies compatibility, but generally violates equilibrium which leads to the well known upper-bound for the homogenized stress (see, e.g., Tutcuoglu et al. [202]). Each grain is further endowed with an individual set of inelastic states $\{\mathbf{Q}_i\}_{i \in \{1, \dots, N_g\}}$, the evolution of which heavily depends on its respective crystallographic orientation $\mathbf{R}_{i \in \{1, \dots, N_g\}}$.

The Taylor model assumes a total energy of the form

$$\begin{aligned} E &= E(\mathbf{F}, \mathbf{Q}, t) \\ &= \sum_{i \in \{1, \dots, N_g\}} \eta_i W(\mathbf{F}, \mathbf{Q}_i, t) - \nu \left(\sum_{i \in \{1, \dots, N_g\}} \eta_i - 1.0 \right), \end{aligned} \quad (3.8)$$

where $\mathbf{Q} = \{\{\mathbf{Q}_i\}_{i \in \{1, \dots, N_g\}}, \{\eta_i\}_{i \in \{1, \dots, N_g\}}\}$ denotes the set of all internal variables. The last term contains a Lagrange multiplier ν , which ensures that the sum of all volume fractions sums up to unity. The above total energy formulation and the energy description of individual grains in (3.3) provide the framework for the modeling of the two mechanisms inherent to discontinuous dynamic recrystallization – migration and nucleation.

In the Taylor model, grain migration is captured by change in relative volume fractions of the grains based on energetic principles. We assume a gradient flow ansatz for the volume fractions as

$$\dot{\eta}_i = -\frac{1}{\kappa_{GBM}} \frac{\delta E(\mathbf{F}, \mathbf{Q}, t)}{\delta \eta_i} = -\frac{1}{\kappa_{GBM}} (W(\mathbf{F}, \mathbf{Q}_i, t) - \nu), \quad (3.9)$$

with grain migration rate κ_{GBM} . Following the ansatz (3.9) in conjunction with the aforementioned constraint yields the Lagrange multiplier [202]

$$\nu = \sum_{i \in \{1, \dots, N_g\}} W(\mathbf{F}, \mathbf{Q}_i, t) / N_g. \quad (3.10)$$

Nucleation is an inherently stochastic phenomenon during which heavily distorted parts of one or multiple grains attain a thermodynamically unstable state, and

reorientation and formation of a new, pristine grain becomes energetically more favorable [98]. We introduce a critical inelastic strain energy density $W^{\text{in,cr}}$, above which nucleation is possible; and further define a nucleation threshold w^{th} to account for an increased likelihood of nucleation with increasing inelastic strain energy density. Adopting the formulation by Zhao et al. [214] and Tutcuoglu et al. [202], the nucleation threshold is given by

$$w^{\text{th}}(W_i^{\text{in}}) = \eta_i \Delta t \kappa_{NCL} \left[1 - \exp \left\{ - \left(\frac{W_i^{\text{in}}}{C W^{\text{in,cr}}} \right)^d \right\} \right], \quad (3.11)$$

with nucleation rate κ_{NCL} , nucleation constant C , and nucleation exponent d . Finally, for every grain with $W_i^{\text{in}} > W^{\text{in,cr}}$, we generate a random number $w_i \sim \mathcal{U}([0, 1])$ and initiate nucleation of a new grain if $w_i < w^{\text{th}}(W_i^{\text{in}})$. The new grain is then endowed with the same total deformation gradient \mathbf{F} as all other grains. However, its internal variables are reset to mimic a pristine grain, i.e., $\mathbf{F}^{\text{in}} = \mathbf{F}^e = \mathbf{I}$ and all entries of \mathbf{g} are set to initial shear resistance g_0 . This, however, requires a redefinition of the multiplicative decomposition of the total deformation gradient as $\mathbf{F} = \mathbf{F}^e \mathbf{F}^r \mathbf{F}^{\text{in}}$ with \mathbf{F}^r set to the total deformation gradient at the time of nucleation. Since nucleation is an inherently atomistic process, we assume the initiation of a pristine grain with a sufficiently small volume fraction, which is appropriate for the purpose of capturing recrystallization in a Taylor model. In this light, Tutcuoglu et al. [202] showed that $\eta_{NCL} = (1/64^3)$ is a rational choice for the initial volume fraction of a nucleated grain based on the migration and nucleation speeds. Based on η_{NCL} and an initial number of grains $N_{g,\text{init}} = 200$, this would allow us to capture a refinement up to a factor of 11, which for the purposes of this contribution is reasonable.

3.2.3 Macroscale: Max-ent & updated-Lagrangian

At the macroscale, we model the ECAE process as a quasi-static mechanical boundary value problem (BVP) (see (2.21)) in a classical Galerkin setting outlined in Section (2.2.2). In a classical total-Lagrangian setting, a deformed configuration is always referenced to the initial configuration. In ECAE, however, the neighborhood around a node undergoes severe distortion, both in terms of deformation and connectivity, rendering the initial reference configuration irrelevant. Furthermore, boundary conditions in ECAE evolve with time and depend on the current location of the nodes, which necessitates an updated-Lagrangian formulation. For example, the transition of boundary nodes from vertical to horizontal walls of the channel requires a change in Dirichlet boundary conditions. Previous attempts at model-

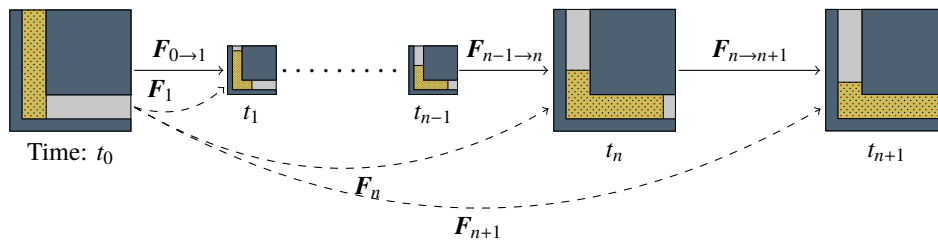


Figure 3.2: Illustration of the total- and updated-Lagrangian frameworks for simulating ECAE. The total deformation gradient \mathbf{F}_{n+1} maps the initial configuration at time t_0 to the configuration at time t_{n+1} . The incremental deformation gradient $\mathbf{F}_{n \rightarrow n+1}$ provides an incremental map between the configurations at t_n and t_{n+1} .

ing ECAE were based on explicit dynamics simulations which do not necessarily require Dirichlet boundary conditions. However, dynamics simulations do not replicate the strongly quasi-static processing conditions of ECAE. To this end, we use the stabilized max-ent meshfree approximation scheme and the updated-Lagrangian formulation introduced in Chapter 2 for quasi-static simulations. For the purpose of subsequent discussions, the updated-Lagrangian formulation in the context of ECAE is recapitulated in Figure 3.2.

Figure 3.3 illustrates the schematics of the ECAE channel, and a 3D billet of length l and a square cross-section of unit length. To avoid any numerical artifacts and allow a smoother transition of boundary nodes from the vertical section to the horizontal section, 45° chamfers of lengths w_1 and w_2 (see Figure 3.3) are introduced at the two corners of the channel. The billet faces that are in contact with the channel walls normal to the x - and z -axes are constrained to in-plane displacements only. The channel walls normal to the y -axis (i.e. the top and bottom walls of the horizontal section) and the chamfers act as planar indenters (with cubic energy based on nodal penetration). Although it is also possible to model the vertical section with indenters, replacing Dirichlet boundary conditions by indenters spoils the conditioning of the consistent tangent matrix. Therefore, the use of planar indenters is only limited to the horizontal section of the channel. The billet is extruded by a plunger near the inlet and hence, the top face is constrained based on the plunger displacement, while the other end of the billet is traction-free. At time $t = 0$, the undeformed billet is positioned just above the outer chamfer, as illustrated in Figure 3.3. The plunger moves a constant distance of u_{top} in each time step Δt until it reaches the lower edge of the inner chamfer. The total duration of the process is given by $t_{\text{max}} = (l + w_1 - 1)\Delta t / u_{\text{top}}$. The recrystallization parameters (see Section 3.2.2 and Appendix 3.A) in the Taylor model of Tutcuoglu et al. [202] were fitted based

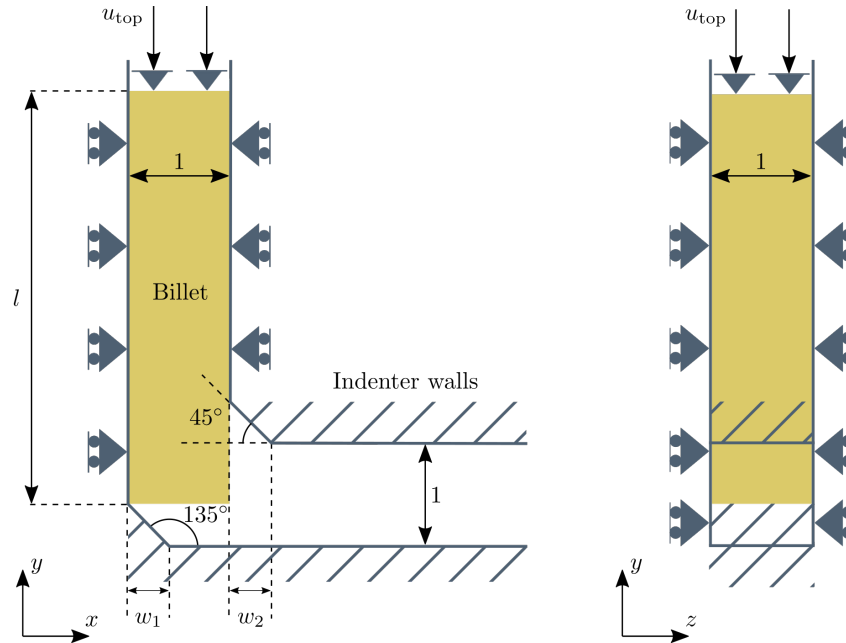


Figure 3.3: Schematics of 3D ECAE model including initial configuration and boundary conditions on the specimen. All lengths are in non-dimensionalized units.

on the uniaxial compression experiments [28] of copper at the true strain rate $\dot{\epsilon}_{\text{true}} = -0.002 \text{ s}^{-1}$. To closely replicate the strain rates, the plunger displacement is related to time step size as $u_{\text{top}} = |\dot{\epsilon}_{\text{true}}|\Delta t$.

Luis et al. [147] and Fu et al. [83] have also modeled the effects of friction against the channel walls in dynamics simulation framework. However, the ECAE process as well as the macroscale simulation is quasi-static wherein dynamic friction is not present. Combined with the assumption that the channel walls are sufficiently lubricated, static or dynamic friction is not included in our model.

3.3 Temporal evolution of internal variables

In this section, we present an explicit integration scheme for temporal evolution of the internal variables. Although implicit updates offer better stability, the lack of a closed form for variational formulation of the dissipation potential in our material model limits the updates to explicit schemes only.

Following the notations of Chapter 2, subscript $(\cdot)_n$ denotes a field in the configuration at time t_n . For the sake of brevity, the superscript $(\cdot)^p$ denoting association of a field with material point p is dropped. In the usual explicit scheme for evolution of internal variables, the macroscale BVP assumes a material response based on the microscale internal variables $\{\mathbf{Q}_{i,n}\}_{i \in 1, \dots, N_g}$ of the previous step t_n , and yields the total

deformation gradient \mathbf{F}_{n+1} that satisfies mechanical equilibrium at time t_{n+1} . This is followed by an update of the internal variables to $\{\mathbf{Q}_{i,n}\}_{i \in 1, \dots, N_g}$ using the current total deformation gradient \mathbf{F}_{n+1} . Despite the simplicity, explicit updates require small time steps to ensure stable evolution of the internal variables. However, this also increases the number of calls to the meshfree solver which performs computationally expensive operations that include construction of the meshfree shape functions (2.10), assembly of the consistent tangent matrix (2.41d), and Newton-Raphson iterations for solving the nonlinear equations in (2.26).

To overcome this stability vs. computational trade-off, we introduce an adaptive multi-stepping approach for time integration outlined as follows. The time step from t_n to t_{n+1} is uniformly discretized into $2n_m$ intermediate steps, where n_m is termed as the *multi-step number*. The incremental deformation gradient admits a polar decomposition

$$\mathbf{F}_{n \rightarrow n+1} = \hat{\mathbf{R}} \hat{\mathbf{U}}, \quad (3.12)$$

where $\hat{\mathbf{U}} = \sqrt{\mathbf{F}_{n \rightarrow n+1}^T \mathbf{F}_{n \rightarrow n+1}}$ denotes the principal stretch tensor, and $\hat{\mathbf{R}} = \mathbf{F}_{n \rightarrow n+1} \hat{\mathbf{U}}^{-1}$ is a rotation tensor. The incremental deformation gradient is then decomposed into $2n_m$ number of compositions as

$$\mathbf{F}_{n \rightarrow n+1} = \underbrace{\hat{\mathbf{R}}^{1/n_m} \dots \hat{\mathbf{R}}^{1/n_m}}_{n_m \text{ times}} \underbrace{\hat{\mathbf{U}}^{1/n_m} \dots \hat{\mathbf{U}}^{1/n_m}}_{n_m \text{ times}}. \quad (3.13)$$

Using the multiplicative composition $\mathbf{F}_{n+1} = \mathbf{F}_{n \rightarrow n+1} \mathbf{F}_n$ of the updated-Lagrangian formulation, the total deformation gradient at each intermediate step between t_n and t_{n+1} is recursively defined as

$$\mathbf{F}_{n+m/(2n_m)} \equiv \begin{cases} \hat{\mathbf{U}}^{1/n_m} \mathbf{F}_{n+(m-1)/(2n_m)} & \text{if } m \leq n_m, \\ \hat{\mathbf{R}}^{1/n_m} \mathbf{F}_{n+(m-1)/(2n_m)} & \text{if } m > n_m, \end{cases} \quad \text{for } 1 < m \leq 2n_m, \quad (3.14)$$

Finally, we leverage the intermediate total deformation gradients in (3.14) to incrementally update the internal variables from $\{\mathbf{Q}_{i,n}\}_{i \in 1, \dots, N_g}$ to $\{\mathbf{Q}_{i,n+1}\}_{i \in 1, \dots, N_g}$ in $2n_m$ steps. Following Section 3.2.1, at each intermediate step $m \in \{1, \dots, 2n_m\}$, the internal variables $\mathbf{Q}_{i,n+m/(2n_m)}$ of the i^{th} grain is computed based on $\mathbf{Q}_{i,n+(m-1)/(2n_m)}$, the inelastic deformation gradient $\mathbf{F}_{i,n+(m-1)/(2n_m)}^{\text{in}}$, and the total deformation gradient $\mathbf{F}_{n+m/(2n_m)}$. This reduces the effective time step at the microscale to $\Delta t^* = \Delta t / 2n_m$, where $\Delta t = (t_{n+1} - t_n)$, allowing improved stability in numerical integration of the internal variables. On the other hand, the macroscale time step (Δt) is maintained to avoid computational expenses arising from increased number of calls to the meshfree solver. An illustration of the multi-stepping integration scheme is presented in Figure 3.4.

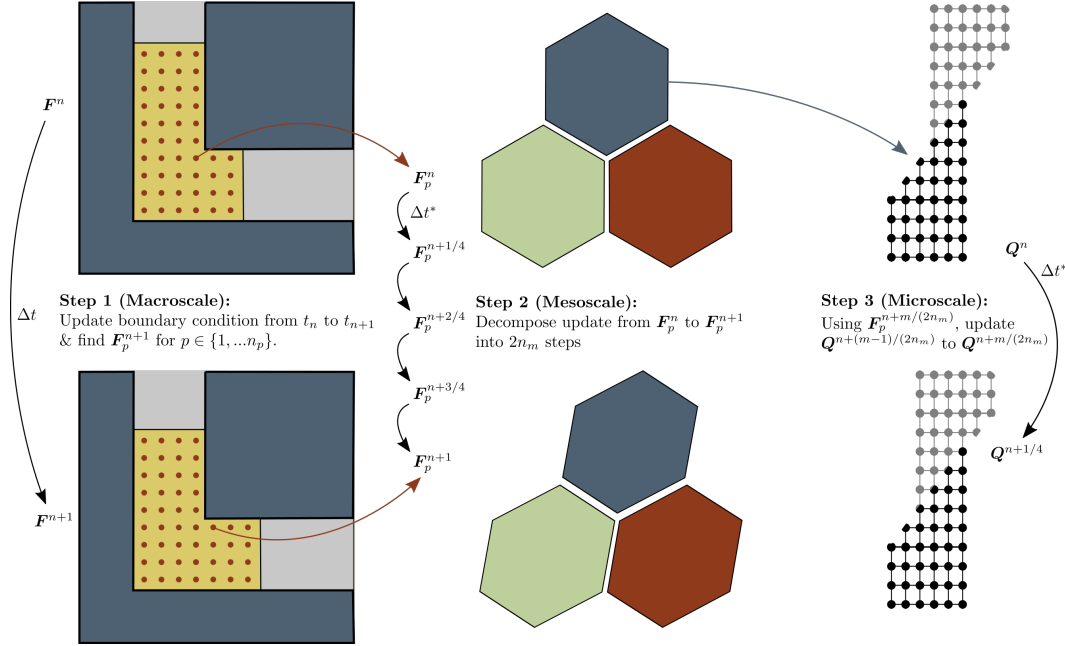


Figure 3.4: Illustration of the time integration scheme at the micro-, meso-, and macroscale with $n_m = 4$.

The multi-step number n_m also determines the computational cost of updating internal variables between two time steps. For a material point undergoing severe plastic deformation near the corner, the exponentiation of normalized resolved shear stress in (3.5) can blow up if the effective time step Δt^* is not small enough. However, as the material point moves into the post-deformation region, i.e. away from the corner, the resolved shear stress does not change significantly and using an extremely small effective time step is unnecessary. We leverage this observation to propose the following scheme that *adaptively* chooses the number of multi-steps at every time step in order to reduce the computational expense. We define a lower bound on the multi-step number as $n_{m,l}$. At the beginning of a simulation, the multi-step number at each material point is initialized to $n_{m,l}$. At time t_n , we compute the following quantity based on the power law in (3.5) for each grain during each multi-step

$$\xi_{n+m/(2n_m)} = \frac{\left| \tau_{n+m/(2n_m)}^\alpha / G_{r,n+m/(2n_m)}^\alpha \right|}{\left| \tau_{n+(m-1)/(2n_m)}^\alpha / G_{r,n+(m-1)/(2n_m)}^\alpha \right|}, \quad (3.15)$$

which is indicative of significant change in the normalized resolved shear stress. If $\xi_{n+m/(2n_m)} > \xi_{cr}$ for some critical value ξ_{cr} (e.g., $\xi_{cr} = 1.1$), the effective time step is reduced (i.e. n_m is increased) by a factor of two, and the multi-step integration is restarted from t_n . At time t_{n+1} , n_m is re-initialized to half the number of multi-steps

used for time-integration at t_n or the lower bound $n_{m,l}$, whichever is smaller. Note that the adaptive scheme may lead to different multi-step numbers between any two material points during the course of the simulation. Algorithm 6 explains the adaptive multi-stepping scheme with the help of a pseudo-code.

Algorithm 6 : Adaptive multi-step evolution of internal variables at a given material point

Input at time t_n :

- Number of multi-steps: n_m (equal to $n_{m,l}$ if $t_n = t_0$)
- Total deformation gradient at material point: \mathbf{F}_n
- Internal variables of each grain: $\{\boldsymbol{\gamma}_{i,n}, i = 1, \dots, N_g\}$, $\{\mathbf{g}_{i,n}, i = 1, \dots, N_g\}$, $\{\mathbf{F}_{i,n}^{\text{in}}, i = 1, \dots, N_g\}$

- 1: ErrorFlag := true
- 2: **while** (ErrorFlag) **do**
- 3: ErrorFlag := false
- 4: **for** $m = 1, \dots, 2n_m$ **do**
- 5: Compute $\mathbf{F}_{n+m/(2n_m)}$ using (3.14)
- 6: **for** $i = 1, \dots, N_g$ **do**
- 7: Compute $(\mathbf{F}_{i,n+m/(2n_m)}^{\text{e}})^* := \mathbf{F}_{n+m/(2n_m)}(\mathbf{F}_{i,n+(m-1)/(2n_m)}^{\text{in}})^{-1}$
- 8: Compute $\boldsymbol{\gamma}_{i,n+m/(2n_m)}$ using (3.5)
- 9: Compute $\mathbf{g}_{i,n+m/(2n_m)}$ using (3.6)
- 10: Compute $\mathbf{F}_{i,n+m/(2n_m)}^{\text{in}}$ using (3.2)
- 11: Compute $\xi_{n+m/(2n_m)}$ using (3.15)
- 12: **if** $(\xi_{n+m/(2n_m)} > \xi_{\text{cr}})$ **then**
- 13: ErrorFlag := true
- 14: **break**
- 15: **end if**
- 16: **end for**
- 17: **if** (ErrorFlag) **then**
- 18: **break**
- 19: **end if**
- 20: **end for**
- 21: **if** (ErrorFlag) **then**
- 22: $n_m := 2n_m$
- 23: **end if**
- 24: **end while**
- 25: // Prepare for next time step t_{n+1} :
- 26: $n_m := \max \{n_m/2, n_{m,l}\}$

3.4 Results

For the subsequent results, all simulations follow the protocols presented in Appendix 3.A, including those related to spatial discretization, simulation parameters,

and material properties, with otherwise stated exceptions. At the mesoscale, migration (3.9) and nucleation (3.11) of grains are by default deactivated, but we activate them only when studying the effects of recrystallization, which is further explained in Section 3.4.3.

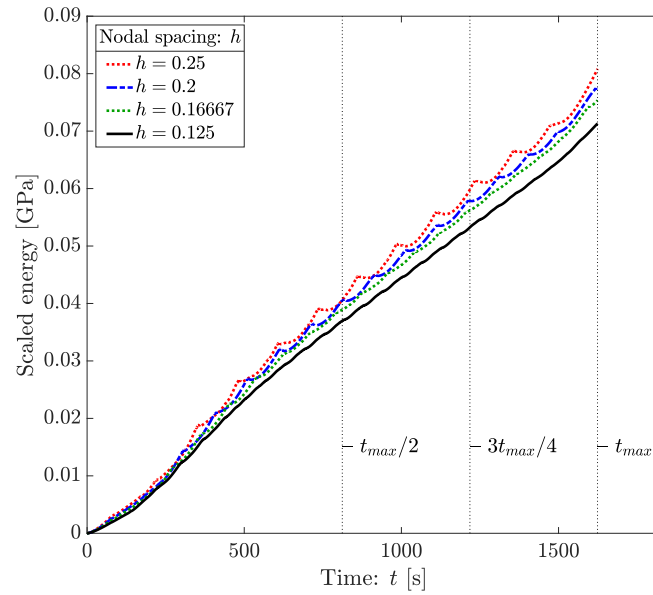
3.4.1 Convergence with refinement in spatial and temporal discretization

Figure 3.5 shows the convergence of total energy stored in the billet (excluding energy penalization due to planar indenters) with respect to h -refinement. At low spatial resolution, we observe some oscillatory artifacts which emerge when a set of nodes passes through the corner causing a sharp increase in energy. With increasing spatial resolution, these artifacts become less apparent. Figure 3.6 shows the convergence of energy with decreasing Δt . Similar oscillatory artifacts are observed at low temporal resolution, which vanish with temporal refinement. While it is possible to further increase the spatio-temporal resolution, updating internal variables of large number of grains at multiple material points quickly becomes computationally infeasible with increasing resolution. Based on the convergence studies, we choose the spatial and temporal discretizations corresponding to nodal spacing equal to 0.16667 and $\Delta t = 0.1$ s, respectively, for a reasonable balance between accuracy and computational costs in the subsequent simulations.

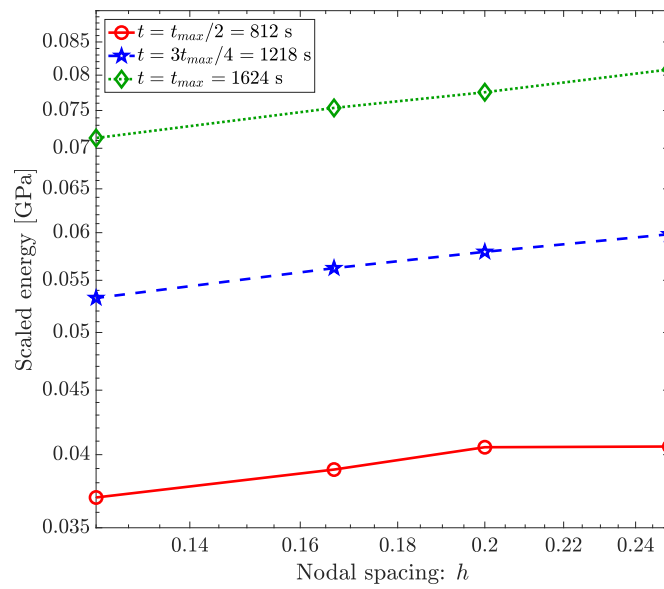
Figure 3.7 illustrates the spatial discretization (chosen based on the aforementioned convergence study) during the course of the simulation. Severe distortion in nodal connectivity (in terms of relative position of the nodes and material points) is observed, particularly near the corner and outlet of the channel. While mesh-based methods such as FEM are limited due to entanglement and inversion of elements, our proposed updated-Lagrangian meshfree framework is able to simulate such deformations without any issues. Furthermore, the total-Lagrangian formulation, even with a meshfree kernel, does not account for changes in connectivity and hence, it will incorrectly introduce non-physical forces and kinematics.

3.4.2 Strain distribution and effect of channel geometry

Figure 3.8 illustrates the strain distribution in a specimen undergoing ECAE, visualized via deformation gradient component F_{xy} . To study the effect of channel geometry on strain distribution, the strains are plotted for two different sets of channel dimensions – (i) $w_1 = 0.25$, $w_2 = 0.1$, and (ii) $w_1 = 0.125$, $w_2 = 0.05$; the latter describes sharper corners in the channel. For both cases, we observe a strong shear region that extends from the outer to the inner corner of the channel.

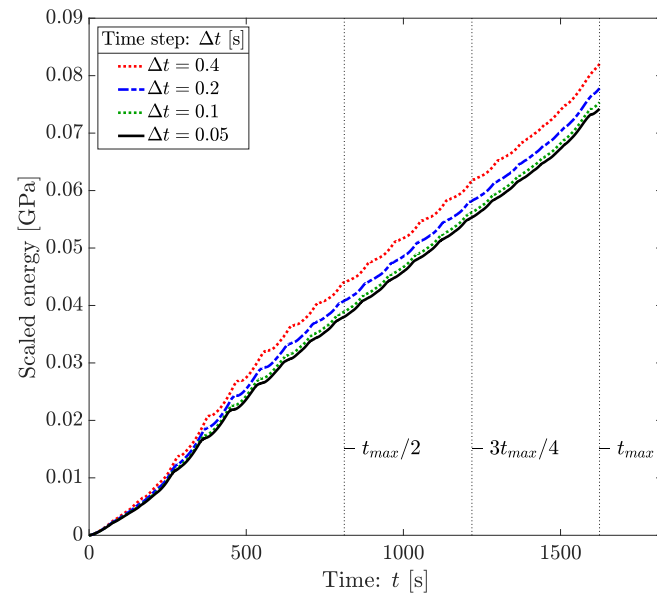


(a)

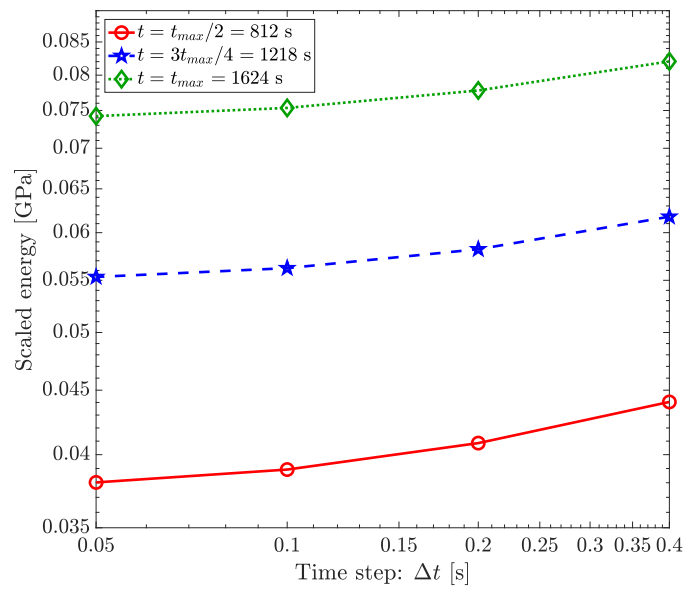


(b)

Figure 3.5: Convergence of energy with respect to h -refinement. (a) Energy stored in the billet vs. time for four different nodal spacings. (b) Energy vs. nodal spacing evaluated at times $t \in \{t_{max}/2, 3t_{max}/4, t_{max}\}$ as indicated in (a).



(a)



(b)

Figure 3.6: Convergence of energy with respect to temporal refinement. (a) Energy stored in the billet vs. time for four different time steps Δt . (b) Energy vs. time step Δt evaluated at times $t \in \{t_{max}/2, 3t_{max}/4, t_{max}\}$ as indicated in (a).

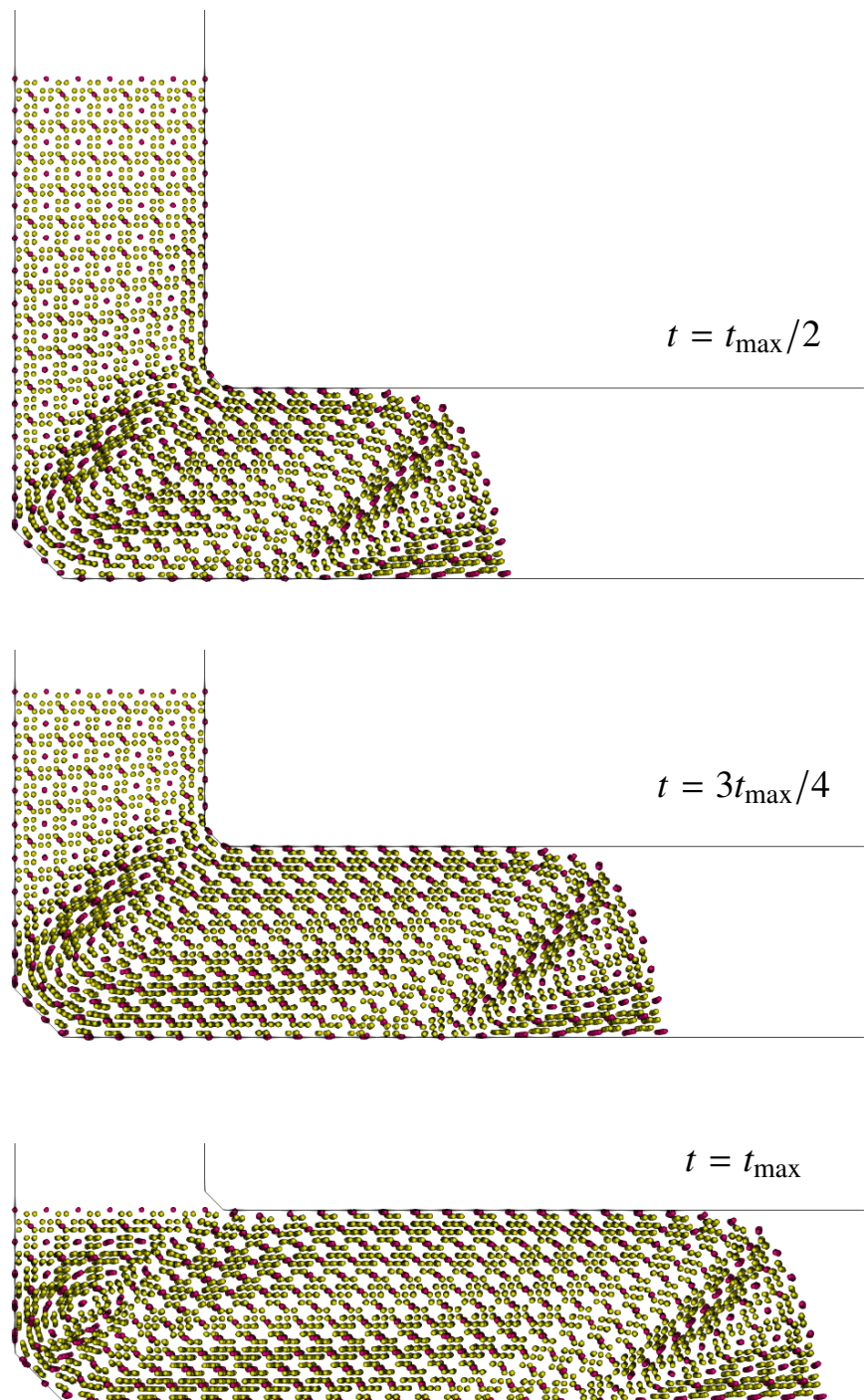


Figure 3.7: Deformed spatial discretization at three different stages of the ECAE simulation. The yellow and red points denote material points and nodes, respectively.

	\mathbf{F}	$\tilde{\mathbf{F}} = \mathbf{R}\mathbf{F}\mathbf{R}^T$
Segal [192]		$\begin{pmatrix} 1 & -2 & 0 \\ 0 & 1 & 0 \\ 0 & 0 & 1 \end{pmatrix}$
(i) $w_1 = 0.25$ $w_2 = 0.1$	$\begin{pmatrix} 1.94 \pm 0.23 & -1.01 \pm 0.05 & 0.00 \pm 0.03 \\ 0.98 \pm 0.05 & 0 \pm 0.03 & 0.00 \pm 0.01 \\ 0.00 & 0.00 & 1.00 \end{pmatrix}$	$\begin{pmatrix} 0.96 \pm 0.13 & -1.97 \pm 0.12 & 0.00 \pm 0.03 \\ 0.03 \pm 0.12 & 0.98 \pm 0.12 & 0.00 \pm 0.02 \\ 0.00 & 0.00 & 1.00 \end{pmatrix}$
(ii) $w_1 = 0.125$ $w_2 = 0.05$	$\begin{pmatrix} 2.11 \pm 0.46 & -1.00 \pm 0.10 & 0.00 \pm 0.05 \\ 0.96 \pm 0.10 & 0.02 \pm 0.06 & -0.01 \pm 0.01 \\ 0.00 & 0.00 & 1.00 \end{pmatrix}$	$\begin{pmatrix} 1.04 \pm 0.26 & -2.03 \pm 0.24 & -0.01 \pm 0.04 \\ -0.07 \pm 0.24 & 1.09 \pm 0.22 & 0.00 \pm 0.03 \\ 0.00 & 0.00 & 1.00 \end{pmatrix}$

Table 3.1: Mean and standard deviation of deformation gradient over material points in the homogeneous section indicated by black rectangles in Figure 3.8. The deformation gradients are reported for $t = t_{\max}$.

Homogeneity of strain distribution in a specimen is crucial for industrial applications. We observe that except the regions near the ends of the billet, there is reasonable homogeneity in strain distribution (see Figure 3.8) throughout the specimen. To quantify this homogeneity, Table 3.1 reports the mean and standard deviation in deformation gradient at the material points that lie inside the black rectangles indicated in Figure 3.8. Following the general convention in previous literature, we also report the deformation gradient under the following coordinate transformation

$$\tilde{\mathbf{F}} = \mathbf{R}\mathbf{F}\mathbf{R}^T, \quad \text{with} \quad \mathbf{R} = \begin{pmatrix} \cos(-\pi/4) & -\sin(-\pi/4) & 0 \\ \sin(-\pi/4) & \cos(-\pi/4) & 0 \\ 0 & 0 & 1 \end{pmatrix}, \quad (3.16)$$

where $\mathbf{R} \in SO(3)$ applies a rotation of $-\pi/4$ about the z -axis. Our findings are in agreement with the analytical derivations of Segal [192] and Iwahashi et al. [104] that predict a 200% simple shear deformation under simplified assumptions. We also note that spatial discretization with higher resolution may reveal more heterogeneity, which is a limitation due to the computational costs of the multiscale framework. Furthermore, the sharper corner ($w_1 = 0.125$, $w_2 = 0.05$) causes a relatively stronger and more localized strain inhomogeneity, which is indicated by the red circles in Figure 3.8 and also evident from the higher standard deviations in Table 3.1. This observation is in contrast to the hypothesis by Segal [192] that a sharper corner would produce a relatively more homogeneous strain distribution.

3.4.3 Grain recrystallization and texture evolution

In the previous simulations, grain recrystallization was ignored. In this section, we activate recrystallization, i.e. migration and nucleation of grains (outlined in Section 3.2.2), in order to capture grain refinement at the mesoscale. Figure 3.9a illustrates evolution of the number of active grains at three representative material

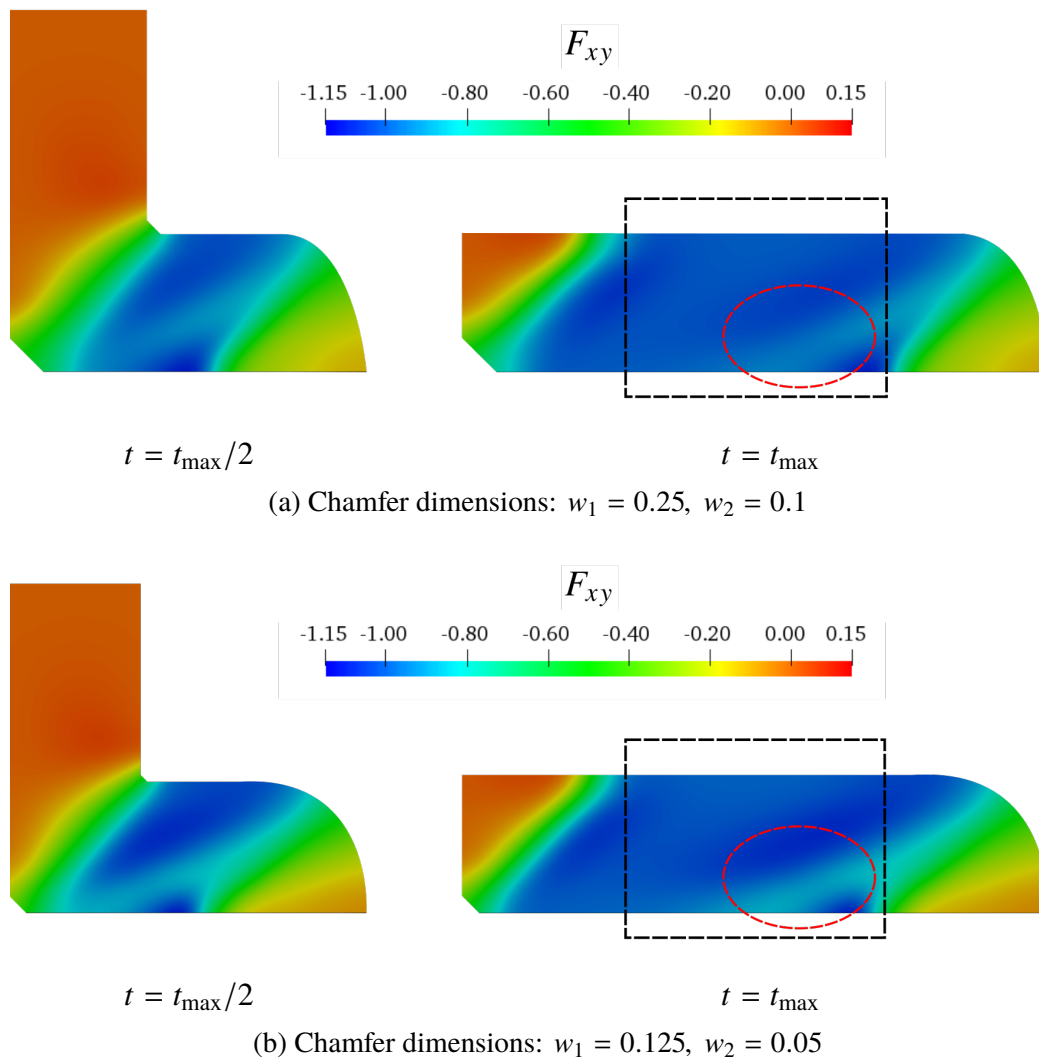


Figure 3.8: Distribution of deformation gradient component F_{xy} for two different sets of chamfer dimensions. The black rectangles indicate regions of relatively homogeneous strain distribution compared to the billet ends. The red circles indicate regions of strong and localized strain inhomogeneity in the middle of the specimen. The plots are obtained by interpolating the deformation gradients onto the cross-sectional mid-plane via Gaussian interpolants of standard deviation equal to 0.3.

points, as well as the mean and maximum over all the material points. When the material points approach the channel corner, the severe shearing deformation causes strong nucleation of new, pristine, and initially stress-free grains, which is evident from the sharp increase (12-15 times) in the number of grains. As the material points move away from the corner and into the post-deformation regime, grain migration becomes dominant and results in gradual decrease in the number of grains at the expense of heavily distorted and high-energy grains. This phenomenon is also known as post-dynamic recrystallization, which is beyond the scope of this work and the interested readers are referred to [190] for more details. The effects of recrystallization are also observed in Figure 3.9b which illustrates the temporal evolution of average grain volume fraction at the three representative material points. Specifically, the shear zone near the corner experiences the strongest grain refinement indicated by the sharp decrease in average volume fraction, followed by gradual coarsening, i.e. gradual increase in average volume fraction due to post-dynamic recrystallization. Figure 3.9b also shows the mean and standard deviation in average grain volume fraction over all the material points. In particular, the mean of average grain volume fraction is reduced by a factor of approximately 3.3 at $t = t_{\max}$ with respect to the initial value, indicating strong grain refinement. The significant standard deviation is indicative of spatial heterogeneity in grain refinement and is attributed to the regions near the ends of billet specimen, similar to strain distribution in Figure 3.8.

Grains at the material point level also undergo reorientation in response to the local deformations and give rise to textures. We illustrate this texture evolution for a representative material point in Figure 3.10 via (inverse) pole density figures which are generated based on stereographic projection of $\langle 111 \rangle$ poles of the face-centered cubic (fcc) copper crystals on the (001) plane (see e.g., [208]). To study the effects of recrystallization, the pole figures are shown for the cases when recrystallization is excluded and included. In both cases, the pole figures at $t = t_{\max}/4$ indicate an initial texture corresponding to a weak compression zone. As the material points plastically flow around the corner, each grain reorients in order to allow shear along the preferred slip systems. This evidently produces the characteristic texture classically associated with shearing, i.e. four to six dominant orientations [208], with some diffused features retained from the weak-compression phase. Moreover, for this set of numerical experiments and using the proposed simulation framework, Tutcuoglu [201] showed that prominence of texture features is correlated to the proximity of a material point to the outer wall. In particular, material points closest to the outer

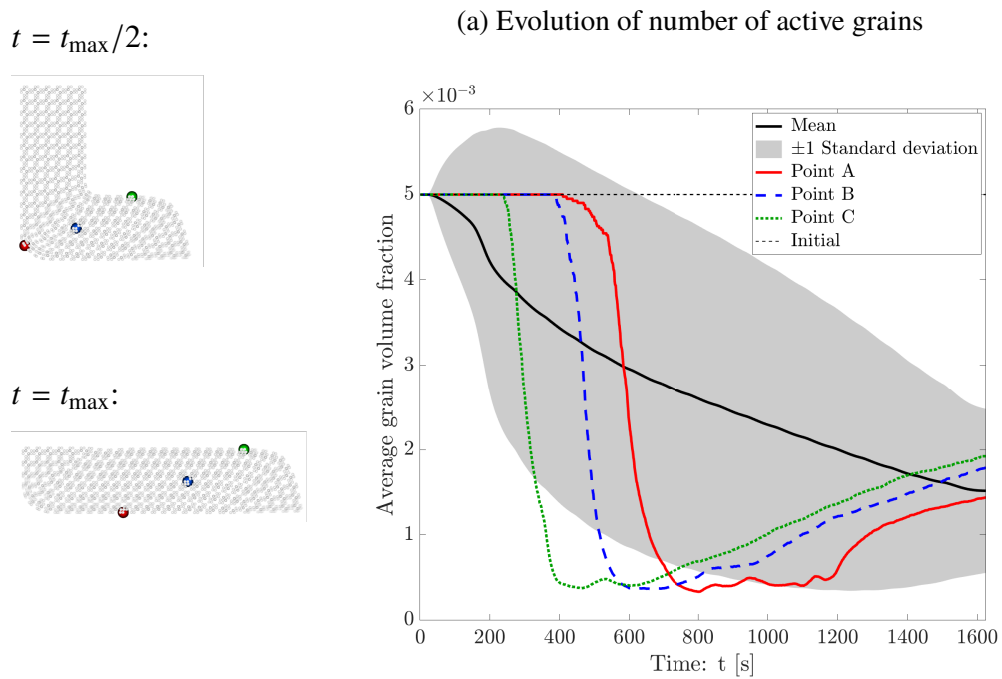
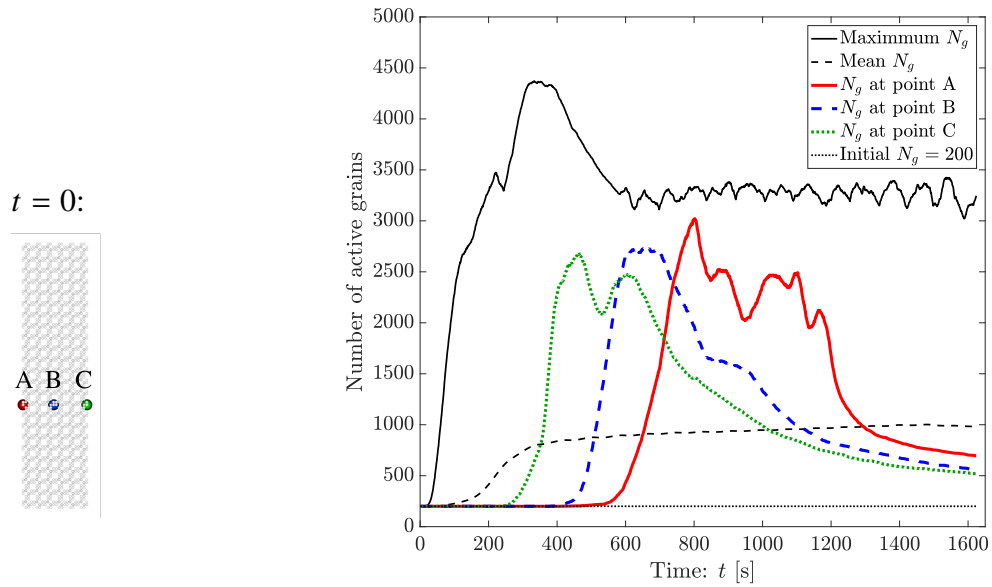


Figure 3.9: Temporal evolution of (a) number of active grains, and (b) average grain volume fraction, evaluated at three representative material points (indicated as A, B, and C).

wall show six distinctly dominant orientations, while the points closer to the inner wall show a more diffused texture. Compared to the case when recrystallization is excluded, the texture at $t = 3t_{\max}/4$ is more diffused with recrystallization included. This is attributed to the random orientation of the new grains arising from the strong nucleation during the shearing phase. In contrast, recrystallization produces a significantly more pronounced shearing-based texture at $t = t_{\max}$. This is due to the post-dynamic recrystallization that plays a crucial role in texture evolution during the post-deformation phase [190]. The texture evolution obtained from our framework corroborates experimental findings (via neutron diffraction of ECAE samples) of Vogel et al. [208] and theoretical predictions (based on sequential lamination type microstructures) of Sivakumar and Ortiz [193]. For more details on the texture and microstructural evolution observed in these numerical experiments, the interested readers are referred to Tutcuoglu [201].

Figure 3.11 shows evolution of the energy stored in the billet and the vertical force exerted by the plunger when recrystallization at the mesoscale is included/excluded. Notably, the total energy and the plunger force reduce significantly in the case when recrystallization is enabled. The soft response is due to the nucleation of pristine stress-free grains, in combination with diminution of highly stressed grains due to migration that results in a decrease in the homogenized energy as well as the plunger force. Compared to evolution of the energy, the oscillatory artifacts in the plunger force due to coarseness of the spatial-temporal discretization (limited by computational expense of the simulation) are more pronounced, but are expected to vanish with refinement. The initial steep increase in force is attributed to the compression in the beginning (as also observed in texture evolution) followed by saturation as the material starts to plastically flow around the corner. The force curves also show similar trends as those obtained by Luis et al. [147] for ECAE of 5083 aluminium alloy via FEM simulations¹

3.4.4 Mutli-pass ECAE

Since the cross-section of the specimen remains unchanged during ECAE, it is possible to extrude the specimen through the channel multiple times. Ferrasse et al. [79] have shown that multiple passes of a specimen through the channel (also known as multi-pass ECAE) further improves the grain refinement and reorientation of grains. Multi-pass ECAE usually involves shearing along different directions

¹The comparison is purely qualitative. The material model and process parameters of simulations by Luis et al. [147] are entirely different from that of the presented study.

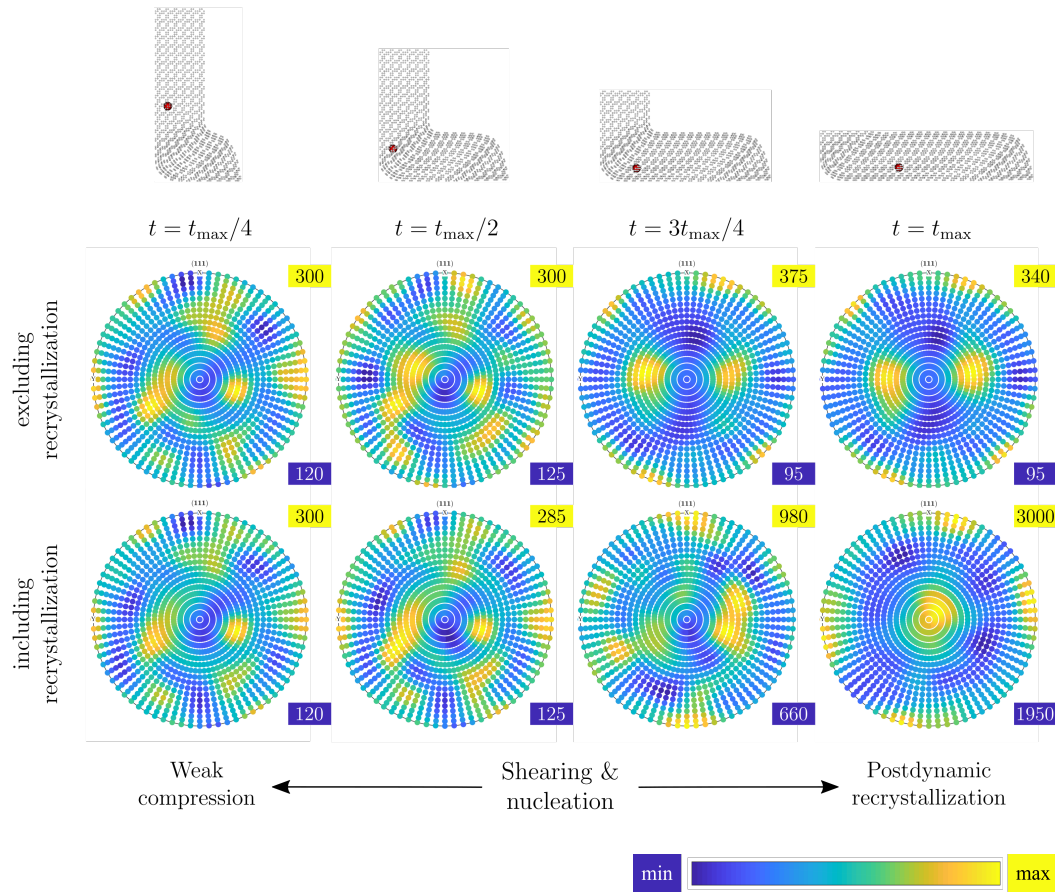


Figure 3.10: Comparison of texture evolution when recrystallization is included vs. excluded. The pole figures are evaluated at four time steps for a representative material point indicated as red dot, along with position in the respective deformed configurations. The minimum and maximum values of each pole figure are denoted in blue and yellow boxes, respectively.

to produce more uniform grain refinement and strain distribution than single-pass ECAE. This is achieved by rotating the specimen along its axis between subsequent single passes, or extruding the specimen through a long channel consisting of multiple in-plane and out-of-plane bends. Computational modeling of both approaches pose their own set of challenges [83] in terms of the realignment of spatial discretization and treatment of boundary conditions and hence will be covered in a future study. For the scope of this thesis, we simulate a relatively simple multi-pass ECAE setup where a specimen of length $2l$ is extruded through a channel shown in Figure 3.12a. Effect of grain migration and nucleation, and hence grain refinement is not considered in this study. Homogeneity in the resulting strain distribution in the specimen, visualized via deformation gradient component F_{xy} , is illustrated in

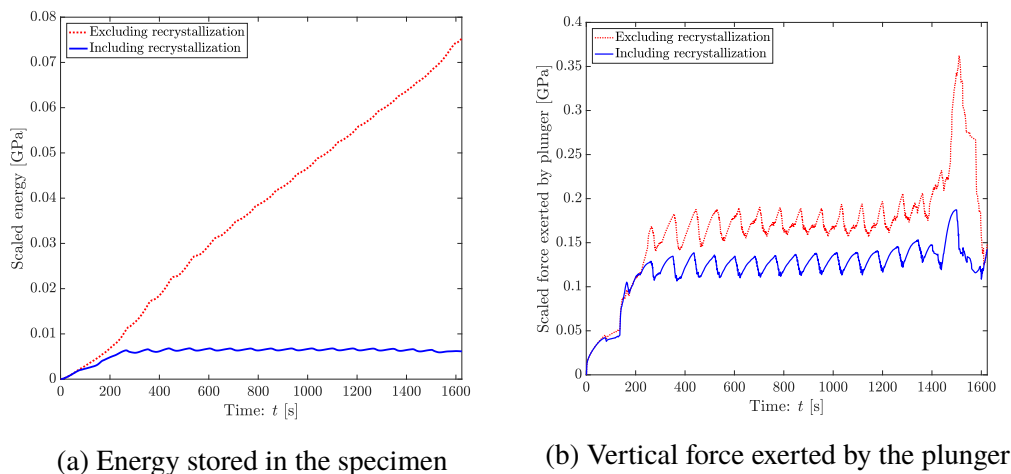
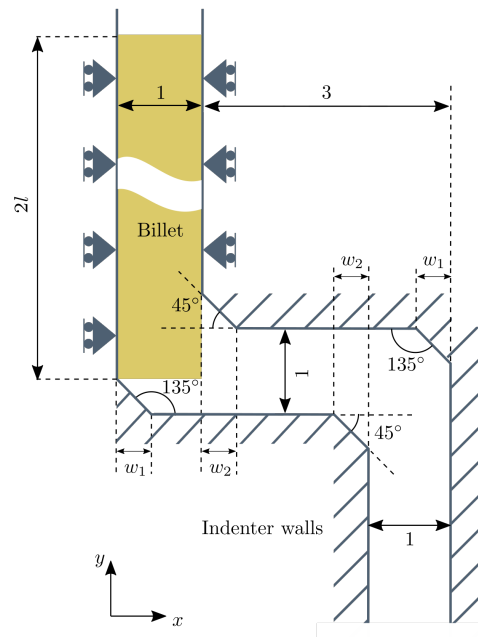


Figure 3.11: Evolution of (a) the total energy stored in the specimen, (b) the vertical force exerted by the plunger, when recrystallization is included/excluded.

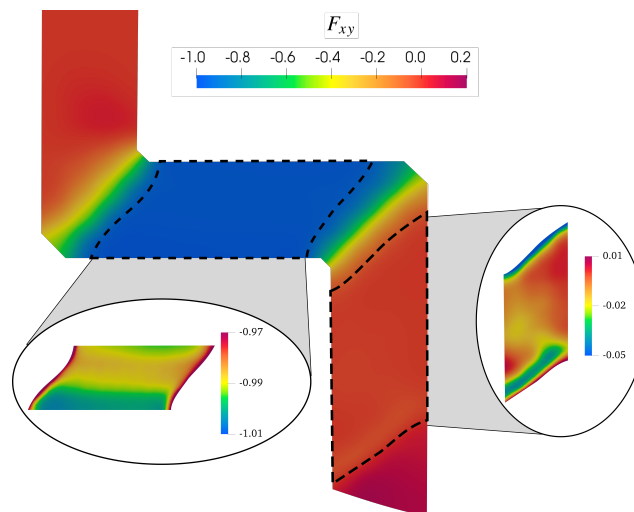
Figure 3.12b. Note that the shear strains vanish after the second corner, as one would expect based on the anti-symmetry of the two corners. Figure 3.13 shows the texture evolution at a representative material point during the simulation. Notably, a strong grain reorientation and texture is retained, in spite of disappearance of shear strains otherwise encountered in single-pass ECAE. This clearly demonstrates the advantage of multi-pass ECAE over single-pass setups, and motivates further research into optimization of such processes with high fidelity simulations.

3.5 Conclusion

In this chapter, we have introduced a novel multiscale framework for high-fidelity simulations of ECAE and in general, SPD processes. The enhanced max-ent based meshfree approximation scheme for stable updated-Lagrangian simulations (introduced in Chapter 2) is used to capture severe deformations at the macroscale. The Taylor model of Tutcuoglu et al. [202] is applied at the mesoscale to capture grain nucleation and migration, while finite strain crystal plasticity model for copper is used at the microscale. Additionally, we have proposed an adaptive multi-stepping scheme for computationally efficient time integration of internal variables at the material point level. Numerical studies draw several conclusions that include reasonable homogeneity in strain distribution of the specimen as well as strong texture evolution due to the reorientation of grains, which are in good agreement with previous theoretical predictions and experimental results. More importantly, grain nucleation and migration enable significant grain refinement and post-dynamic re-



(a) Schematics (in 2D view) of a 3D channel consisting of two in-plane corners with equal chamfer dimensions. The initial configuration and boundary conditions on the specimen are also shown. All lengths are in non-dimensionalized units.



(b) Distribution of deformation gradient component F_{xy} at time $t = 2842$ s. Insets show strain distribution in the relatively homogeneous regions indicated by dashed lines. The plots are obtained by interpolating the deformation gradients onto the cross-sectional mid-plane via Gaussian interpolants of standard deviation equal to 0.3.

Figure 3.12: Multi-pass ECAE

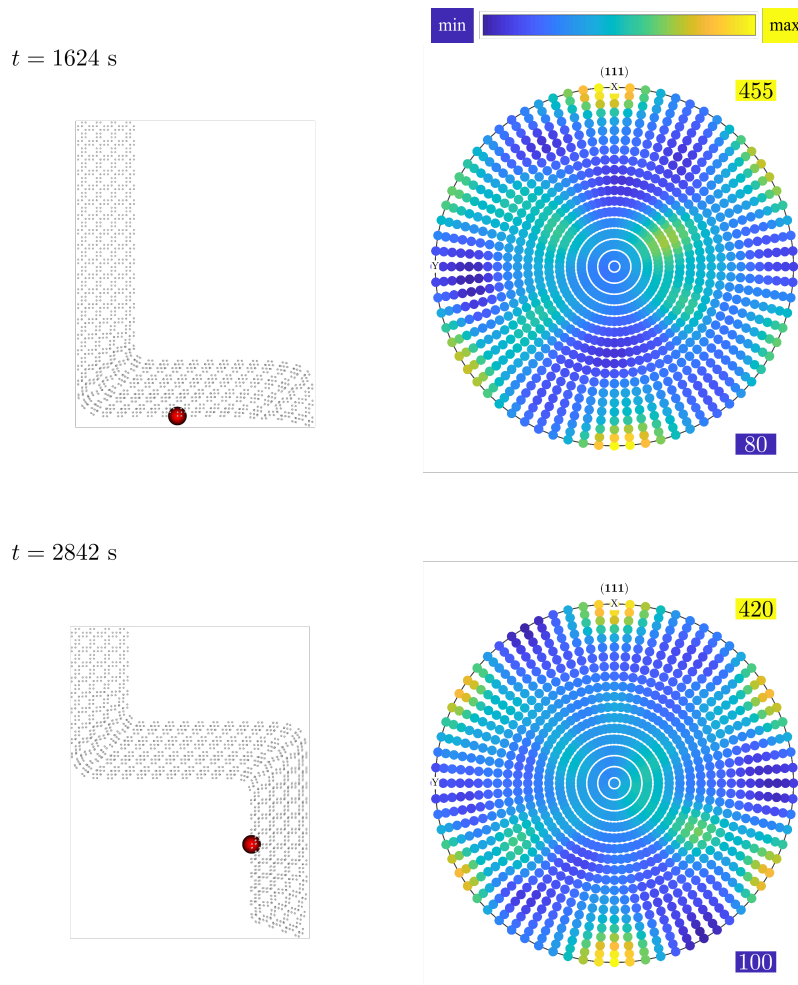


Figure 3.13: Texture evolution in multi-pass ECAE (described by the schematics in Figure 3.12a). The pole figures are evaluated at two time steps for a representative material point indicated as red dot, along with position in the respective deformed configurations. The minimum and maximum values of each pole figure are denoted in blue and yellow boxes, respectively.

crystallization. To conclude this set of experiments and give directions to future work, we have showed possible extension to multi-pass ECAE with the example of double in-plane ECAE of a specimen. Due to the general and flexible nature of the proposed framework, it can also be applied to ECAE with multiple out-of-plane passes, which will be presented in a subsequent study. Overall, the proposed framework offers a computational tool for optimizing process parameters of ECAE and other SPD processes in the metal forming industry.

APPENDIX

3.A Simulation protocols

Tables 3.2, 3.3, and 3.4 lists the default set of parameters used in each simulation, unless explicitly stated otherwise. All simulations use the following protocols to setup the initial configuration; detailed information can be found in Chapter 2.

- A uniform tetrahedral mesh is generated for the initial geometry (cuboid) of the billet. Next, a material point is inserted at the barycenter of each tetrahedron. The volume V_0^p associated with the material point p is initialized with the volume of the containing tetrahedron. For each material point p , a measure of nodal spacing h^p is computed as mean distance to nodes of the containing tetrahedron. The max-ent locality parameter β_0^p is then initialized based on h^p , as listed in Table 3.4. The initial connectivity is determined by $M_0^p = -1/\log(\epsilon_{\text{cut}}) \times \beta_0^p$, where ϵ_{cut} is a small valued tolerance. For details, see Section 2.2.4.
- At the mesoscale, the orientations of each grain, including those nucleated during the loading, are randomly initialized using the *Bunge-Euler* angles: $\phi_1 = 2\pi r_1$, $\theta = \cos^{-1}(1 - 2r_2)$, $\psi = 2\pi r_3$, where $r_{i \in \{1,2,3\}}$ are randomly sampled from $\mathcal{U}([0, 1])$ (for details, the interested reader is referred to [120]).

Parameter	Symbol	Unit	Value	Source
Temperature	T	[K]	775	
Shear modulus	μ	[GPa]	34	[82]
Bulk modulus	κ	[GPa]	128	[131]
Initial shear resistance	G_0	[MPa]	6.5	[152]
Plastic modulus	Q	[MPa]	37.0	[152]
Latent hardening multiplier	q	[-]	1.4	[96]
Hardening exponent	m	[-]	26	[96]
Saturation factor	B	[-]	8	[96]
Initial accumulated slip measure	g_0	[-]	0.007	[96]
Reference slip rate	$\dot{\gamma}_0$	[s ⁻¹]	0.001	[96]
Critical energy density threshold	$W^{\text{in,cr}}$	[MPa]	0.424	[152]
Nucleation exponent	d	[-]	4.4	[214]

Table 3.2: Microscale parameters of the copper material model.

Parameter	Symbol	Unit	Value
Initial number of grains	$N_{g,\text{init}}$	[-]	200
Migration rate	κ_{GBM}	[GPa·s]	204
Nucleation rate	κ_{NCL}	[s ⁻¹]	57.4
Nucleation parameter	C	[-]	10.9
Initial nucleation volume fraction	η_{NCL}	[-]	1/64 ³

Table 3.3: Mesoscale parameters of the Taylor model.

Parameter	Symbol	Unit	Value
Initial length of billet*	l	[-]	4
Lower-left chamfer dimension*	w_1	[-]	0.25
Upper-right chamfer dimension*	w_2	[-]	0.1
Initial max-ent locality parameter	β_0^p	[-]	$(3/h^{p^2})\mathbf{I}$
Shape function cut-off tolerance	ϵ_{cut}	[-]	10 ⁻⁷
Initial connectivity cut-off region	\mathbf{M}_0^p	[-]	$-1/\log(\epsilon_{\text{cut}}) \times \beta_0^p$
Time step	Δt	[s]	0.1
Duration of ECAE process	t_{max}	[s]	1624
Lower bound on multi-step number	$n_{m,l}$	[-]	8
Multi-stepping criterion	ξ_{cr}	[-]	1.1

Table 3.4: Macroscale parameters defining the geometry, boundary conditions, and max-ent approximation scheme. Parameters marked with * are listed in non-dimensionalized units.

NUMERICAL ENERGY RELAXATION IN PROBLEMS WITH NONCONVEX ENERGETIC POTENTIALS

Research presented in this chapter has been adapted from the following publication:

S. Kumar, A. Vidyasagar, and D. M. Kochmann. An assessment of numerical techniques to find energy-minimizing microstructures of nonconvex energy potentials. *Under review*, 2019.

4.1 Introduction: Energy relaxation and microstructural patterns

Microstructural patterns are ubiquitous across materials systems: from the laminate patterns accompanying deformation twinning [56] and martensitic phase transformations [26, 57] to networks of dislocation walls in metal plasticity [66, 116, 168], to bi-continuous arrangements from phase separation [93], and instability-induced pattern formation in periodic metamaterials [81, 87, 170]. The origin of those spatially complex patterns is well understood and has been traced back to nonconvex energetic potentials that result in fine-scale microstructures as energy minimizers [11, 27, 55, 74, 89]. In order to understand both the intricate microstructural details and the resulting macroscopic material response, it is therefore imperative to identify both the (quasi)convex hull of the underlying nonconvex potentials and the corresponding fine-scale patterns. While there is rich literature on (semi-)analytical methods for calculating or approximating the convexified energetic potentials of relatively simple material models, numerically computing the quasiconvexified potentials and predicting the formation of the associated microstructural patterns in general are non-trivial tasks and subjects of this investigation.

By way of introduction, consider the classical mechanical boundary value problem (BVP) of quasistatic equilibrium at finite strains. We seek a deformation mapping $\varphi : \Omega \rightarrow \mathbb{R}^d$, which links the deformed position $\mathbf{x} = \varphi(\mathbf{X}) \in \varphi(\Omega)$ to the undeformed position $\mathbf{X} \in \Omega$ of any material point inside a body $\Omega \subset \mathbb{R}^d$ in d dimensions. By adopting a variational framework [200], the equilibrium deformation map is found by minimization of the total potential energy functional

$$\mathcal{I}[\varphi] = \int_{\Omega} W(\nabla\varphi) dV - \ell(\varphi), \quad (4.1)$$

where W denotes the Helmholtz free energy density, and $\ell(\boldsymbol{\phi})$ represents the linear potential of external forces. In linear elasticity, (4.1) has a unique minimizer [121]; in finite elasticity or inelasticity, the problem becomes more involved and depends on the choice of the energy density W . If W lacks quasiconvexity [64], then (4.1) lacks weakly lower semicontinuity and solutions are to be found as minimizing (or, to be exact, infimizing) sequences; i.e., fine-scale patterns form as energy minimizers, which may be interpreted as microstructural patterns on a lower spatial scale. By assuming a separation of scales between the fine-scale patterns and the macroscopic BVP, the solution to the macro-problem can be found [1] by replacing the energy density W by its quasiconvex hull QW , defined as [158]

$$QW(\nabla\boldsymbol{\varphi}) = \inf \left\{ \frac{1}{|\omega|} \int_{\omega} W(\nabla\boldsymbol{\varphi} + \nabla\boldsymbol{\phi}) \, dV \mid \boldsymbol{\phi} : \boldsymbol{\phi} = \mathbf{0} \text{ on } \partial\omega \right\}, \quad (4.2)$$

where ω denotes a representative volume element (RVE) of arbitrary size. The small-scale fluctuation field $\boldsymbol{\phi} : \omega \rightarrow \mathbb{R}^d$ describes the microstructural patterns at the RVE-level. We note that the same principles hold in linearized kinematics, where $\boldsymbol{\varphi}$ is replaced by the displacement field \boldsymbol{u} and gradients are replaced by symmetrized gradients.

The quasiconvex hull (4.2) and the associated microstructural fluctuations $\boldsymbol{\phi}$ are generally hard to calculate due to the non-local nature of (4.2). Most previous approaches for microstructural pattern prediction relied on (i) analytical energy relaxation, see e.g. [60, 117, 154], or on (ii) RVE-level finite element (FE) simulations [16, 41]. Successful analytical approaches have often relied on the construction of matching upper and lower bounds in terms of, respectively, the rank-one-convex hull and the polyconvex hull [13]. Examples include rate-independent single-slip plasticity [42, 59–61] and isotropic hyperelasticity like the St. Venant-Kirchhoff model [128]. The rank-one-convex hull construction [95, 168] is particularly appealing as it implies a higher-order laminate construction and therefore admits a clear interpretation of the associated microstructural patterns. The energy density of a first-order laminate microstructure is constructed as

$$R_1W(\nabla\boldsymbol{\varphi}) = \inf \left[\lambda_1W(\boldsymbol{F}_1) + \lambda_2W(\boldsymbol{F}_2) \mid \begin{array}{l} \sum_{i=1}^2 \lambda_i = 1, \\ \lambda_i \geq 0, \\ \sum_{i=1}^2 \lambda_i \boldsymbol{F}_i = \nabla\boldsymbol{\varphi}, \\ \text{rank}(\boldsymbol{F}_1 - \boldsymbol{F}_2) \leq 1 \end{array} \right], \quad (4.3)$$

where $\mathbf{F}_1, \mathbf{F}_2 \in GL_+(d)$; i.e., the deformation gradients in both laminate phases must be physically admissible. Recursive repetition leads to higher-order sequential laminates [9, 168], with a laminate of order k defined by

$$R_{k+1}W(\nabla\boldsymbol{\varphi}) = \inf \left[\lambda_1 R_k W(\mathbf{F}_1) + \lambda_2 R_k W(\mathbf{F}_2) \left| \begin{array}{l} \sum_{i=1}^2 \lambda_i = 1, \\ \lambda_i \geq 0, \\ \sum_{i=1}^2 \lambda_i \mathbf{F}_i = \nabla\boldsymbol{\varphi}, \\ \text{rank}(\mathbf{F}_1 - \mathbf{F}_2) \leq 1 \end{array} \right. \right], \quad (4.4)$$

Ultimately, the rank-one-convex hull is obtained as

$$RW(\nabla\boldsymbol{\varphi}) = \lim_{k \rightarrow \infty} R_k W(\nabla\boldsymbol{\varphi}). \quad (4.5)$$

Analytical laminate constructions of the above type are feasible for relatively simple constitutive models such as, e.g., hyperelasticity [128] or single-slip single-crystal plasticity [61]. Numerical approaches have been reported, e.g., for finite-strain crystal plasticity [168]. On the downside, more complex material models produce complex multi-phase patterns that would require intricate higher-order laminate constructions (which are challenging due to the nonconvex problem and a myriad of local and global energy minima). Further, interfaces in reality are not infinitely sharp as in the above lamination model [115] where the computed patterns lack a length scale. Finally, the rank-one-convex hull presents only an upper bound to the sought quasiconvex hull and it can therefore be significantly off.

As an alternative, RVE-level numerical simulations have been performed, which have primarily resorted to low-order local FE interpolations to approximate the microstructural patterns in finite-dimensional spaces. Unfortunately, using the latter in conjunction with unregularized nonconvex potentials results in: (i) ill-conditioned systems due to the loss of convexity, and (ii) coarse microstructural patterns that are mesh- and interpolation-dependent and incur heavy computational costs [14, 15, 40]. All prior examples have therefore been limited to RVEs of low resolution (or small sizes), and primarily to two dimensions (2D).

In an attempt to overcome the limitations of FEM, Vidyasagar [205] proposed the use of a *Fourier spectral formulation* [130, 159, 160] with improved finite-difference-based stabilization [206, 207] for approximating the quasiconvex energy hull and

identifying energy-minimizing microstructural patterns. Since the spectral treatment enforces periodic boundary conditions, the affine boundary conditions in (4.2) are replaced by periodic boundary conditions. This is admissible if the functional is non-negative, continuous and the energy density has bounded growth [3, 12]. Thus, we compute periodic microstructures instead of forcing the perturbation field to vanish on the RVE's boundary $\partial\omega$, i.e., we numerically approximate the quasiconvex hull defined by

$$QW(\nabla\varphi) = \inf \left\{ \frac{1}{|\omega|} \int_{\omega} W(\nabla\varphi + \nabla\phi) \, dV \mid \phi : \phi(X^+) = \phi(X^-) \text{ on } \partial\omega \right\} \quad (4.6)$$

where X^{\pm} implies a pair of periodically matching points on opposite faces (or, in 2D, edges) of the boundary of a fixed-size RVE ω . As demonstrated by Vidyasagar [205], this approach admits simulations of high resolution due to low computational costs and ease of parallelization. The spectral scheme also introduces a relative length scale that is beneficial in realizing physically relevant microstructures [205]. The latter is particularly useful for phase transformations, whose multi-welled energy landscape results in geometrically complex microstructural patterns (see e.g. Bhattacharya [26] and references therein for experimental evidence). Despite the impressive high-resolution of the predicted microstructures, this approach, however, performs poorly in numerical relaxation of energy at the RVE level, as demonstrated in the examples of [205].

With those shortcomings in mind, we use the *meshfree maximum-entropy (max-ent) approximants* as a new numerical avenue to simulate the RVE problem. The meshfree discretization, though coming with higher computational costs, avoids the disadvantageous impact of element size and shape on solutions found by FE interpolants. The specific max-ent approximants are further least biased by the nodal locations. This overall avoids spurious artifacts of the discretization with regards to the simulated microstructural features. Here, we employ the enhanced version of local max-ent based meshfree method for stable quasi-static simulations in total and updated Lagrangian settings, proposed in Chapter 2. The asymptotic computational cost of max-ent is the same as in FEM and hence suffers from a similar computational limitation in terms of predicting high-resolution microstructures. However, as will be shown in Sections 4.4 and 4.5, the non-local nature of max-ent is superior at approximating the quasiconvex hull even at low resolution compared to the spectral approach and FEM.

The remainder of this contribution is organized as follows. Section 4.2 describes

the numerical relaxation challenge. The FEM and finite-difference-improved FFT spectral formulations are outlined in Sections 4.3.1 and 4.3.2, respectively, followed by the max-ent approach in Section 4.3.3. We then compare the FFT, FEM, and max-ent approaches. Section 4.4 studies a hyperelastic St. Venant-Kirchhoff solid as a first benchmark. Next, Section 4.5 summarizes results for double- and multi-phase solid-solid transformations. In Section 4.6, we discuss the importance of microstructural interfaces and the underlying spatial discretization by the aid of numerical and analytical examples; and we provide insight into the numerical limitations and convergence properties of the numerical schemes. Finally, Section 2.4 concludes our study.

4.2 Numerical energy relaxation and pattern prediction

In order to approximate the quasiconvex hull in (4.6), we solve a periodic BVP on an RVE ω whose discretization is denoted by ω_h . Specifically, we aim to calculate an numerical approximation of the quasiconvex hull defined by

$$NW(\nabla\boldsymbol{\varphi}) = \inf \left\{ \frac{1}{|\omega_h|} \int_{\omega_h} W(\nabla\boldsymbol{\varphi} + \nabla\boldsymbol{\phi}_h) \, dV \mid \boldsymbol{\phi}_h : \boldsymbol{\phi}_h(\mathbf{X}^+) = \boldsymbol{\phi}_h(\mathbf{X}^-) \text{ on } \partial\omega_h \right\}, \quad (4.7)$$

where $\boldsymbol{\phi}_h$ is a perturbation field whose discretization depends on the chosen numerical scheme. Since we are only concerned with homogeneous media in our examples (and not materials with pre-existing microstructure), the size of the RVE ω_h is, in principle, irrelevant and only enters through the spatial resolution of the numerical discretization.

We note that the above can be extended to inelastic material models or, generally, material models with a set of local internal variables denoted by $\boldsymbol{z} : \Omega \rightarrow \mathbb{R}^q$ (with some $q \geq 0$) such that $W = W(\nabla\boldsymbol{\varphi}, \boldsymbol{z})$. In such cases, we assume that an effective energy functional $W^* = W^*(\nabla\boldsymbol{\varphi})$ exists, in which the internal variables are condensed out either by energy minimization or by solving an incremental evolution equation, e.g., by invoking variational constitutive updates [169]. Here and in the following, we simply write $W^*(\nabla\boldsymbol{\varphi})$ and assume that W^* is either the elastic energy density (see the hyperelastic examples in Section 4.4) or a condensed effective energy density (see the phase transformation examples in Section 4.5).

We aim to compute the energy density (4.7) by numerically finding $\boldsymbol{\phi}_h : \omega_h \rightarrow \mathbb{R}^d$ such that

$$\boldsymbol{\phi}_h = \arg \min \left\{ \int_{\omega_h} W(\nabla\boldsymbol{\varphi} + \nabla\boldsymbol{\phi}_h) \, dV \mid \boldsymbol{\phi}_h(\mathbf{X}^+) = \boldsymbol{\phi}_h(\mathbf{X}^-) \text{ on } \partial\omega_h \right\}. \quad (4.8)$$

Minimization of the energy functional is equivalent to solving the quasistatic conservation of linear momentum over the RVE ω_h , viz.

$$\text{Div } \mathbf{P}(\mathbf{X}) = \mathbf{0} \quad \text{in } \omega \quad \text{with} \quad \mathbf{P}(\mathbf{X}) = \frac{\partial W}{\partial \nabla \boldsymbol{\varphi}}(\nabla \boldsymbol{\varphi} + \nabla \boldsymbol{\phi}_h(\mathbf{X})), \quad (4.9)$$

where \mathbf{P} represents the first Piola-Kirchhoff stress tensor.

Following classical first-order homogenization [122, 153], we apply periodic boundary conditions on the boundary of an RVE ω_h while imposing an average deformation gradient $\mathbf{F}^0 = \nabla \boldsymbol{\varphi}$. To this end, we constrain any point on the boundary $\partial\omega_h$ to deform according to

$$\begin{aligned} \mathbf{x} &= \mathbf{F}^0 \mathbf{X} + \boldsymbol{\phi}_h(\mathbf{X}) \quad \text{with} \quad \boldsymbol{\phi}_h(\mathbf{X}^+) = \boldsymbol{\phi}_h(\mathbf{X}^-) \\ \text{s.t.} \quad \mathbf{x}^+ - \mathbf{x}^- &= \mathbf{F}^0(\mathbf{X}^+ - \mathbf{X}^-) \quad \text{on } \partial\omega_h, \end{aligned} \quad (4.10)$$

where \mathbf{x}^\pm and \mathbf{X}^\pm are, respectively, deformed and undeformed positions of periodically matching points on opposite surfaces of the RVE. Importantly, our simulations reveal not only the energy density NW but also the associated microstructures emerging as the minimizing fields $\boldsymbol{\phi}_h(\mathbf{X})$ within the RVE ω_h . In order to solve the above RVE-level periodic BVP, we must define a spatial discretization scheme, for which we choose the finite element method (FEM), a Fourier-based spectral formulation (FFT), and a meshfree maximum-entropy (max-ent) approximation. Those will be outlined in the following sections.

For completeness, we point out that from the numerically computed approximate quasiconvex hull $NW(\nabla \boldsymbol{\varphi})$, one may also extract the effective stress–strain response. For example, the effective first Piola-Kirchhoff stress tensor is given by

$$\mathbf{P} = \frac{\partial NW}{\partial \nabla \boldsymbol{\varphi}}(\nabla \boldsymbol{\varphi}), \quad (4.11)$$

and in case of inelasticity the incremental formulation is used. Alternatively, the above definitions admit the calculation of \mathbf{P} as the average stress across the RVE.

4.3 Numerical solution schemes

4.3.1 Finite element solution scheme

We use a regular discretization of the RVE into equal-sized simplicial tetragonal (constant-strain) elements with linear interpolation and a single quadrature point per element. Since no microstructural features are known a priori in general, a regular grid is chosen as the best option. Spatial resolution and number of elements vary and will be indicated for each of the benchmark examples in subsequent sections.

We solve the classical Galerkin form of the underlying variational problem, and we solve the nonlinear system of the equations of equilibrium by an iterative Newton-Raphson solver. The FE discretization is the simplest numerical choice, which has traditionally been used for the purpose of numerical energy relaxation at the RVE-level; see, e.g., Bartels et al. [16], Carstensen and Plecháč [41]. However, FEM comes with significant disadvantages since (i) the element shape and orientation may bias (or even prevent) the formation of microstructural patterns not aligned with the mesh, (ii) fine microstructures require high computational costs stemming from significant mesh refinement (especially the application of periodic boundary conditions destroys the beneficial bandedness of system matrices), (iii) Newton-Raphson solvers are prone to fail to convergence when dealing with nonconvex problems where the stiffness matrix loses positive-definiteness.

4.3.2 Spectral solution scheme

We adopt the spectral framework outlined in Vidyasagar et al. [207], which is why we here review the concepts only briefly to the extent required for the following discussions. Following Moulinec and Suquet [159, 160] and [130], we introduce the deformation gradient $\mathbf{F}(\mathbf{X}) = \nabla\varphi(\mathbf{X})$ and the perturbation stress tensor $\boldsymbol{\tau}(\mathbf{X})$ such that

$$P_{iJ}(\mathbf{X}) = \mathbb{C}_{iJkL}^0 F_{kL}(\mathbf{X}) - \tau_{kL}(\mathbf{X}) \quad \text{in } \omega_h \quad (4.12)$$

with a reference modulus tensor \mathbb{C}^0 which is taken, e.g., as the average

$$\mathbb{C}_{iJkL}^0 = \frac{1}{|\omega_h|} \int_{\omega_h} \mathbb{C}_{iJkL}(\mathbf{X}) \, dV, \quad \mathbb{C}_{iJkL}(\mathbf{X}) = \frac{\partial^2 W}{\partial F_{iJ} \partial F_{kL}}(\mathbf{X}). \quad (4.13)$$

It is important that the obtained solution is independent of the specific choice of the reference modulus tensor \mathbb{C}^0 (it does affect the convergence properties but not the final solution). This implies that a non-positive-definite modulus tensor \mathbb{C}^0 (arising frequently in nonconvex problems) can be replaced by that of an approximate convex energy, which renders the numerical method stable. This will be exploited in our numerical examples and is a significant advantage over, e.g., FE formulations whose Newton-Raphson solver requires \mathbb{C}^0 to be strongly elliptic at all times for convergence.

Insertion of (4.12) into (4.9) and applying a discrete (inverse) Fourier transform, translates the system of ODEs into an algebraic system of equations in Fourier space. Specifically, we discretize the RVE into a regular grid with uniform spacing ΔX in each direction, so that the solution in Fourier space is expressed in terms of the

coefficients in \mathbf{K} -space with discrete \mathbf{K} -vectors $\mathcal{T} = \{\mathbf{K}_1, \dots, \mathbf{K}_n\}$ of the reciprocal grid. For details see, e.g., Vidyasagar et al. [206, 207]. In Fourier space, the system is algebraic and can be solved for the deformation gradient in Fourier space, leading to

$$\hat{F}_{kL}(\mathbf{K}) = \begin{cases} \hat{\mathbb{A}}_{ik}^{-1}(\mathbf{K}) \hat{\tau}_{iJ}(\mathbf{K}) K_J K_L & \text{for } \mathbf{K} \neq \mathbf{0}, \\ F_{kL}^0 & \text{for } \mathbf{K} = \mathbf{0}, \end{cases} \quad (4.14)$$

where $\hat{\mathbb{A}}_{ik}(\mathbf{K}) = \mathbb{C}_{ijkl}^0 K_J K_L$ is the acoustic tensor, and $\hat{\cdot} = \mathcal{F}(\cdot)$ denotes a quantity transformed into Fourier space. Note that $\tau(\mathbf{X})$ depends on $\mathbf{F}(\mathbf{X})$, so that an iterative solver is required; here, we resort to (inefficient but stable and simple) fixed-point iteration. Therefore, this spectral scheme does not require an assembly or inversion of a global stiffness matrix as opposed to FEM. Hence, the number of degrees of freedom that can be simulated scales quite efficiently compared to FE simulations. This is beneficial for capturing high-resolution microstructures by the spectral scheme, which is not realistically possible with other solution schemes due to limited computational resources.

To avoid numerical ringing artifacts typically produced by truncated Fourier series and the associated Gibbs phenomena [85, 86, 99], we employ a discrete spectral differentiation with a finite difference-based scheme [129, 161, 210]. By applying an 8th-order central-difference approximation to all spatial derivatives before the Fourier transform (with $h = 2\pi$, based on the definition of the Fourier kernel), we obtain the approximation [206]

$$\mathcal{F}\left(\frac{\partial f}{\partial X_i}\right) \approx -i \left[\frac{8 \sin(hK_i \Delta X)}{5\Delta X} - 2 \frac{\sin(2hK_i \Delta X)}{5\Delta X} + 8 \frac{\sin(3hK_i \Delta X)}{105\Delta X} - \frac{\sin(4hK_i \Delta X)}{140\Delta X} \right] \mathcal{F}(f), \quad (4.15)$$

which converges to the exact derivative with decreasing grid size ($\Delta X \rightarrow 0$). For optimal performance, these approximated wave vectors are used in the scheme for the calculation of deformation gradients but not in the calculation of the acoustic tensor.

Without the existence of an intrinsic length scale, microstructural patterns are infinitely fine, implying that in fact infimizing sequences, or Young measures [114], are the solution of the non-quasiconvex variational problem, and the associated energy is approached in the limit but not attained [64]. If a length scale exists as, e.g., in strain-gradient plasticity, then laminate-type constructions have proven

useful [6]. It was shown by [207] that the above finite-difference approximation of the Fourier discretization introduces an intrinsic, numerical length scale. It thus establishes nonlocality since the energy density is transformed into the nonlocal form $W \approx W(\nabla\boldsymbol{\varphi}) + W^h(\nabla^m\boldsymbol{\varphi})$ where integer $m \geq 2$ is controlled by the order of the finite-difference approximation (e.g., $m = 8$ for the above 8th-order central-difference approximation). Specifically, we may express the actual energy density when the simulation uses the finite-difference approximation as [207]

$$W(\nabla\boldsymbol{\varphi}) \rightarrow W(\nabla\boldsymbol{\varphi}) + \frac{(\Delta X)^m}{(m+1)!} \frac{\partial W}{\partial \varphi_{i,J}}(\nabla\boldsymbol{\varphi}) \frac{\partial^{(m+1)}\varphi_i}{\partial X_J^{m+1}} \equiv W(\nabla\boldsymbol{\varphi}) + W^h(\nabla^{m+1}\boldsymbol{\varphi}). \quad (4.16)$$

Since $W^h(\nabla^{m+1}\boldsymbol{\varphi})$ scales as $(\Delta X)^m$, the nonlocal energy contribution W^h decays with decreasing grid spacing ΔX . This has two important consequences. On the one hand, it shows consistency of the scheme as $\Delta X \rightarrow 0$. On the other hand, it introduces a length scale that is relative with respect to the RVE size. For a cubic RVE of side length L represented by N^3 grid points, we have $\Delta X = L/(N-1)$. Thus, ΔX is relative to the RVE size, which has the benefit that diffuse interfaces maintain their width irrespective of the absolute RVE size (i.e., microstructural patterns will be independent of the absolute size/discretization of ω_h), and no further numerical regularization is required.

In summary, the finite-difference-improved Fourier scheme outlined above comes with high efficiency and enables high-resolution microstructure prediction at low computational costs (with the added benefit of not requiring a positive-definite incremental average tangent stiffness), while introducing a numerical interface energy for stable diffuse microstructural interfaces.

4.3.3 Max-ent solution scheme

In order to solve the RVE problem, we adopt the quasistatic, total-Lagrangian formulation presented in Section 2.2.2. While the updated-Lagrangian formulation allows simulation of large deformations, the loss of convexity in the energetic potential implies that the incremental stiffness matrix loses positive definiteness, posing numerical challenges. Hence, for the scope of this chapter, we restrict ourselves to only total Lagrangian formulation. Since total-Lagrangian kernels are free from tensile instability [24], and under the assumption that the spatial discretization of the cubic RVE is uniform, anisotropic shape function supports are not needed. Therefore, for simplicity, we employ the original local maximum-entropy shape functions (with scalar locality parameter β) introduced by Arroyo and

Ortiz [7]. A brief review is also presented in Sections 1.4 and 2.2. In summary, we solve the classical Galerkin problem using local max-ent shape functions (as opposed to the piecewise-polynomial FE interpolation) in a total-Lagrangian setting.

The locality parameter β also introduces an implicit length scale relative to the RVE size, which is important when simulating microstructural interfaces. A dimensionless locality parameter is defined as $\gamma = \beta(\Delta X)^2$, so that fixing γ and varying β based on the nodal spacing ΔX for a uniform grid results in self-similar shape functions. In the small- β -regime, the shape functions decay as $\exp\left(-\beta\|\mathbf{X} - \mathbf{X}^a\|^2\right)$ (see (2.10)), and hence the length scale is proportional to $\beta^{-1/2} = \gamma^{-1/2}\Delta X$. In the limit $\beta \rightarrow +\infty$ (where the shape functions converge to simplicial interpolants), the length scale also converges to ΔX . Thus, similar to the FE and FFT schemes, the max-ent scheme maintains the interfacial width and the resulting microstructural patterns irrespective of the RVE size.

All max-ent simulations in subsequent sections follow the same protocol. An auxiliary, structured mesh of tetrahedral elements is created within the RVE. Next, a material point p is created at the barycenter of each tetrahedron with volume V^p equal to that of the containing tetrahedron. Each material point is assigned the locality parameter $\beta = \gamma(\Delta X)^{-2}$, where ΔX is the nodal spacing, and γ is a chosen scalar parameter. Finally, the mesh is discarded while retaining all nodes. Ideally, the meshfree nature of the shape functions provides them with global support. However, the shape functions decay exponentially with relative distance, in particular, as $\exp(-\beta\|\mathbf{X} - \mathbf{X}^a\|^2)$ in (2.10). Hence, for the sake of computational efficiency, only nodes that lie within a cut-off sphere centered around each material point are considered for the approximation. Following the discussion in Section 2.2.4, the radius of the cut-off sphere is given by $R_{cut} = \sqrt{-\log(\epsilon)/\beta}$, beyond which the shape functions are truncated (ϵ is a tolerance chosen here as 10^{-6}). Since, the auxiliary mesh is uniform, β and R_{cut} are also uniform across all material points. For more implementation details, the reader is referred to the algorithms in Appendix 2.B.

When compared to the FEM and FFT schemes, the max-ent approach is the computationally most expensive and scales with system size in a comparable fashion as FEM (solving the linear system is as expensive as with FEM, plus minor added costs of shape function calculations). It therefore does not admit high-resolution simulations of realistic microstructures (like FFT). As we will show below, however, the fact that max-ent is least biased by the node set (unlike FEM and FFT) is an essential advantage when it comes to predicting energy-minimizing microstructures.

4.3.4 Comparison of FEM, FFT and max-ent

The following sections present comparative studies of the three numerical methods – FEM, FFT and max-ent – when applied to RVEs whose material is described by (elastic) nonconvex potentials. Our focus is on both relaxing the nonconvex energetic potentials and identifying the associated microstructures. We choose the representative examples from hyperelasticity and phase transformations proposed by Vidyasagar [205] who studied performance of the FFT scheme only. A brief review of each problem is presented here; for details of the corresponding material models, interested reader is referred to [205]. For each problem, we set up homogeneous RVEs to be treated by the three methods outlined above. Parameterized by the average deformation gradient, we specify a loading path (such that it leads to a loss of quasiconvexity in the energy) and determine the (relaxed) RVE energy and associated patterns numerically during one cycle of loading, i.e., we first load the RVE by increasing the deformation and then unload the RVE by decreasing the deformation back to zero. This way, each average deformation gradient is imposed twice. Since our examples involve pure energy minimization without history dependence, we choose as the relaxed energy whichever energy for a given deformation gradient (resulting from either loading or and unloading) is lower. For each load step, we use as the initial guess of the Newton-Raphson solver the previous solution with added random perturbations of the order 10^{-6} (in order to promote the formation of microstructures).

We stress that finding the global minimum, i.e., the energy-minimizing deformation, is a computationally NP-hard problem due to nonconvexity and due to the presence of very many local minima. Furthermore, convergence in nonconvex optimization problems is highly dependent on the initial guess. While it is possible to artificially construct a good initial guess based on prior knowledge of a minimum-energy microstructure (such as that obtained from recursive lamination) and then accurately reproduce that solution, such an approach does not apply to general problems and is not pursued here. The subsequent simulations instead use random perturbations to initiate microstructure formation. Hence, we are interested in the robustness and general applicability of the numerical methods presented here to approximate the quasiconvex hull and/or to find physically relevant microstructures. This may lead to significant differences between the numerically found relaxed energy density and the actual quasiconvex hull.

4.4 Example 1: hyperelastic St. Venant-Kirchhoff solid

The St. Venant-Kirchhoff hyperelastic model serves as a good benchmark, owing to the availability of an analytical solution for the quasiconvex hull. The energy density reads

$$W(\mathbf{F}) = \frac{1}{8}(\mathbf{F}^T \mathbf{F} - \mathbf{I}) \cdot \mathbb{C}(\mathbf{F}^T \mathbf{F} - \mathbf{I}), \quad (4.17)$$

which is a simple hyperelastic extension of linear elasticity. The isotropic elastic modulus tensor is given by

$$\mathbb{C}_{IJKL} = \lambda \delta_{IJ} \delta_{KL} + \mu (\delta_{IK} \delta_{JL} + \delta_{IL} \delta_{JK}), \quad \lambda, \mu > 0 \quad (4.18)$$

where λ and μ denote the Lamé moduli. The lack of quasiconvexity arises when loading the material, e.g., under combined compression and simple shear, parameterized by the applied average deformation gradient

$$\mathbf{F}^0 = \begin{pmatrix} 1 - \gamma & -2\gamma & 0 \\ 0 & 1 & 0 \\ 0 & 0 & 1 \end{pmatrix}, \quad 0 < \gamma < 1. \quad (4.19)$$

We note that this example is a mathematical one and not a physical one, since the nonconvexity of the energy density and the resulting formation of microstructure has little relevance for actual materials, but is rather a shortcoming of the hyperelastic energy density (which, unfortunately, is still quite popular in the mechanics of materials modeling literature¹). However, the availability of analytical quasiconvex and semi-analytical rank-one-convex hulls makes this a useful benchmark example. The analytical quasiconvex hull $QW(\mathbf{F})$ [128] is given by

$$\begin{aligned} QW(\mathbf{F}) = & \frac{E}{8} [\chi_3^2 - 1]_+^2 + \frac{E}{8(1 - \nu^2)} [\chi_2^2 + \nu \chi_3^2 - (1 + \nu)]_+^2 \\ & + \frac{E}{8(1 - \nu^2)(1 - 2\nu)} [(1 - \nu)\chi_1^2 + \nu(\chi_2^2 + \chi_3^2) - (1 + \nu)]_+^2, \end{aligned} \quad (4.20)$$

where $[\cdot]_+ = \max(\cdot, 0)$, further χ_1, χ_2, χ_3 (arranged in increasing order) are the singular values of \mathbf{F} , and

$$E = \frac{\mu(3\lambda + 2\mu)}{\lambda + \mu}, \quad \nu = \frac{\lambda}{2(\lambda + \mu)}. \quad (4.21)$$

¹The St. Venant-Kirchhoff model is particularly popular, e.g., in modeling finite-strain plasticity, since it provides a simple extension of linear elasticity to finite strains along with the simple adoption of small-strain elastic moduli. The fact that this model shows non(quasi-)convexity for certain loading paths, however, is problematic because – if simulations predict the formation of microstructures or patterns – it is unclear whether those have formed for physical reasons or as artifacts of the non(quasi-)convex energy density. Polyconvex energy densities are therefore a more suitable choice.

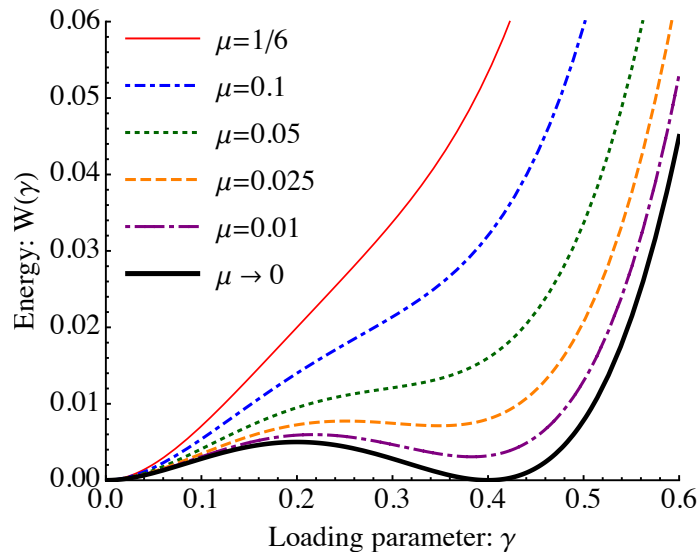


Figure 4.1: Loss of convexity of the normalized energy $W(\gamma) = W(\mathbf{F}^0)/\lambda$ as the modulus ratio μ/λ decreases.

As an upper bound of $QW(\mathbf{F}^0)$, we may compute $RW_k(\mathbf{F}^0)$ from (4.4) for any k by numerical sequential lamination.

The strain energy density (4.17) for the applied average deformation gradient (4.19) becomes

$$W(\mathbf{F}^0) = \frac{1}{8}\gamma^2 \left[2 \left(25\gamma^2 - 20\gamma + 12 \right) \mu + (2 - 5\gamma)^2 \lambda \right]. \quad (4.22)$$

which loses convexity if the Lamé moduli are chosen such that

$$0 < \frac{\mu}{\lambda} < \frac{1}{6}. \quad (4.23)$$

This is illustrated in Figure 4.1, where decreasing the ratio of μ/λ below $1/6$ results in increasing nonconvexity of the energy landscape $W(\mathbf{F}^0)$. We note that, in the limit $\mu \rightarrow 0$, $RW(\mathbf{F}^0) = RW_1(\mathbf{F}^0) = QW(\mathbf{F}^0)$ for $\gamma > 0$, i.e., the quasiconvex hull is attained by a first-order laminate.

We proceed to use the three numerical schemes outlined in Sections 4.3.1, 4.3.2, and 4.3.3 to compute the minimum RVE energy (as an approximation of the relaxed energy density) and the associated microstructures for the **two cases** (i) $\mu/\lambda = 10^{-5}$ and (ii) $\mu/\lambda = 0.01$, so that the two minima of the nonconvex unrelaxed energy $W(\gamma)$ are (almost) symmetric and asymmetric, respectively. The RVE is subjected to the average deformation gradient defined in (4.19).

FE simulations, unfortunately, failed to converge for almost all values of the loading parameters and elastic moduli, so that results cannot be presented for this benchmark

and are omitted in the comparison. For the spectral scheme, the RVE is discretized into 128^3 nodes, and the 8th-order central-difference stencil presented of (4.15) is applied in the FFT solution scheme. Finally, max-ent simulations are performed with 20^3 nodes within the RVE, using $\beta = 0.5(\Delta X)^{-2}$, where ΔX is the nodal spacing.

For **case (i)**, Figure 4.2 shows the numerical results for the relaxed energy density in comparison with the analytical quasiconvex and rank-one-convex hulls. After initially deforming homogeneously (thus reproducing the unrelaxed nonconvex energy density), the RVE forms domains to allow the numerically computed relaxed energy density to approach the quasiconvex hull. The initial phase of increasing energy is much more pronounced for the FFT scheme. Once microstructure has formed, the computed relaxed energy density agrees well with the analytical quasiconvex hull. This is especially the case for the max-ent scheme, which shows perfect agreement, whereas the FFT scheme – though producing beautiful high-resolution microstructures – tends to frequently approach higher energy levels particularly for $\gamma > 0.2$. Shown as insets are also specific RVE microstructures at three different strain levels as obtained from the max-ent and FFT schemes.

For **case (ii)** with an asymmetric potential, the rank-one-convex hull no longer coincides with the quasiconvex hull, as seen in Figure 4.3a. Here, the FFT and max-ent schemes perform quite differently. While the FFT prediction of the relaxed energy is even above the rank-one-convex hull (and thus significantly above the quasiconvex hull), the max-ent prediction is lower than the rank-one-convex hull and reasonably close to quasiconvex hull. Further, the max-ent solution converges towards the quasiconvex hull with h -refinement, as indicated by the convergence plot in Figure 4.3b. The computational expenses associated with max-ent (see the discussion in Sections 4.3.3 and 4.3.4) prevents higher resolution.

In summary, the St. Venant-Kirchhoff benchmark revealed that max-ent is best at approximating the quasiconvex hull by the numerically relaxed RVE energy, while the FFT scheme consistently overpredicts the quasiconvex hull, and the FEM scheme fails to converge for this nonconvex problem.

4.5 Example 2: phase transformations

4.5.1 A simple energetic model for phase transformations

We briefly review the phase transformation model introduced by Vidyasagar [205]. Phase transformations are classically described using multi-welled potential energy

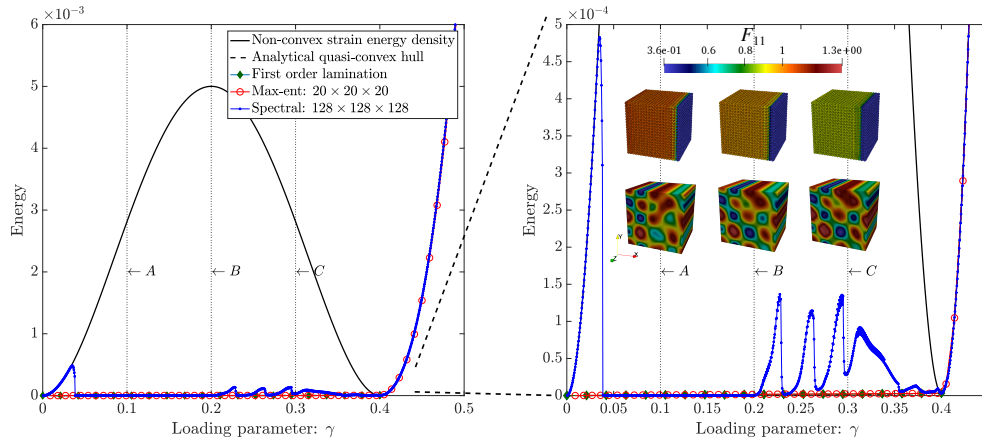


Figure 4.2: Relaxed energy densities computed by the FFT and max-ent schemes along with the analytical quasiconvex hull and the rank-one-convex hull (obtained from lamination) for **case (i)**: $\mu/\lambda = 10^{-5}$. The insets show energy-minimizing microstructural patterns predicted by the max-ent (top row) and FFT (bottom row) schemes at applied strain levels of $\gamma = 0.1, 0.2$, and 0.3 (indicated as A, B, and C, respectively). Microstructural patterns are visualized by plotting the deformation gradient component F_{11} .

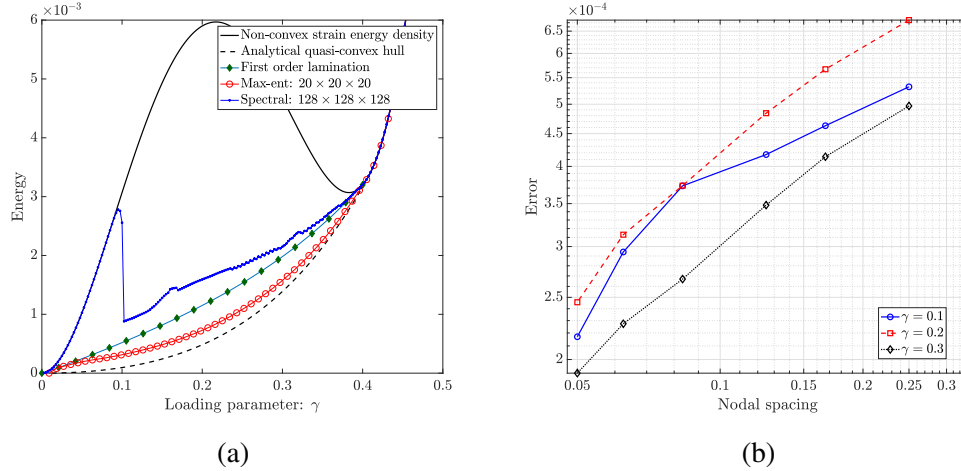


Figure 4.3: (a) Relaxed energy densities computed by the FFT and max-ent schemes along with the analytical quasiconvex hull and the rank-one-convex hull (obtained from lamination) for **case (ii)**: $\mu/\lambda = 0.01$. (b) Convergence of the relaxed energy with h -refinement, computed by max-ent at different strain levels γ . Here, the error is defined as the difference between the numerically computed relaxed RVE energy density and the analytical quasiconvex energy at the three strain levels indicated by γ .

landscapes that arise from a competition between multiple stable phases. We consider a total of q phases, where each phase $\alpha \in \{1, \dots, q\}$ is associated with a transformation strain \mathbf{U}_α and a chemical energy Ψ_α . The deformation gradient in phase α is given by $\mathbf{F}(\mathbf{X}) = \mathbf{F}_e(\mathbf{X})\mathbf{U}_\alpha(\mathbf{X})$, where $\mathbf{F}_e \in GL_+(d)$ denotes the elastic contribution to the deformation gradient and accounts for both rotations and elastic deformations. The effective Helmholtz free energy density W at a material point [11, 89] is defined as

$$W(\mathbf{F}) = \min_{\alpha=1, \dots, q} \left\{ W_\alpha(\mathbf{F}) \right\}, \quad (4.24)$$

with

$$W_\alpha(\mathbf{F}) = W_e(\mathbf{F}\mathbf{U}_\alpha^{-1}) + \Psi_\alpha, \quad \forall \alpha = 1, \dots, q. \quad (4.25)$$

Depending on the choice of the transformation strains and the loading path, $W(\mathbf{F})$ loses quasiconvexity.

In spite of the mathematical simplicity, $W(\mathbf{F})$ from (4.24) is not continuously differentiable, which leads to discontinuity in stresses and poses a challenge for numerical computations. To overcome this numerical issue, a Taylor-type approximation is introduced wherein multiple phases coexist, with volume fractions given by

$$\boldsymbol{\lambda} = \{\lambda_\alpha \in [0, 1], \alpha = 1, \dots, q\}, \quad (4.26)$$

such that the sum of all volume fractions equals unity. Without enforcing compatibility between phases, the free energy density in (4.24) is redefined as

$$W(\mathbf{F}, \boldsymbol{\lambda}) = \sum_{\alpha=1}^q \lambda_\alpha W_\alpha(\mathbf{F}). \quad (4.27)$$

In order to penalize the formation of mixtures that strongly deviate from a single-phase state, a configurational (not physical) entropy based regularization

$$S(\boldsymbol{\lambda}) = - \sum_{\alpha=1}^q k_T \lambda_\alpha \log \lambda_\alpha, \quad k_T > 0, \quad (4.28)$$

is introduced such that the regularized free energy density is given by

$$F(\mathbf{F}, \boldsymbol{\lambda}) = W(\mathbf{F}, \boldsymbol{\lambda}) - S(\boldsymbol{\lambda}) \quad (4.29)$$

In this model, k_T can be used as a tuning parameter that governs the influence of the configurational entropy and hence of the penalization of phase mixtures. Finally, the

regularized free energy $F(\mathbf{F}, \boldsymbol{\lambda})$ is minimized with respect to $\boldsymbol{\lambda}$ to yield the optimal volume fractions

$$\lambda^*(\mathbf{F}) = \arg \min_{0 \leq \lambda_\alpha, \sum_{\alpha=1}^q \lambda_\alpha = 1} F(\mathbf{F}, \boldsymbol{\lambda}) \Rightarrow \lambda_\alpha^*(\mathbf{F}) = \frac{\exp\left(-\frac{W_\alpha(\mathbf{F})}{k_T}\right)}{\sum_{\beta=1}^q \exp\left(-\frac{W_\beta(\mathbf{F})}{k_T}\right)}, \quad (4.30)$$

and the condensed energy density

$$F^*(\mathbf{F}) = F(\mathbf{F}, \lambda^*(\mathbf{F})) = -k_T \log \left[\sum_{\alpha=1}^q \exp\left(-\frac{W_\alpha(\mathbf{F})}{k_T}\right) \right]. \quad (4.31)$$

For $k_T > 0$, (4.31) provides a lower bound to the energy (4.24) and only approximates the latter. Importantly, that approximate formulation uniquely defines continuously differentiable stresses and tangent matrices for all deformation gradients. The first Piola-Kirchhoff stress tensor is given by

$$\mathbf{P}^* = \frac{dF^*}{d\mathbf{F}} = \sum_{\alpha=1}^q \lambda_\alpha^* \frac{\partial W_\alpha}{\partial \mathbf{F}}(\mathbf{F}) = \sum_{\alpha=1}^q \lambda_\alpha^* \mathbf{P}(\mathbf{F} \mathbf{U}_\alpha^{-1}) \mathbf{U}_\alpha^{-T}, \quad (4.32)$$

and the incremental stiffness tensor (in the summation convention) by

$$\begin{aligned} \mathbb{C}_{ijkl}^* &= \frac{dP_{iJ}^*}{dF_{kL}} = \sum_{\alpha=1}^n \lambda_\alpha^* \mathbb{C}_{iMkN}(\mathbf{F} \mathbf{U}_\alpha^{-1}) U_{\alpha, JM}^{-1} U_{\alpha, LN}^{-1} \\ &\quad + \frac{1}{k_T} \sum_{\alpha=1}^n \sum_{\gamma \neq \alpha} \lambda_\alpha^* \lambda_\gamma^* P_{iM}(\mathbf{F} \mathbf{U}_\alpha^{-1}) U_{\alpha, JM}^{-1} P_{kN}(\mathbf{F} \mathbf{U}_\gamma^{-1}) U_{\gamma, LN}^{-1}. \end{aligned} \quad (4.33)$$

For more details, see derivations by Vidyasagar [205] and Tan and Kochmann [198].

In the limit $k_T \rightarrow 0$, (4.30) reduces to

$$\lim_{k_T \rightarrow 0} \lambda_\alpha^*(\mathbf{F}) = \begin{cases} 1 & \text{if } W_\alpha(\mathbf{F}) < W_\beta(\mathbf{F}) \forall \beta \neq \alpha, \\ 0 & \text{if } \exists \beta \text{ s.t. } W_\alpha(\mathbf{F}) > W_\beta(\mathbf{F}), \\ 1/m & \text{if there are } m \text{ phases with equal } W_\alpha(\mathbf{F}) < W_\beta(\mathbf{F}) \\ & \text{for all } q - m \text{ other phases } \beta. \end{cases}, \quad (4.34)$$

and the free energy becomes

$$\lim_{k_T \rightarrow 0} F^*(\mathbf{F}) = \min_{\alpha=1, \dots, q} \{W_\alpha(\mathbf{F})\}. \quad (4.35)$$

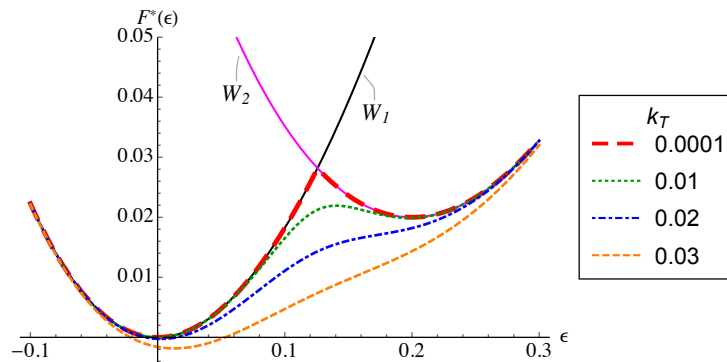


Figure 4.4: Plot of $F^*(\mathbf{F})$ from (4.31) for the deformation gradient defined by (4.38) with $\mu = 1$ and $\kappa = 3$ for various values of k_T .

That is, in the limit $k_T \rightarrow 0$, the Taylor-type model approaches the phase transformation model described by (4.24) with discontinuous stresses. For example, consider a two-phase potential characterized by

$$\mathbf{U}_1 = \mathbf{I}, \quad \mathbf{U}_2 = \begin{pmatrix} 1.2 & 0 & 0 \\ 0 & \frac{1}{1.2} & 0 \\ 0 & 0 & 1 \end{pmatrix}, \quad \Psi_1 = 0, \quad \Psi_2 = 0.02. \quad (4.36)$$

The elastic strain energy density W_e is given by that of a compressible Neo-Hookean solid

$$W_e(\mathbf{F}) = \frac{\mu}{2} \left(\frac{\text{tr}(\mathbf{F}^T \mathbf{F})}{J^{2/3}} - 3 \right) + \frac{\kappa}{2} (J - 1)^2, \quad (4.37)$$

where μ and κ are the shear and bulk moduli, respectively, and $J = \det \mathbf{F}$. The applied deformation gradient is parameterized by

$$\mathbf{F}^0 = \begin{pmatrix} 1 + \epsilon & 0 & 0 \\ 0 & \frac{1}{1 + \epsilon} & 0 \\ 0 & 0 & 1 \end{pmatrix}. \quad (4.38)$$

Figure 4.4 illustrates the dependence of the condensed energy density $F^*(\mathbf{F}^0)$ on the tuning parameter k_T , with $k_T \rightarrow 0$ showing agreement with (4.24).

For the purpose of following results, the condensed energy density $F^*(\mathbf{F})$ in (4.31) along with the stress (4.32) and stiffness tensors (4.33) are used in the numerical energy relaxation methods outlined in Section 4.3. All subsequent simulations use the Neo-Hookean energy density (4.37) with $\mu = 1$, $\kappa = 3$ for each phase, and $k_T = 0.01$ in (4.31). The RVE is subject to the applied average deformation gradient (4.38) for $\epsilon > 0$. FEM and max-ent simulations are performed at an RVE resolution of $16 \times 16 \times 16$ nodes; max-ent uses $\beta = 0.5(\Delta X)^{-2}$. For the spectral scheme, the RVE is discretized into $64 \times 64 \times 64$ grid points.

4.5.2 Results for a double-well potential

As a first example, we consider a double-well energy density defined by the transformation strains

$$\mathbf{U}_1 = \begin{pmatrix} 1 & 0 & 0 \\ 0 & 1 & 0 \\ 0 & 0 & 1 \end{pmatrix}, \quad \mathbf{U}_2 = \begin{pmatrix} 1.2 & 0 & 0 \\ 0 & \frac{1}{1.2} & 0 \\ 0 & 0 & 1 \end{pmatrix}. \quad (4.39)$$

We further consider the two cases of (i) $\Psi_1 = \Psi_2 = 0$ (equal chemical energies, i.e., identical well depths) and (ii) $\Psi_1 = 0$, $\Psi_2 = 4.5 \cdot 10^{-3}$ (i.e., the second phase has higher energy). Figures 4.5a and 4.5b show the numerically relaxed energy densities for the load path described by deformation gradient (4.38) with $0 \leq \epsilon \leq 0.25$, as predicted by the FEM, FFT and max-ent schemes. Figures 4.6a and 4.6b illustrate the evolving volume fraction of the second phase as the RVE transitions from a homogeneous state in the first phase (in the undeformed ground state at $\epsilon = 0$) to a homogeneous state in the second phase (at strains beyond the second energy well, i.e., for $\epsilon \geq 0.2$).

The microstructural patterns obtained for case (i) during the loading stage ($\dot{\epsilon} > 0$) are illustrated in Figure 4.7. The microstructures predicted by the FFT scheme (Figure 4.7b) indicate a complex strain and phase distribution, wherein needle-like second phase domains nucleate that do resemble laminates but show significantly higher complexity. By contrast, the max-ent scheme shows only simple and low-resolution laminate-type microstructures; yet the corresponding relaxed energy density is significantly lower and a better approximation than that from the FFT scheme (this is true for both sets of chemical energies). It is intriguing that FFT and max-ent both show similar evolutions of the second-phase volume fraction and that the laminate orientations are also identical, yet the FFT scheme forms highly detailed structures while max-ent predicts only a single (largest possible) lamellar pattern. For comparison, FEM also forms a laminate microstructure but becomes unstable and fails to converge, which we attribute to the combined effects of low-order interpolation and loss of convexity.

4.5.3 Results for three-well potentials

As a further example that probes the influence of multiple competing wells in the energy landscape, we consider a three-well problem with phases 1, 2 and 3 defined

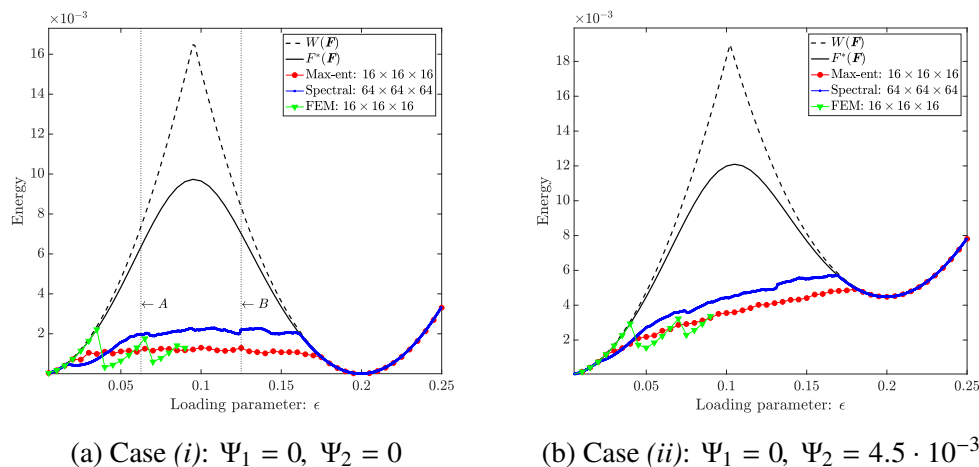


Figure 4.5: Numerically computed relaxed energy density for the phase transformation model with a double-well energy. The dotted line denotes the nonconvex energy potential $W(\mathbf{F}^0)$ obtained from (4.24), while the solid line denotes the corresponding smoothed potential $F^*(\mathbf{F}^0)$ obtained from (4.31). Shown are the three curves obtained from the FFT, max-ent, and FEM schemes (the latter failing to converge early on).

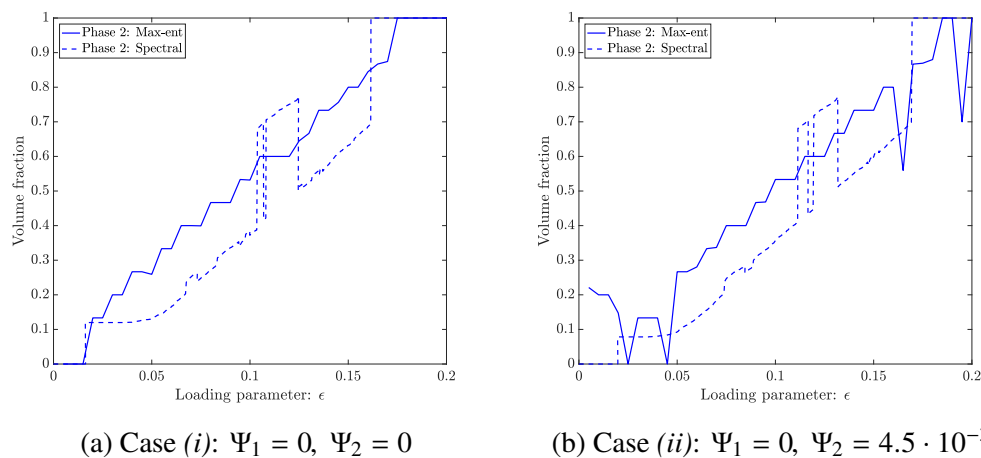


Figure 4.6: Average RVE volume fraction of the second phase corresponding to the numerically computed relaxed energies shown in Fig. 4.5, using the phase transformation model with a double-well energy.

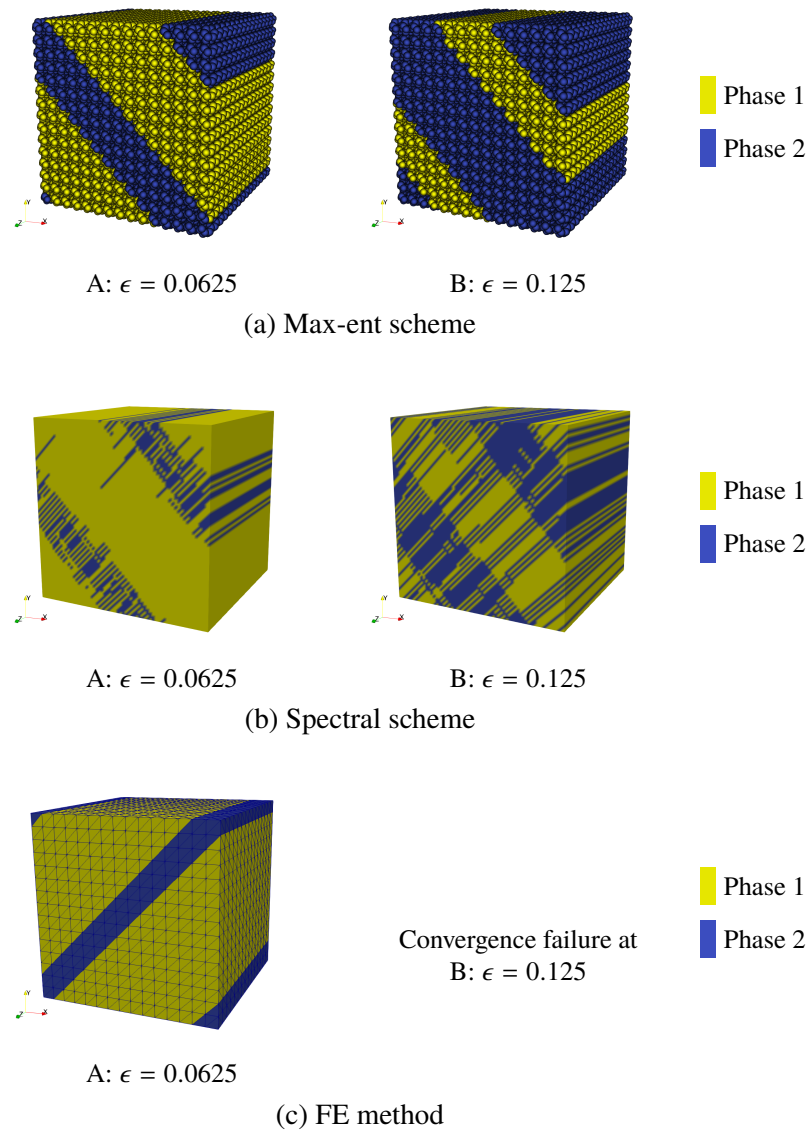


Figure 4.7: Microstructural patterns, color-coded by the dominant phase at each material point in the RVE, obtained numerically from energy relaxation using (a) the max-ent scheme, (b) the FFT scheme, and (c) the FEM scheme for case (i) with $\Psi_1 = 0$, $\Psi_2 = 0$. The two strain levels are indicated in Fig. 4.5, where the corresponding relaxed energy densities are shown. Here, the dominant phase is defined as the phase with higher volume fraction at a given material point.

by the respective transformation strains

$$\mathbf{U}_1 = \begin{pmatrix} 1 & 0 & 0 \\ 0 & 1 & 0 \\ 0 & 0 & 1 \end{pmatrix}, \quad \mathbf{U}_2 = \begin{pmatrix} 1.2 & 0 & 0 \\ 0 & \frac{1}{1.2} & 0 \\ 0 & 0 & 1 \end{pmatrix}, \quad \mathbf{U}_3 = \begin{pmatrix} 1.4 & 0 & 0 \\ 0 & \frac{1}{1.4} & 0 \\ 0 & 0 & 1 \end{pmatrix}. \quad (4.40)$$

We again consider two cases: case (i) assumes the three energy wells having increasing energy levels at the three local minima, using

$$(i) \quad \Psi_1 = 0, \quad \Psi_2 = 4.5 \cdot 10^{-3}, \quad \Psi_3 = 8 \cdot 10^{-3}. \quad (4.41)$$

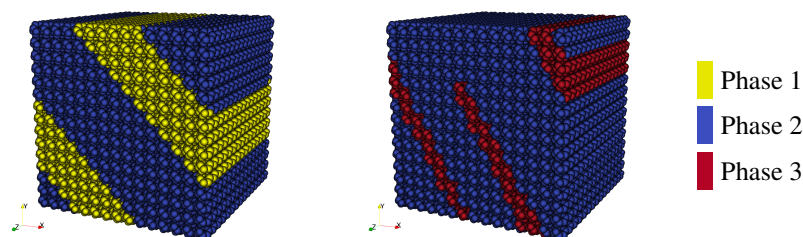
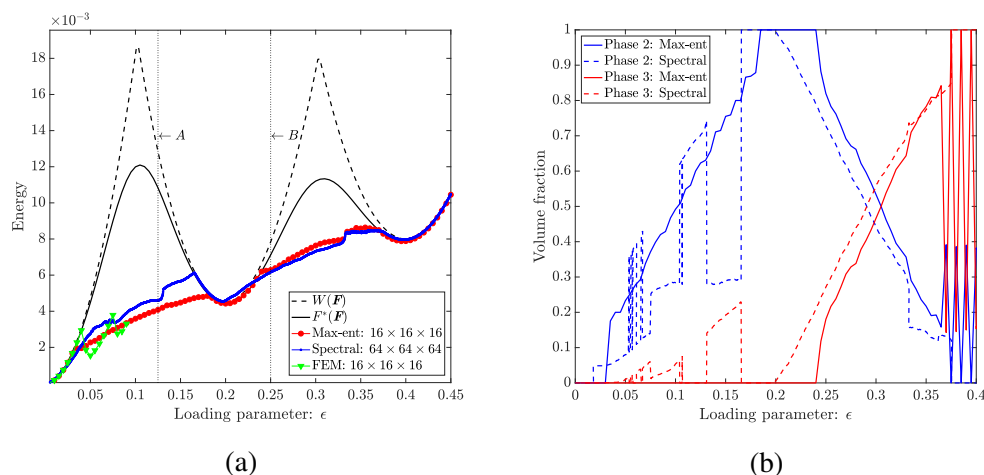
By contrast, case (ii) assumes that the first and third wells have equal depths, defining

$$(ii) \quad \Psi_1 = 0, \quad \Psi_2 = 4.5 \cdot 10^{-3}, \quad \Psi_3 = 0. \quad (4.42)$$

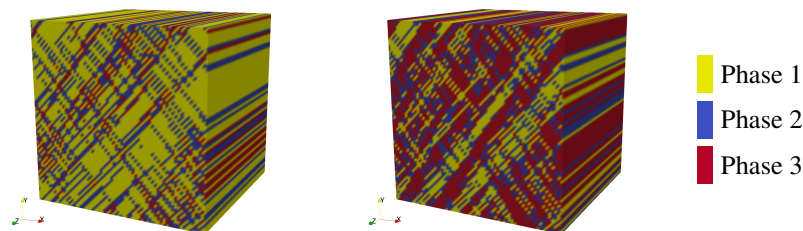
These two cases are quite distinct in that, when loading with \mathbf{F}^0 from (4.38), (ii) is expected to form microstructural patterns that involve only phases 1 and 3 (involvement of phase 2 would lead to higher, non-zero energy levels), while (i) is expected to gradually transition through phases 1, 2 and 3 to minimize the energy along (4.38).

Let us first discuss case (i). In line with previous results, Figure 4.8a shows that, despite the low spatial resolution, max-ent performs significantly better than the FFT scheme in predicting the relaxed energy density. FEM fails to converge as soon as the loading approaches the nonconvex regime of the (unrelaxed) energy density. Figures 4.8c and 4.8d illustrate the corresponding microstructural patterns predicted by the max-ent and FFT schemes, respectively. For both methods, simulations indicate that the RVE undergoes sequential phase transformations from phase 1 to phase 2 to phase 3. Particularly for max-ent, nucleation of phase 3 does not occur until the RVE has first transformed into a homogeneous phase 2, following which it undergoes a second transformation from phase 2 to phase 3. During this latter transformation, phase 1 does not emerge, so at any strain level only two phases co-exist. This is also evident from the volume fractions of the second and third phase, as shown in Figure 4.8b for different strain levels. All three methods predict laminate-type microstructures, with max-ent showing coarse laminates with few interfaces, FFT predicting complex higher-order laminates with abundant interfaces, and FEM showing a laminate aligning with the mesh at low strain levels.

In case (ii), the third well is at the same energy level as the first well. From analytical energy relaxation, one may expect phases 1 and 3 to dominate, since involvement

A: $\epsilon = 0.125$ B: $\epsilon = 0.25$

(c) Max-ent scheme

A: $\epsilon = 0.125$ B: $\epsilon = 0.25$

(d) Spectral scheme

Figure 4.8: (a) Numerically computed relaxed energy densities of the three-well phase transformation model for case (i): $\Psi_1 = 0$, $\Psi_2 = 4.5 \cdot 10^{-3}$, $\Psi_3 = 8 \cdot 10^{-3}$. The dotted line denotes the unrelaxed energy density (4.24), while the solid line denotes the corresponding smoothed energy density (4.31). (b) Average volume fractions of phases 2 and 3 corresponding to the relaxed energy curves, as obtained from the max-ent and FFT schemes (all three volume fractions sum up to 1). (c) and (d) Associated microstructural patterns, color-coded by the dominant phase at each point within the RVE, obtained from the max-ent and FFT schemes, respectively, at strain levels marked as A and B in (a) (the dominant phase is defined as the phase with highest volume fraction at a given point).

of phase 2 would lead to higher energy levels (which is why no sequential transformations as in case (i) are expected here). Yet, this presumes that, given the large transformation strain of phase 3, vanishingly small volume fractions of phase 3 can be nucleated at low strain levels. The latter is strongly limited by the spatial resolution in the numerical schemes. Therefore, simulations show mixed pattern evolutions involving all three phases simultaneously during the loading process. The consequences are visible in Figure 4.9, which summarizes the numerically computed relaxed RVE energies and corresponding microstructures for all three schemes.

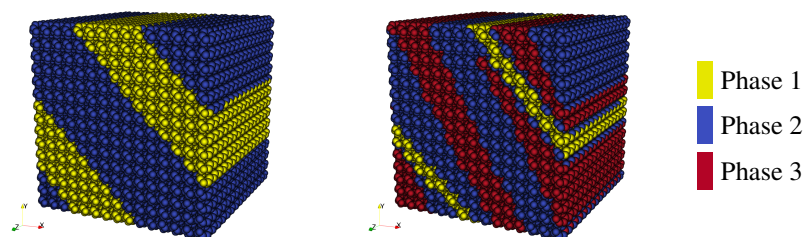
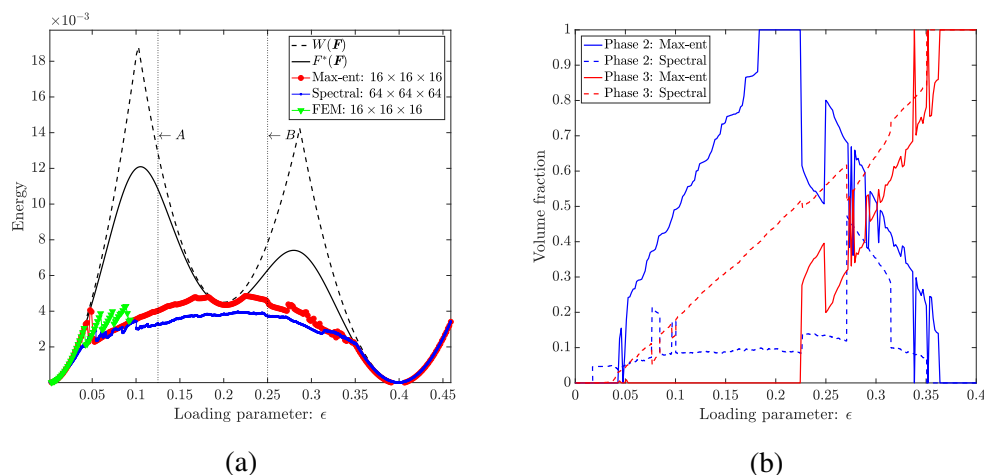
The FFT scheme indeed nucleates phase 3 at low strain levels, and only traces of phase 2 emerge, as demonstrated by the microstructures (Figure 4.9d) and the extracted phase volume fractions (Figure 4.9b). The obtained relaxed energy is too high but well below the second well, so that a homogeneous phase 2 is in fact avoided. We attribute the high, non-zero relaxed energy to the large number of interfaces present in the RVE (which will be discussed in detail in Section 4.6). The benchmark was also repeated with a 256^3 grid², and the corresponding high-resolution microstructures (featuring sharp needle-like domains) are illustrated in Figure 4.10. However, with increase in resolution, the number of interfaces increases proportionally and hence, no significant decrease in the relaxed energy was observed.

By contrast, the spatial resolution of the max-ent scheme is not sufficiently high to resolve complex microstructures involving direct nucleation of phase 3 at low strain levels. Therefore, as observed in Figures 4.9b and 4.9c, phase 2 dominates large fractions of the RVE during straining, leading to an even higher energy than that obtained from FFT and higher than the quasiconvex hull (which is zero for $\epsilon \in [0, 0.4]$). In addition, our solver uses the previous solution as the initial guess for the next load step, which further causes more nucleation of the second phase and prevents the third phase from nucleating at low strains. While this latter issue is resolvable by artificially engineering the initial guess to prevent the second phase from nucleating, this does not generalize to arbitrary problems with unknown microstructures. Therefore, such a strategy only applies if the energy-minimizing microstructure is known a priori, which in turn defeats the purpose of this study.

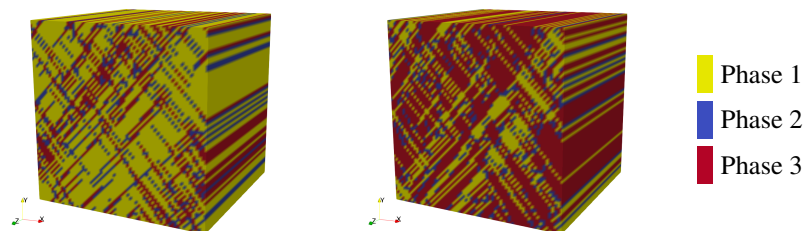
4.6 Influence of spatial discretization and interfacial energy

It is intuitive to expect that increasing the spatial resolution allows for capturing more complex, fine-grained microstructures, such that the numerically relaxed en-

²The spatial resolution of 256^3 was only limited to this benchmark due to high computational costs.



A: $\epsilon = 0.125$ B: $\epsilon = 0.25$
(c) Max-ent scheme



A: $\epsilon = 0.125$ B: $\epsilon = 0.25$
(d) Spectral scheme

Figure 4.9: (a) Numerically computed relaxed energy densities of the three-well phase transformation model for case (ii): $\Psi_1 = 0$, $\Psi_2 = 4.5 \cdot 10^{-3}$, $\Psi_3 = 0$. The dotted line denotes the unrelaxed energy density (4.24), while the solid line denotes the corresponding smoothed energy density (4.31). (b) Average volume fractions of phases 2 and 3 corresponding to the relaxed energy curves, as obtained from the max-ent and FFT schemes (all three volume fractions sum up to 1). (c) and (d) Associated microstructural patterns, color-coded by the dominant phase at each point within the RVE, obtained from the max-ent and FFT schemes, respectively, at strain levels marked as A and B in (a) (the dominant phase is defined as the phase with highest volume fraction at a given point).

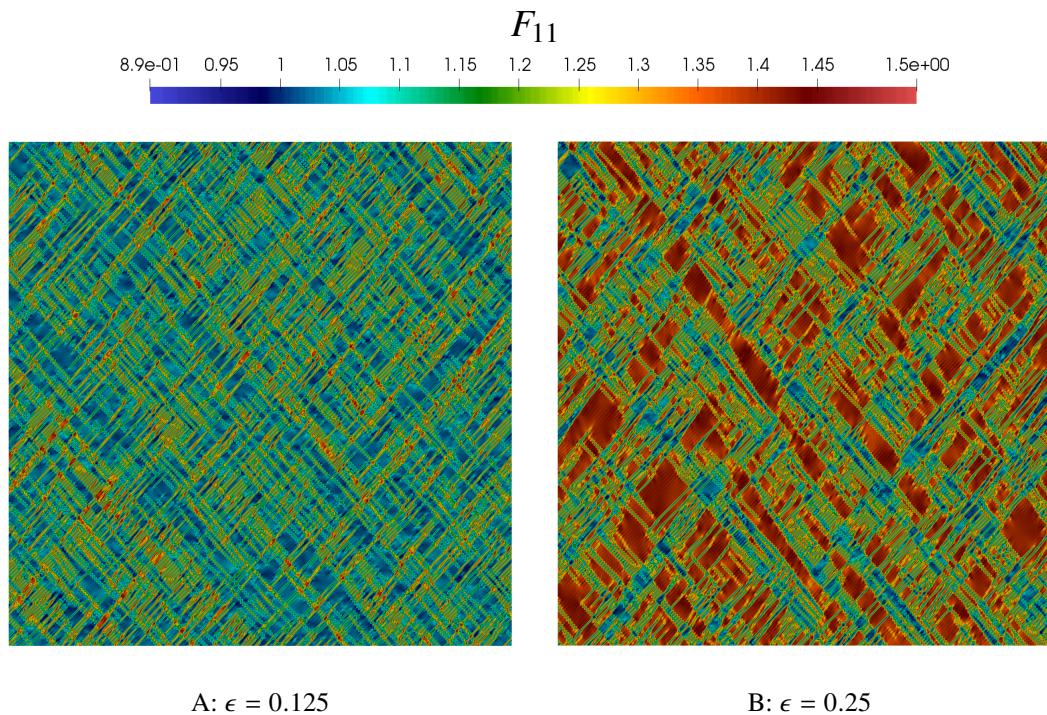


Figure 4.10: Microstructure patterns predicted by the FFT scheme at 256^3 spatial resolution for case (ii): $\Psi_1 = 0$, $\Psi_2 = 4.5 \cdot 10^{-3}$, $\Psi_3 = 0$. The microstructures are visualized by plotting the deformation gradient component F_{11} at strain levels marked as A and B in Figure 4.9a.

ergy density converges to the quasiconvex hull with increasing resolution. However, as observed in all our numerical examples in Sections 4.4 and 4.5, the numerically obtained energy density is always higher than the quasiconvex hull by a non-negligible amount, even at intriguingly high resolution as in the FFT approach. As we demonstrate below, this energy difference stems from considerable interface energy, especially when the true energy-minimizing volume fractions are not accurately resolvable by the spatial discretization. In order to assess the importance of the latter effect, we here present a simplified analytical study of the interface energy for the representative example of our phase transformation model in 2D and 3D (considering the limiting case $k_T \rightarrow 0$, such that the energy density is given by (4.35) and hence (4.24), and the smoothness of approximation (4.31) does not affect our conclusions).

4.6.1 Interfaces in the phase transformation model in 2D

Consider a two-phase square-shaped RVE in 2D of unit length, filled with a material whose constitutive behavior is described by the phase transformation model with

transformation strains and chemical energies (with $\xi_i \geq 1$)

$$\mathbf{U}_1 = \begin{pmatrix} \xi_1 & 0 \\ 0 & 1 \end{pmatrix}, \quad \mathbf{U}_2 = \begin{pmatrix} \xi_2 & 0 \\ 0 & 1 \end{pmatrix}, \quad \Psi_1 = 0, \quad \Psi_2 = 0. \quad (4.43)$$

The RVE is loaded by the average deformation gradient

$$\mathbf{F}^0 = \begin{pmatrix} \hat{\lambda} & 0 \\ 0 & 1 \end{pmatrix} \quad \text{with} \quad \xi_1 < \hat{\lambda} < \xi_2. \quad (4.44)$$

For the elastic strain energy density, we take the Neo-Hookean model in (4.37) and assume plane strain condition along the \mathbf{x}_3 -axis. The reduced strain energy density is given by

$$W_e(\mathbf{F}) = \frac{\mu}{2} \left(\frac{\text{tr}(\mathbf{F}^T \mathbf{F}) + 1}{J^{2/3}} - 3 \right) + \frac{\kappa}{2} (J - 1)^2, \quad \mathbf{F} \in GL_+(2). \quad (4.45)$$

We construct a first-order laminate pattern inside the periodic RVE, as shown in Figure 4.11a, where each of the two phases is uniformly strained by $\mathbf{F}_1 = \mathbf{U}_1$ and $\mathbf{F}_2 = \mathbf{U}_2$, respectively. For the chosen chemical energies, this first-order laminate construction attains the quasiconvex energy hull exactly. Let the width of phases 1 and 2 be, respectively, $\hat{\nu}$ and $1 - \hat{\nu}$. Compatibility requires the laminate volume fractions to satisfy

$$\hat{\nu} \xi_1 + (1 - \hat{\nu}) \xi_2 = \hat{\lambda} \quad \Rightarrow \quad \hat{\nu} = \frac{\xi_2 - \hat{\lambda}}{\xi_2 - \xi_1} \quad \text{for} \quad \hat{\lambda} \in (\xi_1, \xi_2). \quad (4.46)$$

The resulting average RVE energy is identically zero, which coincides with the quasiconvex hull. As is apparent from (4.46), $\hat{\nu}$ rises continuously from 0 to 1 between the two energy wells. In the case of a spatially discretized RVE, only discrete jumps in $\hat{\nu}$ can be resolved by the mesh or grid, so that there are values of $\hat{\lambda}$ for which the energy-minimizing laminate microstructure is unresolvable (as shown in Figure 4.11b) by the spatial discretization. As a consequence, alternative microstructures with non-zero energy emerge. We aim to understand exactly those microstructures and their associated energy by studying subspaces of admissible solutions that are resolvable by a given spatial discretization. We differentiate between two possible solutions in the following (both promising convergence under refinement of the nodal spacing h). First, we assume a *sharp interface* coinciding with a nodal plane, so that the volume fractions are not $\hat{\nu}$ and $1 - \hat{\nu}$ but $\nu \approx \hat{\nu}$ and $1 - \nu$ with $|\nu - \hat{\nu}| \sim h$. In this case, the RVE minimizes its energy by adjusting the deformation gradients in the two phases. Second, we assume a *diffuse interface*, i.e., an interface layer of width $\sim h$ emerges to minimize the RVE energy, while the two phases are homogeneous at zero energy.

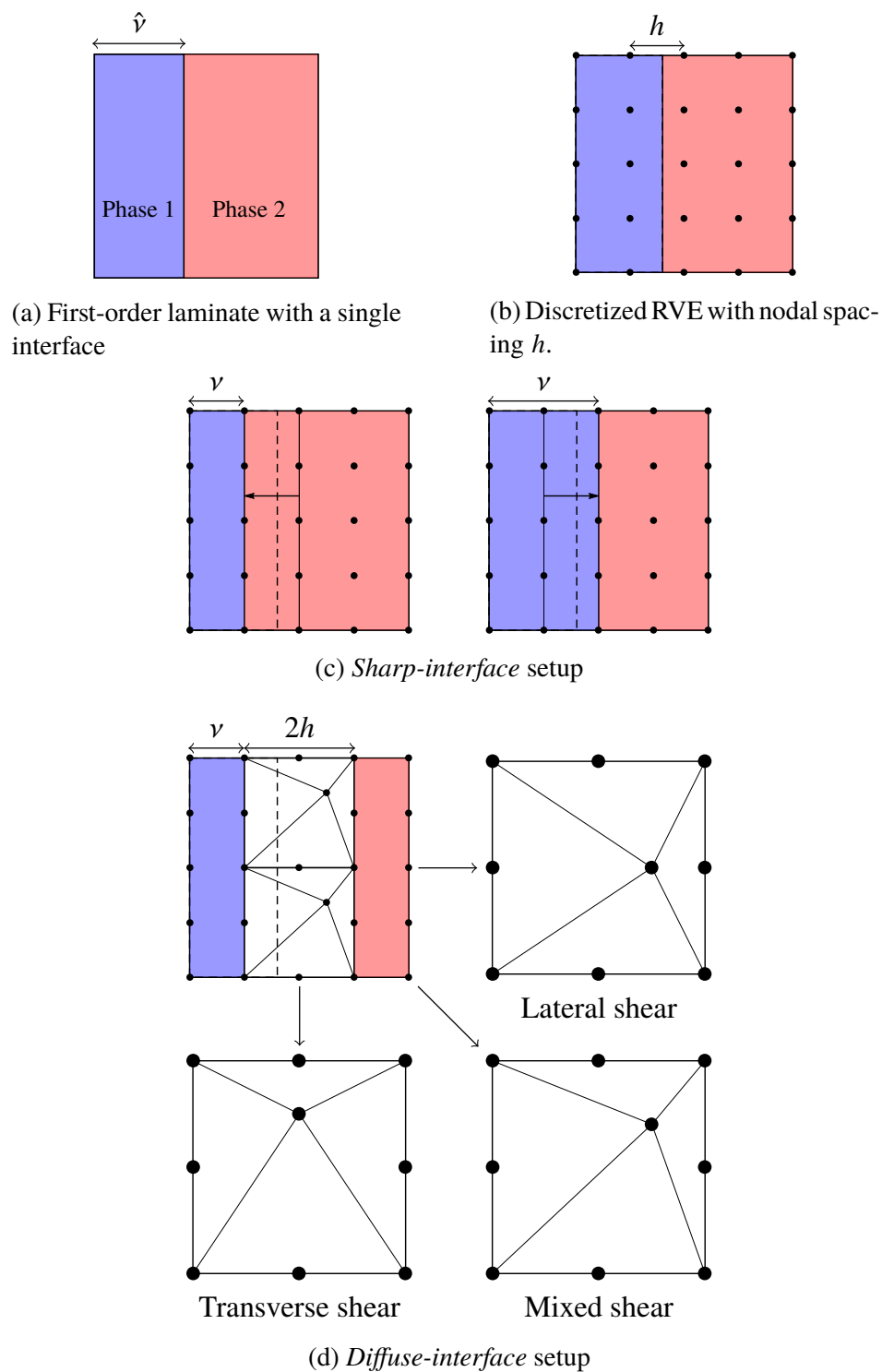
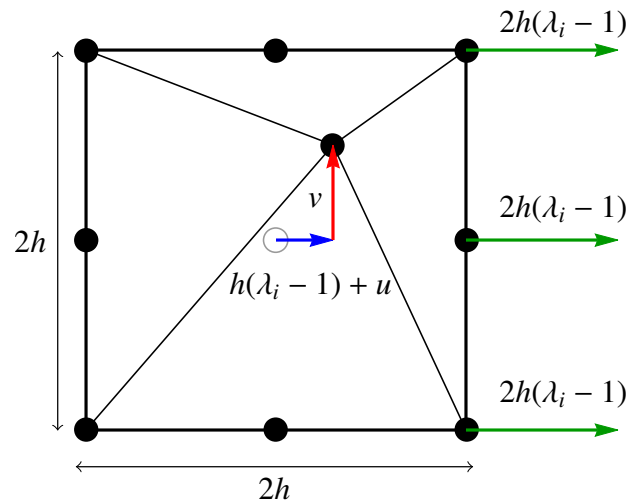
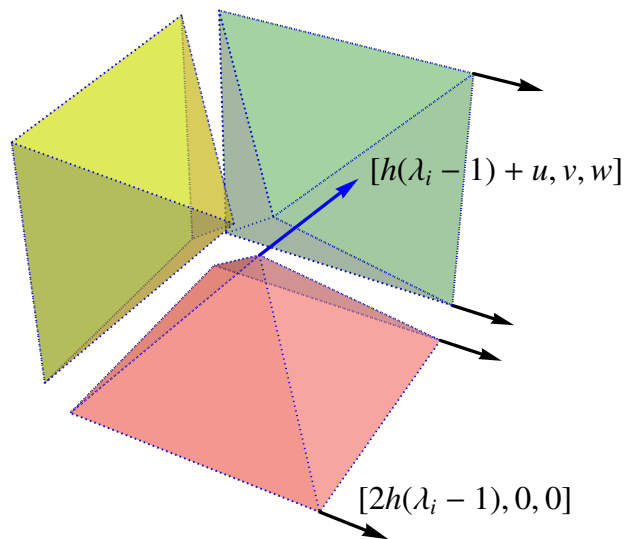


Figure 4.11: Schematic of a laminate interface being unresolvable by the spatial discretization, leading to an approximate energy-minimizing laminate with either a *sharp-interface* or a *diffuse-interface* layer between laminate phases.



(a) Representative 2D shear cell with four constant-strain triangles



(b) Cut of a representative 3D shear cell with six constant-strain tetrahedra

Figure 4.12: Schematics of shear cells in the diffuse interface layer model in 2D and 3D along with their nodal displacements. The interface width is exaggerated for illustration purposes; the real interface width of $2h$ is small relative to the RVE size.

Sharp interfaces

As one possible energy-minimizing microstructure that accommodates the limited RVE resolution, the laminate interface (ideally situated between two nodes) may shift to one of the two nearest nodal planes, as shown in Figure 4.11c. In this case, the RVE energy is minimized in a nonlocal fashion by homogeneously straining each of the two phases. The volume fraction of phase 1 is thus given by

$$\nu = h \left(\left\lfloor \frac{\hat{\nu}}{h} \right\rfloor + \frac{1}{2} \right) \pm \frac{h}{2}, \quad (4.47)$$

where two possible solutions exist, depending on whether the interface shifts to the left or to the right. Due to the structure of \mathbf{U}_i and \mathbf{F}^0 , the homogeneous deformation gradients in both phases are expected of the form

$$\mathbf{F}_1 = \begin{pmatrix} \lambda_1 & 0 \\ 0 & 1 \end{pmatrix}, \quad \mathbf{F}_2 = \begin{pmatrix} \lambda_2 & 0 \\ 0 & 1 \end{pmatrix}, \quad (4.48)$$

where λ_1 and λ_2 are unknowns. Given the macroscopic loading in (4.44), compatibility enforces the constraint

$$\nu \lambda_1 + (1 - \nu) \lambda_2 = \hat{\lambda}. \quad (4.49)$$

Therefore, the relaxed energy in this case is given by minimizing the RVE energy with respect to λ_1 and λ_2 , i.e.,

$$NW(\hat{\lambda}) = \min_{\lambda_1, \lambda_2} [\nu W_1(\mathbf{F}_1) + (1 - \nu)W_2(\mathbf{F}_2) \text{ s.t. (4.49)}]. \quad (4.50)$$

Minimization is again carried out numerically. Note that this class of solutions is nonlocal, i.e., it produces sharp interfaces but leads to the entire RVE being strained. Thus, the increase in energy due to the unresolvable microstructure is not localized at the interfaces but distributed across the entire RVE.

Diffuse interface layer

As an alternative energy-minimizing microstructure that accommodates the limited RVE resolution, we consider a laminate microstructure as shown in Figure 4.11a with two homogeneous phases strained by $\mathbf{F}_1 = \mathbf{U}_1$ and $\mathbf{F}_2 = \mathbf{U}_2$ (thus having zero energy). If the energy-minimizing volume fraction $\hat{\nu}$ is resolvable by the nodal planes, then a first-order laminate with sharp interface is realized and the RVE energy vanishes. If, however, $\hat{\nu}$ cannot be accommodated by the FE mesh in a

simple laminate fashion, as shown in Figure 4.11b, an interface layer of width $2h$ is assumed to arise in order to minimize the RVE energy in a compatible fashion (see Figure 4.11d). Let λ_i be the macroscopic stretch ratio of the interface layer in the x_1 -direction, and let ν again denote the volume fraction (i.e., width) of phase 1 in the laminated RVE. Compatibility imposes

$$\nu \xi_1 + 2h \lambda_i + (1 - \nu - 2h)\xi_2 = \hat{\lambda} \quad \Rightarrow \quad \lambda_i = \frac{\hat{\lambda} - \nu \xi_1 - (1 - \nu - 2h)\xi_2}{2h}. \quad (4.51)$$

Based on the spatial discretization in an RVE of size 1×1 , the interface layer is divided into $n_h = (2h)^{-1}$ cells stacked vertically above one another, each of side length $2h \ll 1$ and consisting of four constant-strain triangles (CST), as shown for a representative cell in Figure 4.12a. The nodal displacements in a representative cell relative to the bottom-left node are also illustrated in Figure 4.12a, where $(h(\hat{\lambda} - 1) + u)$ and v are the horizontal and vertical displacements of the central node, respectively. The relaxed energy of the RVE (exploiting that the energy within each homogeneous phase vanishes) is thus obtained by minimization of the total RVE energy with respect to the displacement of the central node of the shear cells, i.e.,

$$\begin{aligned} NW(\hat{\lambda}) &= n_h \min_{u,v} \left[\sum_{k=1}^4 \min \{W_1(\mathbf{F}_{int,k}), W_2(\mathbf{F}_{int,k})\} V_{\text{CST}} \right] \\ &= \frac{h}{2} \min_{u,v} \left[\sum_{k=1}^4 \min \{W_1(\mathbf{F}_{int,k}), W_2(\mathbf{F}_{int,k})\} \right], \end{aligned} \quad (4.52)$$

where $\mathbf{F}_{int,k}$ is the uniform deformation gradient inside each of the four CSTs, and $V_{\text{CST}} = (2h)^2/4$ is the (undeformed) area of each CST. For the sake of brevity, we here omit the deformation gradients inside the CSTs as derived from the nodal displacements. Minimization in (4.52) is carried out numerically. For illustrative purposes, we find the energy-minimizing solution for four particular cases illustrated in Figure 4.11d. Those correspond to the cases

- $u = 0, v = 0$: none of the CSTs are sheared, no minimization necessary (*no shear*),
- $u \neq 0, v = 0$: only the top and bottom CSTs can shear (*lateral shear*),
- $u = 0, v \neq 0$: only the left and right CSTs can shear (*transverse shear*),
- $u \neq 0, v \neq 0$: all CSTs can shear (*mixed shear*).

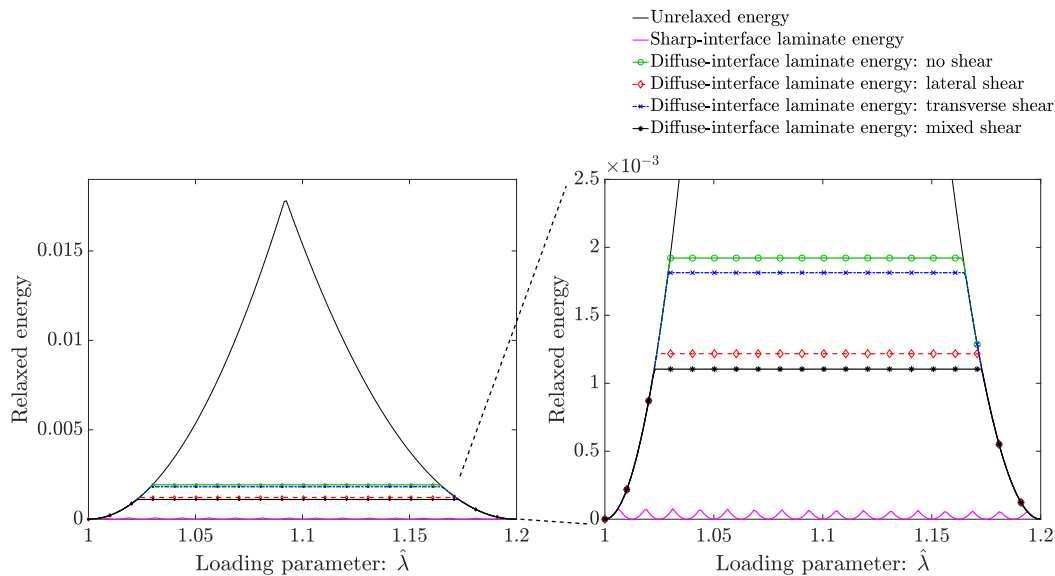


Figure 4.13: Numerically relaxed energy density of a 2D RVE of side length 1, whose uniform spatial discretization with grid point spacing $h = 1/16$ limits the resolvability of the changing laminate volume fraction. Shown are the unrelaxed energy density as well as the approximate relaxed energies obtained from the *sharp-interface* scenario, (4.50), and from the *diffuse-interface* scenario, (4.52). Results are for $\xi_1 = 1.0$ and $\xi_2 = 1.2$, and the elastic moduli $\mu = 1$ and $\kappa = 3$.

The four resulting energies resulting from this diffuse-interface setup (computed from (4.52)) as well as from the previous sharp-interface scenario (obtained from (4.50)) are illustrated in Figure 4.13 for $h = 1/16$. The relaxed energy obtained from the sharp-interface setting with distributed errors is significantly more accurate than that obtained from the diffuse interface layer for any of the above four cases. (Of those, as may be expected, the mixed shear solution produces the lowest energy.) Interestingly, the energy stored in the interface layer is independent of the applied average strain.

4.6.2 Interfaces in the phase transformation model in 3D

To extend the above concepts to a 3D RVE of unit length, consider the double-well phase transformation model with the Neo-Hookean energy density (4.37) and

$$\mathbf{U}_1 = \begin{pmatrix} \xi_1 & 0 & 0 \\ 0 & 1 & 0 \\ 0 & 0 & 1 \end{pmatrix}, \quad \mathbf{U}_2 = \begin{pmatrix} \xi_2 & 0 & 0 \\ 0 & 1 & 0 \\ 0 & 0 & 1 \end{pmatrix}, \quad \Psi_1 = 0, \quad \Psi_2 = 0. \quad (4.53)$$

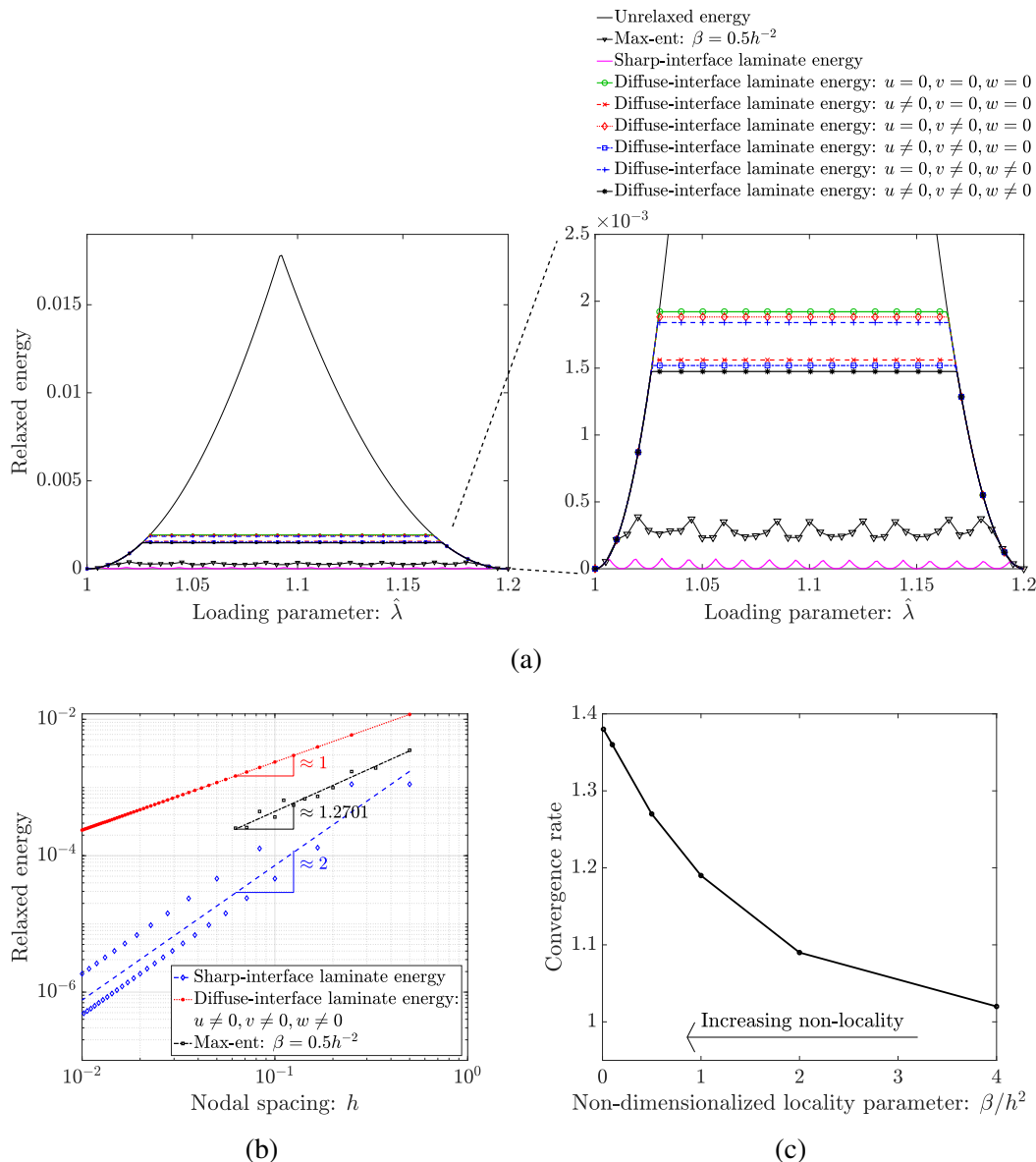


Figure 4.14: (a) Numerically relaxed energy density of a 3D RVE of side length 1, whose uniform spatial discretization with grid point spacing $h = 1/16$ limits the resolvability of the changing laminate volume fractions. Shown are the unrelaxed energy density as well as the approximate relaxed energies obtained from the *sharp-interface* scenario extended to 3D, (4.50), and from the *diffuse-interface* scenario, (4.55). Results are for $\xi_1 = 1.0$ and $\xi_2 = 1.2$, and the elastic moduli $\mu = 1$ and $\kappa = 3$. (b) Convergence of the relaxed energy to the quasiconvex hull (zero for $\hat{\lambda} \in [1, 1.2]$) at fixed $\hat{\lambda} = 1.075$ with h -refinement. (c) Convergence rate of the relaxed energy obtained from max-ent for different values of the locality parameter β .

The RVE is macroscopically strained according to

$$\mathbf{F}^0 = \begin{pmatrix} \hat{\lambda} & 0 & 0 \\ 0 & 1 & 0 \\ 0 & 0 & 1 \end{pmatrix} \quad \text{with} \quad \xi_1 < \hat{\lambda} < \xi_2. \quad (4.54)$$

The mathematical setting for the two classes of laminate solutions with sharp and diffuse interfaces remains unchanged. For the case of a sharp interface, (4.50) applies analogously in 3D. For a diffuse interface, the extension to 3D requires the two laminate phases to be separated by an interface layer containing $n_h = (2h)^{-2}$ cubic cells, each of side length $2h$ and consisting of six constant-strain tetrahedra (see Figure 4.12b). The macroscopic stretch in the interface layer (λ_i) is given by (4.51). Assume the displacement of the central node in each cubic cell is $[h(\hat{\lambda} - 1) + u, v, w]^T$. Relaxation of the RVE energy with respect to the central node's displacement gives the numerically relaxed energy density

$$\begin{aligned} NW(\hat{\lambda}) &= n_h \min_{u,v,w} \left[\sum_{k=1}^6 \min \{W_1(\mathbf{F}_{int,k}), W_2(\mathbf{F}_{int,k})\} V_{\text{CST}} \right] \\ &= \frac{h}{3} \min_{u,v,w} \left[\sum_{k=1}^6 \min \{W_1(\mathbf{F}_{int,k}), W_2(\mathbf{F}_{int,k})\} \right], \end{aligned} \quad (4.55)$$

where $\mathbf{F}_{int,k}$ is the uniform deformation gradient in the k^{th} tetrahedron, and $V_{\text{CST}} = (2h)^3/6$ is the volume of each tetrahedron. Analogous to the 2D case, six different types of solutions may be constructed based on which degrees of freedom of the central node are being constrained (to zero) or relaxed.

Figure 4.14a compares the numerically relaxed energies (4.50) (extended to 3D) and (4.55) for a spatial resolution of $h = 1/16$ (with an RVE side length of 1). Figure 4.14b illustrates the convergence of the relaxed energy from each class of solutions under h -refinement. As in the 2D problem, the ‘‘mixed-shear’’ solution yields the lowest energy for the laminate with interface layer, and the obtained energies are independent of the applied strain. Notably, the error of the sharp-interface solution converges quadratically under h -refinement, which is in contrast to the linear convergence observed for the diffuse-interface layer construction. For reference, the relaxed energy computed by max-ent³ using the same discretizations is also shown. Unlike in prior simulations, here we provide the exact laminate solution with a single interface (see Figure 4.11a) as an initial guess at each load step to ensure that the solver converges to a local minima that is in the proximity of the respective analytical solution.

³The FFT scheme fails to converge in the limit $k_T \rightarrow 0$ (as discussed in Section 4.5) and is therefore omitted in this comparison.

4.6.3 Mesh-dependence of microstructures

In all of the above laminate examples, the energy-minimizing laminate orientation was aligned with the FEM mesh, FFT grid, and max-ent node set. Numerically-predicted microstructures are well-known to be highly mesh-dependent [163], so that laminates tend to align with the discretization such as with the mesh in FEM. Numerical approaches have aimed to reduce the influence of the FE mesh by rotating or adaptively adjusting the mesh [141].

By contrast, the max-ent approximation uses shape functions that are least biased with respect to the position of nodes, so that laminates of arbitrary orientation can be captured without significant artifacts from the spatial discretization. For verification, we perform a numerical experiment. We consider a two-well phase-transformation problem with equal well depths $\Psi_1 = 0$ and $\Psi_2 = 0$ and the rotated transformation strains

$$\begin{aligned} \mathbf{U}_1 = \mathbf{R} \begin{pmatrix} \xi_1 & 0 & 0 \\ 0 & 1 & 0 \\ 0 & 0 & 1 \end{pmatrix} \mathbf{R}^T, \quad \mathbf{U}_2 = \mathbf{R} \begin{pmatrix} \xi_2 & 0 & 0 \\ 0 & 1 & 0 \\ 0 & 0 & 1 \end{pmatrix} \mathbf{R}^T \\ \text{with } \mathbf{R} = \begin{pmatrix} \cos \theta & -\sin \theta & 0 \\ \sin \theta & \cos \theta & 0 \\ 0 & 0 & 1 \end{pmatrix}, \end{aligned} \quad (4.56)$$

and we let $\mathbf{R} \in \text{SO}(3)$ apply a rotation by $\theta \in [0, 2\pi)$ about the x_3 -axis. The average RVE deformation gradient is rotated analogously, i.e.,

$$\mathbf{F}^0 = \mathbf{R} \begin{pmatrix} \hat{\lambda} & 0 & 0 \\ 0 & 1 & 0 \\ 0 & 0 & 1 \end{pmatrix} \mathbf{R}^T \quad \text{with} \quad \xi_1 < \hat{\lambda} < \xi_2. \quad (4.57)$$

This setup yields the same laminate solution as in previous section except that the laminate orientation is rotated by θ . This is equivalent to rotating the RVE mesh while maintaining the original laminate orientation.

Figure 4.15 shows the numerically relaxed energy, evaluated for θ equal to 30° , 40° , 50° , and 60° , using both the max-ent and FEM schemes⁴ on a $10 \times 10 \times 10$ grid. In order to study the effect of the orientation of the grid, we do not provide the exact energy-minimizing laminate solution as the initial guess. Remarkably,

⁴By contrast to Section 4.5.2, FEM convergence was possible in this case only because of the specific transformation strains and loading, which admit first-order laminate solutions.

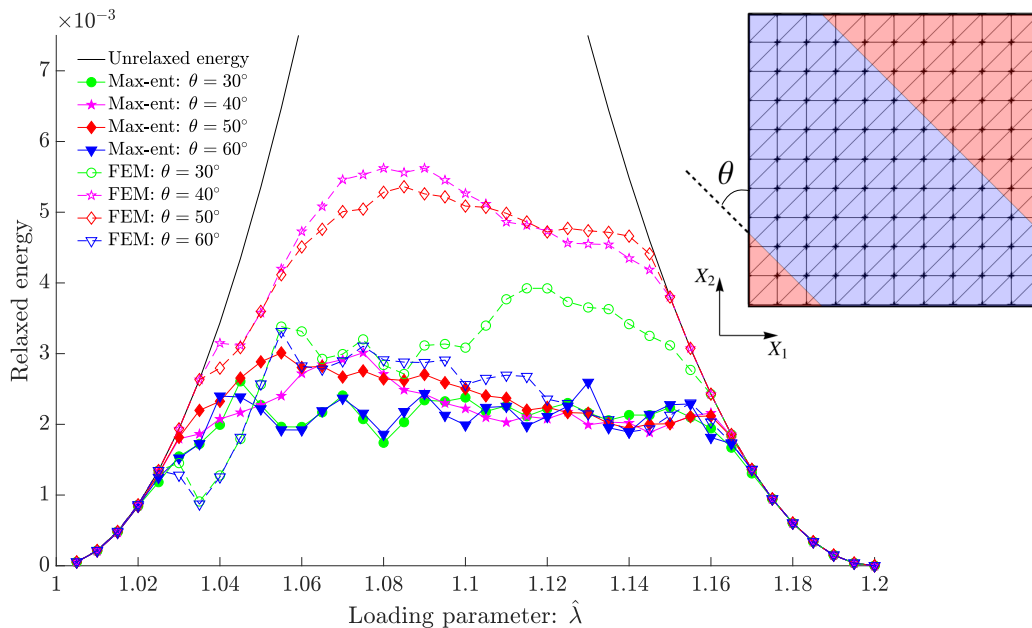


Figure 4.15: Numerically relaxed energy of a 3D RVE discretized by a $10 \times 10 \times 10$ mesh/point set modeled by the max-ent and FEM schemes, using the two-well phase-transformation model with the rotated transformation strains (4.56) and average deformation gradient (4.57). The inset shows an FEM mesh illustrating the laminate orientation with varying θ .

the relaxed energy predicted by max-ent shows considerably smaller variations for varying θ , which are negligible compared to the FEM variations. The latter predicts a significantly higher relaxed energy for $\theta = \{40^\circ, 50^\circ\}$ than for $\theta = \{30^\circ, 60^\circ\}$. This corroborates that the predicted microstructure depends significantly less on the spatial discretization when using the max-ent scheme as compared to the FEM scheme. For completeness, let us note that the FFT scheme bears similar issues based on the RVE orientation's alignment with the Fourier wave vectors. Yet, a fair numerical comparison is hard to provide since FFT comes with much higher resolution (and it also does not convergence in the $k_T \rightarrow 0$ limit).

4.6.4 Sharp vs. diffuse interfaces in the numerical schemes

Despite the previous studies in this section being specific to first-order laminates, the underlying discretization-based issues persist in any microstructured RVE; and they become even worse for complex microstructures with growing numbers of interfaces. Max-ent, being a high-order nonlocal and smooth meshfree approximation, bears another essential advantages over classical FEM. Li and Carstensen [140] argued that smoothing or averaging techniques aid in the process of microstructure prediction

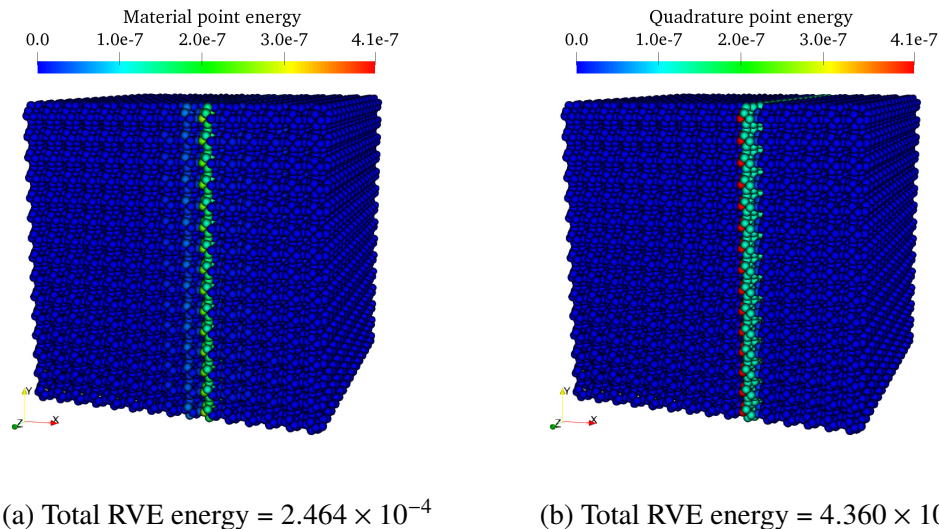


Figure 4.16: Distribution of strain energy within a 3D RVE with $16 \times 16 \times 16$ spatial resolution, obtained by (a) the max-ent scheme (showing all material points) and (b) the FEM scheme (showing all quadrature points). The RVE is strained to $\hat{\lambda} = 1.075$, deliberately such that the optimal laminate interfaces yielding zero relaxed energy for a sharp-interface laminate do not coincide with any nodal planes of a discretized RVE.

by FEM schemes. We make a similar observation here: both our FEM and FFT schemes generate sharp interfaces and, especially in the FFT case, many of those, so that the relaxed RVE energy is dominated by those interfaces. Max-ent, by contrast, introduces an approximate deformation mapping $\varphi^h \in C^\infty$, which generally results in smooth, diffuse interfaces and solutions in the sense of Modica [155]. This, in turn, affects both the interface energy and the total interface area. The degree of nonlocality in the max-ent scheme is controlled by the locality parameter β . This is reflected in the energy convergence rates in Figure 4.14c, which were obtained with different values of β . In particular, when $\beta = 4h^{-2}$ (i.e., max-ent is almost equivalent to simplicial FE, see Arroyo and Ortiz [7]) the converge rate is close to linear. As the value of β decreases and the max-ent approximation becomes increasingly nonlocal, the convergence rate also increases, ultimately reaching a convergence rate between the two interface models presented in previous sections. Hence, max-ent offers a compromise between sharp interfaces at nodal planes (thus raising the energy in the homogeneous phases) and interface layers (thus contributing high interface energy while keeping the homogeneous phases at the energy minima).

In contrast to the energetically-diffuse max-ent interfaces, the FEM and FFT schemes

(the latter employing the finite-difference correction of derivatives⁵ [206, 207]) can accurately capture localized discontinuities. This has two consequences: (i) interfaces inconsistent with the spatial discretization tend to be approximated by high-energy, localized interface layers; (ii) complex high-resolution microstructures contribute many such high-energy interfaces, thereby increasing the total energy of the RVE and decreasing the convergence rate. As an illustrative example, consider the energy distribution within an RVE with a first-order laminate microstructure. Shown in Figure 4.16 is the energy per material/quadrature point for such a first-order laminate, produced by the max-ent and FEM schemes. Clearly, the max-ent interfacial energy is spatially diffused, and the resulting RVE energy is lower than that obtained from FEM.

4.7 Conclusions

We have discussed the ability of three numerical techniques – FEM, an FFT-based spectral scheme, and a max-ent meshfree method – to find energy-minimizing microstructural patterns and the associated relaxed energy density of a representative volume element, when the energy of the underlying material model lacks (quasi)convexity. The numerical strategies were applied to benchmark problems of hyperelasticity and phase transformations. We have showed that the spectral scheme is capable of producing high-resolution microstructures, while max-ent is superior at numerical energy relaxation even at low spatial resolution. Classical FEM was found to be severely limited in both aspects. We note that the NP-hard nature of nonconvex optimization limits the ability of any numerical method to find global minima, in this case energy-minimizing microstructures. Through a simplified analytical study of microstructural interfaces, we have shown that this limitation arises from the inability of a spatial discretization to resolve general energy-minimizing microstructural patterns. While the present study utilized basic Newton-Raphson iterations for energy minimization, the limitations imposed by unresolved interfaces is inherent to the spatial discretization and will persist in any numerical simulation irrespective of the choice of pre-conditioners, line-search techniques, gradient descents, or other nonlinear solvers. Furthermore, we have shown that this can be alleviated to some extent by using meshfree approximants (e.g., local max-ent), whose performance was demonstrated in comparison with the FEM and FFT schemes. While the spatial discretization can be chosen such that interfaces are accurately resolved by nodes,

⁵Without the finite difference approximation, the spectral scheme would suffer from Gibbs phenomena near discontinuities.

the lack of a priori knowledge of the energy-minimizing microstructures prevents the creation of such meshes. Adaptive mesh refinement in terms of nodal positions and spatial resolution, as well as the inclusion of (undeformed) nodal positions in the variational problem, stand as a possible candidates for resolving the interface issue, though these methods are complex and strongly dependent on the initial guess. Therefore, the presented max-ent scheme is a viable and computationally inexpensive strategy for approximating relaxed energies (while the presented, finite-difference-enhanced FFT scheme is a viable solution for generating high-resolution microstructures – with generally higher energy).

CONCLUSION AND FUTURE OUTLOOK

This thesis proposed an enhanced meshfree method based on the local max-ent approximation. This method is the first among the class of meshfree methods that addresses the tensile instability associated with meshfree kernels in updated-Lagrangian setting, and achieves robust stability in simulating large deformation problems. Benchmark results on quasi-static and dynamic simulations showed promising outcomes in terms of accuracy and stability. The enhanced local max-ent method as well as the updated-Lagrangian formulation offer many more possibilities in simulating a plethora of materials under less restrictive settings, and is sufficiently general to be applied to multi-physics and multi-scale problems. Furthermore, we can extend the adaptive shape function strategy necessary for stability to other meshfree approximation schemes such as SPH, MLS, RKPM, etc.

In this thesis, we have also showcased two applications of the proposed max-ent method.

- First, we have developed a novel multiscale framework for modeling ECAE that utilizes the max-ent based meshfree method for large deformations at the macroscale, combined with grain refinement and reorientation at the microscale via material model of Tutcuoglu et al. [202]. The method is also generalizable to a range of SPD processes including HPT, ARB, RCS, etc., which will be covered in subsequent studies. Therefore, the multiscale framework presents itself as a powerful and high-fidelity computational tool for predictive analysis and design optimization in the metal forming industry.
- Second, we have introduced the application of the max-ent based meshfree method for numerically approximating the quasiconvex hull of non-convex potentials. While the max-ent method enables large deformation simulations as shown previously, the smoothness and nonlocality of the shape functions, combined with unbiasedness with respect to nodal-positions/spatial discretization, also allows for superior numerical energy relaxation of non-convex potentials via RVE-level simulations. In a suite of benchmarks, we showed that max-ent method performed better than FEM and FFT at approximating quasi-convex

hulls. A possibility of future work is that we can extend this method for applications to more complicated non-convex potentials such as those that are history-dependent (e.g., crystal plasticity).

The success of applying the proposed max-ent method to the aforementioned engineering problems makes it desirable and relatable to real-world problems. A limitation would be the computational expense of high-resolution simulations for improved accuracy. A framework that handles scalable parallelism would be necessary to achieve large scale and high fidelity meshfree simulations. Another issue is the lack of general reception and slow adoption of meshfree methods, especially in the industry, which poses challenges for new meshfree methods like max-ent to make a concrete impact in engineering applications. Upon addressing these issues, the max-ent method presents a wider range of possibilities in dealing with more complex simulations that would not have been otherwise possible using FEM and traditional meshfree methods.

BIBLIOGRAPHY

- [1] Emilio Acerbi and Nicola Fusco. Semicontinuity problems in the calculus of variations. *Archive for Rational Mechanics and Analysis*, 86(2):125–145, Jun 1984. ISSN 1432-0673. doi: 10.1007/BF00275731. URL <https://doi.org/10.1007/BF00275731>.
- [2] F Al-Mufadi and F Djavaanroodi. Finite element modeling and mechanical properties of aluminum proceed by equal channel angular pressing process. *Int. J. of Mech., Aero., Ind. and Mechatr. Engg*, 8:1411–1416, 2014.
- [3] G. Allaire and G. Francfort. Existence of minimizers for non-quasiconvex functionals arising in optimal design. *Annales de l'Institut Henri Poincaré (C) Non Linear Analysis*, 15(3):301 – 339, 1998. ISSN 0294-1449. doi: [https://doi.org/10.1016/S0294-1449\(98\)80120-0](https://doi.org/10.1016/S0294-1449(98)80120-0). URL <http://www.sciencedirect.com/science/article/pii/S0294144998801200>.
- [4] Fatemeh Amiri, Daniel Millán, Marino Arroyo, Mohammad Silani, and Timon Rabczuk. Fourth order phase-field model for local max-ent approximants applied to crack propagation. *Computer Methods in Applied Mechanics and Engineering*, 312:254 – 275, 2016. ISSN 0045-7825. doi: <https://doi.org/10.1016/j.cma.2016.02.011>. URL <http://www.sciencedirect.com/science/article/pii/S0045782516300330>. Phase Field Approaches to Fracture.
- [5] S. Andersen and L. Andersen. Modelling of landslides with the material-point method. *Computational Geosciences*, 14(1):137–147, Jan 2010. ISSN 1573-1499. doi: 10.1007/s10596-009-9137-y. URL <https://doi.org/10.1007/s10596-009-9137-y>.
- [6] Keith Anguige and Patrick W. Dondl. Relaxation of the single-slip condition in strain-gradient plasticity. *Proceedings of the Royal Society of London A: Mathematical, Physical and Engineering Sciences*, 470(2169), 2014. ISSN 1364-5021. doi: 10.1098/rspa.2014.0098. URL <http://rspa.royalsocietypublishing.org/content/470/2169/20140098>.
- [7] M. Arroyo and M. Ortiz. Local maximum-entropy approximation schemes: a seamless bridge between finite elements and meshfree methods. *International Journal for Numerical Methods in Engineering*, 65(13):2167–2202, 2006. ISSN 1097-0207. doi: 10.1002/nme.1534. URL <http://dx.doi.org/10.1002/nme.1534>.
- [8] S. N. Atluri and T. Zhu. A new meshless local petrov-galerkin (mlpg) approach in computational mechanics. *Computational Mechanics*, 22(2):117–127, Aug 1998. ISSN 1432-0924. doi: 10.1007/s004660050346. URL <https://doi.org/10.1007/s004660050346>.

- [9] Sylvie Aubry, Matt Fago, and Michael Ortiz. A constrained sequential-lamination algorithm for the simulation of sub-grid microstructure in martensitic materials. *Computer Methods in Applied Mechanics and Engineering*, 192(26):2823 – 2843, 2003. ISSN 0045-7825. doi: [https://doi.org/10.1016/S0045-7825\(03\)00260-3](https://doi.org/10.1016/S0045-7825(03)00260-3). URL <http://www.sciencedirect.com/science/article/pii/S0045782503002603>.
- [10] Ivo Babuška, Uday Banerjee, John E. Osborn, and Qiaoluan Li. Quadrature for meshless methods. *International Journal for Numerical Methods in Engineering*, 76(9):1434–1470, 2008. doi: 10.1002/nme.2367. URL <https://onlinelibrary.wiley.com/doi/abs/10.1002/nme.2367>.
- [11] J. M. Ball and R. D. James. Fine phase mixtures as minimizers of energy. *Archive for Rational Mechanics and Analysis*, 100(1):13–52, 1987. ISSN 00039527. doi: 10.1007/BF00281246.
- [12] J. M. Ball and F. Murat. $W^{1,p}$ -quasiconvexity and variational problems for multiple integrals. *Journal of Functional Analysis*, 58(3):225 – 253, 1984. ISSN 0022-1236. doi: [https://doi.org/10.1016/0022-1236\(84\)90041-7](https://doi.org/10.1016/0022-1236(84)90041-7). URL <http://www.sciencedirect.com/science/article/pii/0022123684900417>.
- [13] John M. Ball. Convexity conditions and existence theorems in nonlinear elasticity. *Archive for Rational Mechanics and Analysis*, 63:337–403, 1976. URL <http://dx.doi.org/10.1007/BF00279992>. 10.1007/BF00279992.
- [14] S. Bartels, C. Carstensen, K. Hackl, and U. Hoppe. Effective relaxation for microstructure simulations: Algorithms and applications. *Computer Methods in Applied Mechanics and Engineering*, 193(48-51):5143–5175, 2004. ISSN 00457825. doi: 10.1016/j.cma.2003.12.065.
- [15] Sören Bartels and Andreas Prohl. Multiscale resolution in the computation of crystalline microstructure. *Numerische Mathematik*, 96(4):641–660, 2004. ISSN 0029599X. doi: 10.1007/s00211-003-0483-8.
- [16] Sören Bartels, Carsten Carstensen, Sergio Conti, Klaus Hackl, Ulrich Hoppe, and Antonio Orlando. *Relaxation and the Computation of Effective Energies and Microstructures in Solid Mechanics*, pages 197–224. Springer Berlin Heidelberg, Berlin, Heidelberg, 2006. ISBN 978-3-540-35657-8. doi: 10.1007/3-540-35657-6_8. URL https://doi.org/10.1007/3-540-35657-6_8.
- [17] S.R. Beissel, C.A. Gerlach, and G.R. Johnson. Hypervelocity impact computations with finite elements and meshfree particles. *International Journal of Impact Engineering*, 33(1):80 – 90, 2006. ISSN 0734-743X. doi: <https://doi.org/10.1016/j.ijimpeng.2006.09.047>. URL <http://www.sciencedirect.com/science/article/pii/S0734743X06001734>. Hypervelocity Impact Proceedings of the 2005 Symposium.

- [18] Stephen Beissel and Ted Belytschko. Nodal integration of the element-free Galerkin method. *Computer Methods in Applied Mechanics and Engineering*, 139(1):49 – 74, 1996. ISSN 0045-7825. doi: [https://doi.org/10.1016/S0045-7825\(96\)01079-1](https://doi.org/10.1016/S0045-7825(96)01079-1). URL <http://www.sciencedirect.com/science/article/pii/S0045782596010791>.
- [19] T. Belytschko, Y. Y. Lu, and L. Gu. Element-free Galerkin methods. *International Journal for Numerical Methods in Engineering*, 37(2):229–256, 1994. ISSN 1097-0207. doi: 10.1002/nme.1620370205. URL <http://dx.doi.org/10.1002/nme.1620370205>.
- [20] T. Belytschko, D. Organ, and Y. Krongauz. A coupled finite element-element-free Galerkin method. *Computational Mechanics*, 17(3):186–195, May 1995. ISSN 1432-0924. doi: 10.1007/BF00364080. URL <https://doi.org/10.1007/BF00364080>.
- [21] T. Belytschko, Y. Krongauz, D. Organ, M. Fleming, and P. Krysl. Meshless methods: An overview and recent developments. *Computer Methods in Applied Mechanics and Engineering*, 139(1):3 – 47, 1996. ISSN 0045-7825. doi: [http://dx.doi.org/10.1016/S0045-7825\(96\)01078-X](http://dx.doi.org/10.1016/S0045-7825(96)01078-X). URL <http://www.sciencedirect.com/science/article/pii/S004578259601078X>.
- [22] T. Belytschko, Y. Krongauz, J. Dolbow, and C. Gerlach. On the completeness of meshfree particle methods. *International Journal for Numerical Methods in Engineering*, 43(5):785–819, 1998. doi: 10.1002/(SICI)1097-0207(19981115)43:5<785::AID-NME420>3.0.CO;2-9.
- [23] Ted Belytschko, Yury Krongauz, Mark Fleming, Daniel Organ, and Wing Kam Snn Liu. Smoothing and accelerated computations in the element free Galerkin method. *Journal of Computational and Applied Mathematics*, 74(1):111 – 126, 1996. ISSN 0377-0427. doi: [https://doi.org/10.1016/0377-0427\(96\)00020-9](https://doi.org/10.1016/0377-0427(96)00020-9). URL <http://www.sciencedirect.com/science/article/pii/0377042796000209>.
- [24] Ted Belytschko, Yong Guo, Wing Kam Liu, and Shao Ping Xiao. A unified stability analysis of meshless particle methods. *International Journal for Numerical Methods in Engineering*, 48(9):1359–1400, 2000. ISSN 1097-0207. doi: 10.1002/1097-0207(20000730)48:9<1359::AID-NME829>3.0.CO;2-U. URL [http://dx.doi.org/10.1002/1097-0207\(20000730\)48:9<1359::AID-NME829>3.0.CO;2-U](http://dx.doi.org/10.1002/1097-0207(20000730)48:9<1359::AID-NME829>3.0.CO;2-U).
- [25] W. Benz and E. Asphaug. Simulations of brittle solids using smooth particle hydrodynamics. *Computer Physics Communications*, 87(1):253 – 265, 1995. ISSN 0010-4655. doi: [https://doi.org/10.1016/0010-4655\(94\)00176-3](https://doi.org/10.1016/0010-4655(94)00176-3). URL <http://www.sciencedirect.com/science/article/pii/0010465594001763>. Particle Simulation Methods.

- [26] K. Bhattacharya. *Microstructure of Martensite*. Oxford University Press, Oxford, UK, 2003. ISBN 9780198509349. URL <https://global.oup.com/academic/product/microstructure-of-martensite-9780198509349?cc=ch&lang=en&>.
- [27] K. Bhattacharya, G. Friesecke, and R. D. James. The mathematics of microstructure and the design of new materials. *Proceedings of the National Academy of Sciences*, 96(15):8332–8333, 1999. doi: 10.1073/pnas.96.15.8332. URL <http://www.pnas.org/content/96/15/8332.short>.
- [28] L Blaz, T Sakai, and JJ Jonas. Effect of initial grain size on dynamic recrystallization of copper. *Metal Science*, 17(12):609–616, 1983. doi: 10.1179/030634583790420448. URL <https://doi.org/10.1179/030634583790420448>.
- [29] A. Bompadre, B. Schmidt, and M. Ortiz. Convergence analysis of meshfree approximation schemes. *SIAM Journal on Numerical Analysis*, 50(3):1344–1366, 2012. ISSN 00361429. URL <http://www.jstor.org/stable/41582947>.
- [30] J. Bonet and S. Kulasegaram. Correction and stabilization of smooth particle hydrodynamics methods with applications in metal forming simulations. *International Journal for Numerical Methods in Engineering*, 47(6):1189–1214, 2000. ISSN 1097-0207. doi: 10.1002/(SICI)1097-0207(20000228)47:6<1189::AID-NME830>3.0.CO;2-I. URL [http://dx.doi.org/10.1002/\(SICI\)1097-0207\(20000228\)47:6<1189::AID-NME830>3.0.CO;2-I](http://dx.doi.org/10.1002/(SICI)1097-0207(20000228)47:6<1189::AID-NME830>3.0.CO;2-I).
- [31] B. Bouscasse, A. Colagrossi, S. Marrone, and M. Antuono. Nonlinear water wave interaction with floating bodies in SPH. *Journal of Fluids and Structures*, 42:112 – 129, 2013. ISSN 0889-9746. doi: <https://doi.org/10.1016/j.jfluidstructs.2013.05.010>. URL <http://www.sciencedirect.com/science/article/pii/S0889974613001266>.
- [32] Stephen Boyd and Lieven Vandenbergh. *Convex Optimization*. Cambridge University Press, New York, NY, USA, 2004. ISBN 0521833787.
- [33] P. W. Bridgman. Flow phenomena in heavily stressed metals. *Journal of Applied Physics*, 8(5):328–336, 1937. doi: 10.1063/1.1710301. URL <https://doi.org/10.1063/1.1710301>.
- [34] P. W. Bridgman. On torsion combined with compression. *Journal of Applied Physics*, 14(6):273–283, 1943. doi: 10.1063/1.1714987. URL <https://doi.org/10.1063/1.1714987>.
- [35] P. W. Bridgman. The effect of hydrostatic pressure on plastic flow under shearing stress. *Journal of Applied Physics*, 17(8):692–698, 1946. doi: 10.1063/1.1707772. URL <https://doi.org/10.1063/1.1707772>.
- [36] Ha H. Bui, Ryoichi Fukagawa, Kazunari Sako, and Shintaro Ohno. Lagrangian meshfree particles method (SPH) for large deformation and failure

- flows of geomaterial using elastic-plastic soil constitutive model. *International Journal for Numerical and Analytical Methods in Geomechanics*, 32 (12):1537–1570, 2008. doi: 10.1002/nag.688. URL <https://onlinelibrary.wiley.com/doi/abs/10.1002/nag.688>.
- [37] G.T. Camacho and M. Ortiz. Adaptive lagrangian modelling of ballistic penetration of metallic targets. *Computer Methods in Applied Mechanics and Engineering*, 142(3):269 – 301, 1997. ISSN 0045-7825. doi: [https://doi.org/10.1016/S0045-7825\(96\)01134-6](https://doi.org/10.1016/S0045-7825(96)01134-6). URL <http://www.sciencedirect.com/science/article/pii/S0045782596011346>.
- [38] J. Campbell, R. Vignjevic, and L. Libersky. A contact algorithm for smoothed particle hydrodynamics. *Computer Methods in Applied Mechanics and Engineering*, 184(1):49 – 65, 2000. ISSN 0045-7825. doi: [https://doi.org/10.1016/S0045-7825\(99\)00442-9](https://doi.org/10.1016/S0045-7825(99)00442-9). URL <http://www.sciencedirect.com/science/article/pii/S0045782599004429>.
- [39] R.P. Carreker and W.R. Hibbard. Tensile deformation of high-purity copper as a function of temperature, strain rate, and grain size. *Acta Metallurgica*, 1(6):654 – 663, 1953. ISSN 0001-6160. doi: [https://doi.org/10.1016/0001-6160\(53\)90022-4](https://doi.org/10.1016/0001-6160(53)90022-4). URL <http://www.sciencedirect.com/science/article/pii/0001616053900224>.
- [40] Carsten Carstensen. Ten remarks on nonconvex minimisation for phase transition simulations. *Computer Methods in Applied Mechanics and Engineering*, 194(2-5 SPEC. ISS.):169–193, 2005. ISSN 00457825. doi: 10.1016/j.cma.2004.05.012.
- [41] Carsten Carstensen and P Plecháč. Numerical solution of the scalar double-well problem allowing microstructure. *Mathematics of Computation*, 66 (219):997–1026, 1997. ISSN 00255718. URL <http://www.ams.org/mcom/1997-66-219/S0025-5718-97-00849-1/>.
- [42] Carsten Carstensen, Sergio Conti, and Antonio Orlando. Mixed analytical-numerical relaxation in finite single-slip crystal plasticity. *Continuum Mechanics and Thermodynamics*, 20(5):275–301, 2008. ISSN 09351175. doi: 10.1007/s00161-008-0082-0.
- [43] J.L. Cercos-Pita, M. Antuono, A. Colagrossi, and A. Souto-Iglesias. SPH energy conservation for fluid-solid interactions. *Computer Methods in Applied Mechanics and Engineering*, 317:771 – 791, 2017. ISSN 0045-7825. doi: <https://doi.org/10.1016/j.cma.2016.12.037>. URL <http://www.sciencedirect.com/science/article/pii/S0045782516303644>.
- [44] J.-S. Chen, C. Pan, and C.-T. Wu. Large deformation analysis of rubber based on a reproducing kernel particle method. *Computational Mechanics*, 19(3): 211–227, Feb 1997. ISSN 1432-0924. doi: 10.1007/s004660050170. URL <https://doi.org/10.1007/s004660050170>.

- [45] Jiun-Shyan Chen and Hui-Ping Wang. Meshfree smooth surface contact algorithm for sheet metal forming. In *SAE 2000 World Congress*. SAE International, mar 2000. doi: <https://doi.org/10.4271/2000-01-1103>. URL <https://doi.org/10.4271/2000-01-1103>.
- [46] Jiun-Shyan Chen, C. Pan, C. M. O. L. Roque, and Hui-Ping Wang. A lagrangian reproducing kernel particle method for metal forming analysis. *Computational Mechanics*, 22(3):289–307, Sep 1998. ISSN 1432-0924. doi: 10.1007/s004660050361. URL <https://doi.org/10.1007/s004660050361>.
- [47] Jiun-Shyan Chen, Cristina Maria Oliveira Lima Roque, Chunhui Pan, and Sérgio Tonini Button. Analysis of metal forming process based on meshless method. *Journal of Materials Processing Technology*, 80-81: 642 – 646, 1998. ISSN 0924-0136. doi: [https://doi.org/10.1016/S0924-0136\(98\)00171-X](https://doi.org/10.1016/S0924-0136(98)00171-X). URL <http://www.sciencedirect.com/science/article/pii/S092401369800171X>.
- [48] Jiun-Shyan Chen, Sangpil Yoon, Hui-Ping Wang, and Wing Kam Liu. An improved reproducing kernel particle method for nearly incompressible finite elasticity. *Computer Methods in Applied Mechanics and Engineering*, 181 (1):117 – 145, 2000. ISSN 0045-7825. doi: [https://doi.org/10.1016/S0045-7825\(99\)00067-5](https://doi.org/10.1016/S0045-7825(99)00067-5). URL <http://www.sciencedirect.com/science/article/pii/S0045782599000675>.
- [49] Jiun-Shyan Chen, Cheng-Tang Wu, Sangpil Yoon, and Yang You. A stabilized conforming nodal integration for galerkin mesh-free methods. *International Journal for Numerical Methods in Engineering*, 50(2):435–466, 2001. doi: 10.1002/1097-0207(20010120)50:2<435::AID-NME32>3.0.CO;2-A.
- [50] Jiun-Shyan Chen, Sangpil Yoon, and Cheng-Tang Wu. Non-linear version of stabilized conforming nodal integration for galerkin mesh-free methods. *International Journal for Numerical Methods in Engineering*, 53(12):2587–2615, 2002. doi: 10.1002/nme.338. URL <https://onlinelibrary.wiley.com/doi/abs/10.1002/nme.338>.
- [51] Jiun-Shyan Chen, Michael Hillman, and Marcus RÅCeter. An arbitrary order variationally consistent integration for galerkin meshfree methods. *International Journal for Numerical Methods in Engineering*, 95(5):387–418, 2013. doi: 10.1002/nme.4512. URL <https://onlinelibrary.wiley.com/doi/abs/10.1002/nme.4512>.
- [52] Jiun-Shyan Chen, Ramya Rao Basava, Yantao Zhang, Robert Csapo, Vadim Malis, Usha Sinha, John Hodgson, and Shantanu Sinha. Pixel-based meshfree modelling of skeletal muscles. *Computer Methods in Biomechanics and Biomedical Engineering: Imaging & Visualization*, 4(2):73–85, 2016. doi: 10.1080/21681163.2015.1049712. URL <https://doi.org/10.1080/21681163.2015.1049712>.

- [53] J.S. Chen, W. Hu, M.A. Puso, Y. Wu, and X. Zhang. *Strain Smoothing for Stabilization and Regularization of Galerkin Meshfree Methods*, pages 57–75. Springer Berlin Heidelberg, Berlin, Heidelberg, 2007. ISBN 978-3-540-46222-4. doi: 10.1007/978-3-540-46222-4_4. URL https://doi.org/10.1007/978-3-540-46222-4_4.
- [54] Wei Chen and Tong Qiu. Simulation of earthquake-induced slope deformation using SPH method. *International Journal for Numerical and Analytical Methods in Geomechanics*, 38(3):297–330, 2014. doi: 10.1002/nag.2218. URL <https://onlinelibrary.wiley.com/doi/abs/10.1002/nag.2218>.
- [55] Michel Chipot and David Kinderlehrer. Equilibrium configurations of crystals. *Archive for Rational Mechanics and Analysis*, 103(3):237–277, Sep 1988. ISSN 1432-0673. doi: 10.1007/BF00251759. URL <https://doi.org/10.1007/BF00251759>.
- [56] J. W. Christian and S. Mahajan. Deformation twinning. *Progress in Materials Science*, 39(1-2):1–157, 1995. ISSN 00796425. doi: 10.1016/0079-6425(94)00007-7.
- [57] C. Chu and R. D. James. Analysis of microstructures in Cu-14.0%A1-3.9%Ni by energy minimization. *Journal de Physique IV, Colloque C8*, 5:143, 1995.
- [58] Andrea Colagrossi, Matteo Antuono, and David Le Touzé. Theoretical considerations on the free-surface role in the smoothed-particle-hydrodynamics model. *Phys. Rev. E*, 79:056701, May 2009. doi: 10.1103/PhysRevE.79.056701. URL <https://link.aps.org/doi/10.1103/PhysRevE.79.056701>.
- [59] Sergio Conti. Relaxation of single-slip single-crystal plasticity with linear hardening. In *Proceedings of Multiscale Material Modeling Conference. Freiburg*, pages 18–22, 2006.
- [60] Sergio Conti and Florian Theil. Single-slip elastoplastic microstructures. *Archive for Rational Mechanics and Analysis*, 178(1):125–148, Oct 2005. ISSN 1432-0673. doi: 10.1007/s00205-005-0371-8. URL <https://doi.org/10.1007/s00205-005-0371-8>.
- [61] Sergio Conti, Georg Dolzmann, and Carolin Kreisbeck. *Variational Modeling of Slip: From Crystal Plasticity to Geological Strata*, pages 31–62. Springer International Publishing, Cham, 2015. ISBN 978-3-319-18242-1. doi: 10.1007/978-3-319-18242-1_2. URL https://doi.org/10.1007/978-3-319-18242-1_2.
- [62] L.W. Cordes and B. Moran. Treatment of material discontinuity in the element-free Galerkin method. *Computer Methods in Applied Mechanics and Engineering*, 139(1):75 – 89, 1996. ISSN 0045-7825. doi: [http://dx.doi.org/10.1016/S0045-7825\(96\)01080-8](http://dx.doi.org/10.1016/S0045-7825(96)01080-8). URL <http://www.sciencedirect.com/science/article/pii/S0045782596010808>.

- [63] R. Courant. Variational methods for the solution of problems of equilibrium and vibrations. *Bull. Amer. Math. Soc.*, 49(1):1–23, 01 1943. URL <https://projecteuclid.org:443/euclid.bams/1183504922>.
- [64] B. Dacorogna. Direct methods in the calculus of variations. 1989. URL <http://www.springer.com/gb/book/9783642514401>.
- [65] F. Djavanroodi, B. Omranpour, M. Ebrahimi, and M. Sedighi. Designing of ECAP parameters based on strain distribution uniformity. *Progress in Natural Science: Materials International*, 22(5):452 – 460, 2012. ISSN 1002-0071. doi: <https://doi.org/10.1016/j.pnsc.2012.08.001>. URL <http://www.sciencedirect.com/science/article/pii/S1002007112000883>.
- [66] Olga Dmitrieva, Dierk Raabe, Stefan Müller, and Patrick W. Dondl. Analysis and Computation of Microstructure in Finite Plasticity. *Lecture Notes in Applied and Computational Mechanics*, 78:205–218, 2015. ISSN 16137736. doi: 10.1007/978-3-319-18242-1. URL <http://www.scopus.com/inward/record.url?eid=2-s2.0-84928671115{&}partnerID=tZOtx3y1>.
- [67] R.D. Doherty, D.A. Hughes, F.J. Humphreys, J.J. Jonas, D.Juul Jensen, M.E. Kassner, W.E. King, T.R. McNelley, H.J. McQueen, and A.D. Rollett. Current issues in recrystallization: a review. *Materials Science and Engineering: A*, 238(2):219 – 274, 1997. ISSN 0921-5093. doi: [https://doi.org/10.1016/S0921-5093\(97\)00424-3](https://doi.org/10.1016/S0921-5093(97)00424-3). URL <http://www.sciencedirect.com/science/article/pii/S0921509397004243>.
- [68] John Dolbow and Ted Belytschko. Numerical integration of the galerkin weak form in meshfree methods. *Computational Mechanics*, 23(3):219–230, Apr 1999. ISSN 1432-0924. doi: 10.1007/s004660050403. URL <https://doi.org/10.1007/s004660050403>.
- [69] J. Donea, S. Giuliani, and J.P. Halleux. An arbitrary lagrangian-eulerian finite element method for transient dynamic fluid-structure interactions. *Computer Methods in Applied Mechanics and Engineering*, 33(1):689 – 723, 1982. ISSN 0045-7825. doi: [https://doi.org/10.1016/0045-7825\(82\)90128-1](https://doi.org/10.1016/0045-7825(82)90128-1). URL <http://www.sciencedirect.com/science/article/pii/0045782582901281>.
- [70] Jean Donea, Antonio Huerta, J.-Ph. Ponthot, and A. Rodríguez-Ferran. *Arbitrary Lagrangian-Eulerian Methods*, chapter 14. American Cancer Society, 2004. ISBN 9780470091357. doi: 10.1002/0470091355.ecm009. URL <https://onlinelibrary.wiley.com/doi/abs/10.1002/0470091355.ecm009>.
- [71] C. T. Dyka, P. W. Randles, and R. P. Ingel. Stress points for tension instability in SPH. *International Journal for Numerical Methods in Engineering*, 40(13):2325–2341, 1997. ISSN 1097-0207. doi: 10.1002/(SICI)1097-0207(19970715)40:13<2325::AID-NME161>3.0.CO;2-8. URL [http://dx.doi.org/10.1002/\(SICI\)1097-0207\(19970715\)40:13<2325::AID-NME161>3.0.CO;2-8](http://dx.doi.org/10.1002/(SICI)1097-0207(19970715)40:13<2325::AID-NME161>3.0.CO;2-8).

- [72] C.T. Dyka and R.P. Ingel. An approach for tension instability in smoothed particle hydrodynamics (SPH). *Computers & Structures*, 57(4):573 – 580, 1995. ISSN 0045-7949. doi: [http://dx.doi.org/10.1016/0045-7949\(95\)00059-P](http://dx.doi.org/10.1016/0045-7949(95)00059-P). URL <http://www.sciencedirect.com/science/article/pii/004579499500059P>.
- [73] Yalchin Efendiev and Tom Hou. *Multiscale Finite Element Methods*. Springer New York, 2009. doi: 10.1007/978-0-387-09496-0. URL <https://doi.org/10.1007/978-0-387-09496-0>.
- [74] J. L. Ericksen. Equilibrium of bars. *Journal of Elasticity*, 5(3):191–201, Nov 1975. ISSN 1573-2681. doi: 10.1007/BF00126984. URL <https://doi.org/10.1007/BF00126984>.
- [75] Y. Estrin and A. Vinogradov. Extreme grain refinement by severe plastic deformation: A wealth of challenging science. *Acta Materialia*, 61(3):782 – 817, 2013. ISSN 1359-6454. doi: <https://doi.org/10.1016/j.actamat.2012.10.038>. URL <http://www.sciencedirect.com/science/article/pii/S1359645412007859>. The Diamond Jubilee Issue.
- [76] T. Fagan, R. Das, V. Lemiale, and Y. Estrin. Modelling of equal channel angular pressing using a mesh-free method. *Journal of Materials Science*, 47(11):4514–4519, Jun 2012. ISSN 1573-4803. doi: 10.1007/s10853-012-6296-3. URL <https://doi.org/10.1007/s10853-012-6296-3>.
- [77] Jiang Fan, Huming Liao, Renjie Ke, Erdem Kucukal, Umut A. Gurkan, Xiuli Shen, Jian Lu, and Bo Li. A monolithic lagrangian meshfree scheme for fluid-structure interaction problems within the otm framework. *Computer Methods in Applied Mechanics and Engineering*, 337:198 – 219, 2018. ISSN 0045-7825. doi: <https://doi.org/10.1016/j.cma.2018.03.031>. URL <http://www.sciencedirect.com/science/article/pii/S0045782518301555>.
- [78] Sonia Fernández-Méndez and Antonio Huerta. Imposing essential boundary conditions in mesh-free methods. *Computer Methods in Applied Mechanics and Engineering*, 193(12):1257–1275, 2004. doi: <https://doi.org/10.1016/j.cma.2003.12.019>. URL <http://www.sciencedirect.com/science/article/pii/S0045782504000222>.
- [79] Stephane Ferrasse, K. Ted Hartwig, Ramon E. Goforth, and Vladimir M. Segal. Microstructure and properties of copper and aluminum alloy 3003 heavily worked by equal channel angular extrusion. *Metallurgical and Materials Transactions A*, 28(4):1047–1057, Apr 1997. ISSN 1543-1940. doi: 10.1007/s11661-997-0234-z. URL <https://doi.org/10.1007/s11661-997-0234-z>.
- [80] Mathieu Foca. *On a Local Maximum Entropy interpolation approach for simulation of coupled thermo-mechanical problems. Application to the Rotary Frictional Welding process*. Thesis, Ecole Centrale de Nantes (ECN), 2015. URL <https://tel.archives-ouvertes.fr/tel-01230565>.

- [81] Michael J. Frazier and Dennis M. Kochmann. Atomimetic mechanical structures with nonlinear topological domain evolution kinetics. *Advanced Materials*, 29(19):1605800–n/a, 2017. ISSN 1521-4095. doi: 10.1002/adma.201605800. URL <http://dx.doi.org/10.1002/adma.201605800>. 1605800.
- [82] Harold J Frost and Michael F Ashby. *Deformation mechanism maps: the plasticity and creep of metals and ceramics*. Pergamon press, 1982.
- [83] M. W. Fu, M. S. Yong, Q. X. Pei, and H. H. Hng. Deformation behavior study of multi-pass ecae process for fabrication of ultrafine or nanostructured bulk materials. *Materials and Manufacturing Processes*, 21(5):507–512, 2006. doi: 10.1080/10426910500471557. URL <https://doi.org/10.1080/10426910500471557>.
- [84] B. G. Galerkin. Series solution of some problems of elastic equilibrium of rods and plates. *Wjestnik Ingenerow Petrograd*, pages 897–908, 1915.
- [85] J. W. Gibbs. Fourier’s series. *Nature*, 59:200, 1898. doi: 10.1038/059200b0. URL <http://www.nature.com/nature/journal/v59/n1522/abs/059200b0.html>.
- [86] J. W. Gibbs. Fourier’s series. *Nature*, 59:606, 1899. doi: 10.1038/059606a0. URL <http://www.nature.com/nature/journal/v59/n1539/pdf/059606a0.html>.
- [87] F. Goncu, S. Willshaw, J. Shim, J. Cusack, S. Luding, T. Mullin, and K. Bertoldi. Deformation induced pattern transformation in a soft granular crystal. *Soft Matter*, 7:2321–2324, 2011. doi: 10.1039/C0SM01408G. URL <http://dx.doi.org/10.1039/C0SM01408G>.
- [88] David González, Elías Cueto, and Manuel Doblaré. A higher order method based on local maximum entropy approximation. *International Journal for Numerical Methods in Engineering*, 83(6):741–764, 2010. ISSN 1097-0207. doi: 10.1002/nme.2855. URL <http://dx.doi.org/10.1002/nme.2855>.
- [89] Sanjay Govindjee, Alexander Mielke, and Garrett J. Hall. The free energy of mixing for n-variant martensitic phase transformations using quasi-convex analysis. *Journal of the Mechanics and Physics of Solids*, 51(4): I – XXVI, 2003. ISSN 0022-5096. doi: [https://doi.org/10.1016/S0022-5096\(03\)00015-2](https://doi.org/10.1016/S0022-5096(03)00015-2). URL <http://www.sciencedirect.com/science/article/pii/S0022509603000152>.
- [90] F. Greco and N. Sukumar. Derivatives of maximum-entropy basis functions on the boundary: Theory and computations. *International Journal for Numerical Methods in Engineering*, 94(12):1123–1149, 2013. doi: 10.1002/nme.4492. URL <https://onlinelibrary.wiley.com/doi/abs/10.1002/nme.4492>.
- [91] M. Griebel and M. Schweitzer. A particle-partition of unity method—part ii: Efficient cover construction and reliable integration. *SIAM Journal on Scientific Computing*, 23(5):1655–1682, 2002. doi: 10.1137/S1064827501391588. URL <https://doi.org/10.1137/S1064827501391588>.

- [92] M. Griebel and M. A. Schweitzer. *A Particle-Partition of Unity Method Part V: Boundary Conditions*, pages 519–542. Springer Berlin Heidelberg, Berlin, Heidelberg, 2003. ISBN 978-3-642-55627-2. doi: 10.1007/978-3-642-55627-2_27. URL https://doi.org/10.1007/978-3-642-55627-2_27.
- [93] P. Guyot and J. P. Simon. *Microstructural Patterns and Kinetics of Phase Separation in Binary and Ternary Metallic Systems*, pages 211–221. Springer US, Boston, MA, 1988. ISBN 978-1-4613-1019-8. doi: 10.1007/978-1-4613-1019-8_28. URL https://doi.org/10.1007/978-1-4613-1019-8_28.
- [94] Feras Habbal. *The Optimal Transportation Meshfree Method for General Fluid Flows and Strongly Coupled Fluid-Structure Interaction Problems*. PhD thesis, California Institute of Technology, Pasadena, CA, USA, 2009.
- [95] Klaus Hackl, Ulrich Hoppe, and Dennis M. Kochmann. *Variational modeling of microstructures in plasticity*, pages 65–129. Springer Vienna, Vienna, 2014. ISBN 978-3-7091-1625-8. doi: 10.1007/978-3-7091-1625-8_2. URL https://doi.org/10.1007/978-3-7091-1625-8_2.
- [96] Paul Hakansson, Mathias Wallin, and Matti Ristinmaa. Prediction of stored energy in polycrystalline materials during cyclic loading. *International Journal of Solids and Structures*, 45(6):1570 – 1586, 2008. ISSN 0020-7683. doi: <https://doi.org/10.1016/j.ijsolstr.2007.10.009>. URL <http://www.sciencedirect.com/science/article/pii/S0020768307004192>.
- [97] EO Hall. The deformation and ageing of mild steel: III discussion of results. *Proceedings of the Physical Society. Section B*, 64(9):747, 1951.
- [98] Håkan Hallberg. Approaches to modeling of recrystallization. *Metals*, 1(1): 16–48, 2011. doi: 10.3390/met1010016. URL <http://www.mdpi.com/2075-4701/1/1/16>.
- [99] Edwin Hewitt and Robert E. Hewitt. The gibbs-wilbraham phenomenon: An episode in fourier analysis. *Archive for History of Exact Sciences*, 21 (2):129–160, 1979. ISSN 1432-0657. doi: 10.1007/BF00330404. URL <http://dx.doi.org/10.1007/BF00330404>.
- [100] C.W Hirt, A.A Amsden, and J.L Cook. An arbitrary Lagrangian-Eulerian computing method for all flow speeds. *Journal of Computational Physics*, 14(3):227 – 253, 1974. ISSN 0021-9991. doi: [https://doi.org/10.1016/0021-9991\(74\)90051-5](https://doi.org/10.1016/0021-9991(74)90051-5). URL <http://www.sciencedirect.com/science/article/pii/0021999174900515>.
- [101] A. Hrennikoff. Solution of problems of elasticity by the framework method. *J. Appl. Mech.*, 1941. URL <https://ci.nii.ac.jp/naid/10015257315/en/>.
- [102] K Huang and RE Logé. A review of dynamic recrystallization phenomena in metallic materials. *Materials & Design*, 111:548–574, 2016.

- [103] Antonio Huerta and Sonia Fernández-Méndez. Enrichment and coupling of the finite element and meshless methods. *International Journal for Numerical Methods in Engineering*, 48(11):1615–1636, 2000. doi: 10.1002/1097-0207(20000820)48:11<1615::AID-NME883>3.0.CO;2-S. URL <https://onlinelibrary.wiley.com/doi/abs/10.1002/1097-0207%2820000820%2948%3A11%3C1615%3A%3AAID-NME883%3E3.0.CO%3B2-S>.
- [104] Yoshinori Iwahashi, Jingtao Wang, Zenji Horita, Minoru Nemoto, and Terence G. Langdon. Principle of equal-channel angular pressing for the processing of ultra-fine grained materials. *Scripta Materialia*, 35(2):143 – 146, 1996. ISSN 1359-6462. doi: [https://doi.org/10.1016/1359-6462\(96\)00107-8](https://doi.org/10.1016/1359-6462(96)00107-8). URL <http://www.sciencedirect.com/science/article/pii/S1359646296001078>.
- [105] E. T. Jaynes. Information theory and statistical mechanics. *Phys. Rev.*, 106: 620–630, 1957. doi: 10.1103/PhysRev.106.620. URL <https://link.aps.org/doi/10.1103/PhysRev.106.620>.
- [106] G. R. Johnson and S. R. Beissel. Normalized smoothing functions for SPH impact computations. *International Journal for Numerical Methods in Engineering*, 39(16):2725–2741, 1996. doi: 10.1002/(SICI)1097-0207(19960830)39:16<2725::AID-NME973>3.0.CO;2-9.
- [107] Gordon R. Johnson. Numerical algorithms and material models for high-velocity impact computations. *International Journal of Impact Engineering*, 38(6):456 – 472, 2011. ISSN 0734-743X. doi: <https://doi.org/10.1016/j.ijimpeng.2010.10.017>. URL <http://www.sciencedirect.com/science/article/pii/S0734743X10001636>. Hypervelocity Impact selected papers from the 2010 Symposium.
- [108] Gordon R. Johnson, Robert A. Stryk, and Stephen R. Beissel. Sph for high velocity impact computations. *Computer Methods in Applied Mechanics and Engineering*, 139(1):347 – 373, 1996. ISSN 0045-7825. doi: [https://doi.org/10.1016/S0045-7825\(96\)01089-4](https://doi.org/10.1016/S0045-7825(96)01089-4). URL <http://www.sciencedirect.com/science/article/pii/S0045782596010894>.
- [109] G.R. Johnson, S.R. Beissel, and C.A. Gerlach. A combined particle-element method for high-velocity impact computations. *Procedia Engineering*, 58:269 – 278, 2013. ISSN 1877-7058. doi: <https://doi.org/10.1016/j.proeng.2013.05.031>. URL <http://www.sciencedirect.com/science/article/pii/S1877705813009375>. Proceedings of the 12th Hypervelocity Impact Symposium.
- [110] A. Kamoulakis. A simple benchmark for impact. *Benchmark*, pages 31 – 35, 1990.
- [111] N. H. Kim, K. K. Choi, J. S. Chen, and Y. H. Park. Meshless shape design sensitivity analysis and optimization for contact problem with friction. *Com-*

- putational Mechanics*, 25(2):157–168, Mar 2000. ISSN 1432-0924. doi: 10.1007/s004660050466. URL <https://doi.org/10.1007/s004660050466>.
- [112] Nam H. Kim, Kyung K. Choi, and Jiun S. Chen. Shape design sensitivity analysis and optimization of elasto-plasticity with frictional contact. *AIAA Journal*, 38(9):1742–1753, 2019/01/09 2000. doi: 10.2514/2.1163. URL <https://doi.org/10.2514/2.1163>.
- [113] Nam Ho Kim, Kyung Kook Choi, and Jiun Shyan Chen. Die shape design optimization of sheet metal stamping process using meshfree method. *International Journal for Numerical Methods in Engineering*, 51(12):1385–1405, 2001. doi: 10.1002/nme.181. URL <https://onlinelibrary.wiley.com/doi/abs/10.1002/nme.181>.
- [114] David Kinderlehrer and Pablo Pedregal. Gradient young measures generated by sequences in sobolev spaces. *The Journal of Geometric Analysis*, 4(1): 59, Mar 1994. ISSN 1559-002X. doi: 10.1007/BF02921593. URL <https://doi.org/10.1007/BF02921593>.
- [115] Benjamin Klusemann and Dennis M. Kochmann. Microstructural pattern formation in finite-deformation single-slip crystal plasticity under cyclic loading: Relaxation vs. gradient plasticity. *Computer Methods in Applied Mechanics and Engineering*, 278:765–793, 2014. ISSN 00457825. doi: 10.1016/j.cma.2014.05.015. URL <http://dx.doi.org/10.1016/j.cma.2014.05.015>.
- [116] D. M. Kochmann and K. Hackl. Influence of hardening on the cyclic behavior of laminate microstructures in finite crystal plasticity. *Techn. Mech.*, 30:387–400, 2010. URL http://www.uni-magdeburg.de/ifme/zeitschrift_tm/2010_Heft4/08_Kochmann_Hackl.pdf.
- [117] D. M. Kochmann and K. Hackl. The evolution of laminates in finite crystal plasticity: A variational approach. *Continuum Mechanics and Thermodynamics*, 23(1):63–85, 2011. ISSN 09351175. doi: 10.1007/s00161-010-0174-5.
- [118] Dennis M Kochmann and Gabriela N Venturini. A meshless quasicontinuum method based on local maximum-entropy interpolation. *Modelling and Simulation in Materials Science and Engineering*, 22(3):034007, apr 2014. doi: 10.1088/0965-0393/22/3/034007. URL <https://doi.org/10.1088/0965-0393/22/3/034007>.
- [119] D.M. Kochmann and K. Hackl. Time-continuous evolution of microstructures in finite plasticity. In K Hackl, editor, *IUTAM Symposium on Variational Concepts with Applications of the Mechanics of Materials*, volume 21 of *IUTAM Bookseries*, pages 117–130, 2010. ISBN 978-90-481-9195-6. doi: 10.1007/978-90-481-9195-6_9.
- [120] U Fred Kocks, Carlos Norberto Tomé, H-R Wenk, and Armand J Beaudoin. *Texture and anisotropy: preferred orientations in polycrystals and their effect on materials properties*. Cambridge university press, 2000.

- [121] W.T. Koiter. Energy criterion of stability for continuous elastic bodies. *Proceedings of the Koninklijke Nederlandse Academie van Wetenschappen B*, 868:178–202, 1965.
- [122] V. Kouznetsova, W. A. M. Brekelmans, and F. P. T. Baaijens. An approach to micro-macro modeling of heterogeneous materials. *Computational Mechanics*, 27(1):37–48, Jan 2001. ISSN 1432-0924. doi: 10.1007/s004660000212. URL <https://doi.org/10.1007/s004660000212>.
- [123] Y. Krongauz and T. Belytschko. Enforcement of essential boundary conditions in meshless approximations using finite elements. *Computer Methods in Applied Mechanics and Engineering*, 131(1):133 – 145, 1996. ISSN 0045-7825. doi: [https://doi.org/10.1016/0045-7825\(95\)00954-X](https://doi.org/10.1016/0045-7825(95)00954-X). URL <http://www.sciencedirect.com/science/article/pii/004578259500954X>.
- [124] Y. Krongauz and T. Belytschko. EFG approximation with discontinuous derivatives. *International Journal for Numerical Methods in Engineering*, 41(7):1215–1233, 1998. doi: 10.1002/(SICI)1097-0207(19980415)41:7<1215::AID-NME330>3.0.CO;2-#. URL <https://onlinelibrary.wiley.com/doi/abs/10.1002/%28SICI%291097-0207%2819980415%2941%3A7%3C1215%3A%3AAID-NME330%3E3.0.CO%3B2-%23>.
- [125] Petr Krysl and Ted Belytschko. Element-free Galerkin method: Convergence of the continuous and discontinuous shape functions. *Computer Methods in Applied Mechanics and Engineering*, 148(3):257 – 277, 1997. ISSN 0045-7825. doi: [https://doi.org/10.1016/S0045-7825\(96\)00007-2](https://doi.org/10.1016/S0045-7825(96)00007-2). URL <http://www.sciencedirect.com/science/article/pii/S0045782596000072>.
- [126] S. Kumar, K. Danas, and D. M. Kochmann. Enhanced local maximum-entropy approximation for stable meshfree simulations. *Computer Methods in Applied Mechanics and Engineering*, 344:858 – 886, 2019. ISSN 0045-7825. doi: <https://doi.org/10.1016/j.cma.2018.10.030>. URL <http://www.sciencedirect.com/science/article/pii/S0045782518305346>.
- [127] P. Lancaster and K. Sakauskas. *Surfaces Generated by Moving Least Squares Methods*. Research paper. University of Calgary, Department of Mathematics and Statistics, 1979. URL <https://books.google.nl/books?id=yf3KGwAACAAJ>.
- [128] H. Le Dret and A. Raoult. The quasiconvex envelope of the saint venant-kirchhoff stored energy function. *Proceedings of the Royal Society of Edinburgh: Section A Mathematics*, 125(6):1179–1192, 1995. doi: 10.1017/S0308210500030456.
- [129] Ricardo A. Lebensohn and Alan Needleman. Numerical implementation of non-local polycrystal plasticity using fast Fourier transforms. *Journal*

- of the Mechanics and Physics of Solids*, 97:333 – 351, 2016. ISSN 0022-5096. doi: <http://dx.doi.org/10.1016/j.jmps.2016.03.023>. URL <http://www.sciencedirect.com/science/article/pii/S0022509616301958>.
- [130] Ricardo A. Lebensohn, Anand K. Kanjarla, and Philip Eisenlohr. An elasto-viscoplastic formulation based on fast Fourier transforms for the prediction of micromechanical fields in polycrystalline materials. *International Journal of Plasticity*, 32-33:59–69, 2012. ISSN 07496419. doi: 10.1016/j.ijplas.2011.12.005. URL <http://dx.doi.org/10.1016/j.ijplas.2011.12.005>.
- [131] H. M. Ledbetter and E. R. Naimon. Elastic properties of metals and alloys. ii. copper. *Journal of Physical and Chemical Reference Data*, 3(4):897–935, 1974. doi: 10.1063/1.3253150. URL <https://doi.org/10.1063/1.3253150>.
- [132] B. Li, F. Habbal, and M. Ortiz. Optimal transportation meshfree approximation schemes for fluid and plastic flows. *International Journal for Numerical Methods in Engineering*, 83(12):1541–1579, 2010. ISSN 1097-0207. doi: 10.1002/nme.2869. URL <http://dx.doi.org/10.1002/nme.2869>.
- [133] B. Li, L. Perotti, M. Adams, J. Mihaly, A.J. Rosakis, M. Stalzer, and Michael Ortiz. Large scale optimal transportation meshfree (otm) simulations of hypervelocity impact. *Procedia Engineering*, 58:320 – 327, 2013. ISSN 1877-7058. doi: <https://doi.org/10.1016/j.proeng.2013.05.036>. URL <http://www.sciencedirect.com/science/article/pii/S1877705813009429>. Proceedings of the 12th Hypervelocity Impact Symposium.
- [134] B. Li, A. Pandolfi, and M. Ortiz. Material-point erosion simulation of dynamic fragmentation of metals. *Mechanics of Materials*, 80:288 – 297, 2015. ISSN 0167-6636. doi: <https://doi.org/10.1016/j.mechmat.2014.03.008>. URL <http://www.sciencedirect.com/science/article/pii/S0167663614000519>. Materials and Interfaces.
- [135] Bo Li. *The optimal transportation method in solid mechanics*. PhD thesis, California Institute of Technology, 2009.
- [136] S. Li, W. Hao, and W. K. Liu. Numerical simulations of large deformation of thin shell structures using meshfree methods. *Computational Mechanics*, 25(2):102–116, Mar 2000. ISSN 1432-0924. doi: 10.1007/s004660050463. URL <https://doi.org/10.1007/s004660050463>.
- [137] Shaofan Li, Wei Hao, and Wing Kam Liu. Mesh-free simulations of shear banding in large deformation. *International Journal of Solids and Structures*, 37(48):7185 – 7206, 2000. ISSN 0020-7683. doi: [https://doi.org/10.1016/S0020-7683\(00\)00195-5](https://doi.org/10.1016/S0020-7683(00)00195-5). URL <http://www.sciencedirect.com/science/article/pii/S0020768300001955>.
- [138] Shaofan Li, Wing-Kam Liu, Dong Qian, Pradeep R. Guduru, and Ares J. Rosakis. Dynamic shear band propagation and micro-structure of adiabatic

- shear band. *Computer Methods in Applied Mechanics and Engineering*, 191 (1):73 – 92, 2001. ISSN 0045-7825. doi: [https://doi.org/10.1016/S0045-7825\(01\)00245-6](https://doi.org/10.1016/S0045-7825(01)00245-6). URL <http://www.sciencedirect.com/science/article/pii/S0045782501002456>. Micromechanics of Brittle Materials and Stochastic Analysis of Mechanical Systems.
- [139] Shaofan Li, Wing Kam Liu, Ares J. Rosakis, Ted Belytschko, and Wei Hao. Mesh-free galerkin simulations of dynamic shear band propagation and failure mode transition. *International Journal of Solids and Structures*, 39(5): 1213 – 1240, 2002. ISSN 0020-7683. doi: [https://doi.org/10.1016/S0020-7683\(01\)00188-3](https://doi.org/10.1016/S0020-7683(01)00188-3). URL <http://www.sciencedirect.com/science/article/pii/S0020768301001883>.
- [140] Zhi-Ping Li and Carsten Carstensen. An averaging scheme for macroscopic numerical simulation of nonconvex minimization problems. *BIT Numerical Mathematics*, 47(3):601–611, Sep 2007. ISSN 1572-9125. doi: 10.1007/s10543-007-0140-1. URL <https://doi.org/10.1007/s10543-007-0140-1>.
- [141] Zhiping Li. A mesh transformation method for computing microstructures. *Numerische Mathematik*, 89(3):511–533, Sep 2001. ISSN 0945-3245. doi: 10.1007/PL00005477. URL <https://doi.org/10.1007/PL00005477>.
- [142] Larry D. Libersky and A. G. Petschek. Smooth particle hydrodynamics with strength of materials. In Harold E. Trease, Martin F. Fritts, and W. Patrick Crowley, editors, *Advances in the Free-Lagrange Method Including Contributions on Adaptive Gridding and the Smooth Particle Hydrodynamics Method*, pages 248–257, Berlin, Heidelberg, 1991. Springer Berlin Heidelberg. ISBN 978-3-540-46608-6.
- [143] Wing Kam Liu, Sukky Jun, Shaofan Li, Jonathan Adee, and Ted Belytschko. Reproducing kernel particle methods for structural dynamics. *International Journal for Numerical Methods in Engineering*, 38(10):1655–1679, 1995. doi: 10.1002/nme.1620381005. URL <https://onlinelibrary.wiley.com/doi/abs/10.1002/nme.1620381005>.
- [144] Wing Kam Liu, Sukky Jun, and Yi Fei Zhang. Reproducing kernel particle methods. *International Journal for Numerical Methods in Fluids*, 20(8-9): 1081–1106, 1995. ISSN 1097-0363. doi: 10.1002/flid.1650200824. URL <http://dx.doi.org/10.1002/flid.1650200824>.
- [145] Yan Liu and Ted Belytschko. A new support integration scheme for the weakform in mesh-free methods. *International Journal for Numerical Methods in Engineering*, 82(6):699–715, 2010. doi: 10.1002/nme.2780. URL <https://onlinelibrary.wiley.com/doi/abs/10.1002/nme.2780>.
- [146] L. B. Lucy. A numerical approach to the testing of the fission hypothesis. *Astronomical Journal*, 82:1013–1024, December 1977. URL <http://adsabs.harvard.edu/full/1977AJ.....82.1013L>.

- [147] C. J. Luis, Y. Garcés, P. González, and C. Berlanga. Fem analysis of equal channel angular processes. *Materials and Manufacturing Processes*, 17(2): 223–250, 2002. doi: 10.1081/AMP-120003532. URL <https://doi.org/10.1081/AMP-120003532>.
- [148] Anxin Ma and Alexander Hartmaier. A crystal plasticity smooth-particle hydrodynamics approach and its application to equal-channel angular pressing simulation. *Modelling and Simulation in Materials Science and Engineering*, 24(8):085011, 2016. URL <http://stacks.iop.org/0965-0393/24/i=8/a=085011>.
- [149] Fabricio Maciá, Matteo Antuono, Leo M. González, and Andrea Colagrossi. Theoretical analysis of the no-slip boundary condition enforcement in SPH methods. *Progress of Theoretical Physics*, 125(6):1091–1121, 2011. doi: 10.1143/PTP.125.1091. URL <http://dx.doi.org/10.1143/PTP.125.1091>.
- [150] Arno Mayrhofer, Martin Ferrand, Christophe Kassiotis, Damien Violeau, and François-Xavier Morel. Unified semi-analytical wall boundary conditions in SPH: analytical extension to 3-D. *Numerical Algorithms*, 68(1):15–34, Jan 2015. ISSN 1572-9265. doi: 10.1007/s11075-014-9835-y. URL <https://doi.org/10.1007/s11075-014-9835-y>.
- [151] Y Mellbin, H Hallberg, and M Ristinmaa. A combined crystal plasticity and graph-based vertex model of dynamic recrystallization at large deformations. *Modelling and Simulation in Materials Science and Engineering*, 23(4):045011, 2015. URL <http://stacks.iop.org/0965-0393/23/i=4/a=045011>.
- [152] Ylva Mellbin, Håkan Hallberg, and Matti Ristinmaa. Recrystallization and texture evolution during hot rolling of copper, studied by a multiscale model combining crystal plasticity and vertex models. *Modelling and Simulation in Materials Science and Engineering*, 24(7):075004, 2016. doi: 10.1088/0965-0393/24/7/075004. URL <http://stacks.iop.org/0965-0393/24/i=7/a=075004>.
- [153] C. Miehe, J. Schröder, and M. Becker. Computational homogenization analysis in finite elasticity: material and structural instabilities on the micro- and macro-scales of periodic composites and their interaction. *Computer Methods in Applied Mechanics and Engineering*, 191(44):4971–5005, 2002. doi: 10.1016/S0045-7825(02)00391-2. URL <http://www.sciencedirect.com/science/article/pii/S0045782502003912>.
- [154] C. Miehe, M. Lambrecht, and E. Gürses. Analysis of material instabilities in inelastic solids by incremental energy minimization and relaxation methods: Evolving deformation microstructures in finite plasticity. *Journal of the Mechanics and Physics of Solids*, 52(12):2725–2769, 2004. ISSN 00225096. doi: 10.1016/j.jmps.2004.05.011.
- [155] Luciano Modica. Gradient theory of phase transitions with boundary contact energy. *Annales de l’Institut Henri Poincaré (C) Non Linear Analysis*, 4(5):

- 487 – 512, 1987. ISSN 0294-1449. doi: [https://doi.org/10.1016/S0294-1449\(16\)30360-2](https://doi.org/10.1016/S0294-1449(16)30360-2). URL <http://www.sciencedirect.com/science/article/pii/S0294144916303602>.
- [156] J. J. Monaghan. Smoothed particle hydrodynamics. *Annual Review of Astronomy and Astrophysics*, 30(1):543–574, 1992. doi: 10.1146/annurev.aa.30.090192.002551. URL <https://doi.org/10.1146/annurev.aa.30.090192.002551>.
- [157] J J Monaghan. Smoothed particle hydrodynamics. *Reports on Progress in Physics*, 68(8):1703, 2005. URL <http://stacks.iop.org/0034-4885/68/i=8/a=R01>.
- [158] C. B. Morrey. Quasi-convexity and the lower semicontinuity of multiple integrals. *Pacific J. Math.*, 2:25–53, 1952.
- [159] H. Moulinec and P. Suquet. A numerical method for computing the overall response of nonlinear composites with complex microstructure. *Computer Methods in Applied Mechanics and Engineering*, 157(1-2):69–94, 1998. ISSN 00457825. doi: 10.1016/S0045-7825(97)00218-1.
- [160] H. Moulinec and P. Suquet. Comparison of FFT-based methods for computing the response of composites with highly contrasted mechanical properties. *Physica B: Condensed Matter*, 338(1-4):58–60, 2003. ISSN 09214526. doi: 10.1016/S0921-4526(03)00459-9.
- [161] W.H. Müller. Fourier Transforms and their application to the formation of textures and changes of morphology in solids. In *IUTAM Symposium on Transformation Problems in Composite and Active Materials*, pages 61–72. Kluwer Academic Publishers, 1998.
- [162] B. Nayroles, G. Touzot, and P. Villon. Generalizing the finite element method: Diffuse approximation and diffuse elements. *Computational Mechanics*, 10(5):307–318, Sep 1992. ISSN 1432-0924. doi: 10.1007/BF00364252. URL <https://doi.org/10.1007/BF00364252>.
- [163] R. Nicolaides, N. Walkington, and H. Wang. Numerical methods for a nonconvex optimization problem modeling martensitic microstructure. *SIAM Journal on Scientific Computing*, 18(4):1122–1141, 1997. doi: 10.1137/S1064827595283471. URL <https://doi.org/10.1137/S1064827595283471>.
- [164] J. Nitsche. Über ein variationsprinzip zur lösung von dirichlet-problemen bei verwendung von teilräumen, die keinen randbedingungen unterworfen sind. *Abhandlungen aus dem Mathematischen Seminar der Universität Hamburg*, 36(1):9–15, Jul 1971. ISSN 1865-8784. doi: 10.1007/BF02995904. URL <https://doi.org/10.1007/BF02995904>.

- [165] D. Organ, M. Fleming, T. Terry, and T. Belytschko. Continuous meshless approximations for nonconvex bodies by diffraction and transparency. *Computational Mechanics*, 18(3):225–235, 1996. ISSN 1432-0924. doi: 10.1007/BF00369940. URL <https://doi.org/10.1007/BF00369940>.
- [166] A. Ortiz, M. A. Puso, and N. Sukumar. Maximum-entropy meshfree method for compressible and near-incompressible elasticity. *Computer Methods in Applied Mechanics and Engineering*, 199(25):1859–1871, 2010. doi: <https://doi.org/10.1016/j.cma.2010.02.013>. URL <http://www.sciencedirect.com/science/article/pii/S004578251000071X>.
- [167] A. Ortiz, M. A. Puso, and N. Sukumar. Maximum-entropy meshfree method for incompressible media problems. *Finite Elements in Analysis and Design*, 47(6):572 – 585, 2011. ISSN 0168-874X. doi: <https://doi.org/10.1016/j.finel.2010.12.009>. URL <http://www.sciencedirect.com/science/article/pii/S0168874X10002040>. The Twenty-Second Annual Robert J. Melosh Competition.
- [168] M. Ortiz and E. A. Repetto. Nonconvex energy minimization and dislocation structures in ductile single crystals. *Journal of the Mechanics and Physics of Solids*, 47:397–462, 1999.
- [169] M. Ortiz and L. Stainier. The variational formulation of viscoplastic constitutive updates. *Computer Methods in Applied Mechanics and Engineering*, 171(3-4):419 – 444, 1999. ISSN 0045-7825. doi: [http://dx.doi.org/10.1016/S0045-7825\(98\)00219-9](http://dx.doi.org/10.1016/S0045-7825(98)00219-9). URL <http://www.sciencedirect.com/science/article/pii/S0045782598002199>.
- [170] J. T. B. Overvelde, S. Shan, and K. Bertoldi. Compaction through buckling in 2d periodic, soft and porous structures: Effect of pore shape. *Advanced Materials*, 24(17):2337–2342, 2012. doi: 10.1002/adma.201104395. URL <http://dx.doi.org/10.1002/adma.201104395>.
- [171] A. Pandolfi, B. Li, and M. Ortiz. Modeling fracture by material-point erosion. *International Journal of Fracture*, 184(1):3–16, Nov 2013. ISSN 1573-2673. doi: 10.1007/s10704-012-9788-x. URL <https://doi.org/10.1007/s10704-012-9788-x>.
- [172] C. Peco, A. Rosolen, and M. Arroyo. An adaptive meshfree method for phase-field models of biomembranes. part ii: A lagrangian approach for membranes in viscous fluids. *Journal of Computational Physics*, 249:320 – 336, 2013. ISSN 0021-9991. doi: <https://doi.org/10.1016/j.jcp.2013.04.038>. URL <http://www.sciencedirect.com/science/article/pii/S0021999113003239>.
- [173] NJ Petch. The cleavage strength of polycrystals. *J. of the Iron and Steel Inst.*, 174:25–28, 1953.

- [174] Roman A. Polyak. Regularized Newton method for unconstrained convex optimization. *Mathematical Programming*, 120(1):125–145, 2009.
- [175] D. Ponge and G. Gottstein. Necklace formation during dynamic recrystallization: mechanisms and impact on flow behavior. *Acta Materialia*, 46(1):69 – 80, 1998. ISSN 1359-6454. doi: [https://doi.org/10.1016/S1359-6454\(97\)00233-4](https://doi.org/10.1016/S1359-6454(97)00233-4). URL <http://www.sciencedirect.com/science/article/pii/S1359645497002334>.
- [176] M. A. Puso, J. S. Chen, E. Zywickz, and W. Elmer. Meshfree and finite element nodal integration methods. *International Journal for Numerical Methods in Engineering*, 74(3):416–446, 2008. doi: 10.1002/nme.2181. URL <https://onlinelibrary.wiley.com/doi/abs/10.1002/nme.2181>.
- [177] T. Rabczuk and T. Belytschko. Cracking particles: a simplified meshfree method for arbitrary evolving cracks. *International Journal for Numerical Methods in Engineering*, 61(13):2316–2343, 2004. doi: 10.1002/nme.1151. URL <https://onlinelibrary.wiley.com/doi/abs/10.1002/nme.1151>.
- [178] T. Rabczuk and T. Belytschko. A three-dimensional large deformation meshfree method for arbitrary evolving cracks. *Computer Methods in Applied Mechanics and Engineering*, 196(29):2777 – 2799, 2007. ISSN 0045-7825. doi: <https://doi.org/10.1016/j.cma.2006.06.020>. URL <http://www.sciencedirect.com/science/article/pii/S0045782507000564>.
- [179] T. Rabczuk and E. Samaniego. Discontinuous modelling of shear bands using adaptive meshfree methods. *Computer Methods in Applied Mechanics and Engineering*, 197(6):641 – 658, 2008. ISSN 0045-7825. doi: <https://doi.org/10.1016/j.cma.2007.08.027>. URL <http://www.sciencedirect.com/science/article/pii/S0045782507003738>.
- [180] Timon Rabczuk and Goangseup Zi. A meshfree method based on the local partition of unity for cohesive cracks. *Computational Mechanics*, 39(6):743–760, May 2007. ISSN 1432-0924. doi: 10.1007/s00466-006-0067-4. URL <https://doi.org/10.1007/s00466-006-0067-4>.
- [181] Timon Rabczuk, Goangseup Zi, Stephane Bordas, and Hung Nguyen-Xuan. A simple and robust three-dimensional cracking-particle method without enrichment. *Computer Methods in Applied Mechanics and Engineering*, 199(37):2437 – 2455, 2010. ISSN 0045-7825. doi: <https://doi.org/10.1016/j.cma.2010.03.031>. URL <http://www.sciencedirect.com/science/article/pii/S0045782510001088>.
- [182] P.W. Randles and L.D. Libersky. Smoothed particle hydrodynamics: Some recent improvements and applications. *Computer Methods in Applied Mechanics and Engineering*, 139(1):375 – 408, 1996. ISSN 0045-7825. doi: [https://doi.org/10.1016/S0045-7825\(96\)01090-0](https://doi.org/10.1016/S0045-7825(96)01090-0). URL <http://www.sciencedirect.com/science/article/pii/S0045782596010900>.

- [183] Lord Rayleigh. Xxiv. on the calculation of chladni's figures for a square plate. *The London, Edinburgh, and Dublin Philosophical Magazine and Journal of Science*, 22(128):225–229, 1911. doi: 10.1080/14786440808637121. URL <https://doi.org/10.1080/14786440808637121>.
- [184] Walter Ritz. Über eine neue methode zur lösung gewisser variationsprobleme der mathematischen physik. *Journal für die reine und angewandte Mathematik*, 135:1–61, 1909. URL <http://eudml.org/doc/149295>.
- [185] A. Rosolen, C. Peco, and M. Arroyo. An adaptive meshfree method for phase-field models of biomembranes. part i: Approximation with maximum-entropy basis functions. *Journal of Computational Physics*, 249:303 – 319, 2013. ISSN 0021-9991. doi: <https://doi.org/10.1016/j.jcp.2013.04.046>. URL <http://www.sciencedirect.com/science/article/pii/S0021999113003483>.
- [186] Adrian Rosolen, Daniel Millán, and Marino Arroyo. On the optimum support size in meshfree methods: A variational adaptivity approach with maximum-entropy approximants. *International Journal for Numerical Methods in Engineering*, 82(7):868–895, 2010. ISSN 1097-0207. doi: 10.1002/nme.2793. URL <http://dx.doi.org/10.1002/nme.2793>.
- [187] Sandra Rugonyi and K. J. Bathe. On finite element analysis of fluid flows fully coupled with structural interactions. *CMES - Computer Modeling in Engineering and Sciences*, 2(2):195–212, 2001. ISSN 1526-1492.
- [188] Y. Saito, H. Utsunomiya, N. Tsuji, and T. Sakai. Novel ultra-high straining process for bulk materials-development of the accumulative roll-bonding (arb) process. *Acta Materialia*, 47(2):579 – 583, 1999. ISSN 1359-6454. doi: [https://doi.org/10.1016/S1359-6454\(98\)00365-6](https://doi.org/10.1016/S1359-6454(98)00365-6). URL <http://www.sciencedirect.com/science/article/pii/S1359645498003656>.
- [189] Kenichi Saitoh and Yuuki Ohnishi. SPH analysis of ECAP process by using grain refinement model. *MATERIALS TRANSACTIONS*, 50(1):19–26, 2009. doi: 10.2320/matertrans.MD200814.
- [190] Taku Sakai, Andrey Belyakov, Rustam Kaibyshev, Hiromi Miura, and John J Jonas. Dynamic and post-dynamic recrystallization under hot, cold and severe plastic deformation conditions. *Progress in Materials Science*, 60:130–207, 2014.
- [191] I. J. Schoenberg. *Contributions to the Problem of Approximation of Equidistant Data by Analytic Functions*, pages 3–57. Birkhäuser Boston, Boston, MA, 1988. ISBN 978-1-4899-0433-1. doi: 10.1007/978-1-4899-0433-1_1. URL https://doi.org/10.1007/978-1-4899-0433-1_1.
- [192] V.M. Segal. Materials processing by simple shear. *Materials Science and Engineering: A*, 197(2):157 – 164, 1995. ISSN 0921-5093. doi: [https://doi.org/10.1016/0921-5093\(95\)09705-8](https://doi.org/10.1016/0921-5093(95)09705-8). URL <http://www.sciencedirect.com/science/article/pii/0921509395097058>.

- [193] Srinivasan M. Sivakumar and Michael Ortiz. Microstructure evolution in the equal channel angular extrusion process. *Computer Methods in Applied Mechanics and Engineering*, 193(48):5177 – 5194, 2004. ISSN 0045-7825. doi: <https://doi.org/10.1016/j.cma.2004.01.036>. URL <http://www.sciencedirect.com/science/article/pii/S0045782504002713>. Advances in Computational Plasticity.
- [194] W.G. Strang and G.J. Fix. *An analysis of the finite element method*. Prentice-Hall series in automatic computation. Prentice-Hall, 1973. ISBN 9780130329462. URL <https://books.google.ch/books?id=VZRRAAAAMAAJ>.
- [195] N. Sukumar. Construction of polygonal interpolants: a maximum entropy approach. *International Journal for Numerical Methods in Engineering*, 61(12):2159–2181, 2004. doi: 10.1002/nme.1193. URL <https://onlinelibrary.wiley.com/doi/abs/10.1002/nme.1193>.
- [196] B. Ratna Sunil. Repetitive corrugation and straightening of sheet metals. *Materials and Manufacturing Processes*, 30(10):1262–1271, 2015. doi: 10.1080/10426914.2014.973600. URL <https://doi.org/10.1080/10426914.2014.973600>.
- [197] J.W. Swegle, D.L. Hicks, and S.W. Attaway. Smoothed particle hydrodynamics stability analysis. *Journal of Computational Physics*, 116(1):123 – 134, 1995. ISSN 0021-9991. doi: <http://dx.doi.org/10.1006/jcph.1995.1010>. URL <http://www.sciencedirect.com/science/article/pii/S0021999185710108>.
- [198] W. L. Tan and D. M. Kochmann. An effective constitutive model for polycrystalline ferroelectric ceramics: Theoretical framework and numerical examples. *Computational Materials Science*, 136:223 – 237, 2017. ISSN 0927-0256. doi: <https://doi.org/10.1016/j.commatsci.2017.04.032>. URL <http://www.sciencedirect.com/science/article/pii/S0927025617302240>.
- [199] Geoffrey Taylor. The use of flat-ended projectiles for determining dynamic yield stress. i. theoretical considerations. *Proceedings of the Royal Society of London. Series A, Mathematical and Physical Sciences*, 194(1038):289–299, 1948. ISSN 00804630. URL <http://www.jstor.org/stable/98289>.
- [200] C. Truesdell and W. Noll. The nonlinear field theories of mechanics. In S. Flügge, editor, *Encyclopedia of Physics III/3*. Springer, Berlin, 1965.
- [201] A. D. Tutcuoglu. *Multiscale modeling of dynamic recrystallization*. PhD thesis, California Institute of Technology, Pasadena, CA, USA, 2019.
- [202] A.D. Tutcuoglu, Y. Hollenweger, A. Stoy, and D.M. Kochmann. On the benefits of high-fidelity models in dynamic recrystallization modeling. 2019. (in preparation).

- [203] A.D. Tutcuoglu, A. Vidyasagar, K. Bhattacharya, and D.M. Kochmann. Stochastic modeling of discontinuous dynamic recrystallization at finite strains in hcp metals. *Journal of the Mechanics and Physics of Solids*, 122:590 – 612, 2019. ISSN 0022-5096. doi: <https://doi.org/10.1016/j.jmps.2018.09.032>. URL <http://www.sciencedirect.com/science/article/pii/S0022509618303569>.
- [204] Ruslan Z. Valiev, Yuri Estrin, Zenji Horita, Terence G. Langdon, Michael J. Zechetbauer, and Yuntian T. Zhu. Producing bulk ultrafine-grained materials by severe plastic deformation. *JOM*, 58(4):33–39, Apr 2006. ISSN 1543-1851. doi: 10.1007/s11837-006-0213-7. URL <https://doi.org/10.1007/s11837-006-0213-7>.
- [205] A. Vidyasagar. *Predicting microstructural pattern formation using stabilized spectral homogenization*. PhD thesis, California Institute of Technology, Pasadena, CA, USA, 2018.
- [206] A. Vidyasagar, W. L. Tan, and D. M. Kochmann. Predicting the effective response of bulk polycrystalline ferroelectric ceramics via improved spectral phase field methods. *Journal of the Mechanics and Physics of Solids*, 106: 133–151, 2017. ISSN 00225096. doi: 10.1016/j.jmps.2017.05.017.
- [207] A. Vidyasagar, Abbas D. Tutcuoglu, and Dennis M. Kochmann. Deformation patterning in finite-strain crystal plasticity by spectral homogenization with application to magnesium. *Computer Methods in Applied Mechanics and Engineering*, 335:584 – 609, 2018. ISSN 0045-7825. doi: <https://doi.org/10.1016/j.cma.2018.03.003>. URL <http://www.sciencedirect.com/science/article/pii/S0045782518301208>.
- [208] Sven C. Vogel, D.J. Alexander, Irene J. Beyerlein, Mark A.M. Bourke, Donald W. Brown, Bjørn Clausen, Carlos Tomé, R.B. Von Dreele, Terence G. Langdon, and C. Xu. Investigation of texture in ECAP materials using neutron diffraction. In *THERMEC'2003*, volume 426 of *Materials Science Forum*, pages 2661–2666. Trans Tech Publications, 7 2003. doi: 10.4028/www.scientific.net/MSF.426-432.2661.
- [209] Hui-Ping Wang, Cheng-Tang Wu, and Jiun-Shyan Chen. A reproducing kernel smooth contact formulation for metal forming simulations. *Computational Mechanics*, 54(1):151–169, Jul 2014. doi: 10.1007/s00466-014-1015-3. URL <https://doi.org/10.1007/s00466-014-1015-3>.
- [210] Francois Willot, Bassam Abdallah, and Yves Patrick Pellegrini. Fourier-based schemes with modified Green operator for computing the electrical response of heterogeneous media with accurate local fields. *International Journal for Numerical Methods in Engineering*, 98(7):518–533, 2014. ISSN 10970207. doi: 10.1002/nme.4641.

- [211] Cheng-Tang Wu, Jiun-Shyan Chen, Liqun Chi, and Frank Huck. Lagrangian meshfree formulation for analysis of geotechnical materials. *Journal of Engineering Mechanics*, 127(5):440–449, 2001. doi: 10.1061/(ASCE)0733-9399(2001)127:5(440).
- [212] Sangpil Yoon and Jiun-Shyan Chen. Accelerated meshfree method for metal forming simulation. *Finite Elements in Analysis and Design*, 38(10): 937 – 948, 2002. ISSN 0168-874X. doi: [https://doi.org/10.1016/S0168-874X\(02\)00086-0](https://doi.org/10.1016/S0168-874X(02)00086-0). URL <http://www.sciencedirect.com/science/article/pii/S0168874X02000860>. 2001 Robert J. Melosh Medal Competition.
- [213] L. W. Zhang, A. S. Ademiloye, and K. M. Liew. Meshfree and particle methods in biomechanics: Prospects and challenges. *Archives of Computational Methods in Engineering*, Sep 2018. ISSN 1886-1784. doi: 10.1007/s11831-018-9283-2. URL <https://doi.org/10.1007/s11831-018-9283-2>.
- [214] Pengyang Zhao, Thaddeus Song En Low, Yunzhi Wang, and Stephen R Niezgod. An integrated full-field model of concurrent plastic deformation and microstructure evolution: Application to 3D simulation of dynamic recrystallization in polycrystalline copper. *International Journal of Plasticity*, 80:38–55, 2016. doi: <https://doi.org/10.1016/j.ijplas.2015.12.010>. URL <http://www.sciencedirect.com/science/article/pii/S0749641915002156>.
- [215] T. Zhu and S. N. Atluri. A modified collocation method and a penalty formulation for enforcing the essential boundary conditions in the element free galerkin method. *Computational Mechanics*, 21(3):211–222, Apr 1998. ISSN 1432-0924. doi: 10.1007/s004660050296. URL <https://doi.org/10.1007/s004660050296>.
- [216] Y. Y. Zhu and S. Cescotto. Unified and mixed formulation of the 4-node quadrilateral elements by assumed strain method: Application to thermomechanical problems. *International Journal for Numerical Methods in Engineering*, 38(4):685–716, 1995. doi: 10.1002/nme.1620380411. URL <https://onlinelibrary.wiley.com/doi/abs/10.1002/nme.1620380411>.
- [217] Xiaoying Zhuang, Charles Augarde, and Stéphane Bordas. Accurate fracture modelling using meshless methods, the visibility criterion and level sets: Formulation and 2d modelling. *International Journal for Numerical Methods in Engineering*, 86(2):249–268, 2011. doi: 10.1002/nme.3063. URL <https://onlinelibrary.wiley.com/doi/abs/10.1002/nme.3063>.
- [218] William B J Zimmerman. *Multiphysics Modeling with Finite Element Methods*. WORLD SCIENTIFIC, oct 2006. doi: 10.1142/6141. URL <https://doi.org/10.1142/6141>.